

**A combined experimental, data-driven, and numerical
approach to deform thin Ti6Al4V sheets using laser peen
forming**

Dissertation (monograph) approved by the

Doctoral Degree Committee of
Hamburg University of Technology

in pursuit of the academic degree of

Doktor-Ingenieur (Dr.-Ing.)

written by

Siva Teja Sala
from
Visakhapatnam, India

2024

Supervisor and first reviewer: PD Dr.-Ing. habil. Nikolai Kashaev
Technische Universität Hamburg (TUHH),
Helmholtz Zentrum Hereon

Second reviewer: Prof. Dr.-Ing. Noomane Ben Khalifa
Leuphana Universität Lüneburg, Helmholtz Zen-
trum Hereon

Chairman of the examination board: Prof. Dr.-Ing. Jürgen Grabe
Technische Universität Hamburg (TUHH)

Date of the oral examination: 19th November 2024

DOI: <https://doi.org/10.15480/882.13757>

ORCID: <https://orcid.org/0000-0002-1932-5169>

Creative Commons License

The text is, unless otherwise indicated, under the Creative Commons Attribution 4.0 License (CC BY 4.0). This means that it may be reproduced, distributed and made publicly available, even commercially, as long as the author, the source of the text and the above-mentioned license are always mentioned. The exact wording of the license can be found at <https://creativecommons.org/licenses/by/4.0/legalcode.de> be called.

Acknowledgments

I want to express my deepest gratitude to my supervisor, Dr.-Ing. Nikolai Kashaev, for his invaluable guidance, unwavering support, and encouragement throughout this journey. His expertise, patience, and insightful feedback have been instrumental in shaping this thesis. Under his mentorship, I was afforded the liberty to explore my research independently, a freedom for which I am profoundly grateful. I am especially thankful for the opportunity to work in his research group on the PEENCOR project, which has significantly influenced my development and career as a researcher.

I am also deeply grateful to Prof. Dr.-Ing. Norbert Huber and Prof. Dr.-Ing. Benjamin Klusemann for their insightful technical discussions. Their expertise and guidance have been pivotal in improving this work.

I am thankful to the members of my thesis committee, Dr.-Ing. Nikolai Kashaev, Prof. Dr.-Ing. Noomane Ben Khalifa and Prof. Dr.-Ing. Jürgen Grabe, for dedicating their time to review and evaluate my work.

I would like to thank René Dinse, Falk Dorn, and Dr. Volker Ventzke for their invaluable support and cooperation in the Laser and Metallography laboratories which enabled me to conduct the necessary experiments and material analyses. Special thanks to all the colleagues at the Department of Laser-Materialbearbeitung und Strukturbewertung for their collaboration, and for creating a supportive research environment. Their contributions have enriched my research experience immensely.

I would like to extend my heartfelt thanks to my colleagues, Anton Odermatt, Dominik Pörtl, Frederic Bock, Mengjie Wang, and Ruslan Kuliiev, for their stimulating conversations, exchange of ideas, and openness in sharing knowledge. Their camaraderie and intellectual collaboration have been invaluable throughout my research journey. I also extend my thanks to Richard Körner for pursuing his master's thesis on this topic, which resulted in the development of the CANN model in this study.

I am indebted to my family for their unwavering love, encouragement, and understanding throughout this demanding journey. Their support has been my pillar of strength. Last but not least, I would like to thank my friends for their encouragement, and companionship, and for being a source of inspiration during challenging times.

This thesis would not have been possible without the contributions and support of all those mentioned above. Thank you all for participating in this significant milestone in my academic journey. There are many more people to whom I owe my gratitude, and the list is long. I will forever cherish the support and constructive criticism from all walks of life, which enabled me to complete this work.

Preface

This thesis, titled "*A combined experimental, data-driven, and numerical approach to deform thin Ti6Al4V sheets using laser peen forming*," represents the culmination of several years of research conducted at the Department of Laser Processing and Structural Assessment, Helmholtz-Zentrum Hereon GmbH. The research was inspired by the growing demand for advanced forming techniques in high-performance aerospace applications. I was driven by the challenge of bridging scientific principles with practical engineering solutions.

The foundation of this work was significantly shaped by project PEENCOR, a collaborative effort aimed at developing an autonomous laser peen forming (LPF) process for forming and straightening aerospace components. The project, conducted in partnership with FormTech GmbH, ZAL Zentrum für Angewandte Luftfahrtforschung GmbH, and Leuphana Universität Lüneburg, played a pivotal role in aligning the research with industrial requirements. Funded by the Federal Ministry for Economic Affairs and Climate Action of Germany (BMWK) under the LuFo VI-1 program, Project PEENCOR provided the framework to elevate LPF technology to Technology Readiness Level 4 (TRL 4). This collaborative environment enriched the scope and ambition of this thesis, ensuring its relevance to both scientific inquiry and practical implementation.

The journey to completing this thesis has been a rich and multifaceted experience. It began with exploring the fundamental principles of LPF and, gradually evolved into tackling complex challenges, such as optimizing process parameters, validating numerical models, and training neural networks for predicting the deformation in the treated region. Each stage brought a blend of intellectual rigor and creative problem-solving, shaping my understanding of LPF and its effect on Ti6Al4V, and mathematical computational methods to optimize the process effectively.

On a personal note, this thesis marks the end of a significant chapter in my life, it has taught me that perseverance and curiosity are the keys to tackling the unknown. As I move forward, I carry with me not just the knowledge I've gained but also a profound appreciation for the process of learning itself.

Abstract

The need for complex-shaped, thin-walled structures has surged in the aerospace industry, necessitating resilient and dependable manufacturing techniques. Traditional sheet metal forming (SMF) methods often face challenges such as wrinkling, shearing, and springback, affecting the quality and precision of formed parts. This thesis explores the optimization of the laser peen forming (LPF) process, a modern SMF technique that uses high-intensity, ultra-short laser pulses to deform materials with minimal surface damage. The research focuses on applying LPF in the aerospace sector to shape sheets to specific geometries and correct existing deformations, particularly using titanium alloy Ti6Al4V.

This work is driven by the need to reduce part rejections due to non-conformity to target geometries, tooling and production costs, and CO₂ emissions, aligning with industry trends towards sustainability and automation. As a result, LPF in the present work, is investigated as a method to produce definite geometries as well as to correct the existing geometries. The study is structured around three main approaches: experimental investigations, data-driven methodologies, and numerical simulations.

Experimental investigations focus on identifying optimal LPF process parameters to achieve desired deformations while maintaining surface integrity. Data-driven methodologies employ artificial neural networks (ANN) to predict deformations based on process parameters, enhancing the potential for autonomous forming processes. Numerical simulations using finite element methods (FEM) complement the experimental work, providing insights into the deformation mechanisms and optimizing process parameters. A simplified numerical simulation workflow is developed to generate data that accurately represents experimental deformations for various peening patterns.

The findings demonstrate that LPF can be integrated into automated manufacturing systems, offering precise control over deformation, high accuracy, and repeatability. The developed process planning approach with ANN predictions produces desired deformations in treated regions. This approach is successfully demonstrated on three benchmark cases involving thin Ti6Al4V sheets: unidirectional deformation, bidirectional deformation, and the modification of existing deformations in pre-bent specimens using LPF.

The cellular automata neural network (CANN) approach developed in this study utilizes a convolutional neural network (CNN) to accurately predict peening patterns based on the deformations in the specimen after LPF. This approach enhances the LPF process, providing a reliable tool for achieving precise deformations in various applications involving complex peening patterns.

The research presented in this thesis advances the understanding and application of LPF for thin-walled Ti6Al4V structures. Experimental investigations identified optimal LPF process parameters that achieve the desired deformation while maintaining surface integrity. Numerical simulations using the eigenstrain method validated these findings and demonstrated the feasibility of applying LPF to more complex geometries. Additionally, a data-driven approach utilizing an ANN was developed for process planning, enabling the prediction of deformations for various LPF process parameters. Furthermore, a CNN-based approach presented the applicability of LPF to achieve target shapes on flat specimens by predicting the peening patterns. This integrated methodology, combining experimental, data-driven, and numerical techniques, highlights the potential of LPF as an innovative, autonomous forming process for aerospace applications, addressing both practical implementation and theoretical understanding.

Zusammenfassung

Der Bedarf an komplex geformten, dünnwandigen Strukturen hat in der Luft- und Raumfahrtindustrie stark zugenommen, was belastbare und zuverlässige Fertigungstechniken erfordert. Traditionelle Blechumformungsverfahren (SMF) stehen häufig vor Herausforderungen wie Faltenbildung, Scherung und Rückfederung, was die Qualität und Präzision der geformten Teile beeinträchtigt. Diese Arbeit befasst sich mit der Optimierung des Laser-Peen-Forming (LPF)-Verfahrens, einer modernen SMF-Technik, die hochintensive, ultrakurze Laserpulse verwendet, um Materialien mit minimaler Oberflächenschädigung zu verformen. Die Forschung konzentriert sich auf die Anwendung von LPF im Luft- und Raumfahrtsektor, um Bleche in spezifische Geometrien zu formen und unerwünschte Verformungen zu korrigieren, insbesondere unter Verwendung der Titanlegierung Ti6Al4V.

Diese Arbeit wird durch die Notwendigkeit getrieben, den Ausschuss von Bauteilen aufgrund von Abweichungen von vorgegebenen Geometrien, Werkzeug- und Produktionskosten und CO₂-Emissionen zu reduzieren, im Einklang mit Branchentrends zu Nachhaltigkeit und Automatisierung. LPF wird daher in der vorliegenden Arbeit als Methode zur Erzeugung definierter Geometrien sowie zur Korrektur bestehender Geometrien untersucht. Die Studie gliedert sich in drei Hauptansätze: experimentelle Untersuchungen, datengestützte Methoden und numerische Simulationen.

Die experimentellen Untersuchungen konzentrieren sich auf die Identifizierung optimaler LPF-Prozessparameter, um gewünschte Verformungen unter Beibehaltung der zu erreichen. Datengestützte Methoden nutzen künstliche neuronale Netze (ANN) zur Vorhersage von Verformungen auf der Grundlage von Prozessparametern, was das Potenzial für autonome Umformprozesse erhöht. Numerische Simulationen unter Verwendung der Finite-Elemente-Methode (FEM) ergänzen die experimentelle Arbeit und liefern Einblicke in die Verformungsmechanismen sowie die Optimierung der Prozessparameter. Ein vereinfachter numerischer Simulationsablauf wird entwickelt, um Daten zu erzeugen, die die experimentellen Verformungen für verschiedene Peening-Muster genau darstellen.

Die Ergebnisse zeigen, dass LPF in automatisierte Fertigungssysteme integriert werden kann, präzise Kontrolle über Verformungen bietet und hohe Genauigkeit sowie Wiederholbarkeit gewährleistet. Der entwickelte Prozessplanungsansatz mit ANN-Vorhersagen erzeugt die gewünschten Verformungen in den behandelten Bereichen. Dieser Ansatz wird

erfolgreich in drei Beispielen demonstriert, die dünne Ti6Al4V-Bleche betreffen: unidirektionale Verformung, bidirektionale Verformung und die Modifikation vorhandener Verformungen in vorgebogenen Proben durch LPF.

Der in dieser Studie entwickelte Ansatz eines "Cellular Automata Neural Network (CANN)" nutzt ein "Convolutional Neural Network (CNN)", zur genauen Vorhersage von Peening-Mustern basierend auf den Verformungen der Probe nach LPF. Dieser Ansatz verbessert den LPF-Prozess und bietet ein zuverlässiges Werkzeug zur Erzielung präziser Verformungen bei verschiedenen Anwendungen mit komplexen Peening-Mustern.

Die in dieser Arbeit vorgestellte Forschung erweitert das Verständnis und die Anwendung von LPF für dünnwandige Ti6Al4V-Strukturen. Experimentelle Untersuchungen identifizierten optimale LPF-Prozessparameter, die die gewünschte Verformung bei gleichzeitiger Wahrung der Oberflächenintegrität erreichen. Numerische Simulationen unter Verwendung der Eigendehnungsmethode validierten diese Ergebnisse und zeigten die Machbarkeit der Anwendung von LPF auf komplexere Geometrien. Zusätzlich wurde ein datengestützter Ansatz unter Verwendung eines ANN zur Prozessplanung entwickelt, der die Vorhersage von Verformungen für verschiedene LPF-Prozessparameter ermöglicht. Darüber hinaus zeigte ein auf CNN basierender Ansatz die Anwendbarkeit von LPF zur Erreichung von Zielformen auf flachen Proben durch Vorhersage der Peening-Muster. Diese integrierte Methodik, die experimentelle, datengestützte und numerische Techniken kombiniert, unterstreicht das Potenzial von LPF als innovatives, autonomes Umformverfahren für Luft- und Raumfahrtanwendungen und behandelt sowohl die praktische Implementierung als auch das theoretische Verständnis.

Contents

| | |
|--|------------|
| Acknowledgments | iii |
| Preface | v |
| Abstract | vii |
| List of Figures | xv |
| List of Tables | xix |
| 1 Introduction | 1 |
| 1.1 Motivation and research gap | 1 |
| 1.2 Objectives and approach | 4 |
| 1.3 Thesis structure | 5 |
| 2 Fundamentals and literature review | 9 |
| 2.1 Overview | 9 |
| 2.2 Laser peen forming | 11 |
| 2.2.1 LPF process parameters | 14 |
| 2.2.2 Direct and inverse problem of LPF | 19 |
| 2.3 Data-driven approaches | 20 |
| 2.4 Numerical simulation methods | 26 |
| 2.5 Summary and conclusions | 33 |
| 3 Methodology and approach | 35 |
| 3.1 Experimental techniques and material | 35 |
| 3.1.1 LPF experimental facility | 35 |
| 3.1.2 Experimental setup | 36 |
| 3.1.3 Experimental methodology | 37 |
| 3.1.4 Material: Ti6Al4V | 39 |
| 3.1.5 Deformation measurement | 40 |
| 3.1.6 Surface characterization of the treated region | 41 |

| | | |
|----------|--|-----------|
| 3.2 | Data-driven methods | 42 |
| 3.2.1 | Artificial neural networks | 42 |
| 3.2.2 | Description of experimental and numerical simulation datasets . . | 44 |
| 3.2.3 | Data scaling | 45 |
| 3.2.4 | Hyperparameters of ANN | 47 |
| 3.2.5 | Data-driven process planning for LPF | 47 |
| 3.2.6 | Cellular automata neural network | 52 |
| 3.3 | Numerical simulation of LPF | 55 |
| 3.3.1 | Aspects of FE model | 55 |
| 3.3.2 | Validation with experiments | 60 |
| 3.3.3 | Simplified predictive numerical model for LPF | 63 |
| 3.4 | Summary and conclusions | 66 |
| 4 | Results and discussion | 69 |
| 4.1 | Impact of LPF process parameters on deformation and surface quality . . | 70 |
| 4.1.1 | Effect of overlap and laser energy on LPF | 70 |
| 4.1.2 | Impact of peening sequences and laser energy on deformation in the treated region - using a sacrificial overlay | 72 |
| 4.1.3 | Effect of laser energy, peening sequences, and overlap - without sacrificial overlay | 73 |
| 4.1.4 | Deformation in the peened region - LPF with and without a sacri- ficial overlay | 75 |
| 4.1.5 | Impact of LPF process parameters on surface characteristics of the peened region | 76 |
| 4.2 | Data-driven approaches: predicting deformation and process planning . . | 80 |
| 4.2.1 | Performance of ANN trained on data from LPF experiments . . . | 80 |
| 4.2.2 | Implementation of process planning approach for deforming and modifying thin sheets | 83 |
| 4.2.2.1 | Demonstrating LPF application on flat sheets | 83 |
| 4.2.2.2 | Demonstrating LPF for modifying deformation in pre- bent sheets | 87 |
| 4.2.3 | Prediction of required peening pattern for LPF to obtain a defined target geometry from a flat sheet | 91 |
| 4.3 | Numerical simulation and experimental validation of LPF | 95 |
| 4.3.1 | Findings from LPF simulation using Eigenstrain approach | 95 |
| 4.3.2 | Data-driven approach for finding the equivalent value of maximum plasma pressure | 100 |
| 4.3.3 | Validating the data-driven numerical approach with LPF experi- ments involving complex peening patterns. | 107 |

| | | |
|----------|--|------------|
| 5 | Summary and conclusions | 113 |
| 6 | Future scope of work | 119 |
| | Appendix | 121 |
| A | Application of Buckingham's Pi theorem for LPF process parameters . . | 121 |
| B | Data-driven LPF process planning | 124 |
| C | Simplified numerical model - Bayesian optimizer | 125 |
| D | Experimental 3D data acquisition after LPF | 127 |
| E | Numerical simulation of LPF - Effects of simulation parameters | 130 |
| F | Implementation of CANN | 137 |
| | References | 141 |

List of Figures

| | | |
|------|--|----|
| 1.1 | Thesis structure | 7 |
| 2.1 | Laser peening process schematic | 10 |
| 2.2 | Effect of the depth of induced plastic strains after LPF | 11 |
| 2.3 | Schematic illustrating angle of attack (α) during LPF | 14 |
| 2.4 | Overlap of consecutive laser pulses | 15 |
| 2.5 | Various possible laser pulse patterns in LPF | 16 |
| 2.6 | Direct and inverse problem of LPF | 19 |
| 2.7 | Schematic depicting the significance of a trained model in SMF for different purposes. | 21 |
| 2.8 | Steps in creating a data-driven model for SMF process | 22 |
| 2.9 | Workflow representing the numerical simulation of LPF using ABAQUS | 29 |
| 2.10 | Simulation of LPF using eigenstrain method | 31 |
| 3.1 | Laser peening facility for experimentation | 36 |
| 3.2 | Experimental setup for LPF | 37 |
| 3.3 | Schematic of clamped LPF specimen | 37 |
| 3.4 | Investigated LPF peening patterns in the treated region | 38 |
| 3.5 | Deformation measurement in the treated region after LPF | 41 |
| 3.6 | Illustration of LPF process with experimental variables, material properties, and derived parameters | 45 |
| 3.7 | The experimental and simulation datasets of this study | 46 |
| 3.8 | Flowchart of LPF process planning approach | 49 |
| 3.9 | Discretization of ΔD profile | 50 |
| 3.10 | Architecture of the CANN model | 53 |
| 3.11 | Schematic of components in numerical simulation of LPF process | 56 |
| 3.12 | The source and target geometry for LPF simulation | 57 |
| 3.13 | Temporal distribution of pressure pulse in numerical simulations | 58 |
| 3.14 | Schematic of mapping an LPF peening pattern onto FE mesh | 60 |
| 3.15 | Equivalent functional representation of LPF simulation inputs and outputs | 62 |

| | |
|--|----|
| 3.16 Comparison of residual stresses after LPF to a beam bending problem: simplified FE model | 64 |
| 3.17 Workflow of integrated simplified FE model with LPF experiments | 65 |
| 4.1 Effect of overlap and laser energy during LPF with sacrificial overlay . . | 70 |
| 4.2 Influence of laser energy on the sacrificial overlay during LPF | 71 |
| 4.3 Influence of peening sequences on deformation with LPF treatment | 72 |
| 4.4 Arc radius measurements in LPF-treated region for varying laser energies and peening sequences | 73 |
| 4.5 Deformation and surface characteristics within peened area post-LPF with- out sacrificial overlay | 74 |
| 4.6 Influence of overlap on deformation in the treated region after LPF | 74 |
| 4.7 Influence of sacrificial overlay on arc radius within LPF-treated region . . | 75 |
| 4.8 Impact of LPF process parameters on the surface quality of peened area . | 76 |
| 4.9 Comparison of surface roughness in the peened region after LPF with and without a sacrificial overlay | 77 |
| 4.10 SEM and EDX analyses of LPF processed specimen without sacrificial overlay | 78 |
| 4.11 SEM images of near-surface region of peened and unpeened regions of a specimen after LPF | 79 |
| 4.12 Performance evaluation of the ANN trained using the data from LPF ex- periments | 81 |
| 4.13 Comparison of actual and predicted deformation values in the peened re- gion across different LPF process parameters | 82 |
| 4.14 Exemplary 1 mm and 2 mm thick Ti6Al4V LPF treated specimens bent to target shapes from initially flat shape. | 84 |
| 4.15 Use Case 1: Process planning for deforming a Ti6Al4V specimen to de- sired profile using ANN predictions | 84 |
| 4.16 Exemplary flat specimens bidirectionally bent to target shapes after LPF . | 85 |
| 4.17 Use Case 2: Achieving an S-shaped geometry from a 2 mm thick Ti6Al4V specimen using LPF and ANN-predicted parameters | 86 |
| 4.18 Application of LPF on a pre-bent specimen to modify the existing defor- mation. | 87 |
| 4.19 Use Case 3: Flattening a 1 mm thick curved Ti6Al4V specimen using LPF with ANN predicted process parameters | 88 |
| 4.20 Application of LPF on a pre-bent specimen to modify the existing defor- mation. | 89 |
| 4.21 Use Case 4: Rectifying a curved Ti6Al4V sheet from 75 mm to 100 mm radius using LPF | 90 |

| | | |
|------|---|-----|
| 4.22 | Evolution of predicted peening pattern during the training of CANN | 92 |
| 4.23 | Training loss and gradient magnitude during CANN training. | 92 |
| 4.24 | Evaluation loss of a predicted peening pattern during training of CANN . | 93 |
| 4.25 | The training log-loss plot during training on a training set of 37 different peening patterns with a batch size of 16. [83] | 93 |
| 4.26 | Peening patterns in training and testing dataset predicted by trained CANN model | 94 |
| 4.27 | Visualization of plastic strain field on source geometry surface after LPF by FE simulation | 96 |
| 4.28 | Residual stress field generated on the surface of the source geometry after LPF | 97 |
| 4.29 | Plastic strains resolved by depth and averaged across designated regions in treated area of source geometry | 98 |
| 4.30 | Residual stresses resolved by depth and averaged across designated regions in treated area of source geometry | 99 |
| 4.31 | Deformation in target specimens after LPF simulation with different pressures, showing a transition from convex to concave bending. | 100 |
| 4.32 | ANN performance evaluation during training using simulation dataset . . | 102 |
| 4.33 | Comparison of deformation profiles obtained from LPF experiments with ANN predictions using the simulation data | 103 |
| 4.34 | Correlation between laser energy and equivalent maximum pressure for each peening sequence in case of 1 mm and 2 mm thick specimens. . . . | 104 |
| 4.35 | Performance evaluation of ANN trained using explicit simulation data to predict the eigenstrains | 105 |
| 4.36 | Peening patterns on specimens of varied sizes | 107 |
| 4.37 | Visualization of difference in deformation in the specimen by FE simulation and LPF experiment | 108 |
| 4.38 | Comparison of deformation in the specimen between FE simulation and LPF experiment | 109 |
| 4.39 | Comparison of residual stresses in a specimen after LPF, with the residual stress computed from FE simulation. | 110 |
| C.1 | Averaged height maps from four 1 mm thick experimental samples peened without a sacrificial layer, using four sequences at 2.7 J. | 125 |
| C.2 | Bayesian optimization sampling to find the minimum MSE for initial top/surface stress values from -1000 to 1000 MPa | 126 |
| C.3 | Computed difference between experimental height map and final FE simulation iteration of the simplified model | 126 |

| | | |
|-----|--|-----|
| D.1 | Ti6Al4V sample before LPF, and post-LPF specimen without protective overlay, showing a black oxide layer on the treated surface | 127 |
| D.2 | Transformation of the scanned coordinate system: from scanned sample after LPF to FE coordinate system | 128 |
| D.3 | Height map computation: (a) Sampling visualization, (b) Height map after LPF with 2.7J and 4 peening sequences on 1 mm specimen | 128 |
| D.4 | Computation of curvature map from the height map.[83] | 129 |
| E.1 | Plastic strain ϵ_{11} by depth, averaged across different regions in treated source geometry at different P_{max} values after four peening sequences . . | 130 |
| E.2 | Plastic strain ϵ_{22} by depth, averaged across different regions in treated source geometry at different P_{max} values after four peening sequences . . | 131 |
| E.3 | Residual stress σ_{11} by depth, averaged across regions in treated source geometry at various P_{max} values after four peening sequences. | 132 |
| E.4 | Residual stress σ_{22} by depth, averaged across regions in treated source geometry at various P_{max} values after four peening sequences | 133 |
| E.5 | Deformation in a 2 mm thick specimen after LPF simulation with different plasma pressure pulses and peening sequences. | 134 |
| E.6 | Deformation in a 2 mm thick specimen after LPF simulation with different plasma pressure pulses and peening sequences | 135 |
| E.7 | Dataset of explicit FE simulation to determine the eigenstrains in the source geometry for different values of maximum pressure and peening sequences | 136 |
| F.1 | Training loss (a) without and (b) with scaled curvature data | 138 |
| F.2 | Examining the impact of batch size during training of the CANN model . | 139 |

List of Tables

| | | |
|-----|--|-----|
| 2.1 | Characteristics and limitations of SMF processes | 13 |
| 2.2 | Influence of various process parameters on the achievable bending in the treated region for different materials found in the literature concerning LPF | 17 |
| 2.3 | Summary of ML applications for the prediction of SMF processes categorized as regression and classification tasks | 25 |
| 2.4 | JC material parameters and physical material properties of Ti6Al4V used for FE simulation of LPF [87] | 28 |
| 2.5 | Summary and analysis of the current literature related to FE numerical simulation approaches for LPF process. | 32 |
| 3.1 | The LPF experiments in this study were categorized into distinct parameter sets, determined by the different combinations of process parameters examined | 38 |
| 3.2 | LPF process parameters and their ranges to generate an experimental design matrix. LPF experiments corresponding to these parameters were performed to study the process property relationship | 38 |
| 3.3 | Parameters of the pressure pulse and peening sequences for simulation of LPF using the eigenstrain approach | 61 |
| 4.1 | Performance metrics of the trained ANN on experimental datasets | 80 |
| 4.2 | Performance metrics of the trained ANN on simulation data | 101 |
| 4.3 | Performance metrics of the trained ANN on simulation data corresponding to the prediction of region-specific depth-resolved eigenstrains | 106 |
| B1 | List of LPF process parameters suggested by the optimizer for each discretized unit in the use case specimens [133] | 124 |
| F1 | Peening patterns resembling actual LPF specimens of dimensions 80×20 mm ² used to train the CANN | 137 |

Nomenclature

List of symbols

- α Angle of attack.
- α_p The thermal energy fraction of the total internal energy of the generated plasma.
- I Input vector of the ANN.
- W_{p+1}^T Weight matrix of the $(p + 1)$ th hidden layer.
- Y Output vector of the ANN.
- $\Delta D(x)$ The deviation between initial and target deformation profiles.
- Δ_i The delta image of the dense neural network.
- δ_{scan} Overlap in the scanning direction.
- δ_{step} Overlap in the stepping direction.
- $\dot{\epsilon}_{pl,eq,0}$ Reference strain rate to determine JC parameters.
- $\dot{\epsilon}_{pl,eq}$ Plastic strain rate.
- ϵ^* Eigenstrain (in general, inelastic strain in a solid by definition.)
- \hat{y}_i Predicted value of an output from the ANN.
- ρ Density of the material.
- σ_Y Yield stress of the material.
- τ Duration of single laser pulse.
- τ_{FWHM} Duration of laser pulse at FWHM.
- $\epsilon_{pl,eq}$ Equivalent plastic strain.
- A_f Area of the laser spot at focus.

- A_L Area of the laser optic.
- A_{JC} Material constant in JC model (Yield strength at reference strain rate).
- B_{JC} Material constant in JC model (Strain hardening coefficient).
- C_{CNN} The number of channels in each CANN layer.
- C_{JC} Material constant in JC model (Strain rate hardening coefficient).
- d Side size of the laser optic.
- $D(x)$ Deformation profile of the specimen after LPF.
- D_i The initial deformation profile.
- D_s The length of the discretization step.
- D_t The target deformation profile.
- E Young's modulus of the material.
- E_L Energy of the laser pulse.
- f The number of laser pulses applied per second.
- F_{CNN} The size of filter in a CANN layer.
- H_i Input image of the CANN model.
- H_i The seed image representing the input data of the CANN.
- h_i Hidden layers in the neural network.
- H_o Seed image for the CANN model.
- H_{i+1} The seed image representing the output data of the CANN.
- $H_{j,i}$ Input image to the CANN model with j being the index of the input curvature map.
- I Actual laser power density.
- i The total number of experiments/simulations in the parameter space.
- I_o Idealized laser power density.
- j Index of the position along the length of the peened region.
- k The number of discretizations of the deformation profile.

- m_{JC} Material constant in JC model (Temperature dependency).
- n Number of peening sequences
- n_{JC} Material constant in JC model (Strain hardening exponent).
- O_{CNN} The number of output values of CANN.
- $p(t)$ Plasma-induced pressure at the surface of the specimen as a function of time.
- $p(x, y, t)$ Temporal and spatial resolution of the plasma pressure.
- P_{CNN} The parameters in one layer of the CANN.
- P_{max} Maximum value of the induced pressure.
- r Number of hidden layers of the ANN.
- R_a Surface roughness
- R_k Arc radius corresponding to discretized deformation profile.
- T Thickness of the LPF specimen
- t Duration of the pressure pulse.
- T^* Homologous temperature.
- t_m The time at which the pressure pulse reaches the maximum value of induced pressure.
- V_s The scaled value of the input or output.
- V_{max} The maximum value in the feature range.
- v_{max} The maximum value of the scaled entity.
- V_{min} The minimum value in the feature range.
- v_{min} The minimum value of the scaled entity.
- w Increased side size due to angle of attack.
- y_i True value of an output from the ANN.
- Z The acoustic impedance of the confining medium.

List of abbreviations

- AI Artificial Intelligence

ANN Artificial neural network

BMWK Federal Ministry for Economic Affairs and Climate Action of Germany

DOE Design of experiments

EDX Energy dispersive X-ray spectroscopy

FE Finite element

FWHM Full width at half maximum

GLARE Glass laminate aluminum reinforced epoxy

HEL Hugoniot elastic limit

JC Johnson-Cook material model

LPF Laser peen forming

LSP Laser shock peening

ML Machine learning

MSE Mean squared error

SEM Scanning electron microscopy

SMF Sheet metal forming

SP Shot peening

TRL Technology readiness level

VISAR Velocity interferometer system for any reflector

Other symbols

CO_2 Carbon dioxide

ABAQUS Finite element software

C3D8R Eight-noded general purpose brick element

CANN Cellular automata neural network

CNN Convolutional neural network

KS Kolmogorov-Smirnov test

optoNCDT Non-contact linear displacement optical laser triangulation sensor

1

Introduction

1.1 Motivation and research gap

The aerospace industry has recently shown an exceptionally increasing demand for a wide range of complex-shaped thin-walled structures. The supporting structures of modern aircraft are almost entirely constructed with thin-walled structures to minimize weight [10]. These supporting structures such as large-scale integrally-stiffened wing panels must possess a high degree of resilience and dependability, given their critical role in ensuring the safety and integrity of the aircraft. Low rigidity, complicated shapes, and a propensity to deform in both directions are some of the intrinsic physical characteristics of thin-walled structures [12]. Modern commercial aircraft's contain about 20%-45% of composite materials. Nevertheless, there is still a large share of materials based on aluminum and titanium alloys in aircraft production due to their lightweight, excellent corrosion resistance, good strength, toughness, and compatibility with standard manufacturing techniques [114]. Typically, thin-walled structures are made of sheet metals which constitute secondary structures of the aircraft and are manufactured using techniques such as cold forming [8], hot forming [135], super-plastic forming [70], roll forming [152] and incremental sheet metal forming (SMF) [155].

Traditionally in different SMF procedures, force is applied to a piece of sheet metal in order to plastically distort it into the required shape while leaving no material behind. SMF is a technique that incorporates modern technologies since sheet metal can be twisted or stretched into a wide range of intricate shapes, complex structures may be built with little

material and high strength as well as good surface quality [77]. The mechanical properties of sheet metals and the complicated physical phenomena of the process play a significant role in the applicability of the SMF processes. The quality of formed parts is often affected by problems such as wrinkling, shearing, and springback [56]. With an increase in the demand to reduce production costs and carbon dioxide (CO_2) emissions (currently at 3% with a rising trend [86]), the aerospace industry faces the challenge of revolutionizing the traditional manufacturing processes by automation, intelligent resource management and incorporation of sustainability concept in the manufacturing supply chain [27]. As a result, research into processes such as incremental SMF, emphasizes the need to minimize sheet metal scrap generation to reduce environmental impacts.

SMF processes are distinguished by high productivity, tool-determined component shape, and increasing net shape precision. SMF tool manufacturing is extremely time and cost-intensive, and so does not lend itself to considerable product flexibility. New technological advances in the field of laser optics have given rise to metal-forming technologies by utilizing the laser beam as a primary tool [45]. Some of the earliest applications of laser-based forming [81, 159, 45] in the fields of aerospace [104, 165] and ship planking [138] work on the principle of thermally induced residual stresses in the sheet material. In contrast to this, a new laser-based forming technique known as laser peen forming (LPF), which is a derivative of laser shock peening (LSP), is evolving as an innovative modern manufacturing technology that uses high-intensity laser pulses to deform materials into complex shapes [60, 66]. The process is based on the principle of shot peening (SP), a surface treatment technique that is aimed to improve the mechanical properties of materials [123, 170] as well as for sheet metal forming applications [100, 42, 110] by inducing compressive plastic strains on the surface. Literature studies [100, 143, 82] show that the SP process is extensively used in the aerospace industry for the deformation, straightening, and correction of components and structures. However, during SP, spherical particles of glass, ceramics, or metal are guided at high speed onto the workpiece surface and each particle causes local plastic deformation or pitting on the surface which increases the roughness of the surface and in some cases damages the surface. Furthermore, blind areas in structures with complex shapes are difficult to process by SP [147].

LPF has a similar effect compared to SP, but the intensity of surface damage and roughening is significantly minimized. It also enhances the fatigue life of the treated component. Furthermore, LPF can induce deeper plastic strains in materials in contrast to traditional shot peen forming which allows for a greater degree of formability in the treated region [109, 50]. LPF provides precise control over the deformation process since the laser pulses are ordered, allowing for the production of complex shapes with high accuracy and repeatability. This makes it possible to manufacture parts that would be difficult or impossible to produce with conventional methods. Since LPF can shape the material to the necessary geometry without the need for cutting or machining, it can manufacture components with

little material waste. This yields considerable cost reductions, particularly when working with costly or difficult-to-machine materials. LPF has been thoroughly investigated for various materials such as pure aluminum [129, 63], aluminum alloy 2024-T351 [179], titanium alloy Ti6Al4V [150], and glass-reinforced epoxy laminate aluminum composites [65]. LPF can be integrated into automated manufacturing systems, which can increase production efficiency and reduce labor costs. The process can be performed quickly and efficiently, allowing for high-volume production.

The primary limitation pertains to the economic feasibility of LPF, as it currently presents a higher financial investment than conventional peen forming. Nonetheless, the augmented expenses of LPF may be mitigated in specific circumstances, by obviating supplementary manufacturing phases such as abrasion for the enhancement of surface roughness, the elimination of residual debris after processing, interim monitoring operations, and corrective forming actions that arise from the initial process variability. Further research into the LPF process is crucial to understand the sources of variability and improving economic competitiveness. The application of state-of-the-art experimental techniques, numerical finite element (FE) simulation methods, and data-driven approaches can enhance the applicability and automatability of LPF. These research efforts can also help optimize LPF parameters for materials of interest (such as Ti6Al4V in particular), ultimately leading to the use of the process in industrial applications.

Hence, a research project has been established to conduct research and development for LPF process optimization. This project, entitled "*Development of optimal process parameters and identification of an AI-algorithm for autonomous forming and straightening by Laser Peen Forming*", was carried out at *Helmholtz Zentrum Geesthacht GmbH* (renamed as *Helmholtz Zentrum hereon GmbH* in March 2021), Germany and this thesis falls within the scope of this project. This research project is part of the *PEENCOR* joint project consortium partnering with *FormTech GmbH*, *ZAL Zentrum für Angewandte Luftfahrtforschung GmbH*, and *Leuphana Universität Lüneburg*, which aims to develop and demonstrate an autonomous forming and straightening process using LPF. The developed LPF process takes into account and complies with all the material specifications of titanium structures for aviation requirements. The project *PEENCOR* is intended to raise the LPF technology to *TRL 4*. This project is funded by the *Federal Ministry for Economic Affairs and Climate Action of Germany (BMWK)* as part of the aeronautics research LuFo VI-1 program (Grant number: 20Q1920C).

As LPF has the potential to precisely deform thin sheets as well as to be utilized as a finishing process to straighten parts and structures without compromising the surface quality, correcting dimensional and shape deviations caused in previous processing steps. The current study places its emphasis on the identification of viable experimental conditions for the applicability of LPF to a commonly employed titanium alloy, Ti6Al4V. The central innovation of this research lies in the creation of an AI-supported automated process

framework for the LPF process, which can be employed to deform, straighten, or correct components and structures. In addition to the experimental work, emphasis was also placed on numerical finite element (FE) simulations employing various approaches to reduce the experimental effort by making use of numerically computed data.

1.2 Objectives and approach

This work aims to investigate, develop, and demonstrate an autonomous forming and straightening process for thin-walled titanium components and structures made from Ti6Al4V in the aerospace industry using LPF. This goal is achieved by subdividing it into three main approaches as described below.

- **Experimental investigations**

A comprehensive feasibility analysis is to be conducted to determine the appropriate process parameters and an investigation of process parameter combinations to achieve forming or straightening via LPF while preserving the surface quality of the treated region. This includes identifying the LPF process application spectrum and limitations. Investigations of the material microstructure by microscopic observation methods in the treated region are to be performed to quantify and assess the integrity of the surface. To ensure precise evaluation of deformation in both the treated region and the entire specimen following LPF treatment, a suitable measurement metric must be selected. This metric will serve as a quantitative indicator of the degree of deformation and will play a crucial role in accurately assessing the effectiveness of the LPF process.

- **Data-driven methodology**

The aim is to develop an effective artificial intelligence (AI) algorithm that can determine the process parameters required for autonomous forming and straightening. The methodology should focus on testing available machine learning (ML) models by increasing the complexity of the model and evaluating the learning curves to ensure optimal performance. Emphasis is placed on ANN models due to their capability to make more accurate predictions. The ANN is to be created making use of generated data from the experiments and numerical simulations. The ANN should be able to identify the relationships between the process parameters and predict the deformations generated in the treated region via LPF. The effectiveness of the data-driven methodology must be tested through successful applications involving various scenarios such as one-dimensional bending, bi-directional deformation, and modification of deformation in pre-bent structures. In addition to this, the peening patterns

are to be precisely predicted to obtain target deformations from flat sheets using advanced cellular automata neural networks (CANN). These applications serve to validate the accuracy and reliability of the developed ANN model and showcase its potential in real-world manufacturing processes.

- **Numerical simulation approach**

FE simulation models are currently utilized with satisfactory outcomes in identifying appropriate and efficient LPF process strategies. The FE simulations are to be conducted using specific simulation parameters, including material properties, boundary conditions, and process variables concerning the existing literature and must be validated with the LPF experiments. A careful meshing strategy is to be employed, selecting appropriate element types and densities to capture relevant features and phenomena accurately. To validate the FE simulations, LPF experiments should be performed according to established methodologies found in the existing literature. The experimental setup mirrors the simulated conditions, including the equipment used, experimental conditions, and measurements taken. Validation criteria are established to assess the agreement between the simulations and experimental results. The evaluation measure to assess the simulations is the achieved deformation in the treated region after LPF in the treated region.

To ensure the accuracy and efficiency of the simulations, simplified numerical FE approaches should be formulated. These approaches aim to strike a balance between computational cost and simulation accuracy, producing sufficiently accurate results that can be utilized for the production of simulation data. The data collected from the FE simulations, along with the LPF experiments, are then utilized in the development of data-driven modeling. By incorporating simplified numerical FE approaches and utilizing the data collected from the FE simulations and LPF experiments, the development of data-driven modeling can be enhanced, facilitating improved understanding and decision-making in the LPF process.

1.3 Thesis structure

Taking into consideration the stated objectives and approach, a proposed thesis structure can be delineated. This structure will serve as a framework upon which the thesis is built, guiding the logical flow and organization of ideas, whose key aspects are described below and correlations are illustrated in Fig. 1.1.

Chapter 2 provides an overview of the fundamental concepts addressed in this thesis with reference to the established research. A detailed explanation of LPF, its process parameters, applications, and limitations are summarized. This chapter outlines a literature

review of the current research on LPF. After that, the fundamental aspects of the data-driven methodology are summarized including the theoretical aspects of ANNs and their applications concerning process development. Then, the prevalent numerical FE simulation modeling approaches for LPF are discussed, outlining the potential advantages and limitations.

Chapter 3 describes the experimental setup, methodology, and instrumentation used to conduct the LPF experiments. This chapter includes information on the specimen material used, specimen size, sample preparation, LPF process parameters, and measurement methods after LPF. It includes the details of data-driven approaches developed using AI and ML algorithms implemented within the scope of this work depending on the available data from the simulations and experiments. Additionally, the developed data-driven process planning workflow to determine the optimal process parameters for autonomous forming and straightening is discussed. It concludes by presenting the numerical simulation approaches adopted in the study using FE software (ABAQUS). It describes the FE simulation model used, the simulation parameters, and the results of the simulations.

Chapter 4 delves into the implications and significance of the findings in relation to the established research and the objectives outlined in the thesis. In-depth discussions are carried out to elucidate the underlying mechanisms and phenomena observed during the LPF process, offering insights into the influence of process parameters, process limitations, and potential improvements. The results obtained from both experimental and numerical approaches are compared and contrasted, highlighting any significant correlations or discrepancies.

This chapter also presents the results derived from the data-driven process planning methodology. To validate the effectiveness of the proposed methodology, three benchmark cases demonstrating bending, straightening, and correction by LPF are utilized. The outcomes of these benchmark cases serve as evidence, showing the capability of the methodology to determine optimal process parameters for autonomous forming and straightening.

Furthermore, the results obtained from the numerical simulations are also presented in this chapter. The advantages and benefits of utilizing simulation data are discussed, highlighting how such data can complement and augment the experimental findings. The simulation results are carefully analyzed and compared with the experimental results, enabling a comprehensive understanding of the LPF process and its underlying mechanisms.

Chapter 5 summarizes the main findings and notable contributions made by this thesis. It provides a concise overview of the key results obtained from the experimental investigations, numerical simulations, and data-driven approaches. The chapter emphasizes the significance of these findings in advancing the current knowledge and understanding of LPF.

Chapter 6 focuses on outlining the future scope of work and presenting a vision for the future development of LPF research. This chapter aims to identify potential areas of

improvement, unresolved issues, and unexplored avenues that can be pursued based on the findings and limitations of the current study. It offers suggestions and recommendations for further investigations, experiments, and numerical simulations that can enhance our understanding of LPF and address existing gaps in knowledge.

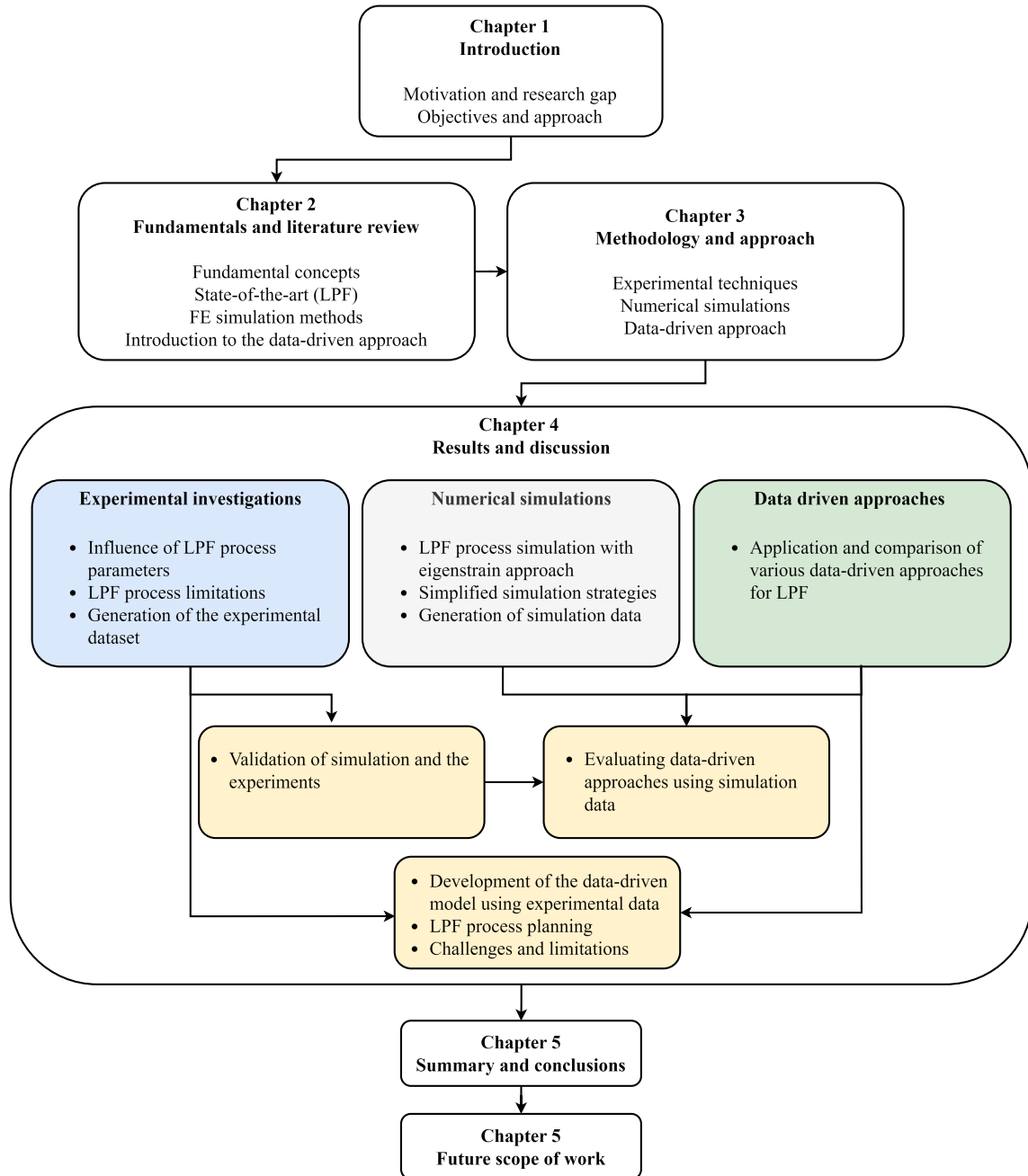


Fig. 1.1: This flowchart outlines the structure of a research thesis, detailing the chapters from introduction and methodology to results, conclusions, and future work.

2

Fundamentals and literature review

2.1 Overview

Since the 1980s, there has been extensive research into the use of high-power laser-induced shock waves on a target. These investigations were carried out in research facilities in USA and France until the early 1990s [26, 31, 119]. In recent decades, the process has been applied as a technique for enhancing material properties, including their resistance to phenomena such as fatigue [13], wear, as well as corrosion [93], and is now widely accepted and frequently used in the industry [147] being referred to as laser peening. Laser peening¹ is a surface processing technique that uses a powerful pulsed laser to induce plastic strains on the surface, which generate residual compressive stresses in materials and components (see Fig. 2.1).

The process involves heating the surface of the material with a short-time and high-power laser beam, creating a rapidly expanding plasma state, which generates high-pressure shock waves that cause local plastic deformation of the material below the surface [26, 31, 36]. The pressure generated during the process is in the order of 2 - 10 GPa within a shock wave duration of 20 - 100 ns as observed in the work of Clauer et al. [26]. The shock wave produces deformation at a strain rate higher than 10^6 s^{-1} [119]. When the pressure exceeds the Hugoniot elastic limit (HEL) of the metal, this mechanical shock wave deforms the material plastically and also produces compressive residual stress in the material [106].

¹Note that laser peening is often referred to as laser shock processing or laser shock peening (LSP) in several literature studies.

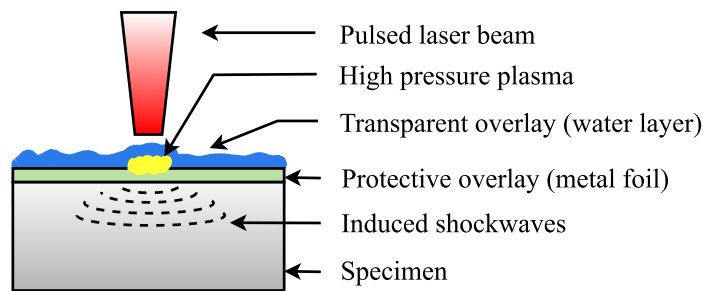


Fig. 2.1: Schematic of laser peening process: the specimen surface is covered with a protective overlay. This layer vaporizes, forming plasma on the surface. The expanding plasma induces pressure waves into the specimen. Confinement of plasma with a transparent overlay increases the intensity of the induced pressure waves.

The efficiency of laser peening can be improved by incorporating a transparent overlay, which acts as a confinement medium. This confinement medium restricts the plasma generated and prolongs the duration of the plasma pressure and increases its maximum value [55, 137]. Water is typically used as a confinement medium due to its cost-effectiveness; however, other alternatives are being researched as water may not always be feasible due to the complexity of the treated region or the possibility to achieve a laminar flow. Early studies conducted by Hong et al. [55] investigated the effect of transparent overlays on the duration and maximum value of plasma pressure. More recently, acrylate-based polymers and cross-linked polydimethylsiloxane have been developed as alternative confinement media, generating comparable plasma pressure to water [20]. Additionally, the aqueous gel has shown promising results as another potential confinement medium as demonstrated in the work of Zhang et al. [174].

Ablative overlays, also known as protective overlays, are used to cover the surface of the treated region to protect the surface from the heat effects of the generated plasma and to enhance the energy absorption from the laser pulses. Frequently used protective overlays for laser peening are black paint [167], and metal foils such as aluminum [136] or stainless steel [132]. The application of protective coatings affects plasma properties, plasma pressure, and the resulting induced shock waves [116] which affect the induced plastic strains. Adhesion of the protective overlay to the target material is a significant challenge that may affect mechanical shock wave transmission. Additionally, high pulse energies or multiple laser pulses may cause damage to the protective coating, particularly in the case of thin foils, resulting in an inconsistent laser peening process.

The specimen or beam is re-positioned relative to each other and the process is repeated, creating a treated region with indents. The induced plastic strains on the surface of a component have the propensity to cause bending or deformation, thereby offering the potential to shape thin sheets to a desired contour by means of precise control of process parameters and treatment regions. This idea has led to the development of forming by laser peening.

This chapter provides a brief explanation of the fundamentals and summarizes the current state of the art concerning laser peen forming. The following section 2.2 presents an overview of the process, and schematics of the experimental setup based on the literature followed by an analysis of the application to various materials. Later in section 2.3, the current trends for numerical simulation of the process are discussed. The chapter concludes by highlighting the recent developments in data-driven methodologies for various applications in section 2.4 and their contributions to efficient understanding and optimization of processes concerning manufacturing in general and emphasizing their application to the development of the laser peening process.

2.2 Laser peen forming

LPF is a derivative of the laser peening process, utilizing a short-pulsed laser to induce shock waves into the specimen, thereby mechanically forming it [113, 66]. LPF can be applicable to accurately bend flat sheets to a desired shape as well as to modify or repair existing components of high value. During LPF, the surface of the material interacts with the pulsed laser beam for an extremely short duration of time (in the order of a few nanoseconds), in which the shock waves are directed into the specimen. These shock waves mechanically distort the top surface and the surrounding material elastically accommodates the misfit strain, generating compressive residual stresses in the near-surface region after LPF treatment [179].

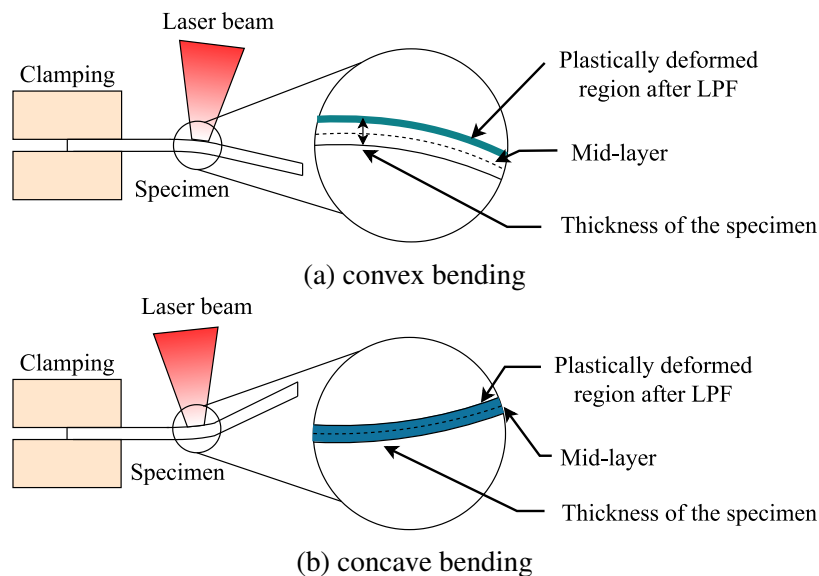


Fig. 2.2: Effect of the depth of induced plastic strains after LPF resulting in (a) convex bending, and (b) concave bending relative to the direction of the laser beam.

Theoretical frameworks depending on the depth of induced compressive stresses, namely the stress gradient mechanism and the stress bending mechanism were formulated to ex-

plain the bending phenomena of sheet metal specimens when they are subjected to localized plastic strains after LPF [63]. In the case of a specimen held with a cantilever fixation as shown in Fig. 2.2, the sample exhibits convex or concave bending relative to the direction of the laser beam depending on the LPF process parameters. In convex bending mode, the laser-induced plastic strains are confined within a thin layer beneath the top surfaces whereas, in concave bending, the plastic strains penetrate all the way through the thickness of the specimen.

Convex bending reportedly occurs at low laser intensities and thick sample material as observed by Pence et al. [113]. During LPF, the laser-induced shockwaves generated by the laser propagate through the specimen, resulting in plastic deformation of the near-surface region of the specimen in the direction of the thickness. However, due to the surrounding material, this plastic deformation is confined, resulting in tensile stress along the transverse direction. After the dissipation of the shockwave, the surrounding material readjusts to the misfit plastic strain resulting in bending away from the direction of the laser beam [63, 113].

Conversely, in thin specimens, concave bending is commonly observed due to the shockwave generated by the laser penetrating the entire thickness of the specimen. This results in plastic deformation that extends through the thickness of the treated region, resulting in a bending moment that enables the specimen to bend toward the laser beam. In some instances, deep drawing can also be observed in the treated region due to the same effect [63, 107]. Taking advantage of the beneficial effects of both convex and concave bending during LPF, it is apparent that the LPF technique has the potential to be a viable method for executing forming operations that involve intricate components and contours. For reasons summarized in Table 2.1 with respect to the process characteristics and limitations, LPF offers several advantages over traditional SMF as well as the shot peen forming methods. LPF outperforms conventional forming methods as it eliminates spring-back, without requiring any hard tooling or external forces. Furthermore, LPF enables the bending of materials in both concave and convex directions without the need for any setup modifications as reported by Hu et al. [63]. Notably, as LPF is a purely mechanical process, the target material is unaffected by undesirable residual stresses that may be induced by heat, resulting in forming, and no microstructural degradation of the material is observed.

The work of Gariépy et al. [44] suggests that shot peen forming is already widely used industrially for shaping complex, gentle-curvature parts such as supercritical wing designs [14, 124], integrated stiffened panels [161], and aerodynamic breaks [110]. It is a viable process for shaping ductile metallic materials, including aluminum alloys, steel, and titanium alloys used in the aerospace industry. As a result, since LPF offers more advantages and flexibility when compared to shot peen forming, this makes it worthwhile exploring the applicability as it has the potential to sustainably revolutionize manufacturing thin-wall structures in the aerospace industry.

Table 2.1: Characteristics and limitations of SMF processes in terms of flexibility of the process, applicability to various materials, required tooling, achievable precision, surface quality, and generated material waste

| Forming Process | Process characteristics | Observed limitations |
|--|---|---|
| Traditional SMF (cold forming, hot forming, roll forming, incremental sheet metal forming) | <ul style="list-style-type: none"> • Flexibility: Versatile for producing small to large components [154]. • Material properties: Significant influence of thickness, strength, and ductility of the material [56]. • Tooling: Often time-consuming and cost-intensive. • Precision and surface finish: High precision and accuracy with low tolerances can be achieved. Finishing processes such as polishing, painting, or coating are required depending on the desired surface properties. • Material waste: Generates a considerable amount of waste and hence requires intensive process planning. | <ul style="list-style-type: none"> • Applicability limited by material properties, process parameters, and strain bounding criteria [11]. • Specialized tooling limitations may restrict the complexity and geometry of the part to be formed. • Not cost-effective for small production runs due to the initial investment for tooling and equipment. |
| Shot peen forming | <ul style="list-style-type: none"> • Flexibility: Ideal for shaping parts with no sudden curvature changes [82]. Widely used on large wing skins [100, 153]. • Material properties such as yield strength and thickness influence the formability by peening [97]. • Tooling, precision, and surface finish: shot peen forming does not require specialized tooling or dies, which can make it a more cost-effective process. Relies on the controlled impact of shot peening to shape and form the metal [115]. The roughness of the treated region increases after processing [95]. | <ul style="list-style-type: none"> • Limited by the thickness of the material. Generally applicable to thin-walled components [110]. • Requirement of surface finishing processes after treatment to improve the quality of the treated region. |
| LPF | <ul style="list-style-type: none"> • Flexibility: Strong laser pulses enable producing larger curvatures or forming thicker plates [110]. • Tooling, precision, and surface finish: Minimal tooling requirement. A highly repeatable process as the laser pulses are ordered thus, desired precision can be achieved. Minimized surface damage in the treated region [145]. | <ul style="list-style-type: none"> • High initial setup cost, however, the process can eliminate other post-processing expenses as surface quality can be preserved. |

2.2.1 LPF process parameters

Many researchers have expressed interest in improving the efficiency of the LPF process by investigating different experimental process setups [66] and exploring various process parameters [63, 65, 113, 129]. Optimal LPF process parameters were identified through experiments involving parameter variations [132]. Typical process parameters investigated in the existing literature include laser energy, number of peening sequences, overlap between two consecutive laser pulses, area of the focus size, and the thickness of the material.

Definitions of process parameters

To ensure consistency, this study adopts the following specific definitions and terminology of LPF process parameters that are commonly used in literature but may differ from those used in some publications.

Area of the laser spot (A_f): Area of the laser beam perpendicular to the direction of the laser beam, measured at the focal point of the laser optic (for a square laser optic, it is defined by the length of the side (d)). It is important to note that when the laser beam and target surface are not perpendicular, the focus size and the area that is irradiated at the target may differ.

Angle of attack ² (α): refers to the angle formed by the axis of the incident laser beam and an axis along the surface normal to the base plate as shown in Fig. 2.3 below. For a certain angle of attack α , the area of the spot size (A_f) at the laser focus is affected, as the length of the spot (d) is enlarged. The enlarged length (w) can be computed as: $w = d/\cos(\alpha)$.

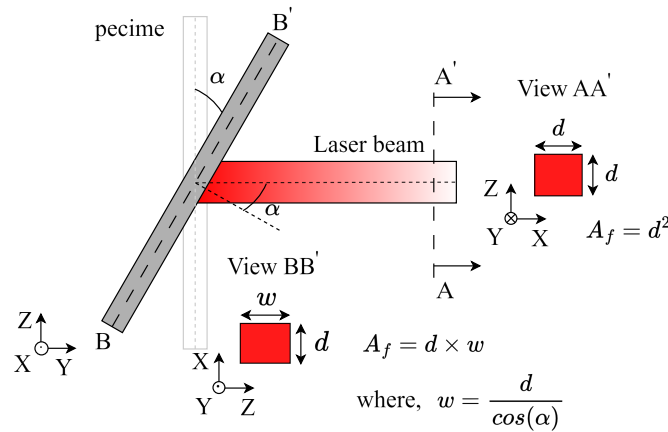


Fig. 2.3: Schematic defining angle of attack (α) during LPF. The length of the spot size (w) at focus increases as the beam is projected over a larger distance on the specimen caused by the rotation of the specimen.

Laser energy (E_L): is the laser pulse energy.

²Please note that the definition is explained assuming a square laser optic. Mathematical equations will change in case of a circular optic

Laser optic area (A_L): The area of the laser optic used in the setup of the laser system.

Laser pulse width (τ): The entire duration of a single laser pulse.

Frequency (f): The number of laser pulses applied per second.

Idealized laser power density (I_o): The ratio of laser energy (E_L) and the product of the laser spot size and the laser pulse duration (τ) full width at half maximum (FWHM) calculated as:

$$I_o = \frac{E_L}{A_f \times \tau_{FWHM}}. \quad (2.1)$$

It should be noted that the actual laser power density $I(t)$ of a laser pulse is a function of the entire duration of the laser pulse (t).

Overlap (δ_{scan} , δ_{step}): The overlap (δ) in the either scanning or stepping direction describes in percentage, the coverage between any two consecutive laser pulses measured by the size of the laser spot along that direction. The overlap in scanning direction (δ_{scan}) and stepping direction δ_{step} according to Fig. 2.4 can be calculated as:

$$\delta_{scan} = \left(1 - \frac{w'}{w}\right) \times 100, \quad (2.2)$$

and

$$\delta_{step} = \left(1 - \frac{d'}{d}\right) \times 100. \quad (2.3)$$

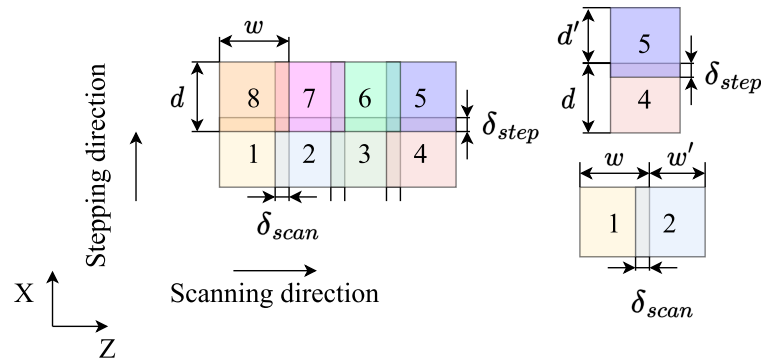


Fig. 2.4: Definition of overlap between two consecutive laser pulses along the scanning direction and stepping direction. The numbers indicate the order in which laser pulses are applied.

Number of peening sequences (n): denotes the repetition rate of a peening pattern applied to a particular region of interest. A pattern is formed by ordering laser pulses in two principal orientations, namely the scanning and the stepping direction. Some of the possible peening patterns are shown in Fig. 2.5. A combination of the direction of application of the laser pulses and overlap together generates complex patterns³.

³The peening patterns indicated in Fig. 2.5 are studied in this work. Greater flexibility in creating more patterns is possible however currently this is limited due to the point-to-point (PTP) programming constraints of the KUKA industrial robot while carrying out this study.

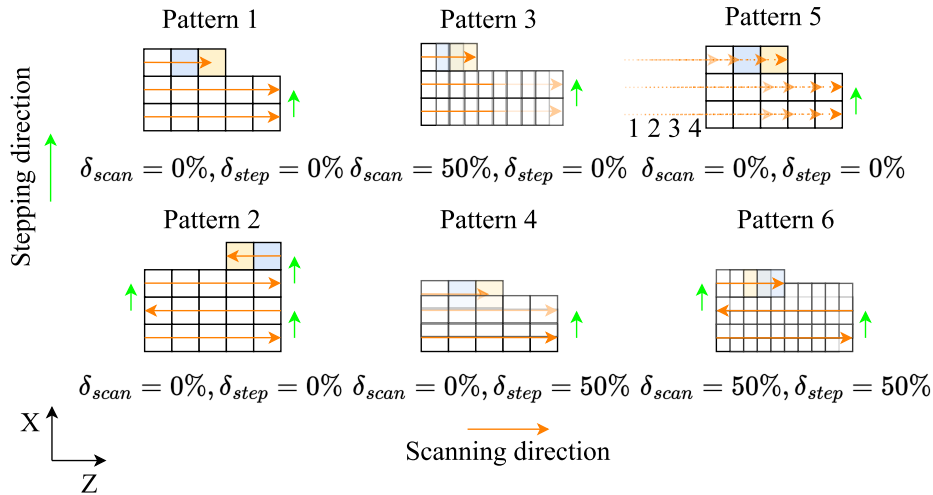


Fig. 2.5: Different patterns formed by the combined ordering of the laser pulses with an overlap in scanning direction and stepping direction. Patterns 1 and 2: have no overlap however, in pattern 1, a unidirectional ordering of pulses can be seen whereas pattern 2 has a zig-zag ordering of pulses. Patterns 3, 4, and 6 indicate the effect of overlap. Pattern 5 is similar to 1 however, the unidirectional ordering of pulses is repeated four times per row.

In a general context of the laser system, experiments reported in the work of Berthe et al. [16] showed that, for a laser power density varying from 2-5 GW/cm², the maximum pressure of induced shock waves increases linearly however, above 5 GW/cm² a saturation is reached due to plasma breakdown. The shape of the laser pulse also affects the induced shock waves. The temporal shape of the pressure pulse is observed to have high intensity over a short width for a short-width laser pulse however, for a Gaussian laser pulse, the corresponding temporal profile of the pressure pulse exhibits a gradual rise to a maximum and relaxes over more than twice the width of the laser pulse [30]. The shape of the laser spot can be controlled by modifying the angle of attack, it is evident that increasing the angle of attack increases the laser spot area (Fig. 2.3) and hence reduces the surface laser power density however, increases the processing rate.

The parameter space for LPF is highly variable, consisting of numerous laser parameters, such as laser energy, pulse duration, spot size, frequency, and overlap. In addition to these laser parameters, peening patterns also play a significant role in determining the feasibility of achieving the desired deformation in the treated region during LPF. As a result, the effects of these parameters and their combinations on the achievable bending for different types of materials are summarized in Table 2.2 with the help findings of from the literature. It was observed from the literature that, the deformation in specimens after LPF is broadly dependent on the parameters of the laser system (such as laser power density, number of peening sequences, overlap, and laser spot size), the material properties (including the thickness of the specimen), and the plasma confinement strategy (i.e. the type of protective and transparent overlays)[169].

Table 2.2: Influence of various process parameters on the achievable bending in the treated region for different materials found in the literature concerning LPF

| Process parameter | Reference | Material | Influence |
|-----------------------------|--------------------|-------------------------------|--|
| Laser power density | [34, 113, 66] | AA1060, AA2024 fiber laminate | <ul style="list-style-type: none"> Degree of bending increases with increasing laser power density. Transition in direction of bending from convex to concave. Upon increasing the laser power density after a certain limiting value, there is a saturation of achieved deformation in the treated region. |
| Overlap | [113, 132, 63, 34] | Aluminum, Ti6Al4V, AA1060, | <ul style="list-style-type: none"> The measured bending angle [63] or arc radius [132] in the LPF-treated region increased with increasing overlap. |
| Number of peening sequences | [63, 59, 132] | Aluminum, AA1060 | <ul style="list-style-type: none"> Bending behavior is dependent on the thickness of the material and is observed to increase with an increasing number of peening sequences, up to a certain threshold. After this threshold, the bending behavior reaches a saturation point, and further increment in peening sequences does not produce any noticeable improvement in bending behavior. |
| Material thickness | [113, 34] | AA1060 | <ul style="list-style-type: none"> For a given material, by varying the material thickness at constant laser process parameters, a critical thickness threshold was found where a transition in bending from convex to concave occurs during LPF [34]. |

Alternative methods of LPF

LPF can be performed with a femtosecond laser as reported by Sagisaka et al. [129] for forming micro-parts. The feasibility of LPF with this laser is limited to small treatment regions since the irradiated area is relatively smaller when compared to traditional LPF applied to larger parts. LPF on micro-parts uses femtosecond and picosecond lasers having a laser pulse duration in the order of 10^{-5} to 10^{-2} ns. Sagisaka et al. [130] demonstrated LPF on pure titanium micro-parts, observed convex deformations in the treated region and produced complex geometries by treating the specimen on both sides, however, noticed a high degree of process variability upon LPF at the edges of the specimen.

Localized heat-assisted LPF was demonstrated in the work of Hu et al. [61] to increase the effect of bending in the case of Ti6Al4V sheets. In this approach, a continuous wave fiber laser is employed in conjunction with LPF to treat the targeted area. LPF is applied on the surface while simultaneously heating the specimen from beneath. As a result of laser heating, there is a local generation of compressive plastic strains in the near-surface region (beneath the specimen) due to elevated temperatures, and thus the specimen bends towards the laser beam [46]. Furthermore, convex bending occurs as a result of the compressive stresses generated near the top surface of the specimen, which is caused by LPF. Therefore, LPF with assisted laser heating increases the arc height in the treated region [61]. On the other hand, the application of heat may have adverse effects by causing defects, such as surface-near small cracks, that can negatively impact the fatigue and ductility of the material. Therefore, it is crucial to regulate temperature effects to minimize damage in heat-assisted LPF.

The two aforementioned types of LPF do not deviate significantly from the fundamental LPF process. Rather, they demonstrate LPF implementation in conjunction with another process or with distinct laser systems, specifically for sub-millimeter scale applications, resulting in the emergence of novel processes. The experimental methods used to study LPF demonstrate the feasibility of the process and its applicability to a range of metallic materials. However, highly complex shapes or components with intricate geometrical features may be challenging to treat effectively via LPF. Nevertheless, LPF offers its ability to induce plastic strains in the surface which are beneficial for bending and modification of deformation of thin-walled structures. Efforts in investigating the influence of process LPF process parameters can reduce process variability and increase the repeatability of the process.

2.2.2 Direct and inverse problem of LPF

The effective use of LPF in various applications requires knowledge of the appropriate LPF process parameters, treatment region, and peening pattern, which pose two primary challenges as illustrated in Fig. 2.6. These challenges can be addressed through experimental methods, numerical simulations, and data-driven approaches. The direct or forward problem involves determining the resulting shape of a specimen after being treated with specific LPF process parameters over a defined region. This problem can be solved using the design of experiments to identify optimal process parameters for achieving the desired deformation in the specimen, or through robust numerical finite element simulations [39].

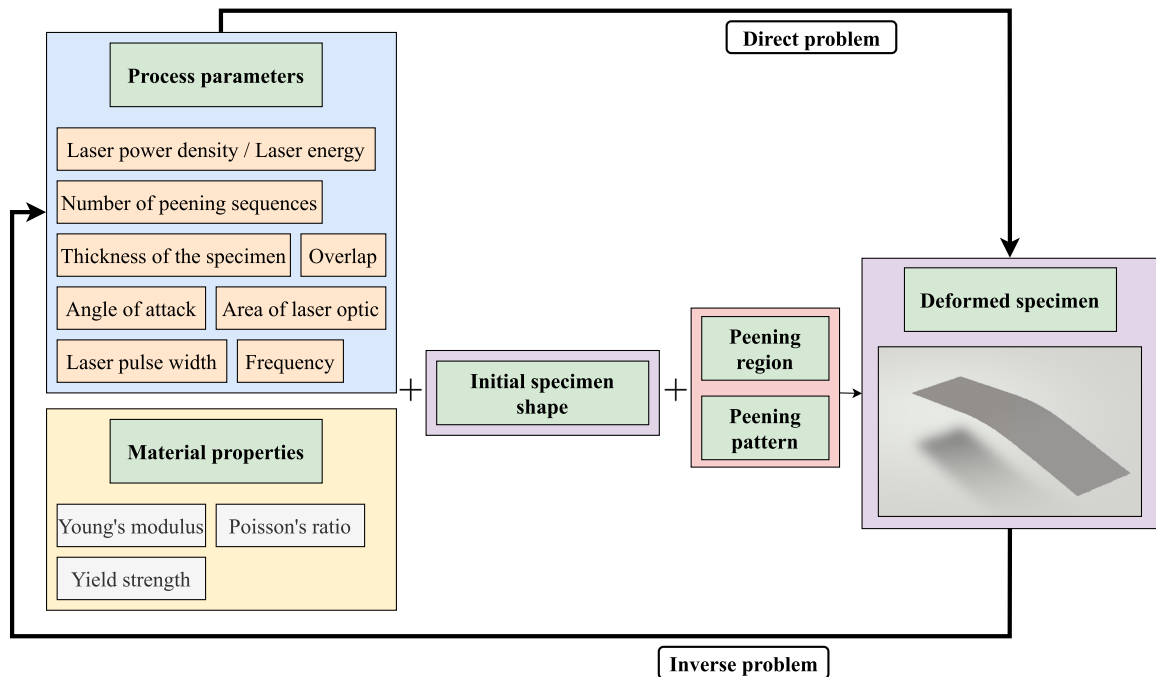


Fig. 2.6: The two main problems concerning LPF. The direct or forward problem involves determining the deformation of the component after processing with a given set of process parameters and the peening pattern corresponding to the region treated. The inverse problem deals with the identification of appropriate process parameters and the region to be opened for obtaining a target deformation.

On the other hand, the inverse problem in LPF involves determining the peening parameters, region to be treated, and the peen pattern to achieve a desired target shape from a given initial shape. In other words, it requires finding the optimal peening process that will deform the component into the desired shape. The inverse problem in LPF presents additional challenges, as it may involve multiple combinations of LPF process parameters that can result in achieving a desired deformation. For example, it is possible that different combinations of laser power density and number of peening sequences can produce the same deformation in the treated region. This could mean that high laser power with fewer repetitions may have a similar effect as low laser power with more repetitions of the treatment. Therefore, determining the optimal combination of process parameters and peening

pattern to achieve a specific target shape requires careful consideration of the interplay between different parameters and their effects on the material response, which adds complexity to the inverse problem in LPF. Nevertheless, by setting constraints on factors such as material properties, the geometry of the specimen, and process parameters, the solution space can be narrowed down to identify the optimal combination of process parameters and peening patterns that will result in the desired target shape. A study by Hu et al. [60] reported the use of eigen-moment as an intermediate variable to quantify the bending deformation due to LPF process parameters. Similarly, an inverse problem in the context of shot peening was solved using ANN with high accuracy and low computation time [141]. However, this approach required large data based on numerical FE simulations.

2.3 Data-driven approaches

Experimental approaches are vital in the study of LPF process concerning thin-walled structures, however, they can be both time and money-intensive. Fundamental studies concerning LPF have focused on numerical simulations, which have been successful in reducing experimental efforts, although it must be remembered that these models are built on assumptions and simplifications of reality. Nonetheless, limitations in numerical models still exist in terms of the lack of specific material parameters, the complexity of their implementation, and the fundamental trials concerning the stability and reproducibility of FE-based numerical approaches. For the aforementioned limitations, it is necessary to recognize the importance of using data-driven models to improve the applicability of existing numerical and experimental methods.

Data-driven models are classified into three types to serve different purposes: white-box models, grey-box models, and black-box models. White-box models are completely transparent models based on physical and mathematical correlations. These models are formulated with the use of simplifying assumptions that reduce complexity however this results in a lack of accuracy in estimating the desired effect. In the context of SMF, white-box models are limited to simple load cases, such as the estimation of bending processes. The underlying reasons are due to the mathematical descriptions and analytical methods used in these models, which lack the ability to capture the complexity of more advanced SMF processes accurately [158]. In spite of the limitations, they can be utilized for the development of numerical process simulations using FE methods. A hybrid modeling approach combining physical and empirical knowledge constitutes grey-box models. On the other hand, black-box models are built exclusively based on the input-output data collected during the process and do not consider prior knowledge about the process [92]. Stochastic or physically-based methods, as well as self-learning algorithms, can be used to determine the relationships between inputs and outputs in data-driven models. While these models are highly accurate in predicting process outcomes and have fast response times, they may

lack transparency and the ability to gain knowledge from the data [92].

The importance of a model in SMF should be initially identified (i.e. model selection) according to the purpose and applications in order to create a data-driven model. In a study by Volk et al. [158], relevant purposes for data-driven modeling for SMF are broadly understood in terms of process design, process control, troubleshooting, process safety, operator training, and environmental impact. Models that describe SMF, as depicted in Fig. 2.7, should possess the capability to make precise predictions regarding the process outcomes across all its working parameters with a fast response time, ensuring safe operation during process execution. The models created are often aimed to solve a specific task within the defined limits and hence the degree of flexibility has low significance. Model-based analyses and optimization (referred to as knowledge in Fig. 2.7) have high importance and offer a greater understanding of the phenomena during the process.

| Model trained for the purpose of | Requirements of the model | | | | | |
|----------------------------------|---------------------------|----------|---------|------------|-------------|-----------|
| | Precision | Accuracy | Runtime | Robustness | Flexibility | Knowledge |
| Process design | High | High | Medium | Medium | Low | High |
| Process control | High | High | High | High | Low | Low |
| Troubleshooting | Medium | Medium | Medium | Low | Low | Medium |
| Process safety | High | High | High | High | Low | Medium |
| Operator training | Medium | Medium | Medium | Medium | Low | Medium |
| Environmental impact | High | High | Low | Medium | High | High |

High
 Medium
 Low

Fig. 2.7: Schematic of the importance of a trained model concerning SMF process with characteristic features against the expectations from it classified into three levels adopted from the study by Volk et al. [158].

The process of creating a data-driven model involves several fundamental steps as described in Fig. 2.8. This includes data acquisition, transformation, modeling, monitoring, and maintenance.

Data acquisition

In the case of SMF, the quality of the product is dependent on product geometry, material parameters, and various process parameters. The first step in the development of a data-driven model involves product and process data collection [160]. Various sensors, such as pressure, temperature, speed, and position sensors, are employed in SMF processes to capture real-time status information pertaining to different physical actions and effects. These sensors are utilized to observe and monitor the functioning of the forming machine or tool (as in LPF) [80, 151, 176].

Data transformation

The collected data must be cleaned ensuring the quality of information is preserved. Feature engineering is a critical aspect of a data-driven model that aims to extract valuable

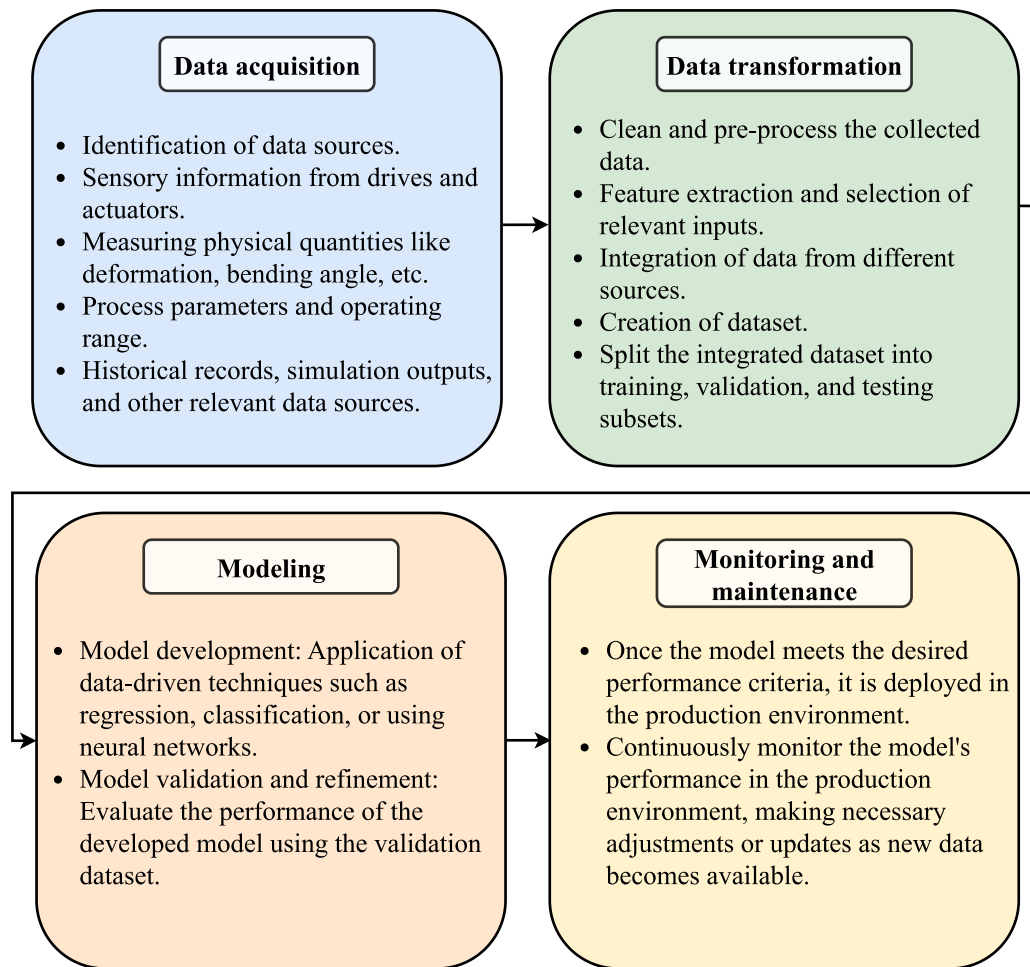


Fig. 2.8: Schematic representation of principle steps in creating a data-driven model for SMF [88].

information from the cleaned data [35]. It involves the process of selecting, creating, reducing, and transforming features to enhance the predictive power and generalization capabilities of the model.

A study by Bellman [15] demonstrates the challenge in data-driven modeling, highlighting the importance of reducing the dimensionality of the model and indicating that data-driven models tend to perform well in low-dimensional regimes. As the dimensionality (i.e. the number of input features) increases, the complexity of models grows exponentially, limiting their generalizability [35]. Additionally, when an advanced data acquisition process is employed, redundant features may be included in the data space, which adds no meaningful information to the model but significantly increases computational requirements for the learning algorithm. Therefore, feature reduction techniques are utilized to decrease dimensionality, eliminate noise, and remove redundancy from the data while preserving relevant information.

Data transformation also involves either normalizing or scaling the features to ensure they have a consistent range or distribution. This step is crucial when using models that are

sensitive to the magnitude of the features. Common techniques include min-max scaling, z-score normalization, or logarithmic scaling [5]. Furthermore, the generation of meaningful features can also be achieved by transforming generic inputs into dimensionless inputs which improves the performance and generalization of the model [85]. The works of Huber and Tsakmakis [68], Huber et al. [67] showcased a hybrid approach to predict the material properties of thin film substrates. Buckingham's Pi theorem [72] and empirical scaling laws were used to transform the input features and outputs. The work of Bakarji et al. [9] shows the applicability of these laws using physical problems such as a bead on a rotating hoop, a laminar boundary layer, and Rayleigh-Benard convection and observed that they enhance the generalization and learning ability of ML models. Bock et al. [18] further demonstrated the effectiveness of physically normalizing inputs and outputs based on Buckingham's Pi theorem in enhancing predictions made by an ANN. This normalization technique led to a reduction in prediction errors and an improvement in the model's generalization capabilities.

Modeling

In recent times, data-driven approaches have played a crucial role in SMF, laser peening, and laser-based forming, creating more accurate models that can better predict the behavior of materials and their response to different forming conditions [88, 52]. In this context, the goal of this section is to understand the requirements for data-driven modeling approaches and their application to various forming processes. A comprehensive review of the literature is discussed in the following section addressing the advancements, applications, limitations, and challenges involving the applicability of data-driven approaches in the field of SMF.

The features that influence the quality and output of SMF processes are process parameters, material properties, and the geometry or shape of the component. The modeling requirement for SMF often entails a complexity that necessarily involves combining several inputs to predict the desired output. Data-driven modeling approaches (especially black-box models) for SMF address this complexity by combining experimental data and FE simulations to predict various outputs of interest [32, 40]. These outputs can include forming defects (e.g., wrinkling, tearing) [4, 1], material parameters [22], bend angles [48, 40], die-punch parameters [51], and the optimization of incremental SMF parameters [43, 54, 149]. Black-box modeling approaches have become essential in achieving high prediction performance without the requirement of developing specific mathematical functions. These approaches are primarily categorized based on their significance into regression models, classification models, and deep neural network models. Table 2.3 summarizes the use cases for black-box models developed in the literature for SMF. Regression-based machine learning (ML) techniques have been implemented in these studies focusing on predicting quantitative parameters, such as angles and thickness after forming. On the other hand,

classification models have been utilized to address qualitative aspects, including surface quality and failure limits of SMF processes.

In addition to data-based methods, SMF also requires the prediction of geometrical features and shapes based on the processing parameters. Convolutional Neural Networks (CNNs) have revolutionized formed shape prediction through their ability to effectively process and analyze visual data [91]. CNNs are utilized to identify and classify defects such as wrinkling, tearing, and surface cracks in formed metal sheets [139, 73, 53]. Low et al. [91] utilized CNNs to predict geometric errors in die-less single-point incremental forming, achieving promising accuracy.

Monitoring and maintenance

Once a model successfully fulfills the desired performance standards, it is deployed either within the production environment or integrated into the SMF process at a laboratory scale. This deployment enables continuous monitoring of the workpiece, starting from its raw material stage all the way to the quality inspection stages [89]. Liewald et al. [88] presented the development of a real-time ML model implementation for predicting tool health during SMF which showcases the need for monitoring these models. Effective monitoring and maintenance of ML models utilized in SMF play a pivotal role in guaranteeing their peak efficiency.

Table 2.3: Summary of ML applications for the prediction of SMF processes categorized as regression and classification tasks

| Regression models | | | |
|------------------------------|----------------------------|---------------------------|--|
| Reference(s) | Forming process | Material | Input features |
| [51, 69, 98] | SMF (V - bending) | Steel and aluminum alloys | Process parameters, sheet thickness |
| [90, 140, 32] | SMF (U - bending) | Steel alloys | Sheet thickness, process parameters, material parameters |
| [126] | SMF (different curvatures) | Steel and aluminum alloy | Sheet thickness, process parameters |
| [48] | Laser forming | Aluminium alloy | Initial deflection, process parameters |
| [162] | Shot peen forming | Aluminium alloy | Process parameters |
| [141] | Shot peen forming | - | Target curvature map of the specimen |
| Classification models | | | |
| [84] | SMF (Blanking) | - | Process parameters |
| [125] | Incremental SMF | Steel alloy | Process parameters and toolpath strategies |
| [33] | SMF (Blanking) | Steely alloy | Process parameters |
| [71] | SMF | Aluminum alloy | Measured strains at forming limits |
| | | | Predicted wear class before failure during SMF. |
| | | | geometrical accuracy |
| | | | Springback and maximum thinning |
| | | | Classes based on visual impressions after SMF |

2.4 Numerical simulation methods

The challenges associated with experimental testing procedures in the context of LPF are the costs and time required for conducting physical experiments, complexities in simultaneous control of all process parameters, and limitations in capturing detailed process dynamics. Nevertheless, numerical FE process simulations have emerged as a valuable tool in overcoming these limitations, offering a cost-effective and efficient means to study and optimize the LPF process. In the present section, a detailed review of state-of-the-art concerning numerical process simulations of LPF is presented, highlighting their significance in advancing process understanding and optimization efforts. The numerical simulations should primarily address the following aspects of the LPF process:

1. Determination of appropriate pressure generated on the surface of the specimen corresponding to the parameters of the applied laser pulse. Furthermore, due to the short duration of the pressure pulse, the propagation of the induced shock wave must be simulated as a short pressure with a certain spatial and temporal distribution.
2. The response of material changes rapidly due to the transient nature of loading and thus the material model must account for high strain rates generated during the process.
3. The induced plastic strains in LPF-treated regions for relatively large specimens must be determined efficiently since simulating every single laser pulse is computationally impractical. Thus, the numerical simulation approach must be scalable to various large geometries.

Modelling plasma pressure and the pressure pulse

Determining appropriate plasma pressure is essential to predict the achievable bending in the treated region during LPF however, it is challenging due to the transient nature of the pressure pulse and the characteristics of the generated plasma. Literature studies show that plasma pressure depends on laser parameters [36, 37] and the confining medium [28, 26]. The duration of the pressure pulse is approximately 2-3 times larger than the applied laser pulses having a pulse width of 10-100 ns as reported in the work of Peyre and Fabbro [119]. The plasma pressure is defined as a function of time t and space (x, y) as $p(x, y, t)$. Nevertheless, the pressure pulse can be simplified by assuming that it has uniform spatial distribution. Fabbro et al. [36] presented an analytical approach for a one-dimensional case. This approach considers the plasma pressure evolution as a three-step process; (1) within the laser pulse duration, the plasma generated induces a pressure pulse, (2) the plasma continues to exert pressure as it cools adiabatically after the laser pulse duration, and (3) as the plasma recombines, the heated gas expands adding momentum to the induced pressure.

The plasma pressure evolution for a one-dimensional case, assuming a constant laser power density (E_L) is derived as:

$$p = 0.1 \sqrt{\left(\frac{\alpha_p}{2\alpha_p + 3}\right) \times E_L \times Z}, \quad (2.4)$$

where p is expressed in the units of kbars, E_L is in the unit of GW/cm^2 , α_p is a constant representing the thermal energy fraction of the total internal energy of the generated plasma, and Z is the acoustic impedance of the confining medium. Although this model has gained widespread acceptance and validation in the literature [64, 118], it only provides a one-dimensional solution and does not consider the spatial distribution of the pressure pulse. Nevertheless, works of Zhang and Yao [172] [173] report improved plasma pressure models, considering complex interpretations of the interactions between the laser pulse with the confining medium and the spatial distribution corresponding to a Gaussian laser pulse. Wu and Shin [166] report a self-closed thermal model considering electron-ion, electron-atom, and photo-ionization interactions of the generated plasma for a water-confined regime.

In addition to these plasma pressure modeling approaches, various shapes of the temporal pressure function $p(t)$ are proposed in the literature for performing numerical FE simulations [21, 146, 75, 120]. The works of Brockman et al. [21] and Spradlin et al. [146] report a triangular temporal pressure pulse for a laser pulse having a width of 20 ns at FWHM. Sticchi et al. [147] and Berthe et al. [17] modeled the pressure pulse based on experimental measurements using a velocity interferometer system for any reflector (VISAR) doppler velocimetry. Keller et al. [75] reported a generic shape of the pressure pulse defined by three independent parameters namely, the duration of the pressure pulse, the time at which the induced pressure reaches a maximum, and the maximum value of the induced pressure. In a recent numerical study by Pörtl et al. [120], the pressure pulse is modeled with a sharp linear raise followed by exponential decay, considering two primary characteristics of the laser pulse which account for short rise time followed by relaxation. These different approaches offer flexibility in modeling the pressure pulse induced by laser pulses with varying characteristics, such as pulse width, rise time, and relaxation.

Material model

After modeling the pressure pulse, it is necessary to accurately predict the effect of the pressure pulse on the target material and record the material response. This is primarily challenging because of the transient nature of the laser peening processes (10-200 ns) and the high magnitude of the induced pressure (2-10 GPa). As a result, the material model involved in the FE simulations should be able to record the material behavior corresponding to this transient nature. Studies show that materials processed by laser peening are subjected to significantly high strain rates in the order of 10^{-6} s^{-1} .

Numerical FE simulations concerning laser peening are widely prevalent in literature with respect to investigating the induced compressive residual stresses [118, 148] however for LPF, the focus is on investigating the deformation in the treated region [59]. In a study reported by Amarchinta et al. [6] to investigate the effect of different non-linear material models for simulating the effect of peening, results showed that the Johnson-Cook (JC) model consistent results with the experiments for laser peening as well as LPF [59]. The JC material model describes the yield stress (σ_Y) as:

$$\sigma_Y = \left[A_{JC} + B_{JC} \varepsilon_{pl,eq}^{n_{JC}} \right] \left[1 + C_{JC} \ln \left(\frac{\dot{\varepsilon}_{pl,eq}}{\dot{\varepsilon}_{pl,eq,0}} \right) \right] [1 - [T^*]^{m_{JC}}], \quad (2.5)$$

where $\varepsilon_{pl,eq}$ is the equivalent plastic strain, $\dot{\varepsilon}_{pl,eq}$ is the plastic strain rate, and T^* is the homologous temperature. $\dot{\varepsilon}_{pl,eq,0}$ is the reference strain rate used to determine JC parameters. A_{JC} , B_{JC} , C_{JC} , n_{JC} and m_{JC} are experimentally determined JC parameters. As laser peening is often regarded as a purely mechanical process [119], the influence of temperature is neglected in the material model [6, 59]. Therefore, the temperature in equation 2.5 is neglected. The numerical simulations performed in this work rely on the material properties and JC parameters available in the existing literature [87]. For Ti6Al4V, the elastic and JC material parameters are tabulated below.

Table 2.4: JC material parameters and physical material properties of Ti6Al4V used for FE simulation of LPF [87]

| Density [g/cm^3] | (ρ), | Young's modulus (E), [MPa] | Poisson's ratio (ν), [-] | Yield strength A_{JC} , [MPa] |
|--|--|---|---|------------------------------------|
| 4.47 | | 108500 | 0.33 | 728.7 |
| Strain hardening coefficient (B_{JC}), [MPa] | Strain hardening exponent (n_{JC}), [-] | Strain rate hard- ening coefficient (C_{JC}), [-] | Reference strain rate ($\dot{\varepsilon}_{pl,eq,0}$), [s^{-1}] | |
| 498.4 | 0.28 | 28×10^{-3} | 10^{-5} | |

Approach for simulating LPF

Numerical FE simulations have proven to be highly effective tools in predicting the deformation behavior of specimens treated via LPF [59]. Understanding the transient response of the material during LPF is challenging due to the short time scale, the high strain rates that are applied on the target surface, and the complicated dynamic material response to reach a steady state. Explicit FE solvers are primarily used to effectively solve problems of transient nature on a short time scale [108]. During experimental conditions, there is a significant interval of time between two consecutive laser pulses however, it is computationally not feasible to simulate this with every single laser pulse on a specimen due to the extremely large time step. As a result, simulating LPF on specimens only with explicit FE solvers is not possible. Nevertheless, literature studies of numerical FE simulations

concerning LPF are developed by simulating the process in a two-step approach (see Fig. 2.9): The first step is to simulate the transient response of the material for the duration of the induced pressure pulse during LPF by an explicit FE solver, and the second step involves transferring the stress and strain fields of the explicit simulation into an implicit solver following a static relaxation [59, 64].

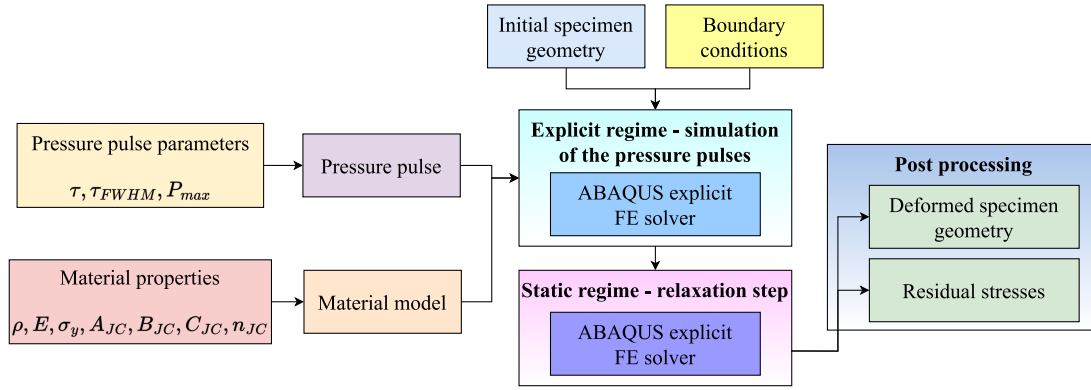


Fig. 2.9: Schematic illustration of LPF using FE simulation. The explicit regime is used to stimulate the pressure pulse that induces a dynamic response in the material, which is then transferred to the ABAQUS static FE solver. The plastic strains and residual stresses at equilibrium are calculated in the static regime. Post-processing of the plastic strains allows for comparison of the deformations from the simulation. Although residual stresses can also be computed, the deformation in the specimen is of primary interest for LPF.

This approach is highly effective for specimens with small treatment areas. However, the computational cost of this method increases significantly when the number of applied laser pulses rises, as the explicit regime requires more time as well [120, 2]. As a result, it may not be feasible for simulating LPF on specimens with large treatment regions. Nevertheless, the computational efforts can be reduced by simulating LPF using the Eigenstrain approach.

In general, a solid subjected to external mechanical loading experiences a change in shape often referred to as elastic and inelastic deformations. Eigenstrain is a term used to describe inelastic deformation that remains in a solid after the removal of an external load. The term *eigenstrain* (ϵ^*) is introduced by Mura [102], used to define the internal stresses that arise in bodies without any external forces or surface constraints. The only type of eigenstrain generated by LPF is the plastic strain and hence the total strain (ϵ) in a material is the sum of elastic strain (ϵ^{el}) and eigenstrain (ϵ^*).

The eigenstrain methodology has been validated as a highly effective technique for quantifying deformation in specimens processed with LPF [60]. This approach enables the incorporation of the cumulative effects of multiple laser pulses on large specimens while maintaining computational efficiency [2, 58, 120]. The eigenstrain approach for LPF employs a linear elastic model, with the input of the eigenstrain due to the applied laser pulses to compute the deformation and residual stress in the specimen however, disregarding the

influence of peening pattern. In general FE simulations, the eigenstrain field (ϵ^*) can be introduced as a pseudo-thermal strain field (α) which is expressed as a product of the tensor of the thermal expansion coefficients and the change in temperature (ΔT) as follows:

$$\begin{pmatrix} \epsilon_{xx} & \epsilon_{xy} & \epsilon_{xz} \\ & \epsilon_{yy} & \epsilon_{yz} \\ & & \epsilon_{zz} \end{pmatrix} = \begin{pmatrix} \alpha_{xx} & \alpha_{xy} & \alpha_{xz} \\ & \alpha_{yy} & \alpha_{yz} \\ & & \alpha_{zz} \end{pmatrix} \times \Delta T, \quad (2.6)$$

where the thermal expansion coefficient tensor (α) contains six independent components (along the principal directions x , y , and z) which can be replaced by the induced plastic strains due to the applied laser pulse. By assuming that $\Delta T = 1$, the strain field problem can be solved by a thermo-mechanical FE analysis. However, it remains crucial to acquire eigenstrains that are specific to the region of interest in order to ensure an accurate simulation of deformations in the LPF-treated region. The eigenstrain approach using ABAQUS explicit and static FE solvers is schematically shown in Fig. 2.10 with an example of a cantilever beam fixed at the left edge and a laser pulse applied from above. The primary inputs to the explicit solver are the parameters of the pressure pulse, material properties, and boundary conditions. A dynamic stress state of the specimen is obtained at the end of the explicit simulation, which clearly constitutes the plastic and elastic affected regions due to the induced shock wave.

Now, the eigenstrains (ϵ^*) resolved along the depth are evaluated by an averaging scheme [75] at the integration points of the FE model where the pressure pulse is applied. These eigenstrains are transferred to the initial geometry in the static solver as thermal coefficients (pseudo-thermal strains). For the static solver, necessary boundary conditions, material properties, and the initial geometry of the specimen are provided as inputs. It is crucial to note that the initial temperature of the sample is increased by 1K during the relaxation step to ensure that $\Delta T = 0$. Thus, the static solver solves this as a thermo-mechanical FE analysis, and the global deformation in the specimen is computed.

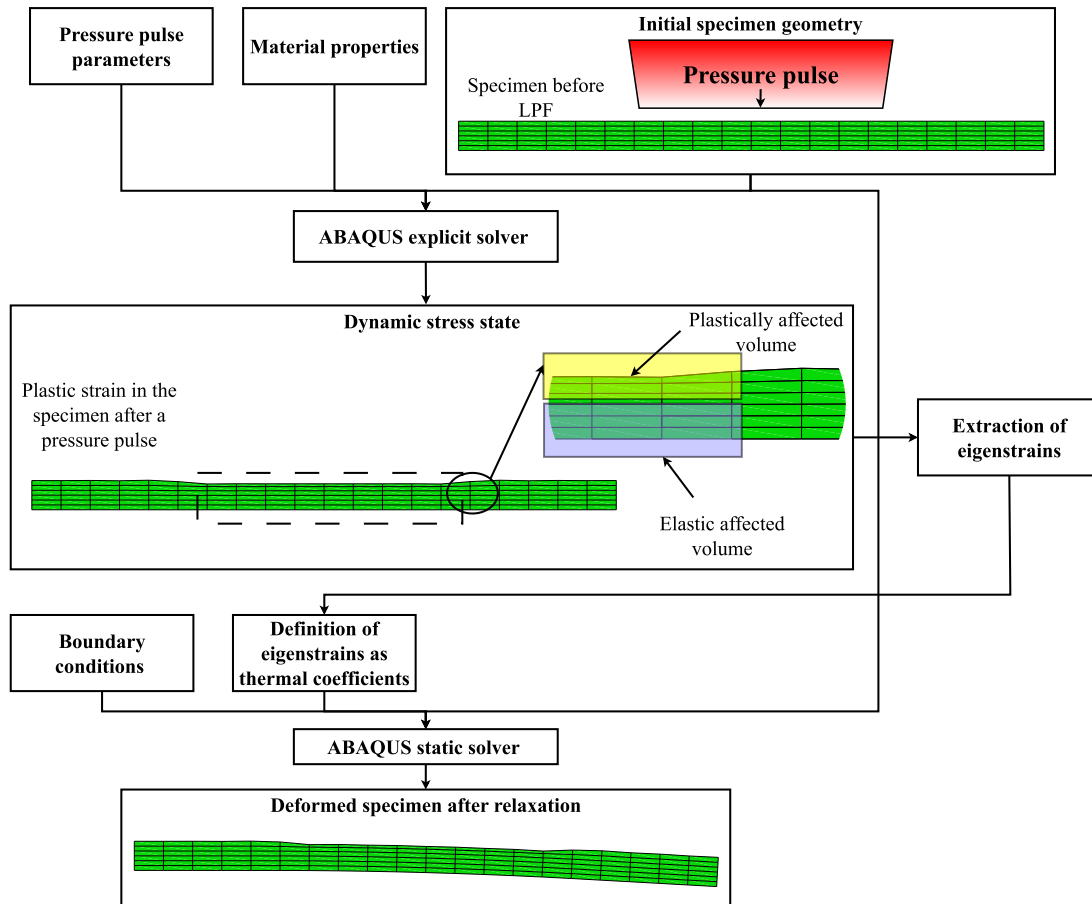


Fig. 2.10: Schematic of the steps in the eigenstrain approach using ABAQUS explicit and static FE solvers.

In a numerical study by Pörtl et al. [120], a three-step FE simulation strategy is applied to simulate the global deformation after a large-scale LPF. This approach involves simulating laser peening on a relatively small specimen, then transferring the eigenstrains by assuming the periodicity of strains in representative volumes to a large geometry, followed by computing stresses, strains, and global deformation as a thermo-mechanical FE simulation. On the other hand, deriving eigen-moment as an intermediate variable for numerical FE simulations to describe the bending deformation after LPF with respect to the process parameters was also found to be consistent with the experimental results to produce complex shapes [62, 60].

Numerical simulation approaches (as summarized in Table 2.5) have been successfully applied for LPF to understand the underlying mechanics considering the laser pulse parameters as well as physical process parameters and predict the global deformation after peening for different materials. Initially, smaller treatment regions were simulated using explicit and implicit solvers. However, simulating the effect of every single laser pulse proved to be computationally infeasible.

Table 2.5: Summary and analysis of the current literature related to FE numerical simulation approaches for LPP process.

| Reference(s) | Materials | Boundary conditions | Characteristic features of the simulations |
|---|--------------------------------------|--|---|
| Hu et al. [59], Ding et al. [34], Zhou et al. [178] | Aluminum 1060, Aluminum alloy LY12CZ | <ul style="list-style-type: none"> One edge of the specimen is fixed (cantilever setup). Spatial resolution of the pressure pulse. Material models: elastic-perfectly-plastic without work hardening, JC model. | <ul style="list-style-type: none"> Explicit simulation using LS-DYNA followed by standard ANSYS simulation. Computationally expensive as every singles shot is simulated. JC material model consistently predicted experimental results. |
| Hu and Grandhi [58], Hu et al. [62, 60] | Aluminum 1060, Ti6Al4V, AA2024-T351 | <ul style="list-style-type: none"> Thick block simulation: a semi-infinite model without considering the geometry dependent effect. Symmetric boundary conditions are applied, modeling only a quarter of the specimen to determine the plastic strain after laser pulse application. LPP simulation: Complete simulation of the sample is performed with an edge of the specimen fixed. | <ul style="list-style-type: none"> Demonstrated two simulation approaches: Standard Explicit/Implicit and eigenstrain approach using ABAQUS. The eigenstrain modeling method is verified to be an effective approach to simulate the LPP process on a large scale with high computational efficiency. |
| Pörtl et al. [120] | Ti6Al4V | <ul style="list-style-type: none"> Source geometry: 50 mm × 50 mm × 1 mm plate. Target geometry: 80 mm × 20 mm × 1 mm. LPP simulation: Complete simulation of the sample is performed with an edge of the specimen fixed. | <ul style="list-style-type: none"> Large scale LPP with a multi-step simulation strategy. The eigenstrains are extracted from the source geometry which considers the laser pulse parameters, the peening pattern, and the position of the representative cells. The eigenstrain approach requires simulation of only 1-7% of the laser pulses which are applied on the target geometry. |

As a result, the simulation methodologies focused on computing the plastic strain induced due to the applied laser pulses in a representative cell and transferring them onto the treatment region of the target specimen (i.e. the eigenstrain approach), which has proved to be very effective for large-scale simulations. Despite the successes, there remain challenges in numerical simulations, such as the accuracy of the determined JC material parameters used in the material model due to the experimental limitations in performing mechanical testing at a high strain rate. Additionally, the eigenstrain approach is dependent on the assumption of the periodicity of the plastic strain field in the plane of the treated surface.

2.5 Summary and conclusions

The fundamentals chapter provides a comprehensive overview of LPF, its principles, and its application in material processing to mechanically deform materials, typically metal sheets, into desired shapes. LPF process involves several critical steps, beginning with surface preparation, where protective overlays, such as black paint or metal foils, are applied to the surface of the material to enhance energy absorption and protect against heat effects during the plasma evolution.

The laser-induced shock waves cause the material to bend or deform, and the direction and extent of deformation can be controlled by adjusting process parameters such as laser power density, pulse overlap, and the number of pulses. An increase in laser power densities increases the degree of bending but may reach a saturation point where further increases do not enhance deformation. Pulse overlap is another factor, with greater overlap between laser pulses resulting in increased bending angles or arc radii. Additionally, material thickness affects the bending behavior, with thicker materials exhibiting different deformation characteristics and critical thickness thresholds impacting whether the deformation is convex or concave.

Data-driven approaches have emerged as essential tools in enhancing the accuracy and predictive capabilities of models utilized in various forming processes, including SMF, laser peening, and laser-based forming. These methodologies, particularly black-box models, utilize experimental and FE simulation data to forecast outcomes such as forming defects, material parameters, bend angles, and die-punch parameters. The principal advantage of data-driven models resides in their superior predictive performance, achieved without the necessity for explicit mathematical formulations, ensuring versatility and efficiency.

Data-driven models are generally categorized into regression models, classification models, and deep neural network models. They serve to complement experimental methods and numerical simulations by utilizing the different forms of data as input and generating desired output, as a result, enhancing the applicability and reliability of existing techniques. Current trends in the literature highlight the application of data-driven techniques

for shape conformity and defect identification, as well as a shift towards hybrid models that integrate physical material properties, process parameters, and empirical knowledge to achieve greater accuracy and insight.

Some of the advanced ML and AI models also facilitate continuous monitoring, maintenance, and optimization of forming processes, thereby ensuring safety and operational efficiency. Previous literature studies show that data-driven approaches significantly enhance predictive accuracy, model efficiency, and process optimization, establishing themselves as indispensable components in the realm of SMF.

Numerical simulations are pivotal in advancing the understanding, optimization, and application of LPF. Utilizing FE models, simulations offer several key advantages, such as enabling detailed predictions of the material response to laser-induced shock waves without the extensive need for physical experiments. This approach not only conserves time and resources but also facilitates the exploration of a broader range of parameters and conditions that might be impractical or costly to test experimentally. Numerical simulations complement experimental methods by providing a deeper insight into the internal stress and strain distributions within materials, which are often difficult to measure directly. This capability allows for the validation and refinement of theoretical models and experimental findings, leading to a more comprehensive understanding of the LPF process.

The literature reveals a trend in integrating data-driven approaches with numerical simulations to enhance predictive accuracy and process efficiency. ML and ANN techniques are increasingly employed to analyze simulation data, predict process outcomes, and optimize parameters, reflecting a significant shift toward hybrid modeling approaches. This integration leverages the strengths of both numerical simulations and data-driven methods, leading to more robust and reliable methodologies for LPF. These advancements underscore the importance of numerical simulations in developing effective LPF strategies and improving the overall efficiency of the process.

Consequently, the devised methodology in this thesis leverages these data-driven approaches, combining them with experimental and simulation data to create a robust framework for modeling LPF.

3

Methodology and approach

3.1 Experimental techniques and material

The experimental techniques and materials used in the LPF process are described in this section. The provided information highlights the critical aspects of the LPF process, including the experimental setup and the technical details of the used laser system.

3.1.1 LPF experimental facility

The experiments described in this study were conducted at the LSP facility located at *Helmholtz Zentrum Hereon GmbH in Geesthacht, Germany*. The LSP facility, as depicted in Fig. 3.1, is equipped with a stationary Q-switched Nd: YAG pulsed laser system and an industrial KUKA robot. The pulsed laser system ensures consistent and accurate laser output, which is crucial for achieving desired effects during the peening process. The robot offers flexibility and precision, allowing for the positioning and movement of a wide range of specimens with different sizes and shapes.

The laser system, produced by QUANTEL, operates within an energy range of 0.5 J to 5 J. The laser pulse frequency is 10 Hz, and the pulse width can be toggled between 10 ns and 20 ns however, only 20 ns pulse is used in this work. The laser pulse has a Gaussian temporal profile with the above-mentioned pulse width near FWHM. The laser beam has a square cross-section with a homogenized beam profile at focus. Additionally, the cross-section of the laser beam can be adjusted at focus, offering options of 1×1 , 3×3 , and 5×5

mm^2 . The present study explores the entire functional regime of the laser energies and available optic sizes to identify suitable laser parameters for LPF.

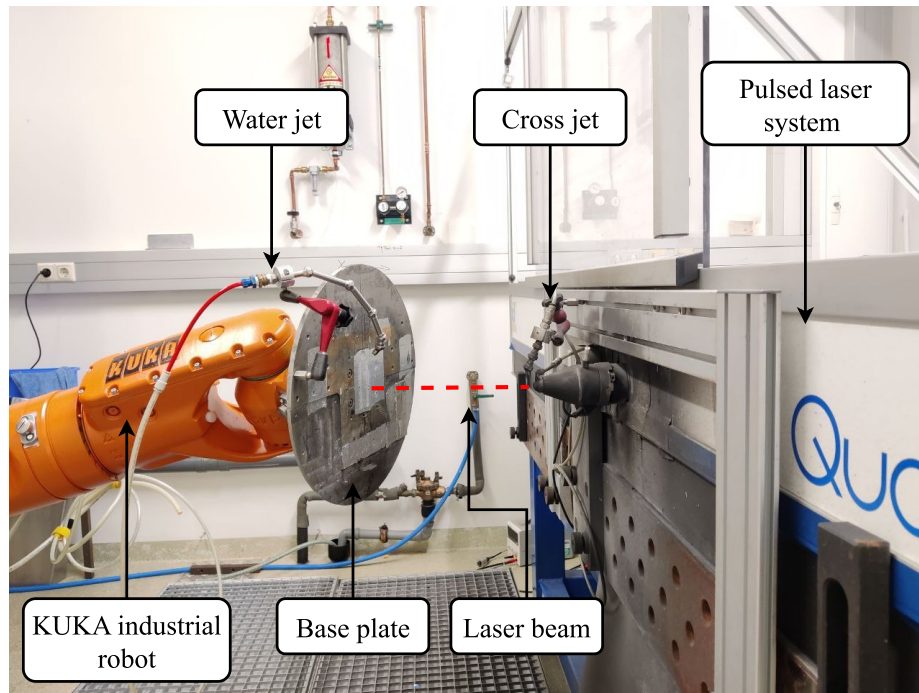


Fig. 3.1: The LSP facility consists of a laser system and an industrial robot. The pulsed laser beam is illustrated by a red dotted line originating from the laser system. A water jet is employed to serve as a transparent overlay. Additionally, a cross jet of pressurized air is utilized for safeguarding the laser optics against foreign particles, process-induced plasma, and splashing water from the specimen during the peening process.

In all experiments, a transparent overlay is achieved by utilizing a laminar water flow generated by the water jet. The specimen is typically covered with black tape, or a metal foil, commonly made of materials such as aluminum or stainless steel. To protect the optics from splashing water and process-induced plasma, a cross jet of pressurized air is directed near the nozzle where the laser pulse is emitted from the laser system.

3.1.2 Experimental setup

In the present work, the experimental setup for LPF is realized using the above facility as shown in Fig. 3.2. The optical system of the laser was protected from back reflection by rotating the specimen around the X-axis at an angle of 25° . As a result, each laser spot had a spot size of $1.1 \times 1 \text{ mm}^2$ for a 1 mm^2 optic. Optic sizes of 3 mm^2 and 5 mm^2 were also investigated with a similar configuration. To serve as a sacrificial overlay, a stainless steel foil or an aluminum foil of $50 \mu\text{m}$ thickness was utilized. A stream of water jet was employed to generate laminar water flow over the specimen, creating a transparent overlay. The size of LPF specimens is $80 \times 20 \text{ mm}^2$, with a treated region as indicated in Fig. 3.3.

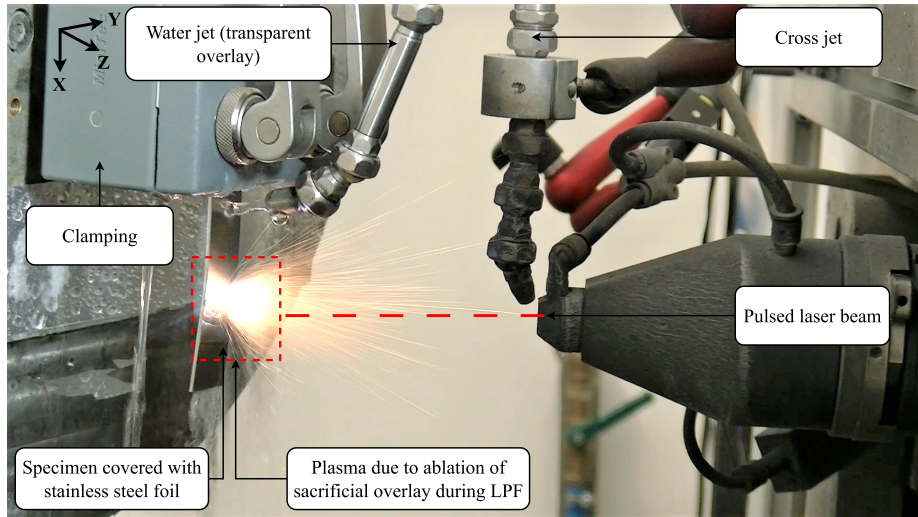


Fig. 3.2: Experimental setup of LPP process, in which the specimen is covered with a stainless steel sacrificial overlay and with a laminar flow of water (created by water jet) as a transparent overlay. Surface ablation of the sacrificial overlay during the process generates plasma.

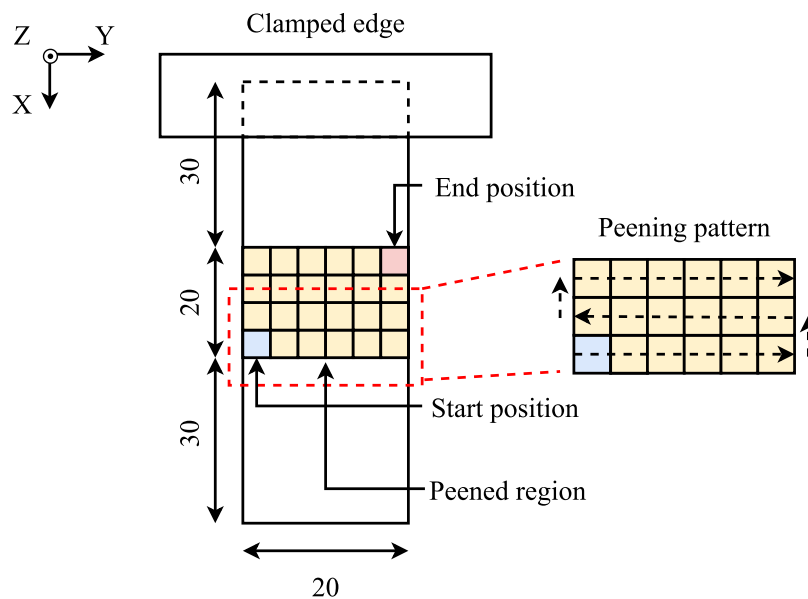


Fig. 3.3: Schematic of the clamped specimen. One edge of the specimen is clamped and the specimen moves relative to the laser beam generating, a zig-zag peening pattern.

3.1.3 Experimental methodology

Using the experimental setup described in this section, the LPP process parameters and their combinations are classified into three parameter sets (as outlined in Table. 3.1) which are investigated in this work. The studied parameters are laser energy, number of peening sequences, overlap, and the type of sacrificial overlay. Furthermore, two types of peening patterns as indicated in Fig. 3.4 are investigated and the deformation after LPP in the treated region is observed.

The experiments were conducted utilizing three parameter sets in Table 3.1. The out-

Table 3.1: The LPF experiments in this study were categorized into distinct parameter sets, determined by the different combinations of process parameters examined

| | Process Parameters | Constant/Varied | Range | Unit |
|------------------------|-----------------------------|-----------------|---------------------------|------|
| Parameter Set 1 | Laser energy | Varied | 0.5 – 5.0 | J |
| | Overlap (scan/step) | Varied | 0/0 – 50/50 | % |
| | Number of peening sequences | Constant | 1 | – |
| | Type of overlay | Varied | Aluminum, Stainless steel | – |
| Parameter Set 2 | Laser energy | Varied | 0.5 – 5.0 | J |
| | Overlap (scan/step) | Constant | 0/0 | % |
| | Number of peening sequences | Varied | 1 – 4 | – |
| | Type of overlay | Varied | Aluminum, Stainless steel | – |
| Parameter Set 3 | Laser energy | Varied | 0.5 – 5.0 | J |
| | Overlap (scan/step) | Varied | 0/0 – 50/0 | % |
| | Number of peening sequences | Varied | 1 – 4 | – |
| | Type of overlay | Constant | None | – |

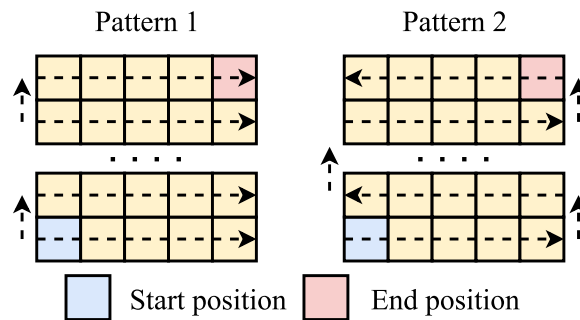


Fig. 3.4: The two types of peening patterns correspond to the LPF-treated regions investigated in this work.

comes of these experiments, presented in Chapter 3 (section 4.1), led to the determination that parameter set 3 successfully attained the desired deformation in the treated region while maintaining the surface quality in the treated region after LPF. Consequently, the process parameters associated with parameter set 3 were selected for further investigation to understand the relationship between the process (i.e. laser parameters and robot movements), and the resulting property relationship (i.e. deformation after LPF).

Table 3.2: LPF process parameters and their ranges to generate an experimental design matrix. LPF experiments corresponding to these parameters were performed to study the process property relationship

| Input | Parameter | Symbol | Range | Levels | Units |
|--------|-------------------------------|--------|-----------|--------|-------|
| 1 | Laser energy | E_L | 1.8 - 3.1 | 4 | J |
| 2 | Number of peening sequences | n | 1 - 4 | 4 | - |
| 3 | Thickness of the specimen | T | 1, 2 | 2 | mm |
| Output | Parameter | Symbol | Range | Levels | Units |
| 1 | Deformation in treated region | $D(x)$ | - | - | mm |

The investigation of the relationship between process and property can be accomplished through systematic experimentation. To optimize resource utilization and maximize knowledge gained, the development of an effective experimentation strategy is essen-

tial. Statistical methods, such as the design of experiments (DOE) are a valuable approach in this process [99, 19]. In this approach, the process parameters are treated as independent factors (inputs), while the deformation in the treated region serves as the dependent parameter, referred to as the response (output) as shown in Table. 3.2. Each experiment is formulated by systematically varying the inputs across the levels defined in the parameter space. The total number of experiments depends on the number of factor levels being investigated [99].

In this case, a full factorial DOE without replicates is chosen since it facilitates examining all possible combinations of the input factors. This comprehensive approach helps in understanding the main effects of each input factor and their interactions with the output. Additionally, a full factorial design provides a basis for statistical analysis. The collected data can be analyzed to determine the significance of each input factor and its interactions, aiding in the optimization of the LPF process. The results obtained from a full factorial design are generally more reliable and informative compared to a limited or partial set of experiments [99, 7]. As a result, the total number of experimental conditions is calculated as $4 \times 4 \times 2 = 32$, representing various unique combinations of the input levels. In each experimental condition, the corresponding output, which refers to the deformation profile in the treated region, is measured respectively. Apart from these experiments, an additional set of ten validation experiments is conducted. These validation experiments are carried out by randomly selecting parameter sets from the defined parameter space. The purpose of these experiments is to provide data for validating the data-driven models that will be developed within the scope of this work.

3.1.4 Material: Ti6Al4V

Ti6Al4V is a highly utilized titanium alloy, constituting approximately 60% of total titanium production [114]. The primary characteristics of Ti6Al4V include a favorable strength-to-weight ratio, exceptional resistance to corrosion, and stability at high temperatures. These properties designate Ti6Al4V as a vital material for structural components. Its applications are reported to be in aircraft engines, turbine blades, and other relevant areas [171]. Ti6Al4V is a two-phase ($\alpha + \beta$) alloy that possesses a noteworthy characteristic in terms of its balance of material properties. Utilizing components made from this alloy extends to various applications, including chemical processing equipment, surgical implants, marine hardware, and automotive applications, where temperatures reach up to 400 °C [114, 164].

Due to its extensive use in structural contexts, there is considerable interest in the formability of Ti6Al4V. Typically, multiple machining processes are required to obtain a functional part from titanium or its alloys. However, Wang and Rahman [163] reported that machining Ti6Al4V poses a significant challenge in the aerospace industry. Addition-

ally, Ti6Al4V exhibits limited formability at room temperature, making conventional SMF processes at this temperature difficult to execute [8]. Given the conventional difficulties encountered in SMF when processing Ti6Al4V alloy, there is a need to explore the suitability of the LPF process to this material for SMF as well as distortion correction, considering its diverse applications across various industries. Additionally, the selection of this particular material for the study is primarily motivated by its alignment with the objectives of the *PEENCOR joint research project*, as highlighted in Chapter 1.

The material used in this study was hot-rolled commercial-grade AMS 4911 Ti6Al4V sheets. The size of the specimens used for the LPF experiments is $80 \times 20 \text{ mm}^2$ with thicknesses of 1 mm, 2 mm, and 3 mm. The dimensions of the LPF treated region are $20 \times 20 \text{ mm}^2$. For validation of numerical simulations, specimens of size $100 \times 50 \text{ mm}^2$ with a thickness of 1 mm are used.

3.1.5 Deformation measurement

After LPF treatment, the specimens deform in the peened region. To measure the deformation in the peened region resulting from LPF, a non-contact linear displacement optical laser triangulation sensor (optoNCDT 2300) was utilized. A deformation profile refers to a curve appearing on the section plane perpendicular to the sample's surface width (refer to Fig. 3.5(a) and (b)). This profile is obtained by averaging measurements taken at five equidistant positions across the specimen's width by the following equation:

$$D(x) = \frac{1}{5} \sum_{i=1}^5 P_i(x), \quad (3.1)$$

where, $D(x)$ is the averaged deformation profile and $P_i(x)$ is the measured deformation profile at position i as indicated in Fig. 3.5(a).

The error bars on the exemplary specimen in Fig. 3.5(c) demonstrate that the observed standard deviation of the averaged deformation values is minimal, indicating uniform bending across the specimen's width. To reduce the margin of error in the measured deformation, a second-order polynomial is fit to the data, and the deformation values from the approximated function are used. Furthermore, a coordinate transformation is applied to rotate the obtained deformation profile, ensuring that the fixed end remains horizontal (see Fig. 3.5(c)).

The measurement technique mentioned above demonstrates reliability, rapid data acquisition, efficient data pre-processing, and user-friendliness when applied to specimens exhibiting uniform bending across their entire width. However, when dealing with deformed specimens subjected to intricate peening patterns, more advanced measurement methods, such as 3D scans, are necessary to obtain a point cloud representing the deformed shape.

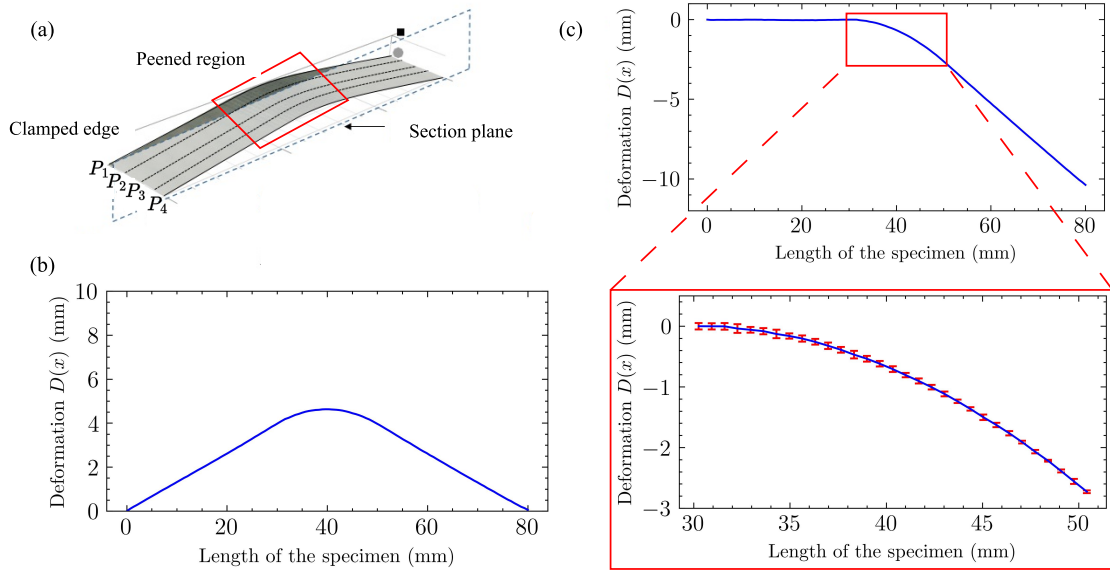


Fig. 3.5: (a) The deformation of a representative specimen is measured following LPF. (b) The graph displays the deformation profile ($D(x)$) measured and averaged across the specimen's length. (c) To align the fixed end parallel to the X-axis, a coordinate transformation is employed to rotate the profile. The error bars in red indicate the standard deviation of the averaged deformation profile within the peened region ($x = 30.0$ to 50.0 mm).

In this study, a 3D scanner named HandySCAN 3D manufactured by Creaform was employed to scan the deformed specimens. The accompanying software facilitated the export of the scans into a mesh format (.stl mesh file) with a resolution of 0.2 mm. The obtained data is post-processed using Meshlab [25].

3.1.6 Surface characterization of the treated region

Surface characterization of the treated region resulting after LPF is of critical importance for evaluating the effectiveness of the process to ensure surface quality in the treated region. To gain further insights into the structural changes induced by LPF, the surface of the peened region was meticulously examined using analytical microscopic characterization techniques. Scanning electron microscopy (SEM) was employed in conjunction with energy dispersive X-ray spectroscopy (EDX) using a Jeol JSM-6490LV microscope and an EDAX Genesis system, respectively. The influence of LPF process parameters on the microstructural features and elemental composition of the treated area is investigated. Additionally, a comprehensive investigation of the surface roughness of the specimens under parameter sets 2 and 3 was carried out utilizing a Keyence VKX 1000 laser confocal microscope. This thorough examination facilitates comprehending the influence of LPF process parameters affecting the surface roughness of the peened region.

3.2 Data-driven methods

The optimization of the LPF process is necessary for the precise production and shaping of thin-walled structures. Traditional experimental and simulation approaches have been fundamental in understanding LPF, but are constrained by resource, time, and cost-intensive nature poses challenges for implementation. As a result, data-driven models are to be developed (as they are proven to be promising alternatives for SMF [158]), leveraging data from numerical simulations and LPF experiments to enhance the applicability of LPF. The present work aims to develop a robust methodology for the application of various data-driven models in optimizing the LPF process. By analyzing the input and output process parameters from experimental data, valuable insights into the complexities of LPF are obtained, and efficient solutions can be devised for process design, control, and troubleshooting. The simulation data, which can be validated/fitted to the experimental data, is also used to utilized to develop data-driven models, which reduce the need for generating large experimental datasets. The tools and methods used for developing data-driven models are explained in this section.

3.2.1 Artificial neural networks

ANNs represent abstract computational tools inspired by the functionality of biological neurons. These networks are utilized to comprehend complex data by identifying underlying trends and patterns. The simplest form of an ANN, described by McCulloch and Pitts [96], is called a perceptron, consisting of a single input layer and an output node. In this study, a fully connected, feed-forward neural network is employed to create the data-driven models. This network architecture comprises a multi-layer perceptron model with an input layer, one or more hidden layers (the number of which was determined during hyperparameter tuning of the ANN), and an output layer. In a feed-forward network, the outputs of one layer serve as inputs to the next layer, progressing from inputs to outputs in a forward direction. The mathematical formulation of a feed-forward ANN is elaborated below.

Assuming there are n number of inputs represented by a vector I (Eq. 3.2). Hence, the input layer is:

$$I = [i_1, i_2, i_3, \dots, i_n]. \quad (3.2)$$

If this neural network comprises p_1, p_2, \dots, p_k units within each of its k hidden layers, the vector representations of these outputs, as denoted by h_1, h_2, \dots, h_k , possess dimensionality that aligns with p_1 through p_k . Consequently, the quantity of units within each layer is referred to as the dimensionality of that specific layer. Then, the weights of connections from the input layer to the 1st hidden layer (h_1 , in Eq. 3.3) are represented by matrix W_1 whose size is $n \times p_1$ in the form of:

$$h_1 = f(\mathbf{W}_1^T \mathbf{I}), \quad (3.3)$$

where, f is a non-linear activation function. Similarly, the weights between the r^{th} hidden layer and the $(r+1)^{\text{th}}$ hidden layer are denoted by the matrix denoted by \mathbf{W}_r with the dimensionality of $p_r \times p_{r+1}$. The recursive equation of input from r^{th} hidden layer to $(r+1)^{\text{th}}$ hidden layer can be formulated as:

$$h_{p+1} = f(\mathbf{W}_{p+1}^T h_p) \quad \forall p \in \{1, 2, \dots, k-1\}. \quad (3.4)$$

If the number of outputs (m) are denoted by a vector \mathbf{Y} , then the corresponding output layer contains m nodes and the final matrix \mathbf{W}_{k+1} has a dimension of $p_k \times m$ which can be represented as:

$$\mathbf{Y} = [y_1, y_2, y_3, \dots, y_m] = g(\mathbf{W}_{k+1}^T h_k). \quad (3.5)$$

where, g is a linear activation function of the output layer in case of regression tasks.

ANNs can be trained to predict non-linear relationships between inputs and outputs by adjusting weights to minimize an error function using the back-propagation algorithm outlined by Rumelhart et al. [128]. Initially, a training instance, also known as batch size, representing the number of samples from the training dataset, is inputted into the neural network, initiating forward computations across the layers with an initial set of weights. Subsequently, the back-propagation algorithm utilizes the chain rule of differentials to compute error gradients as the sum of local gradient products of different connections from a node to the output. The weights corresponding to individual neurons of the ANN are then adjusted to minimize the computed error. This adjustment is achieved by controlling the learning rate of the ANN, a critical tuning parameter that determines the step size at each iteration towards minimizing the loss function. An adaptive learning rate is implemented using available optimizers such as Adam, a popular open-source Python implementation from the Keras library [24]. Finally, the ANN is trained with all available instances from the training dataset. The weights at each neuron are iteratively adjusted to minimize prediction error, and a model with the best weights is retained after the training process.

The performance of the ANN significantly relies on both the quantity and quality of the data used for training, validation, and testing. However, it's critical to prevent over-fitting. A well-known approach, called "Early Stopping," regulates the number of iterations based on a specified performance criterion [168], typically MSE. During each training iteration, prediction performance is assessed using a validation dataset kept strictly unknown to the ANN. Early stopping halts the training process and restores the best weights acquired when the performance criterion is met on the validation dataset. Additionally, understanding the impact of variables or hyperparameters, which define the ANN's architecture, on perfor-

mance and generalization is vital. In this study, hyperparameters such as the number of hidden layers, neurons in each hidden layer, learning rate, and activation function type were simultaneously varied using random-search-based Python implementations using Keras-Tuner [111].

Model performance is assessed by the MSE and the determination coefficient (R^2) which are defined as:

$$\text{MSE} = \frac{1}{n} \left\{ \sum_{i=1}^N (y_i - \hat{y}_i)^2 \right\}, \quad (3.6)$$

$$R^2 = 1 - \frac{\sum_{i=1}^N (y_i - \hat{y}_i)^2}{\sum_{i=1}^N (y_i - \bar{y})^2}, \quad (3.7)$$

where, y_i represents the true value, \hat{y}_i is the predicted value and \bar{y} is the mean of true values. The parameter N is the size of the dataset. These statistical indicators were computed based on model predictions versus the true values corresponding to training, validation, and testing datasets.

3.2.2 Description of experimental and numerical simulation datasets

Selecting the right input parameters for the LPF process is crucial for establishing a dependable and resilient data-driven model, utilizing the available experimental and physics-based numerical data. The studies by Huber et al. [67] and Bock et al. [18] provide valuable insights into addressing this challenge through physical normalization techniques, leveraging Buckingham's Pi theorem. By identifying key physical quantities involved in the LPF process, such as process parameters and material constants, and deriving relevant variables from them, meaningful normalization of inputs and outputs can be obtained (see Fig. 3.6). This not only reduces prediction errors but also enhances the model's generalization capabilities, as demonstrated by previous research. Therefore, a similar physical normalization strategy has been applied to the considered LPF process parameters, and corresponding dimensionless inputs and outputs are obtained.

Considering the LPF process-related parameters, such as laser energy (E_L), number of peening sequences (n), and thickness of the LPF specimen (T), is crucial due to their significant influence on the deformation within the treated region [132]. Additionally, incorporating other experimental process parameters, such as the area of the cross-section of the focused laser beam (A_f) and the duration of the laser pulse (τ), is important for a comprehensive understanding of the process, although they are not varied in the experiments.

Moreover, material parameters such as Young's modulus (E), density (ρ), and the wave speed ($C = \sqrt{E/\rho}$), which represents the speed of transverse propagation of shockwaves through the specimen during LPF, are considered. Including these material properties helps encapsulate the effects of the material on the deformation process.

The output variable, the deformation profile $D(x)$ in the peened region, is influenced

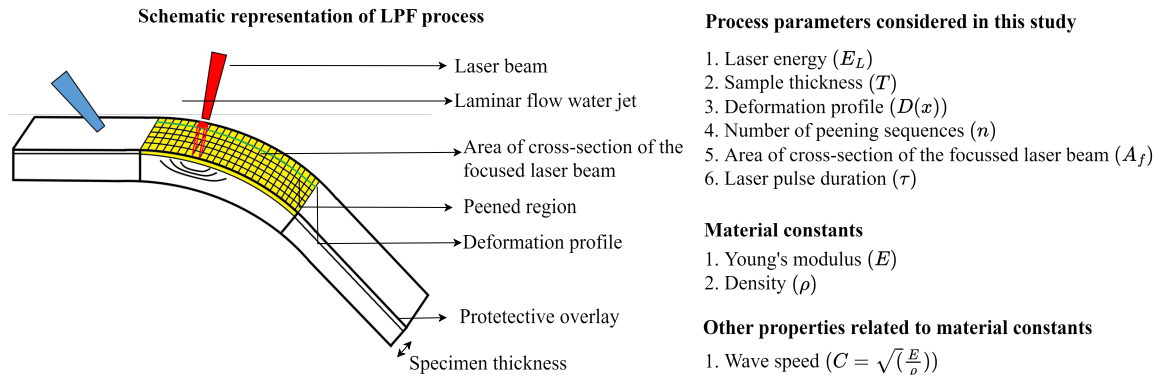


Fig. 3.6: Illustration of the LPF process with the considered experimental process variables, material properties, and the derived parameters which provide relevant physical information to the data-driven model.

by these process parameters and material properties. Incorporating all relevant input and output variables into the developed data-driven model is essential for ensuring its robustness and generalizability. This enables the model to account for various factors that affect deformation in the LPF-treated region, making it capable of generating predictions across different materials and processing conditions.

While the inputs and outputs governing the LPF process are clearly defined, they cannot be directly employed to construct a data-driven model due to the lack of direct physical correlation between input quantities and outputs. Therefore, it is necessary to convert the actual inputs and outputs into dimensionless terms, referred to as dimensionless inputs and outputs, utilizing the Buckingham Pi theorem. This transformation facilitates improved generalization of the developed data, as evidenced by previous findings [18, 68, 85]. The underlying principles of Buckingham's Pi theorem and its application to LPF process parameters are elucidated in Appendix A. The experimental dataset comprises a set of 52 experiments and the simulation data comprises 88 simulations which are divided into training testing and validation sets as shown below.

3.2.3 Data scaling

The original data distribution shape is preserved while constraining it to a specific value range. A min-max scaling was employed on both inputs and outputs. This approach proves advantageous when dealing with outliers or variations in scale within the data. By scaling them to fit within the range of $[-1, 1]$, this normalization process facilitates effective learning by the ANN and ensures numerical stability throughout the training process. The scaling operation was executed through the following equations:

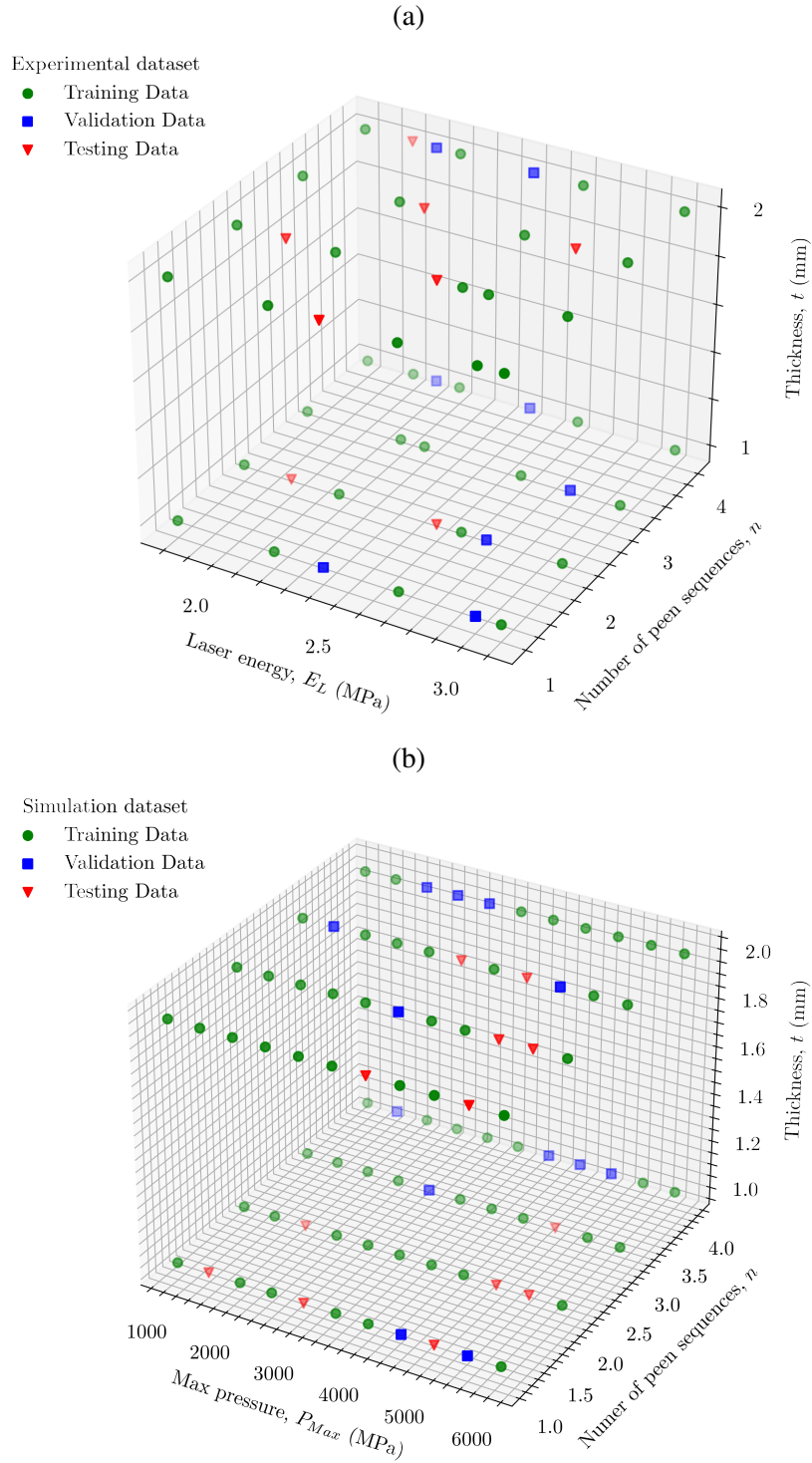


Fig. 3.7: Illustration of the (a) experimental and (b) simulation datasets that are considered in this study.

$$V_{std} = \left\{ \frac{V - v_{min}}{v_{max} - v_{min}} \right\}, \quad (3.8a)$$

$$V_s = V_{std}(V_{max} - V_{min}) + V_{min}, \quad (3.8b)$$

where V_s represents the scaled value of the input or output, V is the original value, v_{min} and v_{max} are the minimum and maximum values in the scaled entity, V_{max} and V_{min} are the minimum and maximum values in the feature range. (available in scikit-learn library [112] as 'MinMaxScaler').

3.2.4 Hyperparameters of ANN

The essential hyperparameters of an ANN include the number of neurons and hidden layers, learning rate, batch size, epochs, activation function types, and optimizer choices. In this study, two separate ANN's are trained on experimental and simulation data, featuring two hidden layers activated by sigmoid function, each containing six neurons (which were determined by an automated random search process by varying the above-mentioned parameters to a certain range until satisfactory learning is achieved by the ANN). The output layer employs a linear activation function, appropriate for continuous output prediction (such as the deformation in the LPF-treated region). Evaluation of model performance during training relies on the MSE as the loss function. This error is gradually minimized via weight adjustments facilitated by the gradient descent optimization technique, a widely adopted method for finding the local minimum of differentiable convex functions, elucidated by Ruder [127].

An adaptive learning rate enhances training performance, leveraging the Adam optimizer with a preset learning rate of 0.001, while other optimizer parameters maintain default settings [78]. Given the modest dataset size, a batch size of 1 is chosen, prompting weight updates after each presentation of a sample to the ANN during the training. The training process spans 1000 epochs, with preemptive measures against overfitting instituted through early stopping mechanisms. Specifically, monitoring of model performance during training incorporates a patience value of 250 epochs and a minimum tolerable improvement threshold (δ) of 10^{-3} . Patience denotes the number of epochs without observed enhancement in the prediction metric on the validation set, beyond which the training halts. Meanwhile, δ signifies the minimum change in MSE required to qualify as an improvement; thus, an MSE change less than δ for two consecutive epochs signifies no advancement. The ANN implementation in this investigation is realized within a Python framework, leveraging open-source libraries such as Scikit-learn and Keras (ref. [112, 111]).

3.2.5 Data-driven process planning for LPF

The process planning for LPF involves solving an inverse problem, aiming to identify the precise process parameters necessary to achieve the desired deformation in the treated region. This inverse nature often yields multiple solutions, given the potential for various combinations of LPF parameters to yield identical deformations. The approach proposed by Hu et al. [57] introduces a hybrid numerical and experimental process planning method,

leveraging the eigenmoment as an intermediary variable linking LPF parameters to resultant deformations. This methodology was tested in crafting a target geometry with a saddle-shaped profile.

This study aims to devise a process planning approach based on predictions derived from a trained ANN and apply it to effect one-dimensional bending and correction of deformation in thin sheets using LPF. As this approach is formulated based on experiential data, the necessity for additional numerical simulations is eliminated. The possibility of multiple solutions can be avoided by defining a range of constraints, influenced by process parameters such as laser energy and the number of peening sequences applied in the treated areas. For example, depending on the application, it may be required to restrict the number of peening sequences to uphold specimen surface integrity. Conversely, a lower laser energy setting might be preferred for precise correction purposes. Thus, adapting LPF process planning to account for such physical constraints becomes necessary in real scenarios, and hence justifies the definition of constraints.

A data-driven approach to process planning is realized, as depicted in Fig. 3.8, across various applications that require obtaining a specific deformation profile either from flat specimens or those already curved to a certain extent. The primary aim of this method is to utilize the predictive capabilities of a trained ANN while adhering to predefined process constraints. The proposed workflow encompasses an initial profile, a target profile, a trained ANN, an optimizer, and input process constraints, each serving distinct functions elaborately explained below.

An ANN undergoes training to predict deformation within the treated region based on specific combinations of experimental parameters within the process parameter domain. Subsequent validation and testing against unknown datasets. As a result, a well-trained ANN is obtained with the capability to predict deformation within the treated region, on various combinations of process and material parameters, including laser energy, peening sequences, and specimen thickness. A comprehensive database encapsulating all conceivable process parameter permutations within the confines of the parameter space corresponding to the training dataset is compiled. Consequently, the ANN predicts a deformation profile for each unique process parameter combination, thereby generating a repository housing deformation profiles for all potential parameter configurations.

The initial profile (D_i) and target profile (D_t), measured along the specimen's span (x) to be processed, are acquired as illustrated in Fig. 3.8. The deviation in deformation between these initial and target profiles is calculated as $\Delta D(x) = D_i(x) - D_t(x)$, representing the disparity to be corrected by LPF to achieve the target profile. Subsequently, the $\Delta D(x)$ profile undergoes discretization into smaller units along the span of the specimen, essential for identifying localized deformations or curvatures. The length of the discretization step (D_s) is chosen based on the nature of the $\Delta D(x)$ profile, thus varying depending on the complexity of the peened profile. Naturally, the discretization step size is not constrained

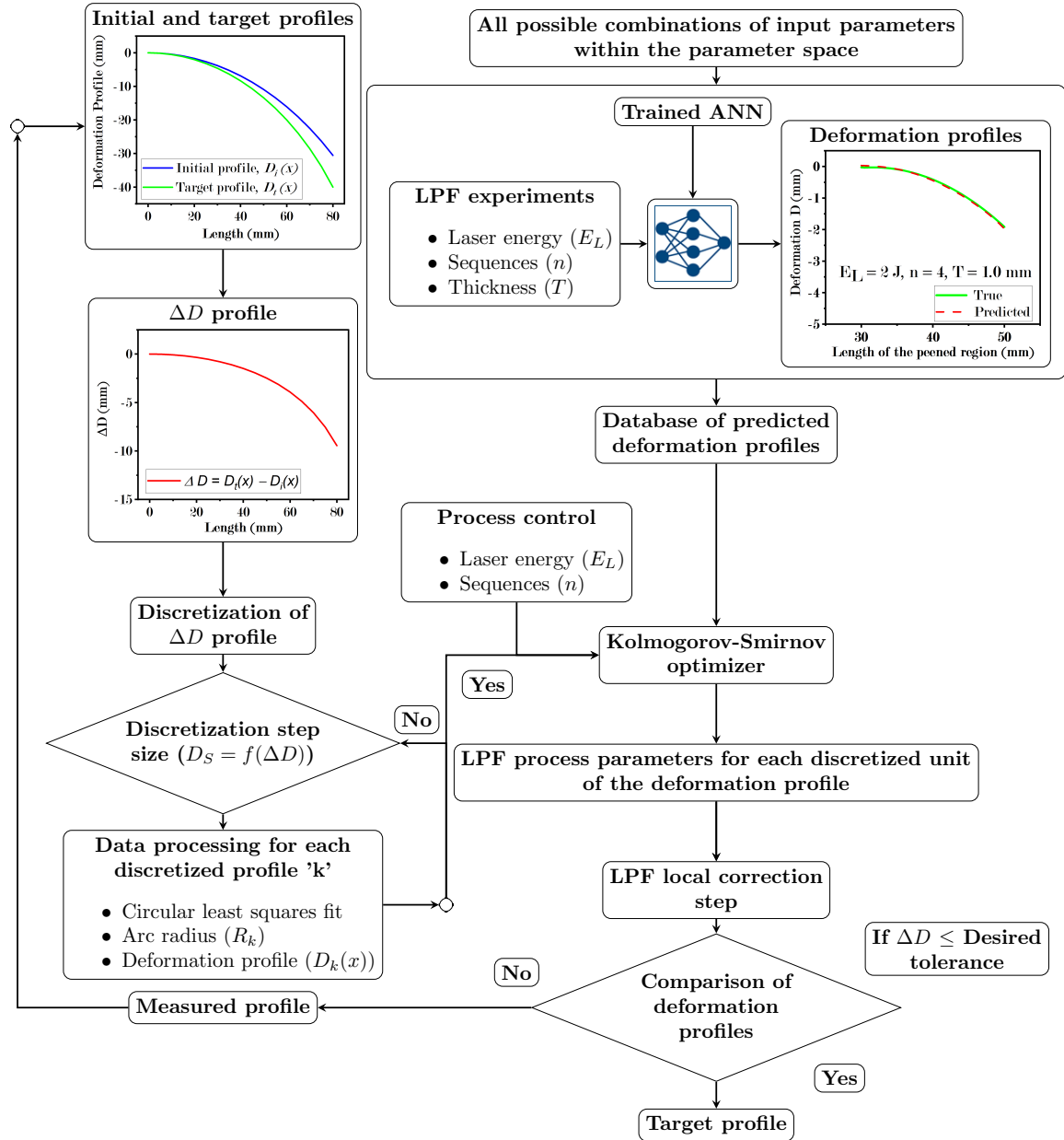


Fig. 3.8: The flowchart illustrates the data-driven LPF process planning, showcasing the integration of ANN-generated predictions for shaping initial deformation to a target deformation. The initial phase involves acquiring deformation profiles for both the initial specimen shape and the desired deformation target. Subsequently, the ΔD profile, representing the disparity between these two profiles, is computed. This ΔD profile is then segmented into distinct sections, and the corresponding arc radius for each segment is determined. Leveraging the arc radius as a pivotal parameter, the optimizer endeavors to identify process parameters conducive to the desired deformation profiles while accommodating external process constraints. A peen-and-measure cycle is initiated to iteratively reduce ΔD until the requisite target deformation is attained within the specified tolerance threshold. [131]

to a constant value and must be adjusted accordingly.

While a constant value of D_s suffices for peening specimens with compound curvatures,

structures with intricate curvatures necessitate varying discretization step sizes across the span. Following the discretization of the ΔD profile into 'k' parts, each discretized segment of size $D_{s,k}$ (refer to Fig. 3.8) can be mathematically represented as follows:

$$\Delta D_k(x) := \{x, \Delta D(x)\}, \forall x \in [D_{s,(k-1)}, D_{s,k}]. \quad (3.9)$$

Every discretized segment $\Delta D_k(x)$ within the ΔD profile indicates the localized variation in deformation between the initial and target deformation profiles, requiring correction via LPF. Corresponding to each discretized unit 'k', the $\Delta D_k(x)$ profile is approximated using a circular fitting function to derive the arc radius (R_k), as depicted in Figure 3.9

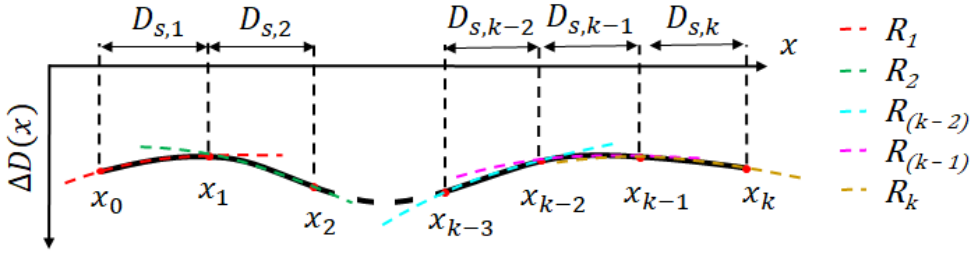


Fig. 3.9: The discretization of the ΔD profile, defined as $\Delta D(x) = D_i(x) - D_t(x)$, involves partitioning the profile into smaller segments. Here, D_i represents the initial profile, D_t denotes the target profile, and $D_{s,k}$ signifies the discretization step size for the k^{th} segment of the profile. [131]

The approach involves employing the least squares fitting method of circles to the discretized data (i.e., $\{x, \Delta D(x)\}$) for each of the 'k' discretized units, following the methodology outlined in the study by Chernov and Lesort [23]. A circular fit is chosen due to the observation that all predicted deformation profiles can be accurately approximated by a circular arc. By fitting circular arcs to the discretized $\Delta D_k(x)$ profiles, corresponding arc radii R_k are derived, as depicted in Fig. 3.9. Subsequently, the arc radius (R_k) is utilized to construct a deformation profile ($D_k(x_j)$), as demonstrated below:

$$\Delta D_k(x_j) = \begin{cases} -R_k - \sqrt{R_k^2 - x_j^2} & \text{if } \Delta D_k(x_j) \leq 0 \\ -R_k + \sqrt{R_k^2 - x_j^2} & \text{if } \Delta D_k(x_j) \geq 0. \end{cases} \quad (3.10)$$

where, x_j denotes the position along the length of the peened region, similar to the predicted output generated by the ANN. Consequently, the discretized $\Delta D_k(x)$ profiles undergo transformation into interpretable deformation profiles.

Reasonably selecting the discretization of the $\Delta D(x)$ profile allows for the peening of realistic target shapes without further optimization. However, employing an excessively small discretization step size can introduce deviations from the desired profile due to accumulated errors and escalate the number of processing steps required (see Fig. 4.14). Conversely, choosing a large discretization step size might lead to erroneous interpreta-

tions, especially when approximating utilizing a circular fit. Ideally, the discretization step size (D_s) should adapt to the characteristics of the $\Delta D(x)$ profile, which vary depending on the specific profile under consideration.

The current process planning approach employs an iterative method where the number and length of discretization are strategically determined based on the characteristics of the $\Delta D(x)$ profile, aiming to minimize the number of segments and maximize the length of each segment. The strategy for selecting the size $D_{s,k}$ of the k^{th} discretized part of the ΔD profile generally leans towards larger discretization step sizes whenever possible. This recommendation ensures optimal processing by significantly reducing processing time through minimizing required peening cycles. Consequently, it not only enhances operational efficiency but also substantially contributes to conserving energy resources.

During the initial iteration, each discretized segment of the deformation profile undergoes approximation using a circular fitting function as outlined previously. The discretization step size for a segment of the deformation profile is evaluated based on the quality of fit, utilizing the R^2 value (set to be greater than 0.99) and the arc radius of the fit. The arc radius of the fit for each discretized unit should fall within the minimum and maximum achievable arc radii within the defined process parameter space.

A large arc radius value suggests a flat region that requires no LPF treatment; however, it could also indicate that the discretization step size is excessively small, necessitating a reassessment of the deformation profile by incrementally increasing the step size. In such cases, the discretization step size for each segment is manually adjusted in small increments until a satisfactory fit is achieved while ensuring the arc radius remains within the desired bounds. This iterative approach proves advantageous as it allows for the adjustment of the number of discretizations and the length of each segment, thereby reducing processing steps. Upon successful discretization of the $\Delta D(x)$ profile, the processed deformation data along with the corresponding fit data is provided as an input into the optimizer.

The optimizer, based on the two-sample Kolmogorov-Smirnov (KS) test as described by Simard and L'Ecuyer [142] and implemented using the Scipy library [156], is employed to assess whether the estimated profiles ($D_k(x)$) align with the deformation profiles predicted by the ANN within the database. A two-sample KS test is conducted for each discretized profile and the predicted deformation profile from the database. The KS test may identify multiple matches of the $D_k(x)$ from the database of predicted deformation profiles, as different combinations of process parameters may result in the same deformation. However, such situations can be avoided by restricting the search criteria based on physical and process constraints. For example, a physical constraint can be defined by filtering the database of deformation profiles ($D(x)$) based on input process parameters like the material thickness (T) being peened.

In this study, LPF process constraints refer to limitations or boundaries that must be followed for the process to operate correctly and generate dependable deformation in the

treated area. The current research has specific limitations for the process; for instance, the laser energy should not exceed 3.0 J, and the number of peening sequences should not exceed four. This is because higher laser energy damages the sacrificial overlay, and increasing peening sequences beyond four doesn't significantly enhance deformation in Ti6Al4V sheets [132]. For practical applications, it might be preferable to have operational constraints on process parameters such as laser energy (E_L) and the number of sequences (n), which can further reduce the occurrence of multiple matches of $D_k(x)$. The optimizer provides an index of the deformation profile from the database that matches the formulated deformation profile ($D_k(x)$). This index serves as a key to identify the corresponding process parameters. Through this approach, a suggested set of LPF process parameters is found for each discretized profile as an output from the optimizer.

3.2.6 Cellular automata neural network

In the present work, a cellular automata neural network (CANN) adapted from Mordvintsev et al. [101], in which a convolutional neural network (CNN) is used as a tool to predict the peening pattern on a flat sheet given the curvature of the sample (ref. Appendix D) computed from the deformation of the specimen as an input. Using this information, CANN learns rules that enable each cell to classify itself into the correct peening pattern, indicating whether it is peened or not. CANN inherently considers both local and global interactions in the curvature data, enabling it to propagate information across the entire image and achieve global awareness. This is crucial since deformation in one direction affects the deformation in the other direction, as deformation in a flat specimen is a 2D problem. Additionally, unlike traditional ANNs, CANN preserves the dimensions of the input data throughout processing, making it advantageous for tasks where retaining spatial information is crucial.

The CANN processes input channels iteratively, which include curvature along different axes (x and y , typically representing the length and the width), the multiplication of curvatures, and the distance to the edge of the specimen. The smallest unit of distance is 1 mm which is equal to the side size (d) of the laser spot. The curvature values are in the order of 10^{-5} and as a data scaling operation, the curvature data is multiplied by an order of 10^5 (the influence of this scaling on training is shown in Fig. F.1 in Appendix F).

To ensure adequate information for pattern generation, a 5-channel input image may not suffice. For instance, when a peen induces stresses that propagate through the sample, it can affect the peen pattern forming further away. To address this, each cell is provided with more information by expanding the channels to 16, a value chosen empirically. This expansion allows information to propagate from one end of the sample to the other. The resulting 16-channel image, with the first 5 channels representing the input data, is referred to as the seed image or H_o .

To ensure adequate information for pattern generation, in this work, 8 channels for the seed were found to be sufficient as the peening patterns were not overly complex. Out of these, 5 channels represented the dataset input, while one channel was reserved for the predicted peening pattern, and the remaining two were used to propagate other relevant information. The seed image, denoted as H_o , is passed to the model, which consists of 2 CNN layers. The first layer takes the nearest neighbors of each cell, along with the cell itself, using a 3×3 filter as its input. It then processes this information through a dense neural network, resulting in an image with 128 channels (an empirically chosen value) instead of the original 16 channels. At the border of the image, it assumes the same values. The second layer is a 1×1 filter CNN, which only considers the cell itself (without its neighbors) and passes the 128 values through another dense neural network to create a delta image, Δ_i , of the same dimensionality as the input. This delta is then added to H_o to create H_1 . This iterative process is repeated multiple times, allowing the model to converge towards the target pattern.

The size of the model can be calculated using the formula:

$$P_{CNN} = (C_{CNN} \times F_{CNN}^2 + 1) \times O_{CNN} \quad (3.11)$$

where P_{CNN} represents the parameters in one layer, C_{CNN} represents the number of channels, F_{CNN} represents the size of the filter and O_{CNN} represents the number of output values. As a result, for the first layer: $1168 = (8 \times 3^2 + 1) \times 16$; and for the second layer: $136 = (16 \times 1^2 + 1) \times 8$. Combining these, the total number of parameters is 1304. Fig. 3.10 depicts this architecture and model for one iteration.

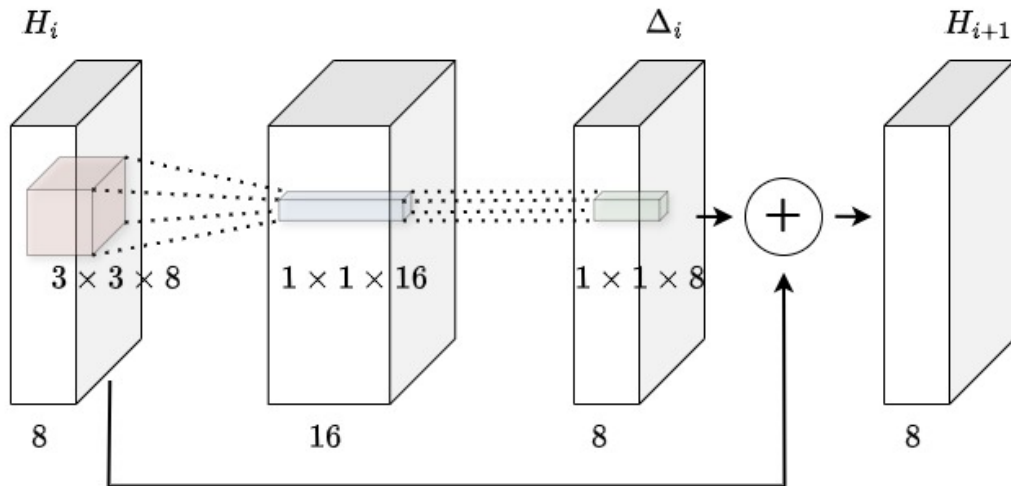


Fig. 3.10: The architecture of the model processes an input image H_i with 8 channels using two convolutional layers. First, a 3×3 CNN converts it to a 16-channel image, followed by a 1×1 CNN that produces an 8-channel delta Δ_i . Adding Δ_i to H_i results in the updated image H_{i+1} .

Training the CANN involves running it for multiple steps, calculating the loss at the end of each iteration, and using back-propagation through time to adjust the weights. The optimizer used in this process is Adam [78], which is an industry-standard. The number of iterations must be carefully chosen to ensure that the pattern has enough time to be generated or that the effect of the current update rules becomes significant. However, too many iterations should be avoided as it can lead to increased memory usage and training time. The loss is computed by taking the MSE between the target pattern and the grown pattern at the end of each iteration.

When training the network, all weights and biases are adjusted, affecting all input channels. However, the target pattern relies on the 5 dataset input channels, which must remain unchanged to prevent the model from forgetting or altering its target over multiple iterations. There are two ways to preserve these input channels: either by freezing the weights and biases that affect the input channels, setting them to zero after each gradient application, or by outputting only the 3 dynamic channels and concatenating them with the original 5 fixed input channels for the next iteration. While the first method was initially implemented, the second method is more efficient as it involves fewer parameters to train (1219 compared to 1304). Although this difference is marginal, reducing the number of channels in H_i or the middle layer is generally more effective. This approach is utilized to ensure that the essential input channels remain unaltered, allowing the model to consistently target the correct peening patterns throughout the training process. The dataset of the peening patterns used for training the CANN is shown in Appendix F (see Table F1).

3.3 Numerical simulation of LPF

This section focuses on simulating the LPF process in order to obtain the deformation of the specimen after LPF. The simulation is carried out using FE analysis and adopts the eigenstrain approach, which is explained in section 2.4 of Chapter 2. The discussion includes simplifications made to the numerical model using the eigenstrain approach. The simulation of the LPF process involves several challenges, such as determining the appropriate plasma pressure, capturing the material response at high strain rates using relevant material properties, calculating induced plastic strains, and transferring these strains from a source geometry to a target geometry. In addition, a simplified simulation strategy is developed to produce sufficiently accurate simulations, which are crucial for developing data-driven models. This strategy aims to strike a balance between computational efficiency and simulation accuracy. The workflow for the simplified approach includes validation with LPF experiments to ensure the reliability of the simulations.

Furthermore, emphasis on the challenges with regard to validation and the shortcomings in validation are discussed. Moreover, the focus is on the challenges related to validation and its associated limitations. The post-processing of the output obtained from the FE analysis, which can be compared to the LPF experiments, is also addressed.

3.3.1 Aspects of FE model

The present study utilizes the eigenstrain method as the basis for the FE model, aiming to effectively simulate LPF [2, 63, 59]. To conduct the numerical simulation of the LPF process, the commercial software ABAQUS/Explicit and ABAQUS/Standard (v6.24) were employed. Additionally, all the pre-processing, automation, and post-processing for data analysis are performed using publicly available standard libraries implemented in Python (v3.8). The simulations were carried out on nodes in an HPC cluster at *Helmholtz Zentrum Hereon* equipped with a 24-core 2.1 GHz Intel Xeon Scalable Platinum 8160 processor. The components corresponding to FE simulations are schematically represented in Fig. 3.11.

- *Geometry*: The study considers two specific geometries: a “source geometry” where laser pulses are applied to compute the corresponding eigenstrains and a “target geometry” where these computed eigenstrains are imported to observe the resulting deformation. The dimensions of the source geometry are $50 \times 50 \text{ mm}^2$, while the target geometry has measurements of $80 \times 20 \text{ mm}^2$, with a thickness of either 1 mm or 2 mm, depending on the specific sheet thicknesses being investigated. In this study, a series of 25 laser pulses are applied along the right edge of the source geometry, as depicted in Fig. 3.12. The selection of the edge of the source geometry is based on its suitability for investigating the eigenstrains that arise specifically at the edges following the application of the

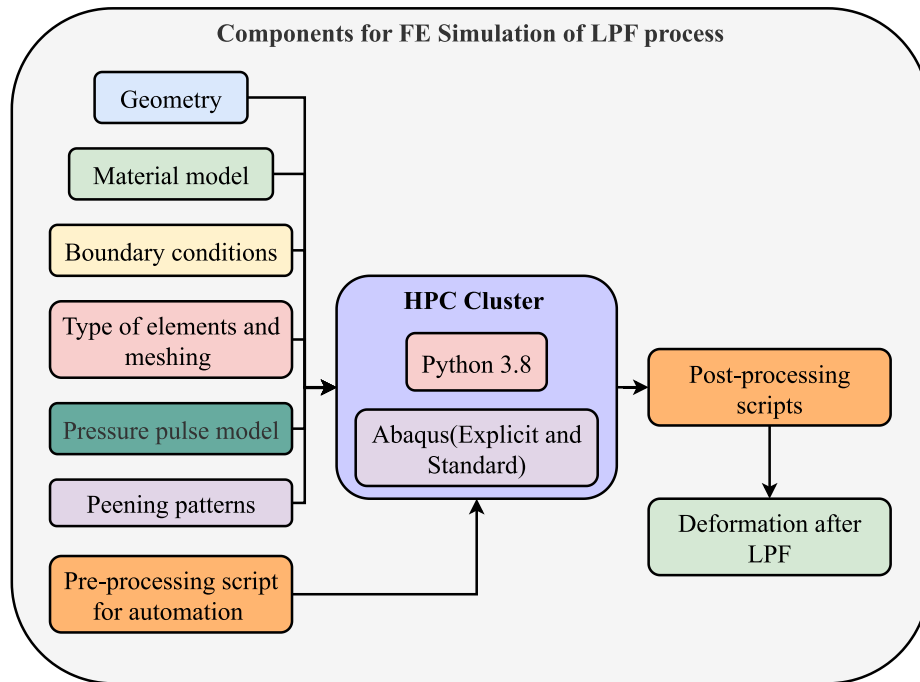


Fig. 3.11: Schematic representation of components in numerical simulation of LPF process.

laser pulse. The simulated peening pattern is similar to the one used in the LPF experiments. The FE model employed in this study does not incorporate a sacrificial overlay, as it assumes that the deformation resulting from LPF is solely a mechanical effect. Consequently, the model disregards any heating effects that may arise from the ablation of the sacrificial overlay.

For each pattern, assuming periodicity of the plastic strain field in the peening plane (the XY-plane), the source geometry pattern is divided into four equally shaped rectangular patches at the corners (NE, NW, SE, SW), a central patch (C), and four edge patches (N, E, W, S). The eigenstrains in these regions are extracted based on a volume-weighted scheme (according to [120]) onto the target geometry.

- *Material model:* For the numerical simulations, the LPF process is considered a purely mechanical process, and the underlying heat effects are neglected. The simulations were performed using the JC material model (Eqn. 2.5) without the temperature term and the material constants (Table 2.3) for the model are obtained from literature [87].
- *Boundary conditions:* The boundary conditions include the type of clamping for the geometries used in the simulations. For the source geometry, the base of the specimen is fixed whereas for the target geometry, an edge of the geometry is clamped similar to the clamping shown in Fig. 3.3 and the length of the clamped region is 10 mm (also indicated in Fig. 3.12).
- *Type of elements and meshing:* For the source geometry, the FE model incorporates

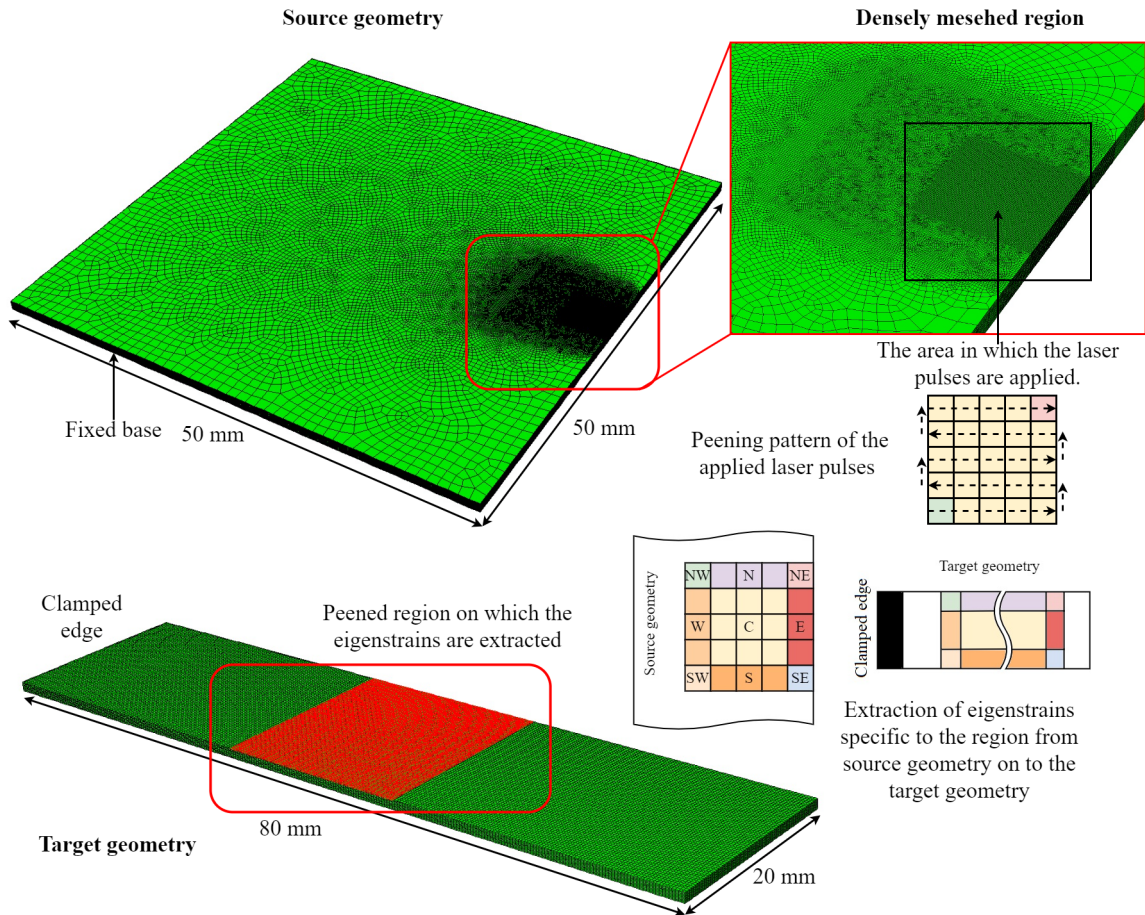


Fig. 3.12: The source and target geometries used for simulating the LPF process in 1 mm thick sheets.

7.6×10^5 nodes (7.26×10^5 elements) when considering a 1 mm thick sheet, and 1.5×10^6 (1.45×10^6 elements) nodes when considering a 2 mm thick sheet. These nodes collectively comprise an eight-noded brick element with reduced integration (C3D8R) of linear order. In the region where laser pulses are applied, the element size is set to $50 \times 50 \times 50 \mu\text{m}^3$, which is deemed adequately small to achieve a mesh-independent solution, as confirmed through a convergence study (similar mesh resolution was reported in the work of Keller et al. [75] for the source geometry).

The target geometry comprises 2×10^5 nodes (1.8×10^5 elements) for the 1 mm thick sheet and 3.8×10^5 nodes (3.6×10^5 elements) for the 2 mm thick sheet. The chosen element size is $0.3 \times 0.3 \times 0.1 \text{ mm}^3$.

- *Pressure pulse model:* The induced pressure ($p(t)$) due to the plasma during LPF is modeled as a temporal pressure load acting on the surface of the specimen. The actual pressure distribution also has a spatial resolution along the specimen surface. Although the pressure distribution across the specimen surface possesses spatial variation, this study assumes a constant spatial resolution due to the utilization of a square focus that has been observed to generate uniformly distributed energy at the focus [74]. The pressure

pulse used for modeling the pressure pulse in this study is similar to the work of Keller et al. [75].

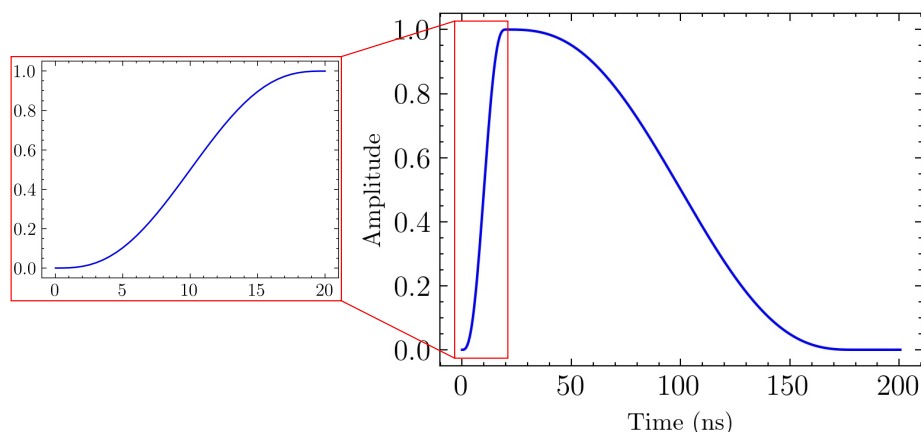


Fig. 3.13: The temporal distribution of the pressure pulse used in the numerical simulations. The pulse reaches maximum amplitude at 20 ns, followed by a relaxation phase until 200 ns.

The temporal distribution of the pressure pulse, denoted as $p(t)$, remains consistent across all simulations. It is determined using the smooth step definition in ABAQUS Explicit, as described in the ABAQUS software 6.14 user manual. The pressure pulse (Fig. 3.13) is characterized by three key parameters: the total duration of the pulse (t), the maximum pressure-induced (P_{max}), and the time (t_m) at which the pulse reaches its maximum pressure. The total duration of the pressure pulse (t) is assumed to be 200 ns which agrees with the experimental observations from the literature [118, 117], for applied laser pulses that have a width of 10-20 ns at FWHM. The time at which the induced pressure reaches a maximum value is assumed to be 20 ns. The maximum value of induced pressure (P_{max}) is varied from 1000 MPa to 6000 MPa. After each applied pressure pulse a relaxation time of 50 μ s. In the FE model, the maximum pressure value is modified based on the experimentally measured deformation in the treated area following LPF.

- *Peening patterns:* The peening patterns, also referred to as peen patterns, serve as visual indicators of the treated region on the specimen. In the case of a typical specimen, LPF treatment can be applied to both surfaces. These peening patterns can be effectively represented as images, illustrating three possible outcomes: forward peening, backward peening, or no peening (unpeened). The dimensions of the peen pattern image, measured in pixels, correspond to the dimensions of the specimen in millimeters. In cases where the specimen undergoes peening on only one surface, the peening pattern is selected as a black-and-white image. In this representation, the treated region is depicted in white, while the unpeened region is depicted in black. The peening pattern in the form of an image is then transferred to the FE mesh which can be processed by ABAQUS.

- *Pre-processing*: In order to set up an accurate simulation, a comprehensive pre-processing procedure is undertaken. The pre-processing involves the simulation of both the source geometry and the target geometry to determine the deformation after LPF.
- *Source geometry*: The process begins with conducting ABAQUS/Explicit simulations on the source geometry, as shown in Fig. 3.12. The simulations involve varying the maximum pressure (P_{max}) and the number of peening sequences (n). At the end of the explicit simulation, the dynamic stress state of the material is obtained. A simulation using ABAQUS/Standard is performed by importing the stress state of the material after peening, to ensure that the stresses reach an equilibrium state after relaxation. Once the static simulation is completed, a volume-weighted averaging scheme according to the literature [75, 120], is employed to compute the plastic strain tensors resolved along the thickness of the specimen. The extracted strain tensors are transferred to the peened region of the target geometry as eigenstrains.
- *Target geometry*: The simulation of the target geometry involves several steps for accurate analysis. Initially, the nodes and elements corresponding to the target geometry are extracted from the ABAQUS input file. Subsequently, the element centers for all nodes are computed. To ensure accurate depth-dependent analysis, the elements of the target geometry are resolved along the thickness. The extracted plastic strains are applied from the source geometry to the target geometry, node sets, and element sets are created exclusively at each depth through the thickness of the geometry. This is necessary because the extracted plastic strain from the source geometry is depth-dependent.

As a result, the extracted plastic strain from a specific depth in the source geometry must be applied as an eigenstrain in the corresponding depth of the target geometry. The peening pattern image (as shown in Fig. 3.14) is utilized to classify the elements based on whether they are peened on the top surface, peened from the bottom surface, or remain unpeened. However, since the mesh density in the FE model is higher than the pixel density of the peen pattern image, an initial scaling process is performed to match the mesh density while accounting for aliasing. The elements corresponding to each element set are mapped to the pixel index of the scaled peen pattern image. By using the pixel ID, which represents the state of peening, as a mask for the element ID, the element sets can be further classified into subsets indicating whether a particular element is peened from above, peened from below, or remains unpeened. All classified element sets are assigned depth-resolved plastic strains, which are extracted from the source geometry.

- *Simulation and post-processing*: After completing the simulation using the ABAQUS Standard solver, the output deformation data is extracted from all the nodes in the top surface of the target geometry. The extracted deformation data provides a detailed understanding of the material response for different peen patterns at specified LPF process

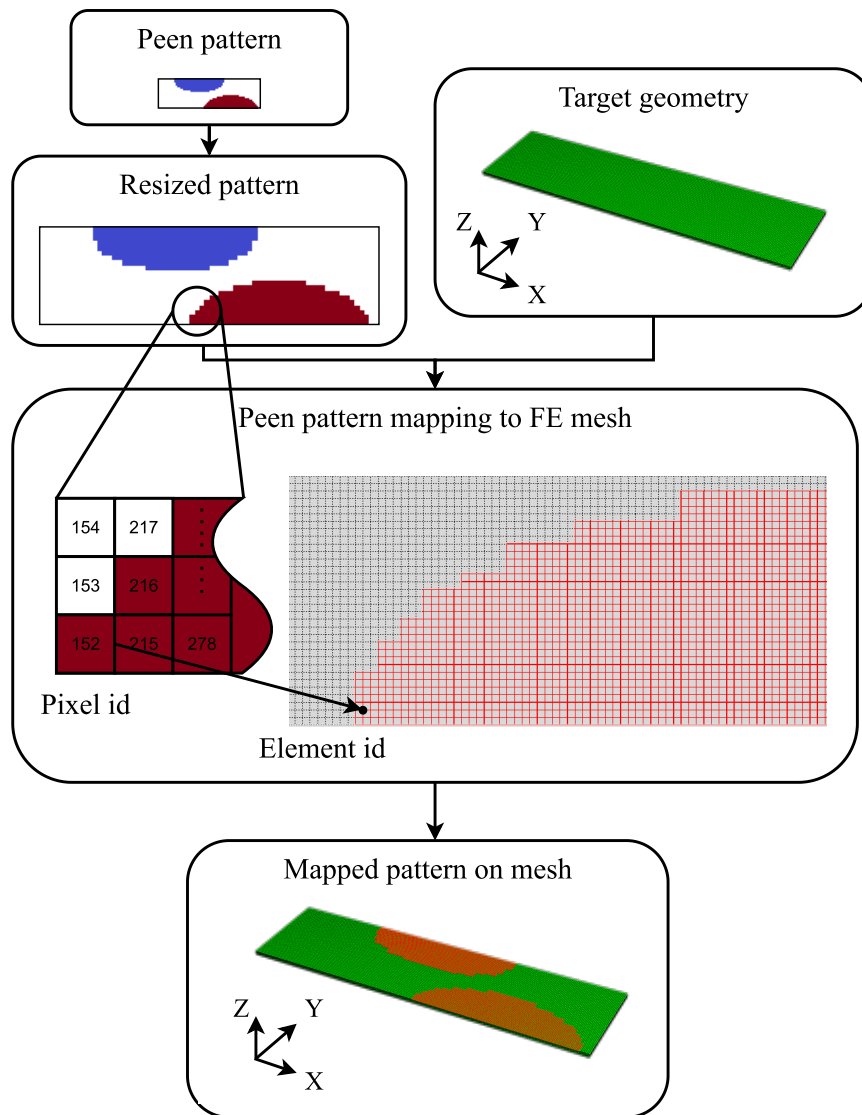


Fig. 3.14: Schematic illustration of the mapping process of an exemplary peening pattern onto the FE mesh of the target geometry. Within the peen pattern image, different regions are designated by the color of the pixel: the blue region represents the peening treatment applied to the top surface, the brown region signifies the peening on the back surface, and the white region represents the unpeened area. Through the pre-processing script, the peen pattern is transferred onto the FE mesh of the target geometry. This script prepares the input file for subsequent processing using the ABAQUS/Standard solver.

parameters. Simulations in this work are performed using the simulation parameters described below.

3.3.2 Validation with experiments

The simulations performed in this study are validated with the LPF experiments by determining the maximum pressure (P_{max}) of an applied pulse which produces identical deformation in the treated region while maintaining an equivalent number of peening sequences

Table 3.3: Parameters of the pressure pulse and peening sequences for simulation of LPF using the eigenstrain approach

| Input | Parameter | Symbol | Range | Levels | Units |
|--------|-------------------------------|-----------|-------------|--------|-------|
| 1 | Max pressure | P_{max} | 1000 - 6000 | 11 | MPa |
| 2 | Number of peening sequences | n | 1 - 4 | 4 | - |
| 3 | Thickness of the specimen | T | 1, 2 | 2 | mm |
| Output | Parameter | Symbol | Range | Levels | Units |
| 1 | Deformation in treated region | $D(x)$ | - | - | mm |

as in the LPF experiment for a Ti6Al4V sheet. The primary challenge of the simulation is the determination of the appropriate induced plastic strain tensor using an equivalent pressure pulse for an applied laser pulse. The simulation of the LPF (see Fig. 3.15) process can be interpreted as a function that associates pressure pulse parameters and the number of peen sequences with eigenstrains and, subsequently, relates these eigenstrains to the desired deformation in the target geometry for specific material properties and thickness. The induced eigenstrains are a function of applied pulse parameters and process parameters as:

$$\epsilon_{ij} = g(P_{max}, n, T), \quad (3.12)$$

where n is the number of peening sequences, and T is the thickness of the specimen. In addition to this, the equivalent max pressure (P_{max}) for simulations should be obtained by solving an inverse of function defined as:

$$D = f(\epsilon_{ij}) = f(g(P_{max}, n, T)) \quad (3.13)$$

where D represents the induced deformation due to the eigenstrains (ϵ_{ij}) in the treated region ($i, j = 1, 2$ or 3 indicating the principle directions).

By recognizing the inherent functions (as in Eqn. 3.12 and 3.13) that govern the relationship between pressure pulse parameters, the number of peening sequences, and the resulting induced deformations in the treated region, data-driven approaches can be leveraged to approximate them. Specifically, this work utilizes two different ANNs to effectively predict the eigenstrains and deformation in the treated region, given the pulse parameters as inputs. The first ANN aims to solve the direct problem represented by the Eqn. 3.12 and the second ANN approximates the Eqn. 3.13. This approach offers significant advantages over traditional analytical methods, as it simplifies the process of solving the direct problem. By training and validating the ANNs using simulation data encompassing a wide range of input combinations, a robust data-driven simulation framework capable of generalizing well to all possible combinations in the defined parameter space is generated, reducing the need for individual simulations corresponding to each experimental LPF process parameter combination. Once the ANNs are successfully trained, they can be utilized to generate a comprehensive database of deformation profiles for all conceivable

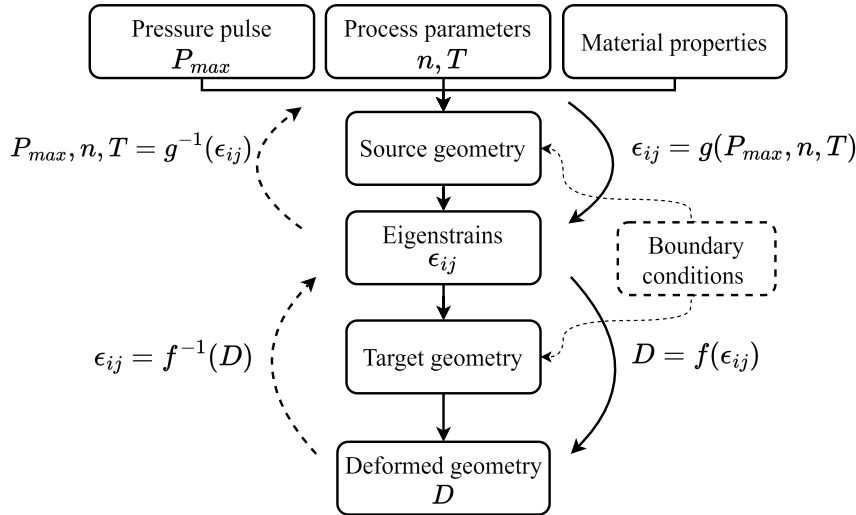


Fig. 3.15: Schematic of simulation of LPF using an equivalent pressure pulse, number of peen sequences, and thickness of the specimen as inputs and deformation in the target geometry as an output. Upon solving the inverse functions of f and g the equivalent pressure pulse can be obtained.

simulation parameter combinations. This database serves as a valuable resource containing a wide range of deformation patterns in the treated region corresponding to various input maximum pressures and peening sequences. Subsequently, this database can be effectively searched to find the deformation profile and its corresponding simulation parameters that best match the deformations obtained from actual LPF experiments. This search process enables us to identify simulation parameters that yield results consistent with experimental data.

In contrast, solving the inverse problem, which aims to obtain the equivalent maximum pressure (P_{max}) for simulations to match experimental results, can be a time-consuming and challenging task. Inverse problems are often ill-posed, meaning that there can be multiple solutions that lead to the same experimental outcome. In the context of LPF, there can be multiple combinations of process parameters (P_{max}, n) that can produce similar eigenstrains leading to identical deformation in the treated region [60]. This ambiguity in the solutions makes the inverse problem more intricate and resource-intensive to solve, as it requires meticulous exploration of the parameter space and careful consideration of various factors influencing the results. Nevertheless, by employing the data-driven approach to approximate the direct functions, the strenuous effort required to solve the inverse problem can be avoided. This can be accomplished by comparing the deformation profile obtained from the actual experiment with the predicted deformation profiles in the database, and a mean squared error (MSE) is computed for every potential match. The deformation profile with the minimum MSE is assumed to be the best fit, and its corresponding maximum pressure is extracted from the database. This procedure allows the identification of the simulation parameters that closely replicate the experimental outcomes, effectively validating the sim-

ulations against experimental data however, the maximum pressure in the simulation does not explicitly represent the plasma pressure during the process.

The simulation data with inputs: maximum pressure and the number of peening sequences according to Table. 3.3 for each thickness of the specimen and the corresponding output deformation is set up accounting for 176 simulations for each ANN. This simulation data will be used to determine the direct functions by training ANNs, which can effectively predict the eigenstrains and deformation in the treated region, given pulse parameters as inputs, however, the real inputs are converted into dimensionless inputs using dimensional analysis for better generalization. Once the ANNs are successfully trained, validated, and tested to approximate the direction function, they can be employed to create a comprehensive database. This database will encompass eigenstrains and deformations in the treated region for all conceivable input maximum pressure and the number of peening sequences within the predefined parameter space. The purpose of this database is to determine the appropriate maximum pressure (P_{max}) of the pressure pulse, which produces necessary eigenstrains thereby, deformation in the treated region that matches the LPF experiments corresponding to a specific parameter set. This approach facilitates the possibility of eliminating the strenuous simulation effort required for validation with experiments.

3.3.3 Simplified predictive numerical model for LPF

In the present study, there has been a significant emphasis on numerically simulating LPF and validating the results with experiments using the Eigenstrain approach, as discussed in earlier sections. Furthermore, an effort has been made to explore the possibility of simplifying the simulation process while still achieving sufficiently accurate results. This model, devised to streamline computational efficiency and mitigate complexity, is meticulously designed to replicate bending phenomena resulting in a flat specimen after LPF.

In the model, the deformation of the sample is visualized through the concept of beam bending, a familiar phenomenon where stresses within the material lead to bending as shown in Fig. 3.16. Specifically, the model focuses on the distribution of compressive and tensile stresses across the cross-section of the sample. After LPF, the surface of the material typically exhibits compressive stresses, while tensile stresses are present deeper within the material and the intensity of the stresses might not be equibiaxial.

The model simulates bending behavior using ABAQUS, enabling the definition of initial stresses within the material. It is presumed that each peening action induces biaxial residual stresses in both in-plane directions, thus affecting the overall deformation. This assumption aligns well with the symmetrical nature of the peening process and the assumed isotropic properties of the material.

The material parameters used in the simulation were consistent with those in the Eigenstrain approach, ensuring continuity in the modeling approach (Table. 2.4). The workflow

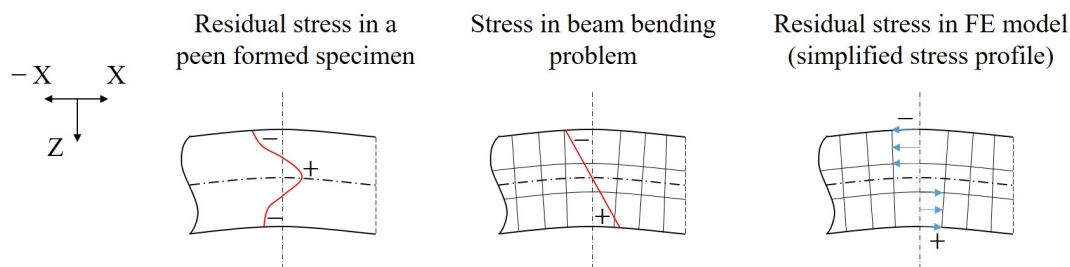


Fig. 3.16: Difference in the residual stress profile through the cross-section of the specimen after LPF compared with the stress profile in a beam bending problem and a simplified FE model. Instead of a linear continuous stress gradient, the FE model assumes a simplified stress field consisting of three elements with discrete stress steps.

of the simplified FE simulation model is illustrated in Fig. 3.17. The simulation begins with the creation of a finite element mesh representing the geometry of the sample. The peening pattern on the sample is translated to the FE mesh. This mesh was then deformed based on the specified initial stresses to mimic the effects of peening. The resulting deformed mesh was analyzed to generate height, providing a quantitative understanding of the deformation (ref. Appendix D).

To validate the simulation results, a comparison was made with experimental deformation data obtained by 3D scanning the sample after LPF. An MSE value is computed based on the difference in height maps between the actual deformation and the simulated deformation data. The model iteratively adjusts the initial stress values using Bayesian optimization to minimize the MSE between the simulated and experimental height maps. This iterative process continued until a satisfactory level of agreement was achieved (ref. Appendix C).

Furthermore, the model addressed edge effects, where deviations between experimental and simulated results were observed near the edges of the sample. Although attempts were made to mitigate these effects through adjustments in stress profiles, the focus remained on optimizing the simulation accuracy within the sample's central region. Additionally, the model underwent mesh grid testing to determine the optimal resolution for accurate simulation results. Through this testing, it is confirmed that a mesh grid density of 3 linear elements per millimeter across the thickness of the specimen adequately met the required level of accuracy. This resulted in a total of 53,667 linear C3D8R elements covering the entire specimen, striking a balance between computational efficiency and modeling precision.

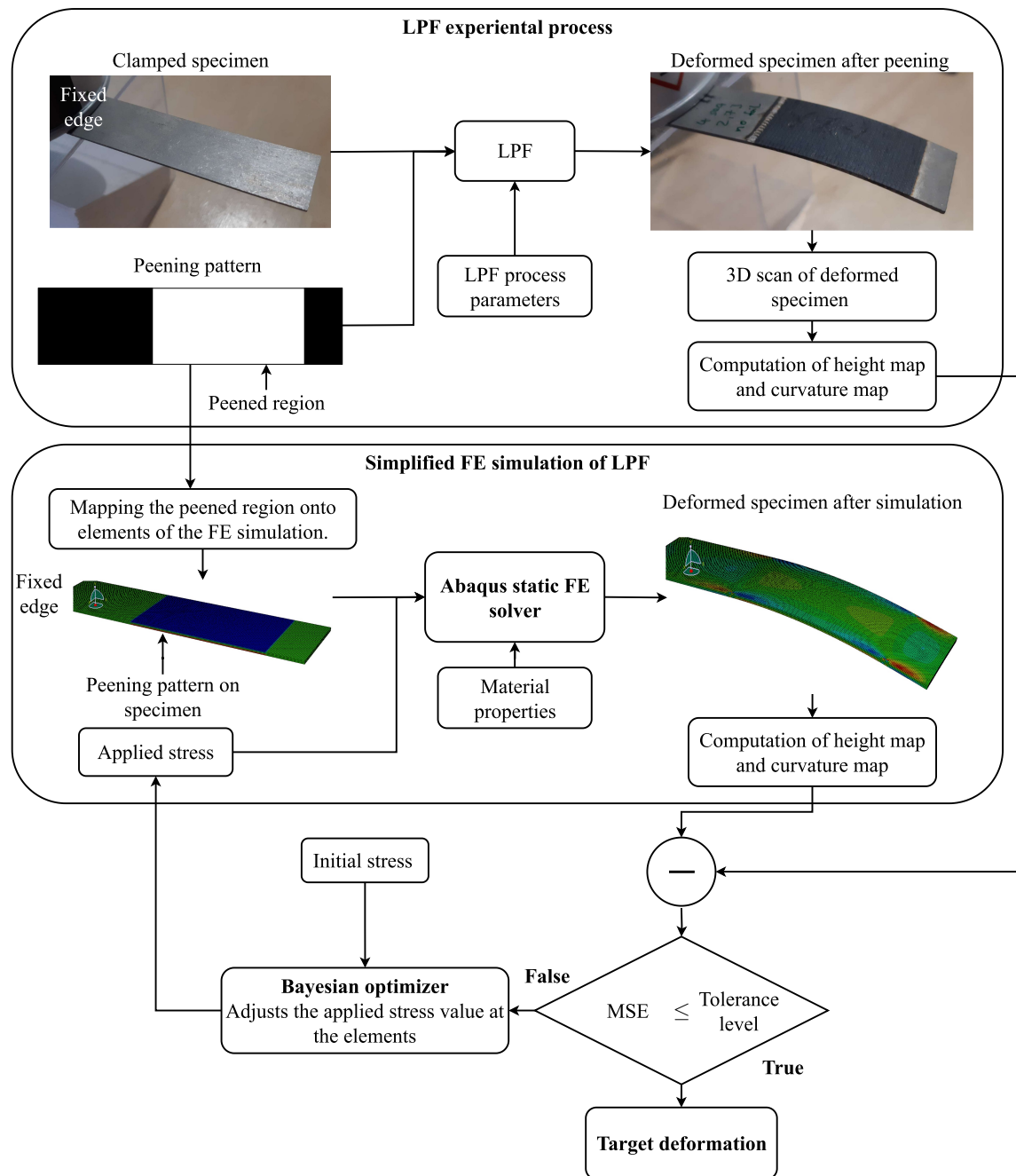


Fig. 3.17: Illustration of the workflow for simplified FE model for stimulating LPF. Initially, a peening experiment with predefined parameters produces a deformed specimen, which undergoes 3D scanning using a Creaform HandySCAN 3D scanner. From the scan results, height and curvature maps are derived. Subsequently, the peening pattern image is overlaid onto corresponding elements in the FE simulation. An initial stress value is then assigned to the treated region, and height and curvature maps are generated. The MSE indicating the disparity between the FE simulation and experiment is computed. Through iterations, the Bayesian optimizer fine-tunes the applied stress value to minimize the MSE, progressively enhancing accuracy until reaching the desired tolerance level. [133]

3.4 Summary and conclusions

The methodology chapter of this thesis outlines a comprehensive approach to investigating LPF and its optimization through systematic experimentation, data-driven modeling, and numerical simulation approaches. The chapter describes the experiments conducted using three parameter sets, with combinations of considered LPF process parameters and an objective to determine the most effective combination in achieving the desired deformation in the treated region while maintaining surface quality. The experimental study employs a full factorial DOE approach to systematically vary the input factors such as laser energy, number of peening sequences, and specimen thickness to examine their effects on the deformation of the treated region. Various measurement techniques, including line-based profile measurement and 3D scanning, were used to obtain accurate deformation profiles, while surface characterization was performed using optical microscopy, SEM, and EDX to analyze microstructural changes.

After completing the experimental phase, the collected data were thoroughly analyzed to draw meaningful conclusions. The study employed data-driven approaches to model the intricate relationships between LPF process parameters and deformation outcomes. ANNs were the primary tools used for this purpose. These ANNs were trained and validated using the experimental data, enabling the prediction of deformation patterns based on various parameter sets. The learning approach leveraged by ANNs is particularly effective in handling the non-linear and multi-factorial nature of the LPF process, offering significant improvements in predictive accuracy. The trained ANN based on the experimental data is used as a tool to develop a process planning methodology to demonstrate the usability of the ANN predictions to obtain desired deformations via LPF. The application of this process planning approach was tested on benchmark cases to validate its effectiveness. These benchmark cases involved specific scenarios representative of potential industrial applications of LPF. Furthermore, a CANN is trained to predict the peening pattern using the deformation of the specimen as an input. This enables the prediction of the peening patterns to obtain complex deformations on a flat specimen.

This chapter also encompasses numerical simulations to validate and complement the experimental and data-driven approaches. The simulations utilized the eigenstrain approach, which simplifies the representation of plastic deformation induced by LPF. Additionally, a simplified predictive numerical model to predict deformation after LPF is developed, to enable the generation of sufficiently accurate data that can be used to create a CANN model to predict the peening patterns for LPF. By comparing the simulated deformation profiles with experimental results, the validity and reliability of the computational models were confirmed. These simulations provide detailed insights into the LPF process, facilitating the prediction of deformation profiles and aiding in the fine-tuning of process parameters.

This methodology was applied to study and optimize the LPF process to obtain and correct deformations in thin Ti6Al4V sheets. The systematic investigation of LPF process parameters and the development of data-driven models significantly enhance the ability to control deformation outcomes accurately. The ANN prediction integrated process planning approach not only improves the efficiency and precision of the LPF process but also provides a scalable solution for practical applications. The results and findings from these investigations are discussed in the following chapter. The subsequent chapter delves into a detailed analysis of the outcomes, offering insights into the practical implications and potential applications of the optimized LPF process. This detailed exploration ensures that the theoretical concepts and practical findings are well-connected and aligned, providing a robust foundation for future research and application in the field of laser peening.

4

Results and discussion

The results and discussion chapter present the comprehensive findings of this research, which aimed to advance LPF process as an innovative technique for fabricating thin-walled Ti6Al4V structures in the aerospace industry. This chapter explores three essential aspects of the study, each contributing valuable insights and outcomes to the overall goal of developing an autonomous forming and straightening process using LPF. These aspects include experimental investigations and process parameter studies, numerical simulations utilizing the eigenstrain method, and data-driven methodologies for process optimization as well as process planning.

The experimental investigations identify optimal LPF process parameters for the desired deformation without compromising surface quality. Numerical simulations based on the eigenstrain method validate experimental findings. Data-driven techniques are tested, and an ANN-based process planning approach is presented and validated on benchmark cases of deformation and correction applications. The challenge of finding optimal peening patterns using a simplified modeling approach with CANN is discussed. This chapter integrates experimental, data-driven, and numerical simulation findings, providing comprehensive insights into the potential of LPF and its challenges.

This chapter brings together the experimental, numerical, and data-driven findings, providing comprehensive insights into the potential and challenges in the application of LPF. The successful integration of these three aspects highlights the innovative and interdisciplinary approach taken in this research.

4.1 Impact of LPF process parameters on deformation and surface quality

The experimental investigations delve into the identification of an optimal LPF process parameter window that achieves the desired deformation without compromising the surface quality of the peened region. By systematically varying laser energy, overlap, sacrificial overlay, and the number of peening sequences in various parameter sets as shown in Table 3.1, insights into the influence of these parameters on deformation and surface integrity were obtained.

4.1.1 Effect of overlap and laser energy on LPF

The investigation of LPF process parameters in parameter set 1 included varying laser energy, overlap, and the type of sacrificial overlay. In these experiments, both sacrificial overlays, namely aluminum and stainless steel foils, were found to be destroyed during the peening process, even at an overlap as low as 10/10. This failure of the sacrificial overlay resulted in imperfect peening, leading to surface damage in the peened region. Several factors may have contributed to this outcome, such as poor adhesion of the overlay with the specimen surface, air entrapment between the overlay and the specimen, or overlap that caused multiple laser shots in close proximity. Despite taking precautions to avoid air entrapment or poor adhesion between the sacrificial overlay and the specimen, the overlay still experienced breakage during peening at the lowest laser energy, as depicted in Fig. 4.1. This indicates that the failure is predominantly influenced by the overlap parameter.

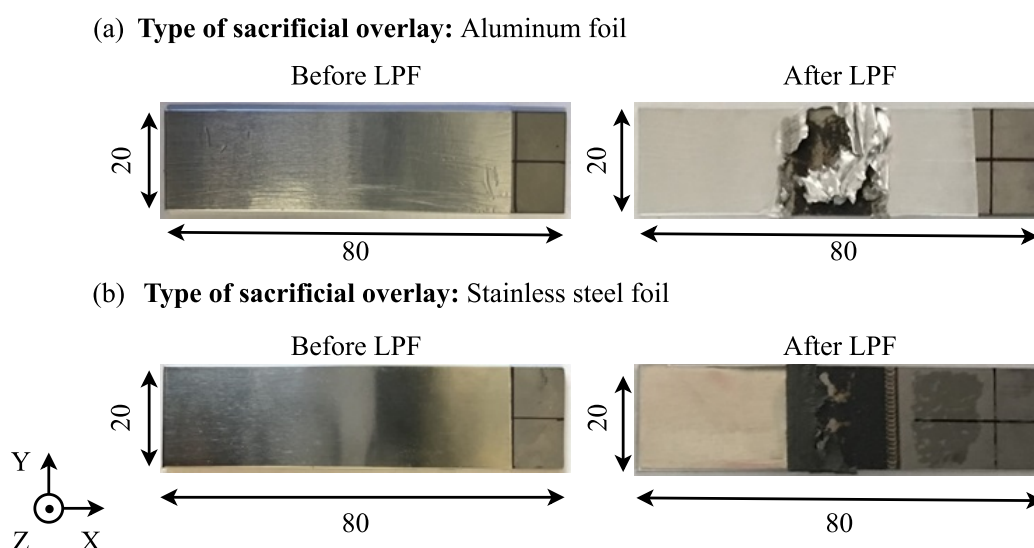


Fig. 4.1: Effect of overlap (50/50) on sacrificial overlay at a laser energy of 1.8 J for (a) Aluminium foil and (b) stainless steel foil. (Reprinted from [132]).

During the peening process with high overlap, the top surface of the sacrificial overlay experiences multiple shock waves with extremely high magnitudes in a short period [17].

The energy from the laser vaporizes the near-surface region of the sacrificial overlay, making it thinner, which could be a contributing factor to its fracture (also reported in [123]). Additionally, the intense shock wave propagation may have caused cracks in the sacrificial overlay. Based on the above findings from parameter set 1, it becomes evident that having an overlap during the LPF process with a sacrificial overlay is not recommended.

In the case of parameter set 2 (ref. Table 3.1), the laser energy is varied without overlap with the goal of identifying the maximum energy that sacrificial overlay can sustain without getting damaged. Initially, aluminum foil with a thickness of $50\ \mu\text{m}$ was used as a sacrificial overlay for peen-forming Ti6Al4V. However, it was found that even at the lowest laser power density within this parameter set, the aluminum foil was damaged, rendering it unsuitable for the experiments. As a result, all further experiments were carried out using stainless steel foil as the sacrificial overlay. The experiments with stainless steel foil demonstrated that it could withstand laser energies ranging from 0.5 J to 3.1 J (refer to Fig. 4.2(a) to Fig. 4.2(e)). As a result, a safe working range for laser peening of Ti6Al4V sheets without causing surface damage in the treated region was identified without any overlap, using stainless steel foil as the sacrificial overlay.

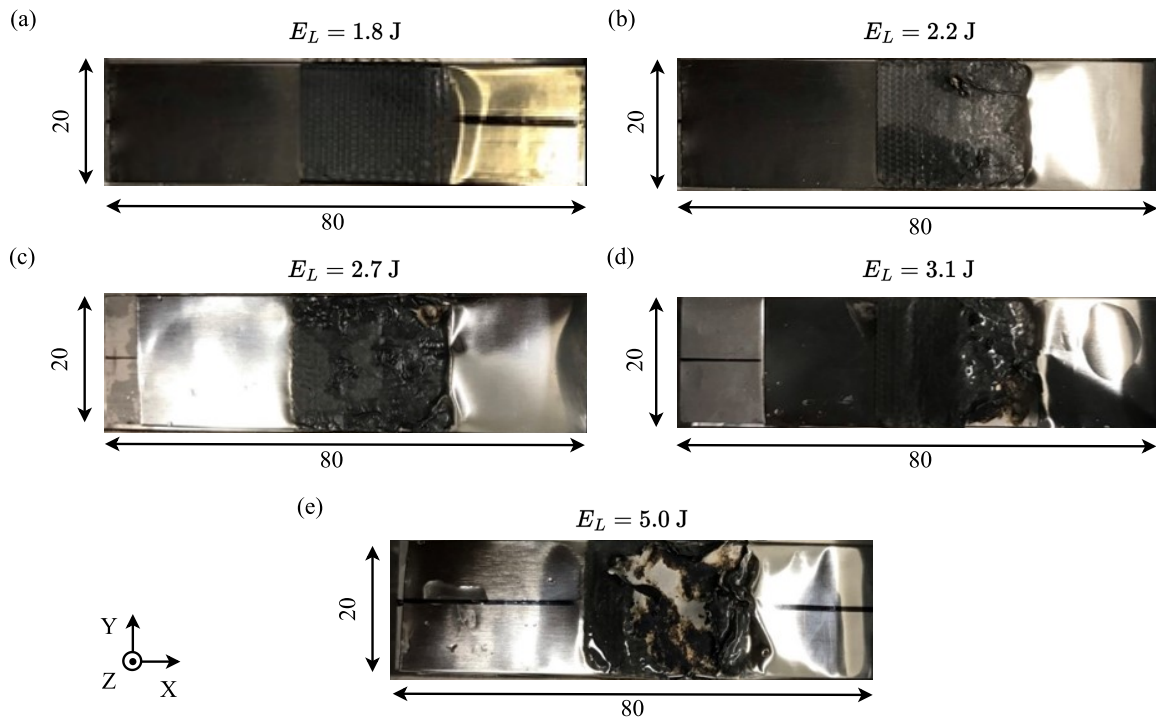


Fig. 4.2: Impact of laser energy on stainless steel sacrificial overlay in the treated region at (a) 1.8 J (b) 2.1 J (c) 2.7 J and (d) 3.1 J (Reprinted from [132]).

4.1.2 Impact of peening sequences and laser energy on deformation in the treated region - using a sacrificial overlay

Significant deformation in the treated region was achieved by varying the laser energy within the range of 1.8 J to 3.1 J, ensuring no overlap (parameter set 2). Stainless steel was utilized as a sacrificial overlay for these experiments. The number of peening sequences was increased from 1 to 4, as illustrated in Fig. 4.3. This investigation encompassed specimens with thicknesses of both 1 mm and 2 mm.

These LPF parameters yielded a distinctive deformation phenomenon where the peened region exhibited convex curvature, diverging away from the laser source (also observed in [63]). The convex deformation is attributed to the intensified local plastic deformations through the thickness of the specimen, caused by increasing the number of peening sequences. Consequently, an observable cumulative effect manifests as an amplified deformation phenomenon across the peened area.

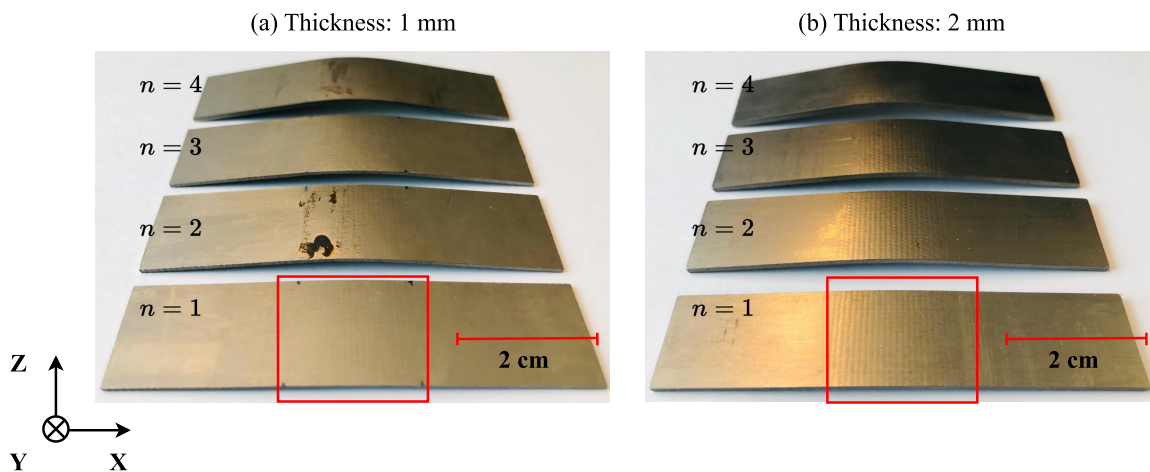


Fig. 4.3: Influence of peening sequences(n) on deformation at a laser energy of 3.1 J using stainless steel as a sacrificial overlay for (a) 1mm, and (b) 2 mm thick specimens. The region indicated inside the red square is treated by LPF. (Reprinted from [132]).

The arc radius measured in the peened region decreases with an increase in the laser energy and the number of peening sequences (see Fig. 4.4). Furthermore, a saturation in arc radius can be observed with increasing the number of peening sequences in the treated region (also reported by [63]). This outcome is attributed to the increase in laser energy causing a significant increase in local plastic strains through the specimen within the peened area. A study by Pence et al. [113] demonstrated comparable convex deformation behavior during an experimental investigation aimed at comprehending the impact of process parameters on post-LPF deformation. The plastic strains generated within the treated area lead to compressive residual stresses near the surface. Consequently, a tensile strain emerges along the lateral direction, instigating an outward deformation moment that manifests as concave deformation [63].

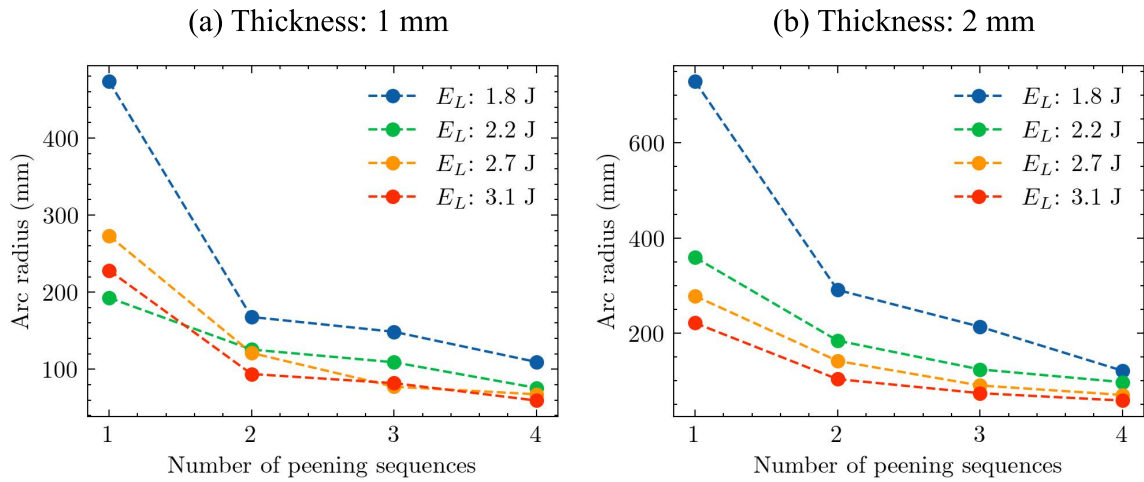


Fig. 4.4: Measured arc radius in the LPF-treated region for different laser energies and the number of peening sequences in (a) 1mm, and (b) 2 mm thick Ti6Al4V sheets.

The successful application of LPF utilizing a stainless steel foil as a sacrificial overlay, allowed for the controlled generation of various arc radii within the treated area by varying laser energy and the number of peening sequences. However, a notable limitation is the eventual saturation of arc radii after a certain number of peening sequences which could potentially restrict the maximum achievable arc radii across the treated region. Additionally, the experimentation process is labor-intensive and time-consuming due to the need to remove the sacrificial overlay after each peening sequence. Consequently, it becomes imperative to explore the impact of LPF process parameters in the absence of a sacrificial overlay, and the ensuing discoveries are presented in the following section.

4.1.3 Effect of laser energy, peening sequences, and overlap - without sacrificial overlay

In experiments corresponding to the parameter set 3, all the key process parameters influencing the LPF process were varied to understand their influence on deformation in the treated region. In this particular parameter set, the absence of a sacrificial overlay was deliberate due to the previous findings indicating that the sacrificial overlay sustains damage when peening involves overlapping. The omission of a sacrificial overlay in LPF allows for a more comprehensive exploration of the combined effects arising from alterations in laser energy, overlap, and the number of peening sequences, all impacting the resulting arc radius in the treated region. Nevertheless, it should be noted that the surface quality of the treated region experiences an impact due to the peening process as shown in Fig.4.5, which involves surface ablation.

Investigating overlap in the treated region: The LPF experiments were conducted on 1 mm thick Ti6Al4V sheets at a laser energy of 3.1 J. These trials encompassed three different levels of overlap in the scanning direction: no overlap, 25% overlap, and 50% overlap,

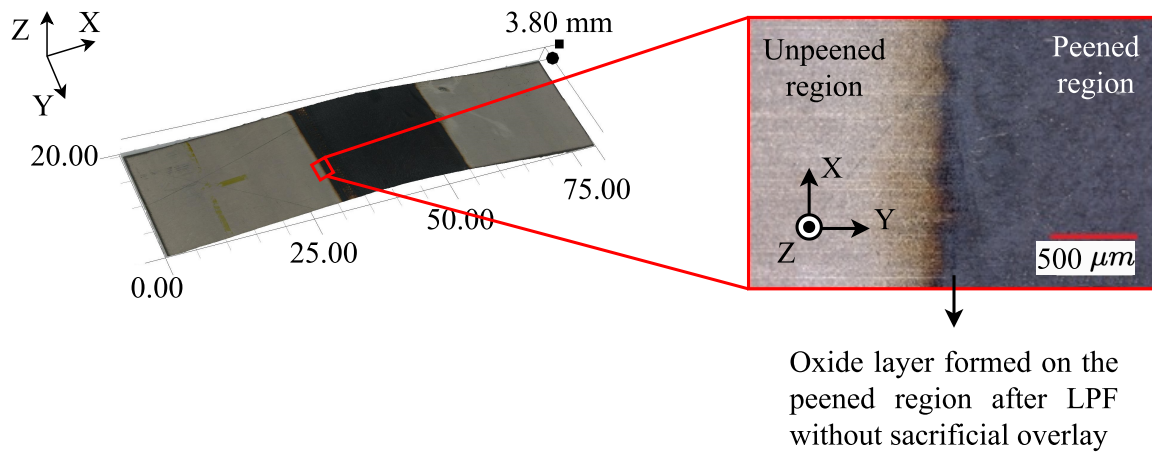


Fig. 4.5: Deformation obtained within the peened area following LPF in the absence of the sacrificial overlay. The presence of a blackened surface signifies the development of an oxide layer within the treated region. (Reprinted from [132])

and the number of peening sequences varied from 1 to 4. An evident trend emerged as shown in Fig. 4.6, wherein an increase in overlap led to enhanced deformation within the peened area compared to lower overlap conditions. As the overlap increases, the effective number of laser shots per unit area within the peened region also rises. Consequently, this leads to higher induced local plastic strains, and subsequently increasing global deformation. This observation aligns well with the findings of Luo et al. [94], who reported a similar correlation between increasing overlap ratios and higher levels of induced plastic strains within the peened region.

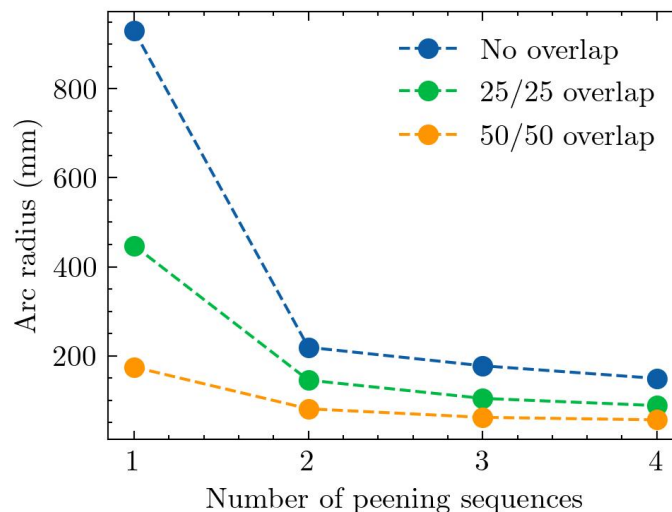


Fig. 4.6: The influence of overlap (%scan/%step) on arc radius in Ti6Al4V specimens of 1 mm thickness after LPF process at a laser energy of 3.1 J, progressively increasing the peening sequences.

Additionally, for the specimen treated with 50% overlap and only one peening sequence, the arc radius closely resembles that of specimens treated with 0% overlap and

two peening sequences. This similarity in arc radii arises since, while processing with 50% overlap, two shots per unit area are effectively applied to 95% of the peened region which is similar to having two peening sequences. The remaining 5% near the edges receive a single shot per unit area. As a result, performing LPF at higher levels of overlap and fewer peening sequences yields deformation results comparable to those achieved with lower overlap percentages but a higher number of peening sequences.

Higher overlap ratios with fewer peening sequences present a notable technological advantage. This strategy could lead to reduced process times, as the efficient utilization of laser shots over a larger area reduces the need for numerous repetitions.

4.1.4 Deformation in the peened region - LPF with and without a sacrificial overlay

A notable contrast in deformation within the treated region was evident for the same laser energy and number of peening sequences, between instances where no sacrificial overlay was employed during the LPF process and situations involving the use of a sacrificial overlay, as illustrated below (Fig. 4.7).

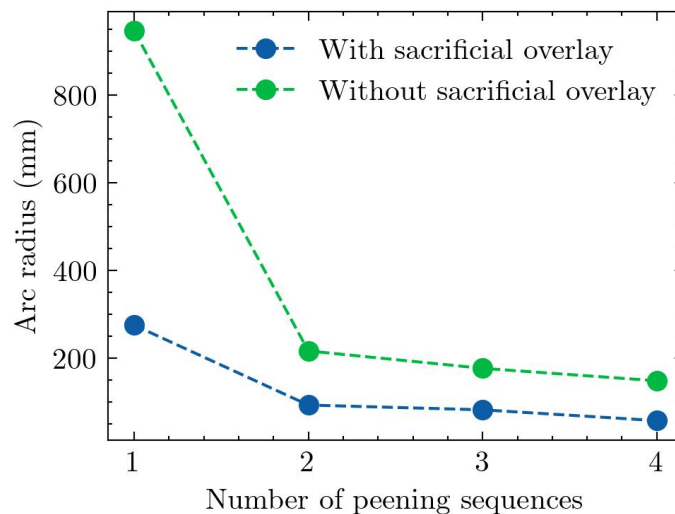


Fig. 4.7: The influence of sacrificial overlay on arc radius within the LPF processed area for 1 mm thick Ti6Al4V specimens at a laser energy of 3.1 J with varied peening sequences without an overlap.

In cases over one peening sequence, the achieved deformation without the presence of an overlay is notably reduced by approximately 60% when compared with the deformation achieved through LPF employing stainless steel as a sacrificial overlay. The increase in deformation can be attributed to the fact that the induced shock pressure is higher when a sacrificial overlay is used, which results in greater plastic deformation [38].

4.1.5 Impact of LPF process parameters on surface characteristics of the peened region

The surface of the peened region, achieved through LPF, exhibits unique characteristics determined by the chosen combinations of process parameters. A crucial factor impacting surface quality is the incorporation of a sacrificial overlay during the LPF process. When considering samples processed using LPF with a sacrificial overlay, the chemical composition of the peened region remained unaffected. However, the impact of laser shots led to the formation of micro-indentations as shown in Fig. 4.8(a, c). On the other hand, the peened region lacking a sacrificial overlay displayed indications of both surface re-melting and oxidation (Fig. 4.8(b)).

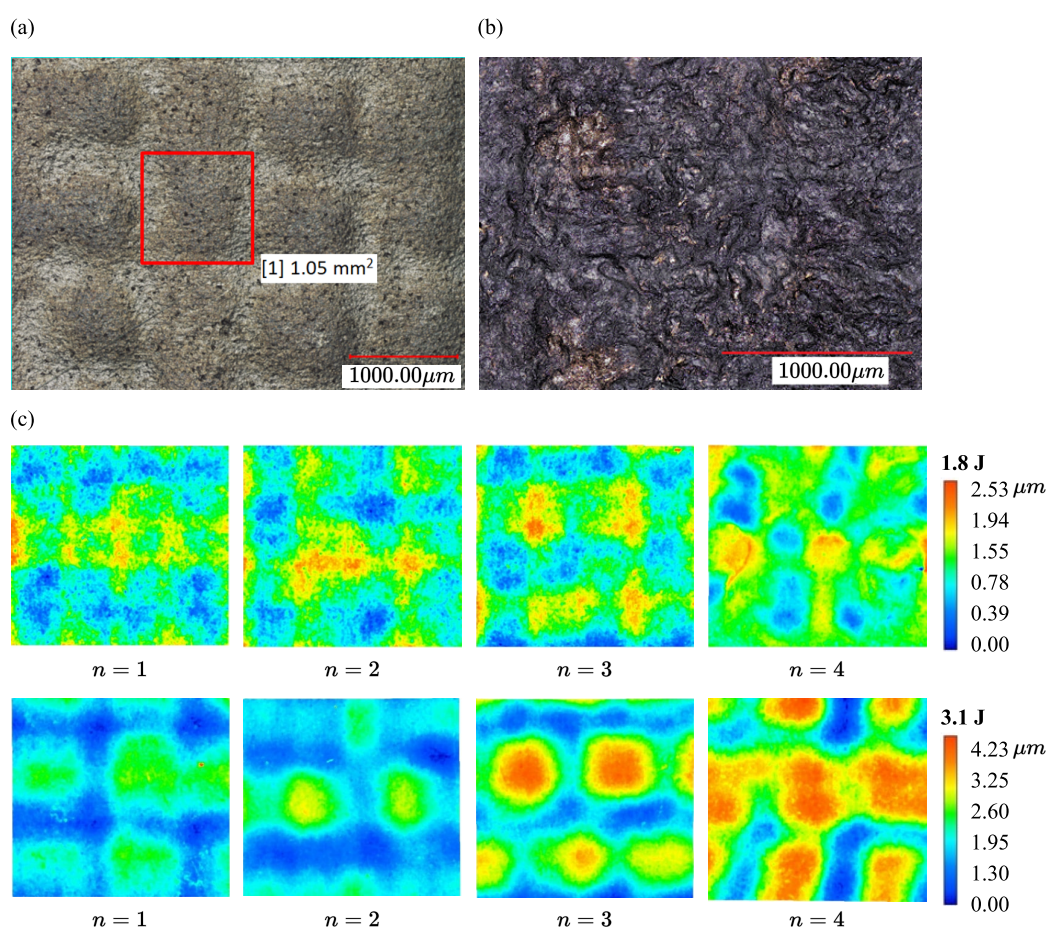


Fig. 4.8: Impact of LPF process parameters on the surface quality of the peened area in specimens treated at 3.1 J following four peening sequences: (a) using a sacrificial overlay, (b) without a sacrificial overlay. (c) Measurement of surface micro-indentations on peened regions treated at 1.8 and 3.1 J with a sacrificial overlay, considering different peening sequences. (Reprinted from [132])

Each micro-indent formed corresponds approximately to the cross-sectional area of the utilized laser shot as indicated in Fig. 4.8 and the height of these indents is proportionally influenced by the laser energy. A transition from 1.8 to 3.1 J in laser energy resulted in

distinct micro-indentations with well-defined characteristics, featuring an average height range of 2.5 to 4 μm . These trends align closely with the observations derived from surface topography investigations on the peened region for materials such as TiAl alloy [122] and LY2 alloy [175].

In accordance with the ISO 4288:1998 standard, the surface roughness of the unpeened region and the peened region in LPF specimens from parameter sets 2 and 3 were measured. The roughness of the base material was 0.84 μm . Fig. 4.9 illustrates the roughness value, denoted as R_a (μm), of the peened region in LPF specimens under various laser energies as well as peening sequences with and without the incorporation of a sacrificial overlay. Notably, an observable trend emerged wherein the roughness of the peened surface increased after LPF without a sacrificial overlay in correlation with higher laser energy and an escalating number of peening sequences. Conversely, when applying peening with a sacrificial overlay, there is no substantial increase of roughness within the peened region. This observation suggests that utilizing LPF with a sacrificial overlay is suitable for applications that prioritize superior surface quality.

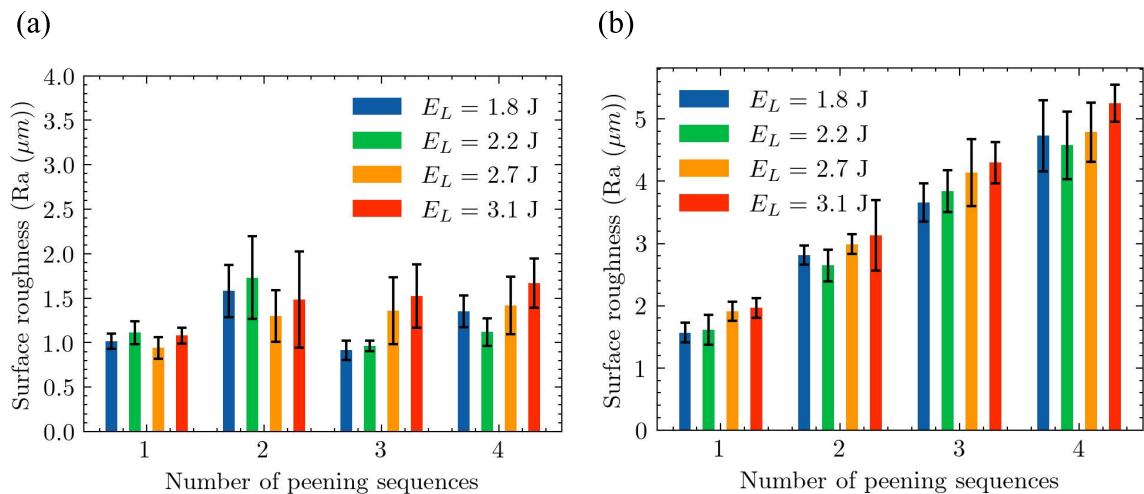


Fig. 4.9: Surface roughness in the peened region after LPF (a) with and (b) without a sacrificial overlay.

A similar trend emerged, wherein an increase in the overlap corresponded to a significant escalation in roughness within the peened region [132]. This rise in roughness is primarily attributed to the intensified processes of surface ablation and re-melting, both stemming from the impact of multiple high-overlap laser shots [134, 29, 47].

With a comprehensive examination of macroscopic surface attributes, a detailed exploration of the surface characteristics and chemical composition is performed in the treated region due to the observed surface oxidation and ablation after LPF without using a sacrificial overlay. Both the untreated and treated regions of an LPF-processed specimen were subjected to SEM and EDX analyses. The chemical profiles at specified locations are illustrated in Fig. 4.10. A marked disparity in surface topography between the peened and

unpeened regions was observed, as indicated in region 1 of Fig. 4.10(a) and Fig. 4.10(b).

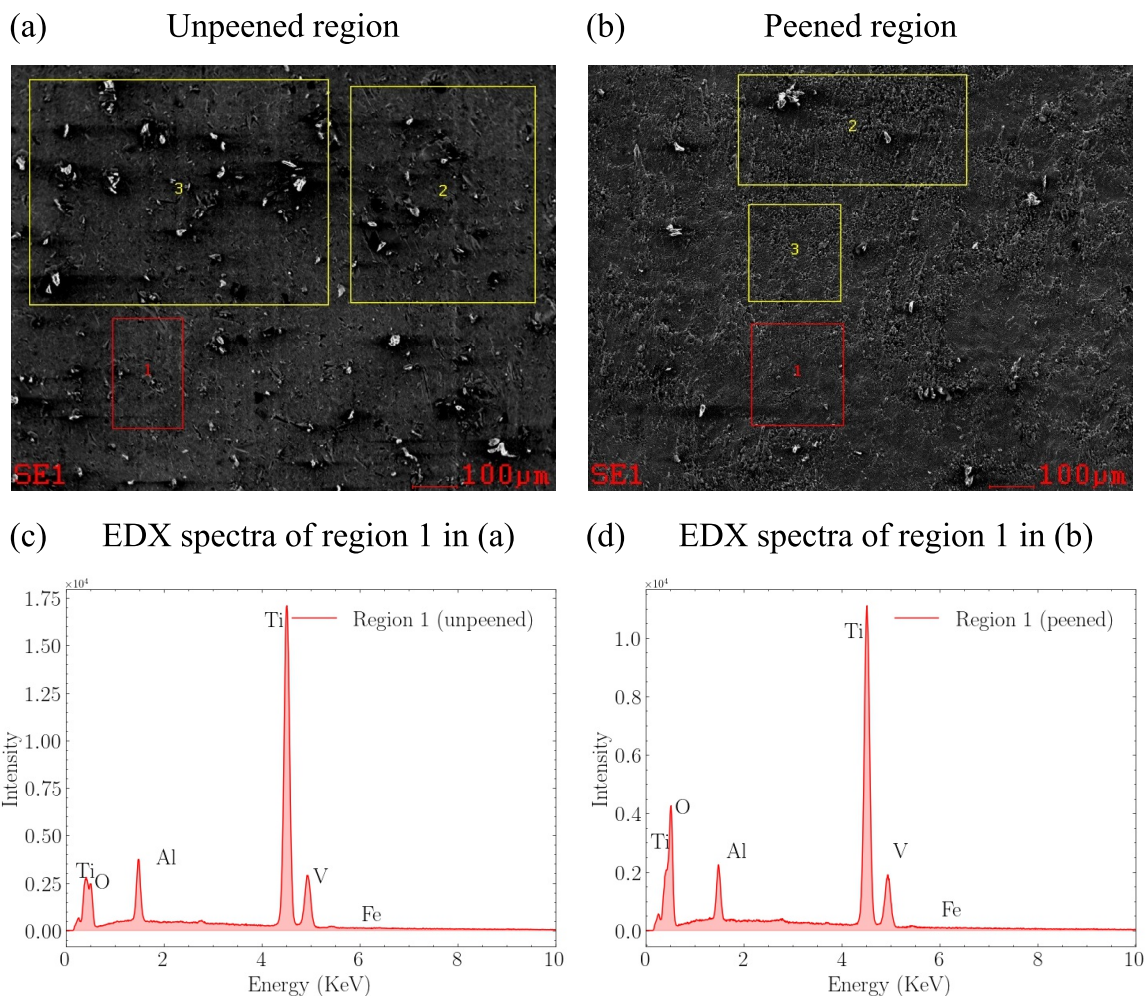


Fig. 4.10: SEM and EDX analyses of the unpeened region and peened region of LPF processed specimen without a sacrificial overlay at a laser energy of 3.1 J (a) Unpeened region (b) Peened region (c) EDX spectra of region 1 in the unpeened area (d) EDX spectra of the region 1 in LPF area

Notably, the presence of an oxide layer was affirmed by comparing the EDX spectra from the marked area 1 of the unpeened region with that of the peened region. Spectral data acquired from the unpeened and peened regions, showcased in Fig. 4.10(c) and Figure 4.10(d), distinctly reveal the presence of key elements. Specifically, strong signals associated with titanium are evident, represented by the $L\alpha_1$ and $L\alpha_2$ lines at approximately 0.45 keV, as well as a robust $K\alpha_1$ line at 4.51 keV. Furthermore, peaks corresponding to aluminum ($K\alpha_1$) and vanadium ($K\alpha_1$) are discernible at 1.48 keV and 4.95 keV, respectively.

The appearance of elements such as silicon (Si) and iron (Fe) may be attributed to surface contamination originating from prior manufacturing processes. Intriguingly, the spectra obtained from the peened region closely resemble those from the unpeened region. Nevertheless, a notable disparity arises in the form of a significant upsurge in the oxygen peak intensity at 0.52 keV in the peened region's spectrum (Fig. 4.10(d)). This heightened

oxygen (O) presence is indicative of pronounced surface oxidation within the peened region, a consequence attributed to direct plasma ablation at the target surface during LPF in the absence of a sacrificial overlay.

In addition to the formation of an oxide layer in the treated region, while peening without a sacrificial overlay, micro-cracks were also observed. The length of these micro-cracks typically ranges from 1 to 2 μm at the near-surface region in the oxide layer formed after the peening process as indicated in Fig. 4.11. The appearance of micro-cracks may result from the rapid re-melting and vaporization of the surface during each laser pulse.

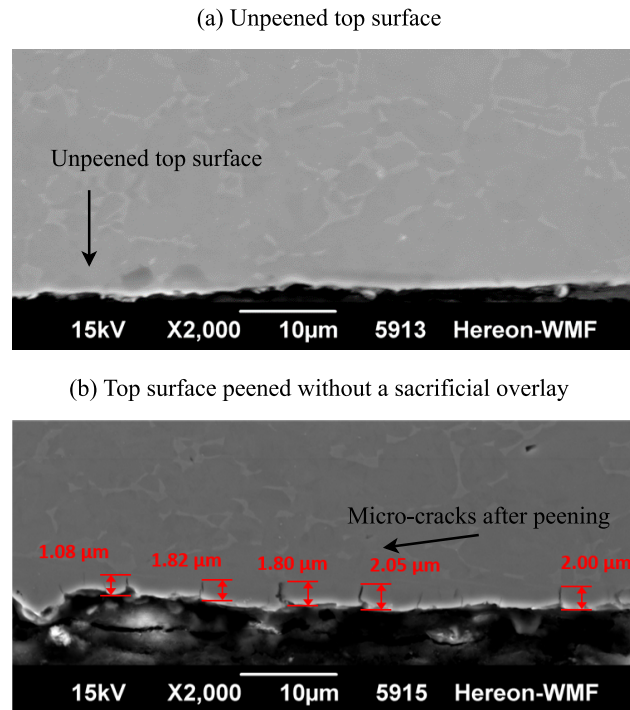


Fig. 4.11: Near surface region of the (a) unpeened specimen, and (b) the peened specimen without a sacrificial overlay at 1.8 J after one peening sequence without an overlap.

The LPF experiments, both with and without a sacrificial overlay, clearly reveal distinct surface features within the peened region. Increasing laser energy and peening sequences resulted in greater bending in the treated region. The peened region exhibited micro-indentations of varying heights (2-5 μm), with no significant chemical damage observed on the surface. LPF with a sacrificial overlay is advantageous as it eliminates the need for additional surface processing. However, it involves the removal and application of the sacrificial overlay in the treated region for every peening sequence.

In contrast, LPF without a sacrificial overlay led to surface oxidation and micro-crack formation on the specimen's peened region. To achieve significant bending, more overlap and peening sequences were needed, but this compromised surface quality. The peened area had increased roughness, and EDX analyses revealed a 1.5 μm oxide layer. Post-processing may be required to achieve the desired surface quality. These micro-cracks were primarily confined to the near-surface regions of the specimen.

4.2 Data-driven approaches: predicting deformation and process planning

Various data-driven techniques are tested using the data acquired from the LPF experiments and their performance is evaluated. A data-driven process planning approach using ANN to predict deformation induced by LPF is presented and validated using benchmark cases of deformation and correction applications. The challenge of finding optimal peening patterns, using a simplified modeling approach with an ML-based cellular automata neural network (CANN) is presented. The results and implications of this pattern prediction endeavor are discussed in the context of potential advancements and limitations.

4.2.1 Performance of ANN trained on data from LPF experiments

This section discusses the outcomes of the ANN, trained using experimental data. Throughout the training process, the MSE metric was calculated for both the training and validation datasets after each epoch. The graphical representation of the performance metric derived from the training and validation data across the epochs is referred to as the learning curve. Learning curves play a crucial role in comprehending the model's development during training and identifying behaviors such as underfitting or overfitting. Additionally, they aid in diagnosing the appropriateness of the training and validation datasets. The resulting learning curve for this ANN is depicted in Fig. 4.12. It is evident from the curve that the MSE gradually decreases and stabilizes as training progresses, indicating that further training is unnecessary.

The training concludes at 500 epochs, with early stopping triggered at epoch 159 due to a patience threshold of 250 epochs. The optimal weights of the model are restored at this point. The performance of the ANN post-training is depicted in Fig. 4.12(a). It is evident that the majority of predicted deformation values from the training, validation, and test datasets fall within the $\pm 10\%$ range. However, a few outlier values are observed in predicting the test data. Overall, the values of R^2 and MSE, as presented in Table 4.1, demonstrate acceptable agreement between predicted and true deformations across the training, validation, and test datasets.

Table 4.1: Performance metrics of the trained ANN on experimental datasets

| Performance metrics | | |
|---------------------|-----------|------------------------|
| Dataset | R^2 (%) | MSE (mm ²) |
| Train | 97.95 | 0.04758 |
| Validation | 93.95 | 0.07101 |
| Test | 88.99 | 0.08183 |

The scatter plot illustrated in Fig. 4.12(b) presents the comparison between true and predicted data obtained from the ANN. The ANN's ability to generalize can be assessed

by its performance on the test dataset, achieving a coefficient of determination of 88.9%.

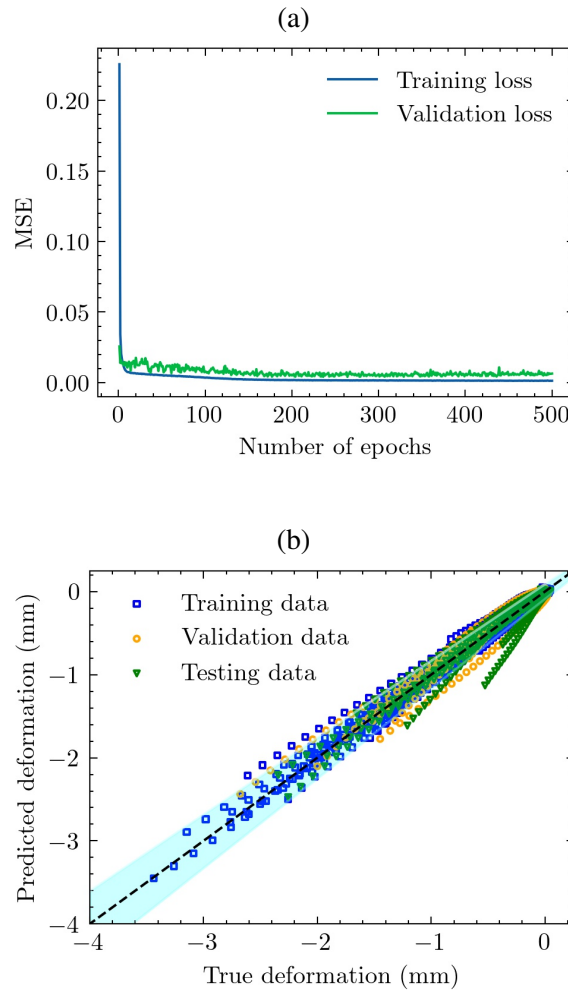


Fig. 4.12: The performance of the ANN is evaluated using the experimental dataset. (a) The performance metric (MSE) is tracked during training on both the training and validation datasets. (b) The visualization illustrates the predicted deformation values compared to the true deformation values from the trained ANN across the training, validation, and test datasets. A dashed line indicates perfect prediction (predicted value equals true value), while the shaded conical region represents a relative error of $\pm 10\%$ deviation from the true value.[131]

The true deformation profile within the peened region is compared with the predicted deformation obtained from the trained ANN. Notably, a reasonable agreement between the true and predicted deformation profiles is observed for exemplary cases from the test dataset, as depicted in Fig. 4.13(a) - Fig. 4.13(f). In instances where the deformation after LPF measures below 1 mm (as shown in Fig. 4.13(d)), it was noted that the predicted deformation from the ANN tends to be higher than the measured deformation. Nonetheless, for significant deformations exceeding 1 mm, the predicted profiles exhibit insignificant deviations from the true deformation observed in the experiments.

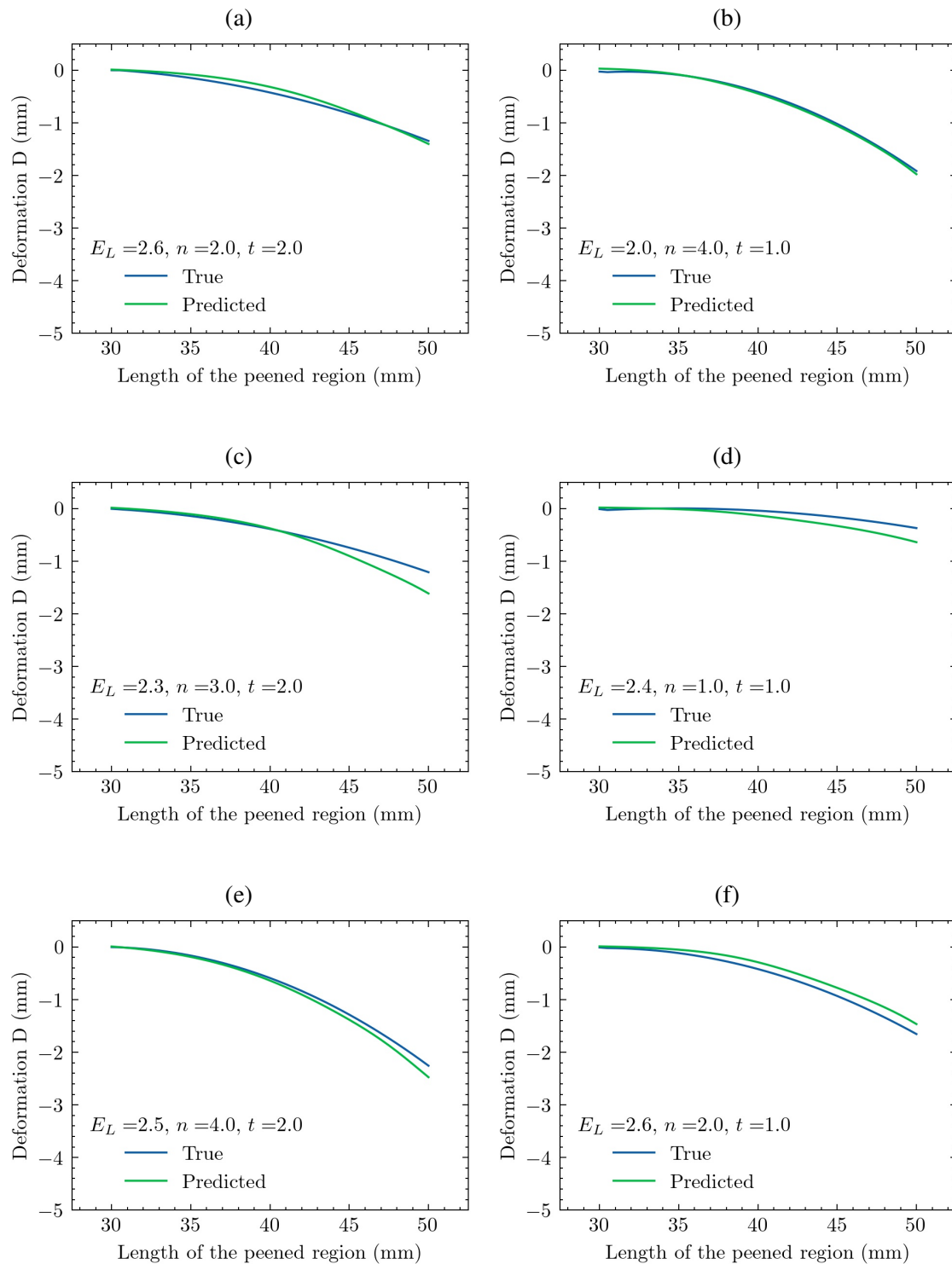


Fig. 4.13: A comparison is made between the actual and predicted deformation values in the peened region, exemplified across different process parameters corresponding to the test dataset, which remains strictly unknown to the trained ANN. The process parameters include E_L for laser energy, n for the number of sequences, and T for the specimen thickness. The actual profile is derived from real experiments, while the predicted profile is generated by the ANN.

The findings indicate that the ANN is capable of accurately predicting deformation in the peened region. However, to effectively utilize these results in addressing complex scenarios, such as those encountered in typical LPF applications, a robust framework is necessary. LPF applications commonly involve inducing deformations in flat specimens or rectifying deformations caused by various processing conditions [44]. Hence, to showcase the practical application of deformation predictions post-LPF, a data-driven planning framework is proposed in this study. This framework leverages an ANN trained on experimental data to modify and deform thin Ti6Al4V sheets, ultimately achieving the desired target shapes.

4.2.2 Implementation of process planning approach for deforming and modifying thin sheets

LPF can be applied to large structures with complex geometries and varying curvatures. Achieving the desired target deformation often involves employing multiple laser energies across different regions of the specimen. In this study, a data-driven process planning methodology is proposed (ref. Sec. 3.2.5), utilizing deformation predictions generated by a trained ANN. The objective is to modify deformation via LPF without the need to solve an inverse problem. The iterative discretization and optimizer, guided by physical and process constraints, offer flexibility in tailoring the process planning strategy to accommodate different initial deformation profiles. Additionally, employing a peen-and-measure cycle reduces the necessity for redundant LPF treatments.

As such, the presented process planning approach is evaluated across four distinct use cases. The first two cases demonstrate the feasibility of using LPF on flat sheets to achieve desired target deformations, while the latter cases showcase the modification of pre-bent structures. In all scenarios, the process control constraints of the optimizer were defined with maximum laser energy ($E_L \leq 3.0$ J) and a limit of four sequences (n) due to process constraints. The thickness (T) of the sheet material varied according to the specimen thicknesses utilized.

4.2.2.1 Demonstrating LPF application on flat sheets

The first use case showcases the direct application of LPF treatment at various locations on a flat Ti6Al4V sheet (as in Fig. 4.14), measuring 1 mm in thickness and 80 mm in length, to achieve a desired target deformation. The ΔD curve, representing the initial specimen before peening and the target profile, was computed.

As depicted in Fig. 4.15(a), a discretization step size of 10 mm was selected. The discretized parts $\Delta D_1(x)$, $\Delta D_2(x)$, $\Delta D_3(x)$, and $\Delta D_8(x)$ remained untreated as they remained flat, indicating a radius beyond the upper limit of the prediction database of the ANN. The regions of the specimen corresponding to the remaining discretized units were subjected to

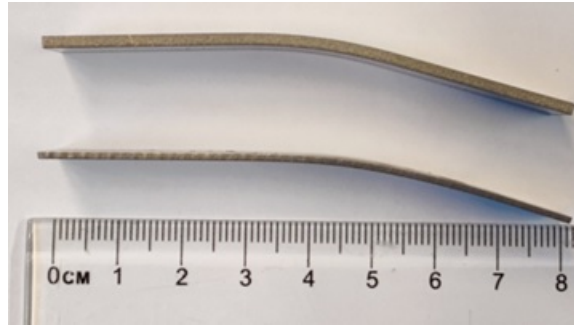


Fig. 4.14: Exemplary 1 mm and 2 mm thick Ti6Al4V LPF treated specimens bent to target shapes from initially flat shape.

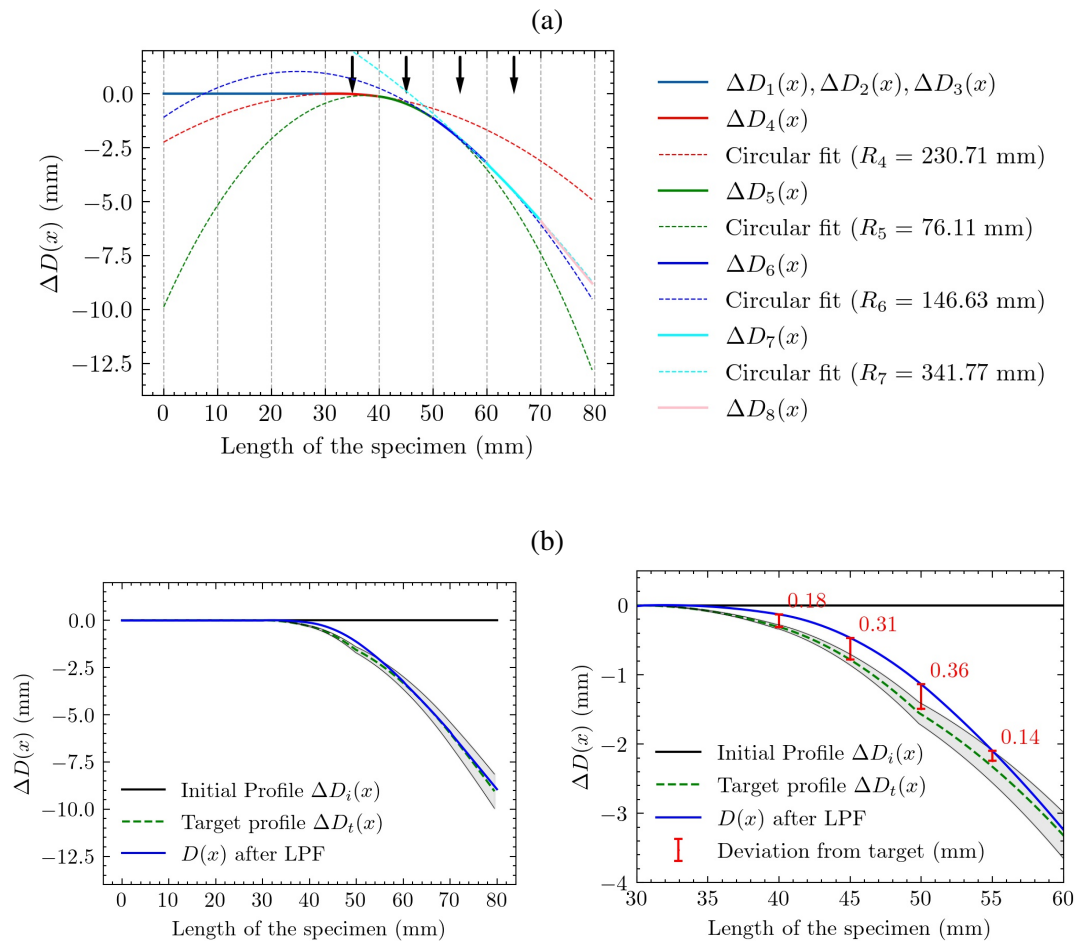


Fig. 4.15: Use Case 1: Illustration of process planning for peening a flat Ti6Al4V specimen, 1 mm thick, to achieve a target profile utilizing predictions from a trained ANN. (a) Discretization of the ΔD profile is conducted with a step size of 10 mm. The circular fit data for each discretization is employed to reconstruct the deformation profile, which is then compared with the database of predicted deformation profiles to map the corresponding parameters for the LPF process. (b) Evaluation of the achieved deformation profile with the target profile post-LPF treatment across various regions. The shaded grey area highlights regions with a relative error of $\pm 10\%$ deviation from the target deformation.

LPF using process parameters (E_L, n) recommended by the optimizer (refer to Table B1 in Appendix B) based on the fit with the ANN-predicted profiles. A cyclic peen-and-measure cycle, as illustrated in Fig. 3.8, was implemented.

The true versatility of LPF becomes evident when both sides of the specimen are peened. As observed by Takeshi et al. [153] in the context of shot peening, when both sides of a panel receive equal energy, the material primarily elongates due to opposing bending moments. However, by employing different LPF process parameters and peening both sides in various regions, the bending direction can be altered from convex to concave (as shown in Fig. 4.16), resulting in shapes like saddles or twists, as demonstrated by Hu et al. [65]. Therefore, an important application is the ability to achieve more intricate shapes through LPF, such as the S-shaped curved specimens depicted in Fig. 4.17. To illustrate such an application, a target profile resembling this geometry was considered. A 2 mm thick flat Ti6Al4V specimen was utilized and peened with ANN-predicted process parameters to attain the desired (S-shaped) deformation profile.



Fig. 4.16: Exemplary 1 mm and 2 mm thick Ti6Al4V LPF treated specimens bidirectionally bent to target shapes from initially flat shape.

To effectively accommodate variations in the curvature of the target deformation profile, a variable discretization step size (D_s) is selected. Recognizing that the $\Delta D(x)$ profile comprises both flat regions and areas where the bending direction changes from convex to concave, four discretizations $\Delta D_1(x)$, $\Delta D_2(x)$, $\Delta D_3(x)$, and $\Delta D_4(x)$ are identified. These correspond to different curvature changes within the profile.

Peening of the specimen with the anticipated process parameters from the trained ANN is carried out on both sides in the regions associated with $\Delta D_2(x)$ and $\Delta D_3(x)$ to induce curvature changes. However, circular approximation in the regions of $\Delta D_1(x)$ and $\Delta D_4(x)$ results in excessively large arc radii, exceeding the bounds of deformation profiles predicted by the ANN. Consequently, no LPF treatment is administered in these areas.

Initially, one side of the region $\Delta D_4(x)$ is peened, while the other side of the region $\Delta D_3(x)$ is treated, as depicted in Fig. 4.17(a). Comparison of the deformation profile post LPF treatment with the target profile reveals that the deformation profile $D(x)$ falls within a 10% tolerance of the desired target profile. The achieved profile after peening closely matches the target profile up to a length of 60 mm (Fig. 4.17(b)), with a maximum deviation of 0.11 mm observed at a length of 67.5 mm. Corrective measures beyond this

point are impractical since the measured deviation falls within the limits of relative error from the ANN predictions.

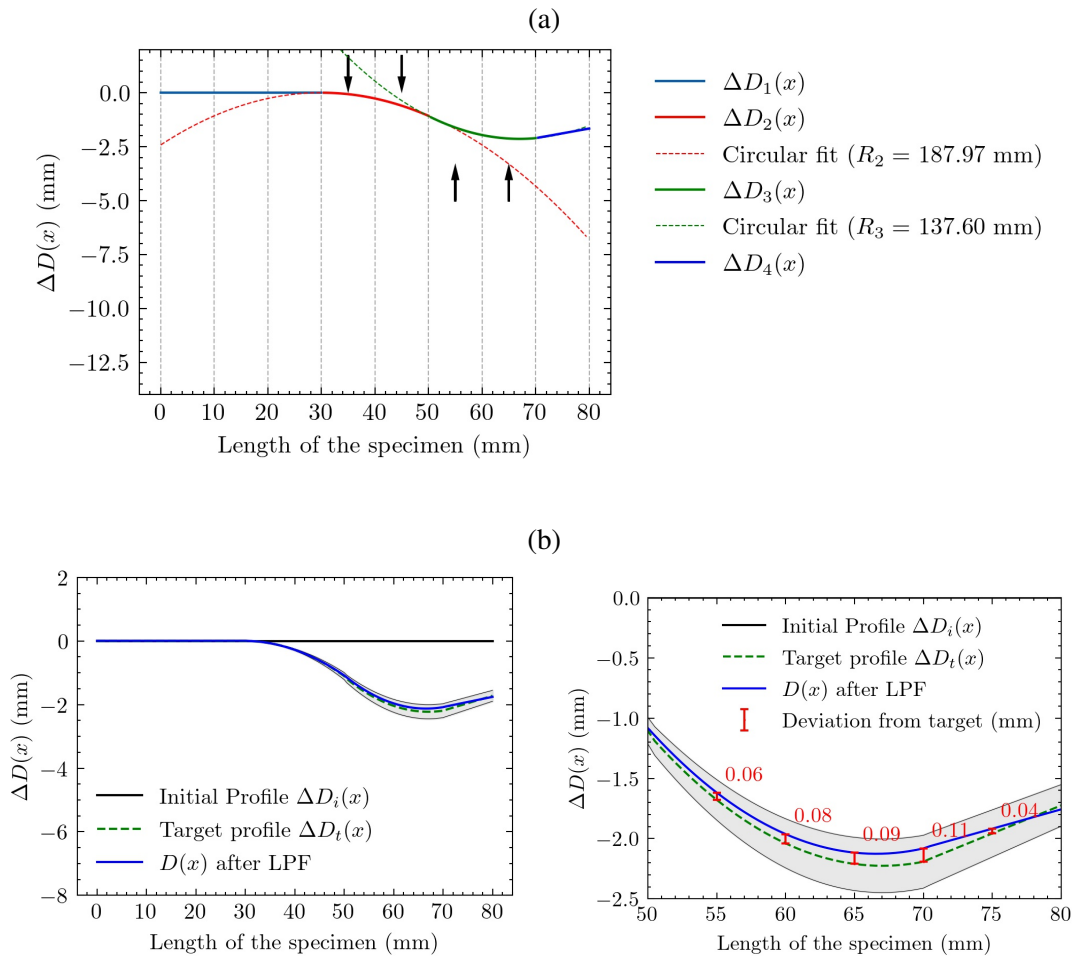


Fig. 4.17: Use Case 2: Employing LPF to achieve an S-shaped desired geometry from a flat Ti6Al4V specimen, 2 mm in thickness. (a) Employing varying discretization step sizes (D_s) for effective peening of the specimen. Utilizing LPF process parameters predicted by ANN, the specimen undergoes peening on both sides at appropriate locations. (b) Comparative analysis between the deformation profile of the LPF-treated specimen and the desired profile. A shaded region illustrates a relative error of $\pm 10\%$ deviation from the target shape.

In both instances of LPF application on flat specimens, a convex bending relative to the peening direction was achieved. This convex bending occurs as a result of plastic deformation near the surface of the treated region, leading to strain incompatibility between the surface and the remaining area of the specimen Hu and Grandhi [58]. In summary, the process planning methodology proposed in this work can be effectively employed to manipulate flat specimens, enabling them to conform to predetermined target geometries. For the fabrication of complex shapes with deformation transitioning from convex to concave, it is necessary to apply LPF treatment to both sides of the specimen.

4.2.2.2 Demonstrating LPF for modifying deformation in pre-bent sheets

In addition to its capability to shape flat specimens, LPF can also be effectively utilized for precise correction of deformations in pre-bent specimens. Such corrections are frequently required for various structural components due to distortions arising from thermal interactions during diverse manufacturing processes. An illustrative instance of reshaping with LPF is documented in Friese et al. [41], where reshaping was necessary for a laser-welded fuselage of an Airbus A380 aircraft. Additionally, O'Hara [109] reported on the application of peen forming for thin sheets, emphasizing the process's ability to rectify deformations. This capability holds particular appeal for the restoration of large structural components, given their substantial associated costs. Therefore, in this study, two use cases were examined to demonstrate the alteration of the radius of curvature in pre-bent specimens to achieve a desired target shape through the application of the process planning methodology.

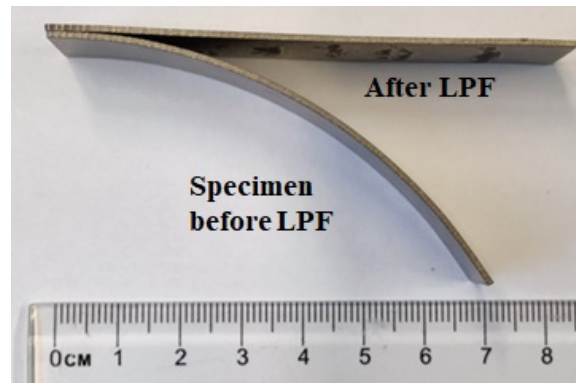


Fig. 4.18: Application of LPF on a pre-bent specimen to modify the existing deformation.

To illustrate a use case of transforming a bent specimen into a flat one using LPF, a 1 mm thick Ti6Al4V specimen is manually rolled to achieve a radius of 140 mm, representing the initial deformation (Fig. 4.18). This pre-bent specimen undergoes local treatment with LPF using process parameters predicted by the ANN corresponding to each discretized unit.

Given that the $\Delta D(x)$ profile equals $D_i(x)$ (since $D_i(x) = 0$ for a flat sample), a discretization step size (D_s) of 65 mm is chosen (as shown in Fig. 4.19(a)). This decision is based on the observation that the arc radius remains constant over the entire span of the pre-bent specimen, except for the initial flat region. LPF treatment is specifically applied to the concave region of the specimen to reduce the radius of curvature and achieve a flat specimen.

It is noted that deviations of approximately 0.10 mm occur within the specimen between 20 mm and 50 mm measured from the left edge (Fig. 4.19(b)), which fall within the $\pm 10\%$ tolerance level. However, larger deviations from the target deformation profile (approximately -0.18 mm) are observed at both ends of the specimen, possibly due to foil

delamination during peening [132]. Consequently, it can be deduced that pre-bent specimens with a constant arc radius can be transformed entirely flat through the successful application of LPF. Nonetheless, a maximum deviation of ± 0.2 mm may occur due to the limitations of the ANN prediction.

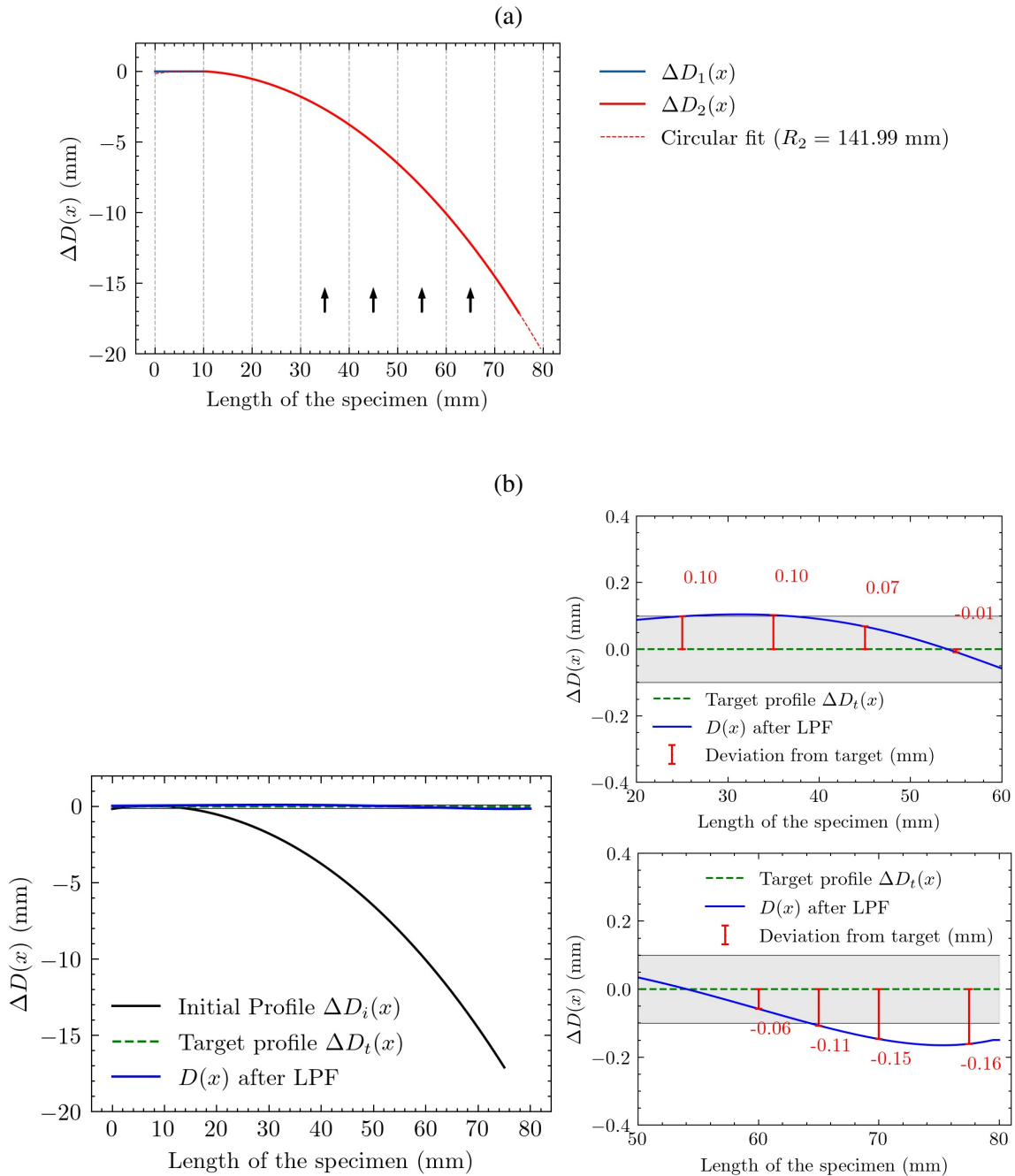


Fig. 4.19: Use Case 3: Flattening a 1 mm thick curved Ti6Al4V specimen with a radius of 140 mm through LPF treatment utilizing process parameters obtained from optimization.

(a) The ΔD profile is divided into two segments: $\Delta D_1(x)$ spanning 10 mm for the flat region and $\Delta D_2(x)$ covering 70 mm for the curved region of the specimen. (b) Analysis of the deviation of the deformation profile from the desired target following LPF treatment along the length of the specimen.

LPF proves effective in rectifying minor local deviations or errors that may occur during the manufacturing process of curved components. An instance of this arises when making slight adjustments to the arc radius in pre-formed structures or addressing spring-back during the uniform incremental forming of sheet metal structures. Such correction applications are exemplified by considering a 1 mm thick Ti6Al4V sheet, 80 mm in length, initially bent by hand rolling to a radius of curvature of 75 mm (as shown in Fig. 4.20). However, a deviation of about 5 mm occurred during the rolling process. Approximately 10 mm at the beginning of the specimen was intentionally left unbent to facilitate clamping.

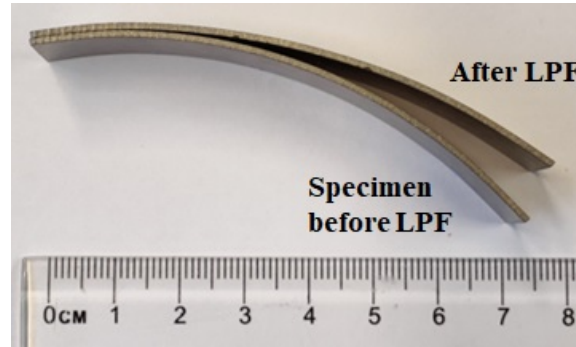


Fig. 4.20: Application of LPF on a pre-bent specimen to modify the existing deformation.

The objective was to reduce the radius of curvature to 100 mm using LPF across the span of the specimen, except for the flat region. However, due to the deviation at the right edge of the specimen, it became evident during discretization that multiple subdivisions were necessary to rectify the curvature effectively.

Following the described procedure for discretization, a $\Delta D(x)$ was computed and divided into three segments (refer to Fig. 4.21(a)): $\Delta D_1(x)$ spanning 10 mm, $\Delta D_2(x)$ covering 40 mm, and $\Delta D_3(x)$ spanning 30 mm, respectively. The region $\Delta D_1(x)$ remained untreated, while $\Delta D_2(x)$ underwent peening using process parameters optimized through the optimizer.

In this corrective process aimed at reducing curvature, the discretized unit $\Delta D_2(x)$ from the fixed end was prioritized for peening first. This strategic approach was chosen because even minor deformations in this region could significantly mitigate the deviation at the right edge of the specimen. Conversely, peening $\Delta D_3(x)$ initially would have been counterproductive, as it would further diminish deformation at the edge while treating $\Delta D_2(x)$.

Following a cycle of peening and measurement, it was observed that the target deformation profile was attained, rendering the peening of the region corresponding to $\Delta D_3(x)$ unnecessary. The curved region of the specimen, with an initial arc radius of 75 mm, could be corrected to achieve an arc radius of 108 mm after LPF treatment, while the target radius was 110 mm (see Fig. 4.21(b)). This resulted in a maximum deviation of 0.51 mm at the free end of the specimen.

Utilizing the database established by the trained ANN, the proposed LPF process plan-

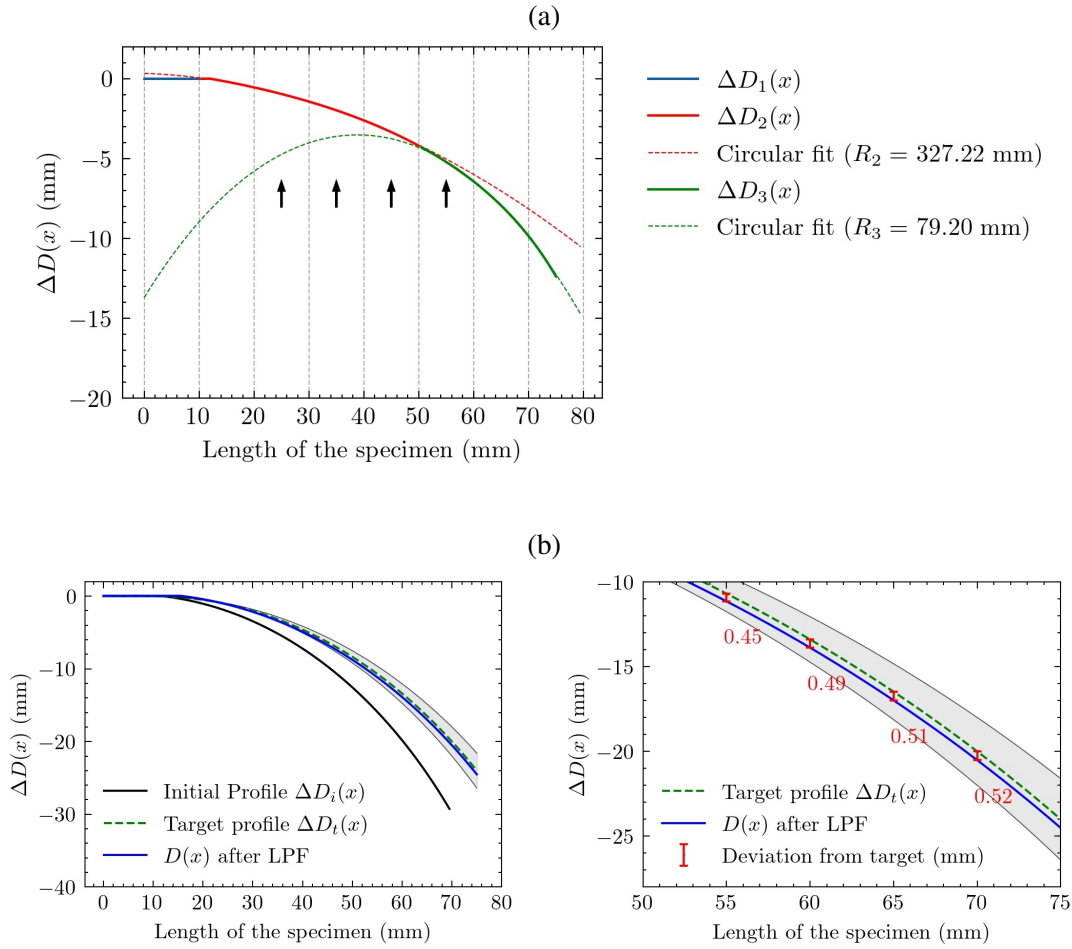


Fig. 4.21: Use Case 4: Implementing LPF to rectify a curved Ti6Al4V sheet with an arc radius of 75 mm, adjusting it to a radius of 100 mm. (a) The computed ΔD profile of the specimen is segmented into three parts: $\Delta D_1(x)$, $\Delta D_2(x)$, and $\Delta D_3(x)$. LPF treatment is applied to the concave region of the specimen to decrease the radius of curvature. (b) A comparison is made between the deformation profile post LPF treatment in region $\Delta D_2(x)$ and the target deformation profile. Evidently, the desired target profile is achieved after peening in the region $\Delta D_2(x)$; thus, further processing is deemed unnecessary.

ning methodology facilitates successful deformation of both flat and pre-bent specimens by inducing deformations in 1 mm and 2 mm thick sheets, as demonstrated in the aforementioned use cases. Employing a cyclic peen-and-measure technique ensures a broad spectrum of process variability, enhances efficiency, and obviates the need for excessive peening treatments.

From these experimental use cases, it was observed that a maximum deviation within $\pm 10\%$ from the desired target may occur, and the minimum deformation correctable by LPF is constrained by the prediction accuracy of the trained ANN. By incorporating process control inputs, the recommended LPF process parameters can be effectively determined using the proposed process planning workflow. However, this approach necessitates critical pre-processing input, namely the discretization step size (D_s), which governs the

number of processing steps. As observed in use case 1 (refer to Fig. 4.15(a)), excessively small discretization can lead to increased deviations in crucial regions. Therefore, the discretization step size must be carefully chosen to ensure that the fitted arc radii (R_k) are not excessively large, indicating that the discretized unit is flat and does not necessitate LPF treatment.

Use cases 1 and 2 illustrate the applicability of the LPF process in obtaining components with uniform arc radius as well as those with a transition in arc radius from convex to concave. Conversely, use cases 3 and 4 showcase the successful modification of pre-bent specimens. In these scenarios, when the required $\Delta D(x)$ profile values are less than 0.5 mm, the technique exhibits limitations in suggesting appropriate process parameters, as the deformation profile tends to be linear. This could potentially lead to inaccurate conclusions in certain instances due to extremely large values of arc radius (R_k) when approximated by a circular fitting function. Nonetheless, significant deformations in thin sheets exceeding 0.5 mm can be precisely corrected or modified to attain the desired target profile.

4.2.3 Prediction of required peening pattern for LPF to obtain a defined target geometry from a flat sheet

Predicting the required peening pattern for LPF to transform a flat sheet into a defined target geometry is a critical challenge, as it necessitates the precise control of numerous parameters, as illustrated in Fig. 2.6. The effectiveness of LPF relies on specific process parameters such as laser power density, the number of peening sequences, and the thickness of the specimen. Previous results have demonstrated that data-driven approaches can effectively predict deformation in the peened region for a specific set of process parameters, typically resulting in a consistent radius of curvature change along one direction, while remaining constant along the shorter edge of the specimen. However, for deformation that occurs in two directions on a flat sheet, the application of LPF depends on accurately determining the optimal peening pattern. This highlights the complexity and importance of identifying the right combination of parameters to achieve the desired geometry. Thus, the present section summarises the findings from the trained CANN, which can predict a peening to obtain a desired deformation using LPF (ref. section 3.2.6).

Throughout the training process, the model refines its ability to predict the actual peen pattern that induces the curvature specified in the input channel. The evolution of these predicted peen patterns is depicted in Fig. 4.22. From Fig. 4.23 it can be seen that the loss progressively decreases from an initial value of 10^{-1} (corresponding to random initialization of weights and biases) to approximately 5×10^{-4} . The gradient magnitude is depicted on the right vertical axis, where a larger magnitude indicates significant changes in the weights and biases. Peaks in the log-loss sometimes coincide with rises in gradient magnitude. Furthermore, a comparison of the training loss with a change in batch sizes can

be observed in Appendix F (see Fig. F.2).

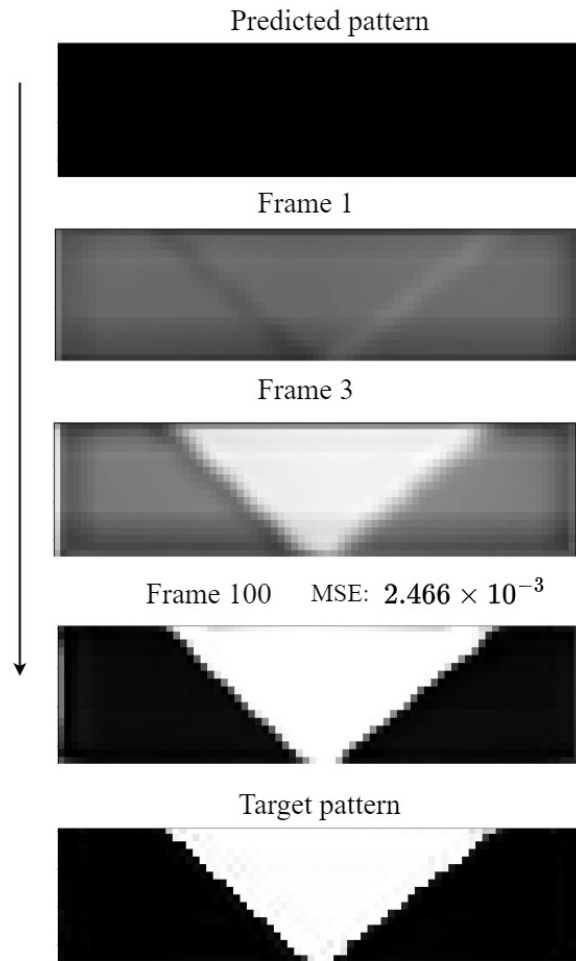


Fig. 4.22: The evolution of the predicted peening pattern (frames 0, 1, 3, 100) during the training of the CANN model. The bottom-most pattern is the target pattern [132].

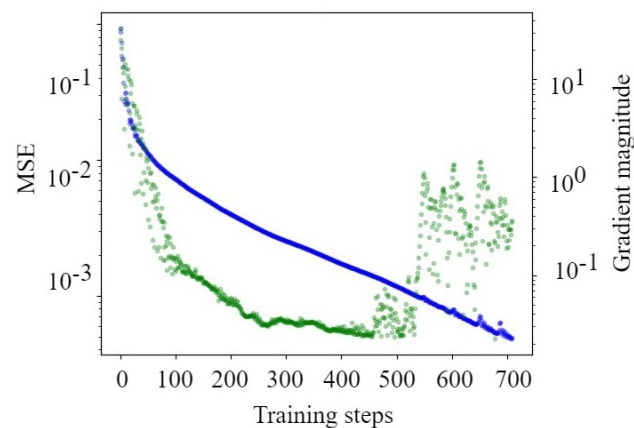


Fig. 4.23: The training loss and gradient magnitude during training of the CANN. As observed on the left, the loss decreases as the training progresses and the CANN learns to predict the peened pattern. The gradient magnitude is indicated on the right, generally, a large gradient magnitude means large changes in the weights and biases. [83]

A crucial aspect to consider is long-term stability and to ensure that there is no catastrophic forgetting [79] during the training process. This is avoided by using a "pool" of inputs H_i at different phases in time/iterations, not to be confused with CNN pooling layers. The pool might be an array like $[H_{100}, H_{200}, \dots, H_{900}, H_0, H_{600}]$. For each training step, a dozen or so randomly chosen H_i are taken from the pool, trained, and then put back in. Over time, this leads to very high iterations, ensuring the model maintains the correct pattern. This approach prevents "catastrophic forgetting," one or more H_i are reset to H_0 , allowing effective training over thousands of iterations (see Fig. 4.24).

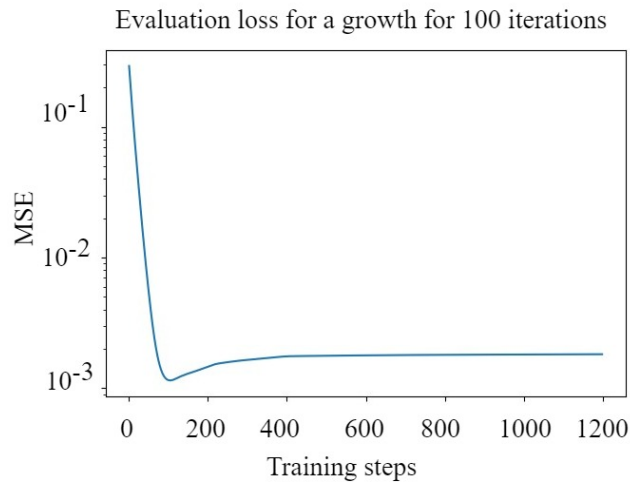


Fig. 4.24: The evaluation log-loss plot demonstrates that using pooling achieves long-term stability. The loss reaches its minimum at 100 iterations and then increases slightly until 400 iterations. [83]

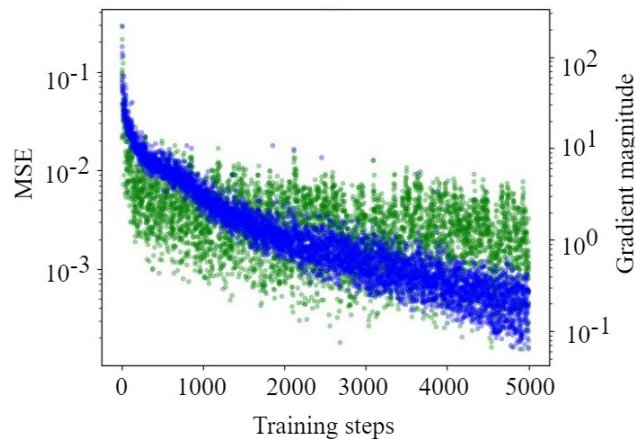


Fig. 4.25: The training log-loss plot during training on a training set of 37 different peening patterns with a batch size of 16. [83]

In the present work, the goal is to generate the target from arbitrary input curvatures, requiring simultaneous training on multiple curvatures. Thus, it involves not just H_i but $H_{j,i}$,

with j representing the index of the input curvature map. The pool was helpful for this purpose, allowing extension with images of other indices, such as $\{H_{1,100}, H_{1,500}, \dots, H_{15,200}\}$. In this case, the loss achieved after 5000 training steps with a batch size of 16 is shown in Fig. 4.25.

The predicted peening patterns of the training data set and the evaluation data set (strictly unknown to the training dataset) are shown below (Fig. 4.26). It can be seen that MSE is in the range of 10^{-4} to 10^{-3} indicating an accurately trained model.

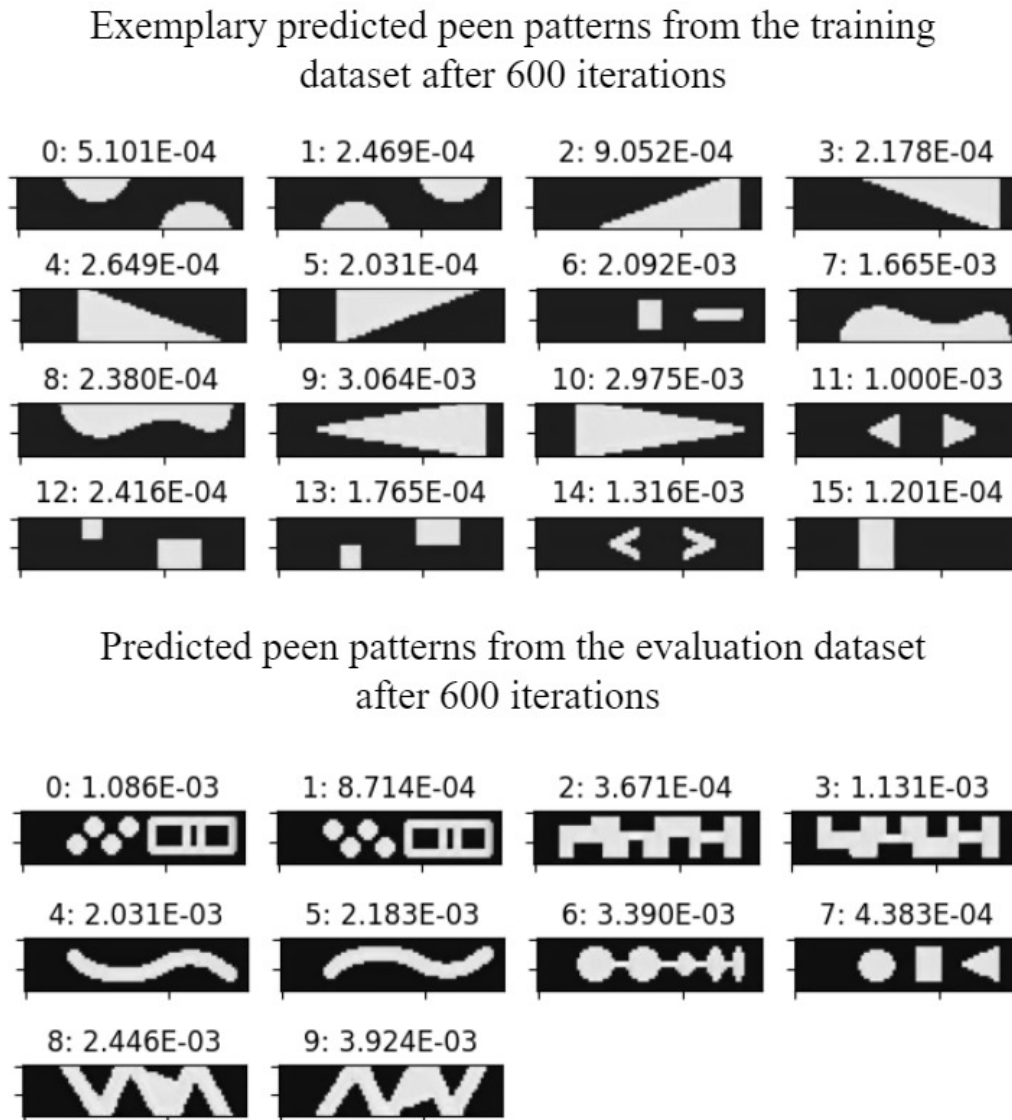


Fig. 4.26: The peening patterns predicted by the trained CANN model after training for 600 iterations. The first set of patterns are a few exemplary patterns collected from the training dataset. The second set of peening patterns is from the evaluation dataset. The numbers on top indicate the index of the image (not of any relevance) and the MSE when compared to the true peening pattern. [83]

4.3 Numerical simulation and experimental validation of LPF

In tandem with experimental efforts, numerical simulations based on the eigenstrain method were carried out to model the LPF process for thin-walled Ti6Al4V strips. These simulations enable a cost-efficient calculation of the resulting deformation and provide a valuable validation tool for experimental findings. Furthermore, the scalability of the numerical simulation approach allows for its application to larger specimens and complex peening patterns, enhancing its versatility and utility.

4.3.1 Findings from LPF simulation using Eigenstrain approach

The plastic strains in the region subjected to pressure pulses (which is the equivalent of a laser pulse) are obtained after simulation on the source geometry according to the Eigenstrain approach (ref. Sec. 3.3.1). As depicted in Fig. 4.27(a) and 4.27(b), it is evident that the peened area exhibits localized plastic strains. These strains arise when the pressure of the shock wave induced by peening surpasses the dynamic yield stress of the target material [119]. The induced plastic strains in the treated region are primarily responsible for bending after LPF [63]. In the central region of each laser shot, in-plane plastic strains are observed to be negative, while towards the edges of the shot, they are positive which is an effect caused due to wave reflection and interference in the center during each shot [119]. This effect can be better visualized in an equivalent plastic strain field as shown in Fig. 4.27(c) and 4.27(d). It is important to observe that the distribution of plastic strain changes throughout the depth of the specimen, and it also varies depending on the position of the laser shot on the source geometry. At the edges of the source geometry, the plastic strain distribution differs significantly from that observed away from the edges, resulting in an edge effect (also observed in [3]).

The in-plane residual stresses in the treated region after peening exhibits the phenomena of a 'residual stress hole' at the center of each shot, similar to the observations reported in the literature [119, 120]. The residual stresses on the surface post-peening typically exhibit a positive trend at the center and a negative trend towards the edges of each laser shot (see Fig. 4.28). This pattern is noticeable in shots located away from the edges, while a more intricate stress distribution emerges at the edge of the specimen.

The surface edge effects observed underscore the necessity for a tessellated distribution of the treated region, contingent upon the distance from the edges. Consequently, eigenstrains must be analyzed in specific regions (N, E, W, S, NE, NW, SE, SW, and C as illustrated in Fig. 3.12), achieved by averaging in-plane strains at various depths throughout the thickness of the specimen.

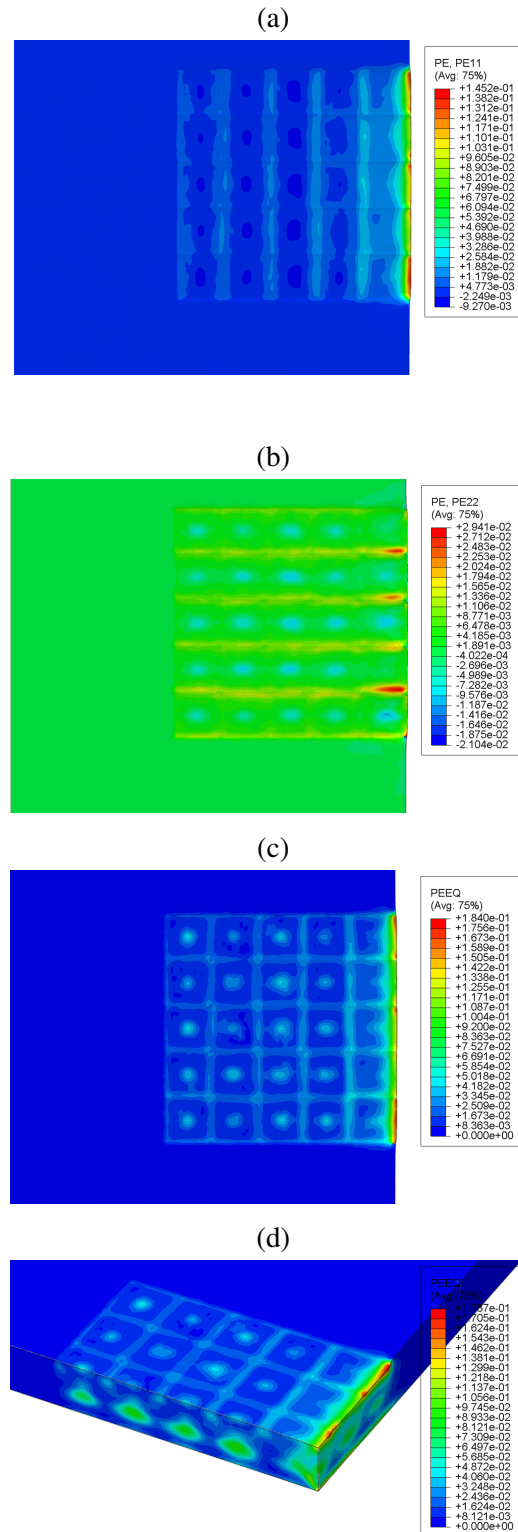


Fig. 4.27: Visualization of the plastic strain field of the surface of source geometry following four layers of peening (i.e. $n = 4$) with a plasma pressure pulse having a maximum pressure (P_{max}) of 3000 MPa. (a) The in-plane strain ϵ_{xx} and (b) ϵ_{yy} . (c) Illustration of the equivalent plastic strain on the surface and (d) through 1 mm thick specimen.

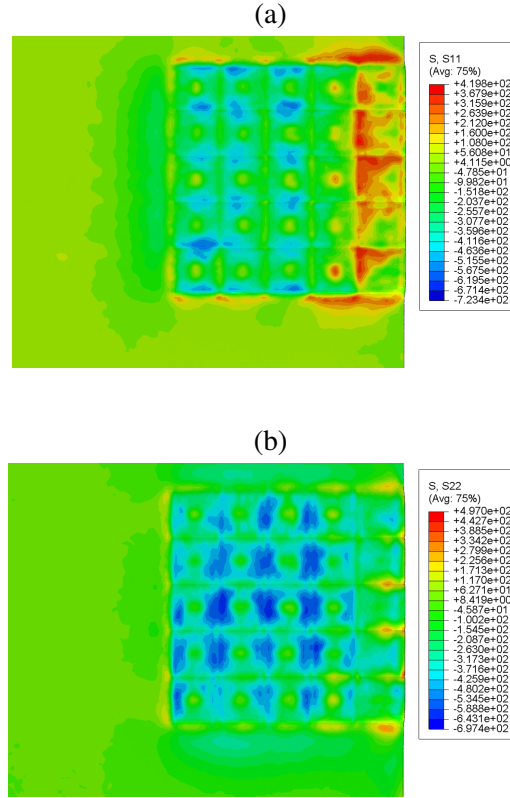


Fig. 4.28: The residual stress field visualization of the in-plane stresses (a) σ_{xx} (MPa) and (b) σ_{yy} (MPa) in the treated region of the source geometry with a plasma pressure pulse having a maximum pressure (P_{max}) value of 3000 MPa after four peening sequences (n).

To explain the edge effects observed on the surface of the plastic strain fields, volume-averaged plastic strains resolved along the depth (or through the thickness) of the specimen in specific regions of the treated area exhibit distinct trends. As illustrated in Fig. 4.29, considering an exemplary case of applied laser pulse with a maximum pressure of $P_{max} = 3000$ MPa and four peening sequences, the in-plane plastic strains ϵ_{xx} are approximately equal to ϵ_{yy} in regions located away from the edges of the source geometry. However, in regions such as NE, E, and SE, which are specifically situated at the edge of the source geometry, the in-plane plastic strains ϵ_{xx} are not equal ϵ_{yy} .

The plastic strains observed in the regions NW, W, and SW indicate a consistent profile without significant changes. This suggests periodicity in the strain distributions, implying that while peening larger areas, there is a predictable pattern to the distribution of strains [58]. This effect demonstrates that the plastic strains in specific regions can be extrapolated and applied to the nodes in the target geometry, eliminating the need to simulate each individual shot [120].

The intensity of the plastic strain induced in the treated region is dependent upon several factors, including the maximum value of the applied pressure pulse, the number of peening sequences, and the thickness of the material. These dependencies are plotted for each region, illustrating their variations, and are provided in the Appendix E.

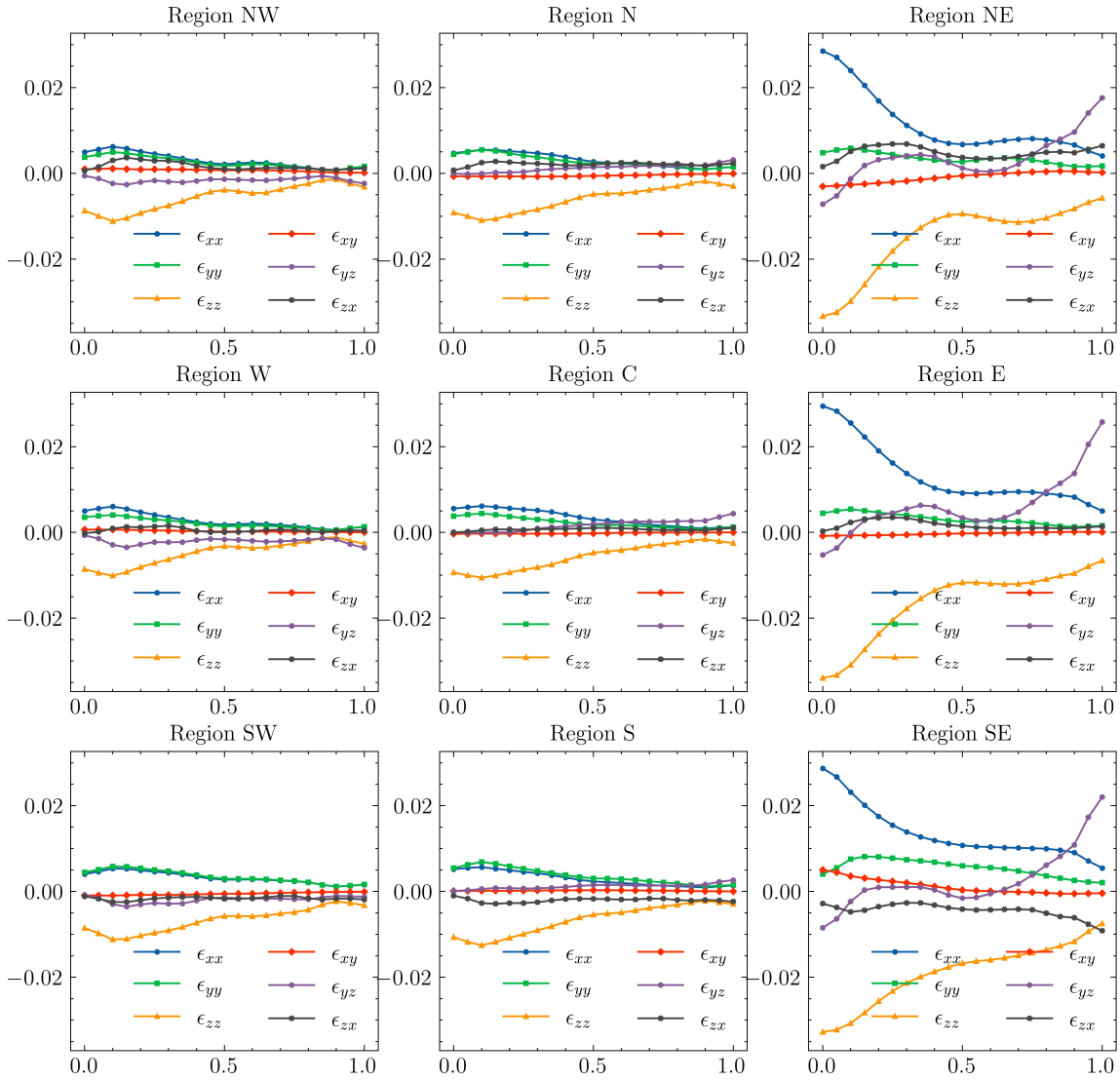


Fig. 4.29: The plastic strains, resolved by depth and averaged across designated regions (N, E, W, S, NE, NW, SE, SW, and C), in the treated area of the source geometry subjected to a plasma pressure pulse with a maximum pressure (P_{max}) of 3000 MPa following four peening sequences (n).

Similar trends can be observed regarding the induced residual stresses in specific regions, as depicted in Fig. 4.30. Near the top surface of the sheet, the induced residual stresses are compressive, with the intensity of these compressive residual stresses decreasing along the thickness of the sheet. These observations align with findings reported in the literature [59, 58, 177]. The intensity of the induced residual stresses increases along the depth with a rise in the maximum value of the pressure pulse up to 5000 MPa (ref. Appendix E), after which it tends to saturate. This indicates that there is no significant further increase in residual stress induced beyond a certain threshold value of maximum pressure.

The depth of induced residual stresses increases as the number of peening sequences increases, particularly near the top surface region of the specimen. Eventually, it tends to reach a nominal steady-state condition within the thickness of the specimen, consistent

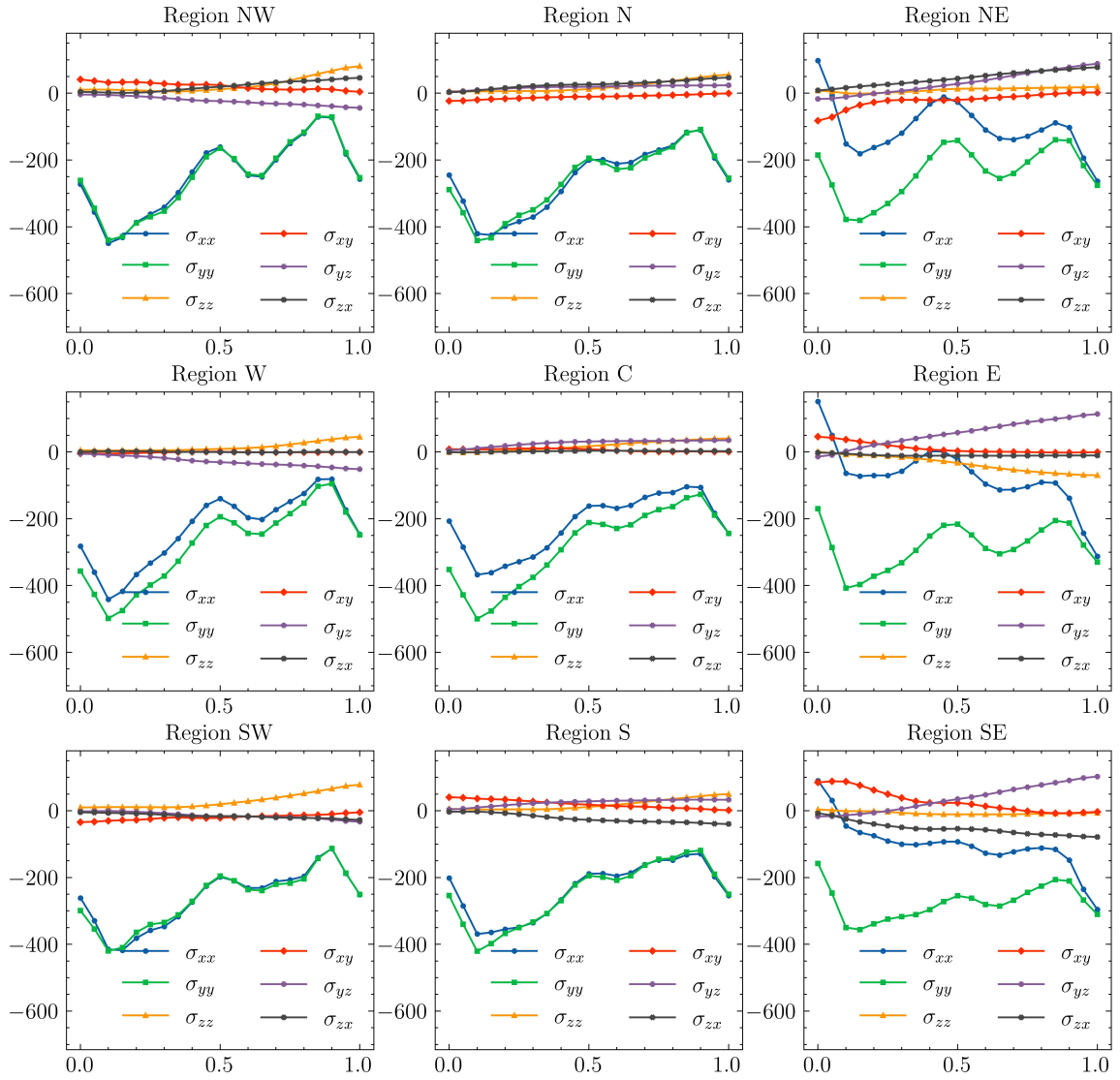


Fig. 4.30: The residual stresses, resolved by depth and averaged across designated regions (N, E, W, S, NE, NW, SE, SW, and C), in the treated area of the source geometry subjected to a plasma pressure pulse with a maximum pressure (P_{max}) of 3000 MPa following four peening sequences (n).

with the effect observed in experimental cases [144]. Following the transfer of the averaged eigenstrains to the designated regions within the target geometry and executing a static relaxation step, the overall deformation of the target geometry is determined.

In the present work, the target geometry is a rectangular specimen of 1 mm and 2 mm thickness as illustrated in Fig. 3.12. After LPF, there are two possible deflections observed (as shown in Fig. 4.31(a)). A convex deflection is a curve that exhibits a downward bending. In contrast, a concave deflection is an upward bending concerning the direction of the laser beam. An increase in maximum pressure (P_{max}) leads to a transition of bending. The change from convex to concave is called bending mode change, which is also observed in experiments [63] and numerical simulations [120]. The intensity of the pressure pulse dictates the distribution of local in-depth plastic strain. This distribution, in turn,

induces either a positive or negative bending moment. The reflections and interference of shock waves can be amplified with increasing maximum pressure, leading to deeper plastic strains and hence increasing the deformation in the treated region. It is further noted that increasing the maximum pressure (P_{max}) and the number of peening sequences (n) results in greater deformations in the treated region. These trends are observed in specimens of 1 mm and 2 mm thickness, measuring $80\text{ mm} \times 20\text{ mm}$, with LPF treatment conducted within a $20\text{ mm} \times 20\text{ mm}$ region (illustrated in Appendix E in Fig. E.5 and Fig. E.6).

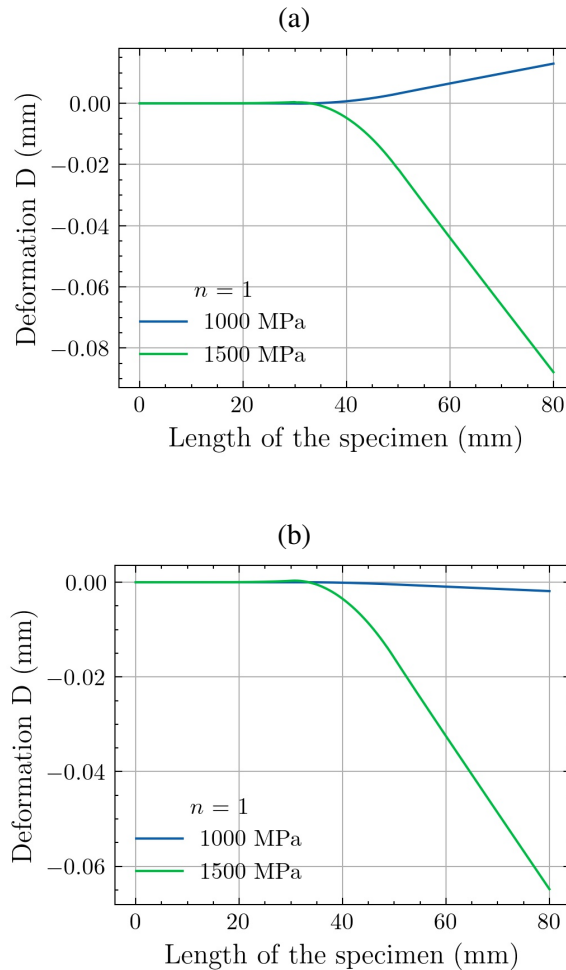


Fig. 4.31: The deformation of (a) 1 mm and (b) 2 mm thick, $80 \times 20\text{ mm}^2$ target geometry subjected to a plasma pressure pulse (P_{max}) of 1000 MPa and 1500 MPa following one peening sequence. Increasing the value of maximum pressure leads to a transition of bending from convex to concave.

4.3.2 Data-driven approach for finding the equivalent value of maximum plasma pressure

The results of the numerical simulation exhibit similar trends to the experimental findings. However, the numerical simulations must be both accurate and stable to align with the ex-

perimental results. In LPF simulations, the challenge lies in determining the precise value of the maximum pressure needed to achieve the desired deformations in the treated region. This process of determining the plasma pressure has been extensively studied in the literature, utilizing theoretical calculations based on the base material and the experimental setup [36, 37, 119]. These models require complex experimental setups and VISAR measurement techniques for precise determination, which are often difficult techniques to implement.

This section generalizes the plasma pressure adjustment for different laser pulse energies to offer an approach to deal with the main challenge of determining the deformation in the treated region by LPF process simulation – by the determination of the maximum value of plasma pressure (P_{max}) and the material behavior. The underlying idea of the following approach is the determination of an equivalent pressure pulse having a maximum value of pressure P_{max} , which produces approximately the same deformation in the LPF-treated region when compared to the real plasma pressure. The time dependency of the equivalent pressure pulse is not considered because the time dependency parameters corresponding to the actual laser pulse were not altered during the experiments. Once the equivalent pressure is determined, the eigenstrains produced in the source geometry are computed by numerical simulation. These eigenstrains are then applied to the target geometry in the treated region to obtain the global deformation (as explained in Fig. 3.15 in section 3.3.2).

Computing eigenstrains for each value of maximum pressure is very time-consuming due to the nature of explicit numerical simulations. Therefore, in the present work, this is replaced by using ANNs. ANNs are initially trained on simulation data generated with pressure pulse parameters as shown in Table 3.3, following the concept of Buckingham’s Pi theorem (as explained in Appendix A). This results in predicting the maximum pressure of the equivalent pressure pulse that can produce the desired deformation, given that the thickness of the material and the number of peening sequences are defined.

The performance curves of the ANN trained on the simulation data are illustrated in Fig. 4.32. As the training progresses, MSE on both training and validation data decreases. The training was set to a maximum of 1000 epochs with a patience of 250; however, early stopping was triggered at 312 epochs.

Table 4.2: Performance metrics of the trained ANN on simulation data

| Performance metrics | | |
|---------------------|-----------|------------------------|
| Dataset | R^2 (%) | MSE (mm ²) |
| Train | 99.78 | 0.01837 |
| Validation | 99.58 | 0.02538 |
| Test | 99.73 | 0.02201 |

The Table 4.2 displays the MSE and R^2 value after the completion of the training process. It is observed that the R^2 value is greater than 99.5% for all the training, validation, and testing datasets, indicating a well-trained model.

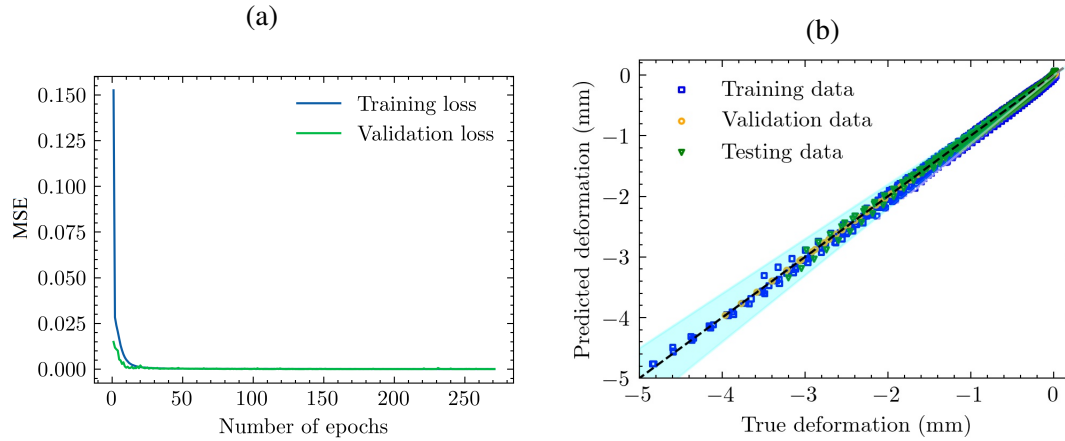


Fig. 4.32: The performance of the ANN is evaluated using the simulation dataset. (a) The performance metric (MSE) is tracked during training on both the training and validation datasets. (b) The visualization illustrates the predicted deformation values compared to the true deformation values from the trained ANN across the training, validation, and test datasets. A dashed line indicates perfect prediction (where the predicted value equals the true value), while the shaded conical region represents a relative error of $\pm 10\%$ deviation from the true value.

This trained model is utilized to generate a database of deformation data based on various values of maximum pressure, the number of peening sequences, and the thickness of the specimen. This eliminates the necessity for running additional numerical simulations. The trained model effectively creates a database that accurately represents actual experimental data. The experimentally obtained deformation data can be mapped onto the generated equivalent simulation data. This is achieved by utilizing LPF process parameters such as the number of peening sequences, and the thickness of the specimen.

Constraining the number of peening sequences and the thickness of the specimen is essential due to underlying reasons. The thickness of the specimen is a physical parameter that remains constant depending on the sample being treated. Additionally, laser energy and the number of peening sequences are not entirely independent, as their combinations can produce the same deformation. For instance, high laser energy with a lower number of peening sequences can achieve similar deformation in the treated region as lower laser energy with multiple peening sequences [132]. Therefore, it is reasonable to assume one as constant and map the experimental deformation data to the simulation deformation data accordingly using a KS optimizer [142] (ref. section 3.2.5). The mapped profiles of ANN predicted simulation vs. experimental deformation data corresponding to the test dataset are illustrated in Fig. 4.32. It is observed that the deformation in the treated region predicted by the ANN trained on the simulation data is in good agreement with the experimentally obtained deformation profiles.

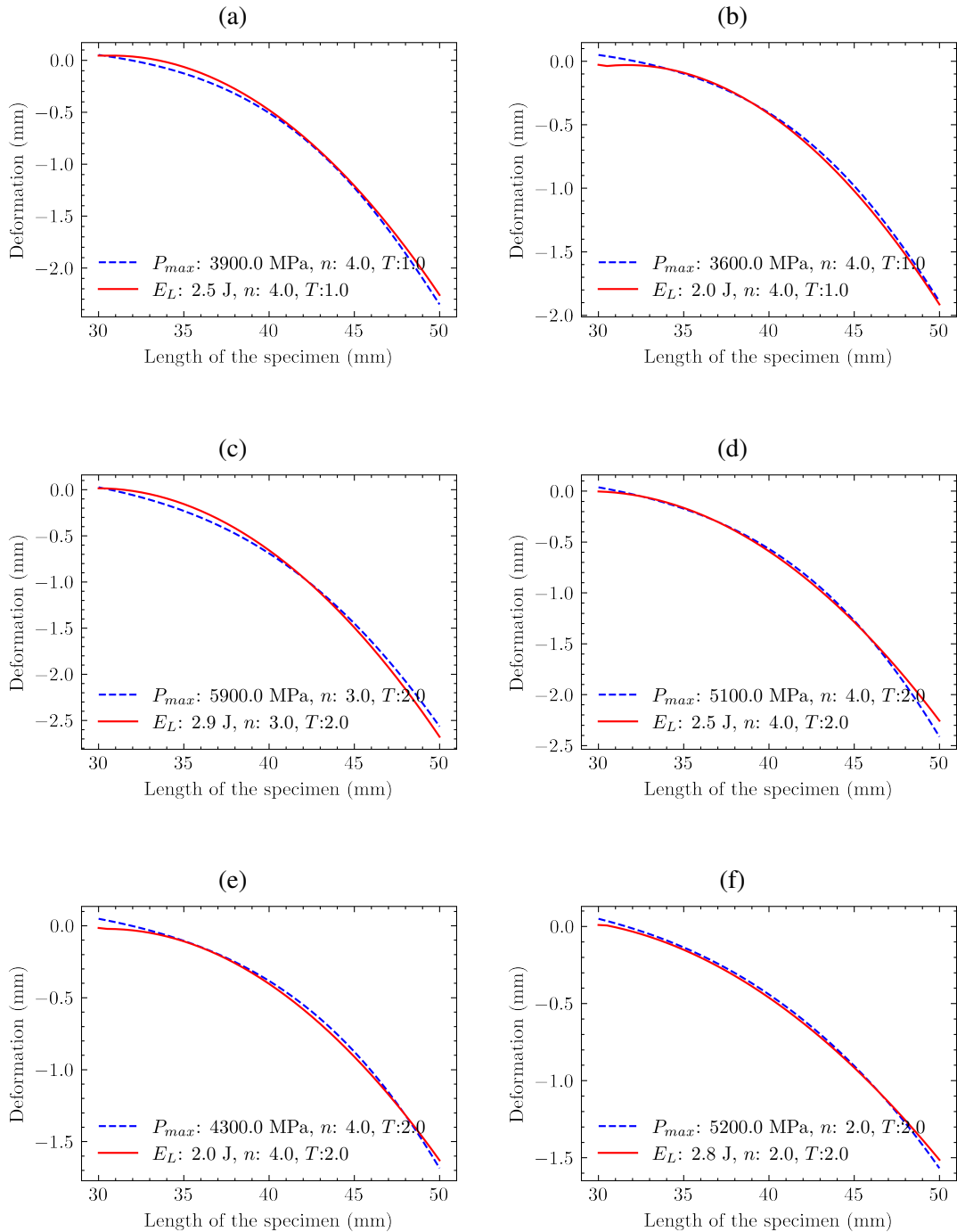


Fig. 4.33: Exemplary deformation profiles of the LPF treated region processed with different LPF process parameters in the test dataset, mapped with deformation data generated by a trained ANN based on numerical simulations.

Such a mapping produces a correlation between the laser energy and equivalent maximum pressure for each peening sequence as illustrated in Fig. 4.34. After mapping all the deformation profiles corresponding to the experimental data with the numerical simulation data, it is observed that a linear trend emerges between the equivalent maximum pressure versus laser energy for all the peening sequences in the training data.

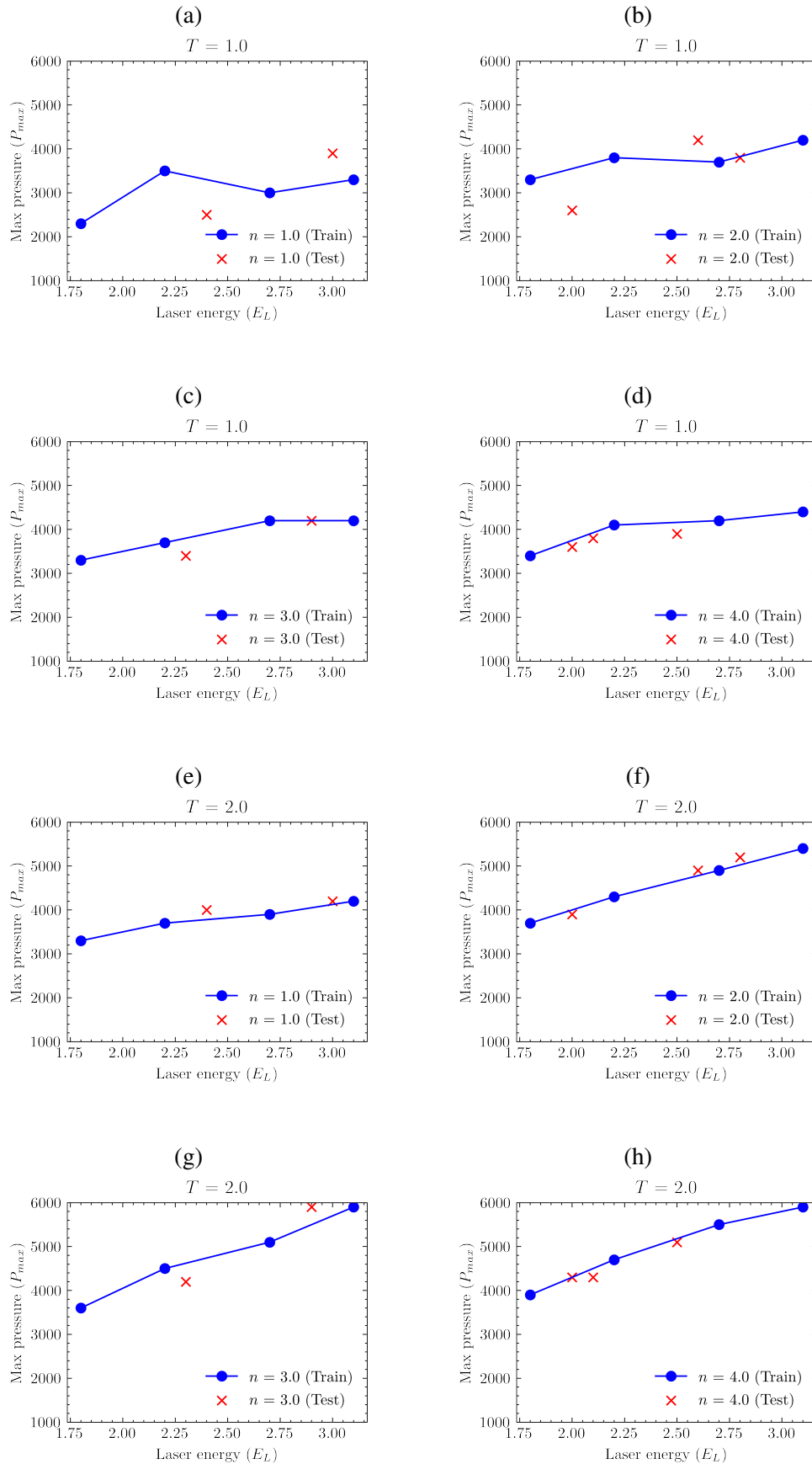


Fig. 4.34: Correlation between laser energy and equivalent maximum pressure for each peening sequence in case of 1 mm and 2 mm thick specimens.

As seen in Fig. 4.34, for 1 mm thick specimens, the equivalent pressure is in the range of 2000 MPa to 4000 MPa for the range of experimentally possible laser energies. However, in the case of 2 mm thick specimens, the equivalent maximum pressure is in the range of 3500 MPa to 6000 MPa. In practical laser peening experiments, the maximum pressure induced remains constant regardless of the material thickness. However, the distribution of induced plastic strains or residual stresses throughout the thickness varies due to the back reflection of induced pressure waves [103]. The present methodology depends on correlating experimental deformation with simulated deformation using an equivalent pressure pulse. Consequently, the maximum value of the equivalent pressure pulse differs due to the temporal profile of the equivalent pulse not precisely replicating the actual temporal profile of the induced pressure pulse in real-world experiments.

Furthermore, it is observed that the equivalent pressures mapped according to the ANN-predicted deformation profiles corresponding to the experimental test dataset are coherent and lie within the linear trend observed between equivalent maximum pressure versus the laser energy on the training dataset. The trained ANN effectively serves as an inverse function ($g^{-1}(f^{-1}(D)) = (P_{max}, n, T)$) when the parameters n and T are defined (ref. section 3.3.2). This eliminates the necessity of explicitly computing the inverse function, as an ANN inherently represents complex relationships without relying on specific mathematical equations.

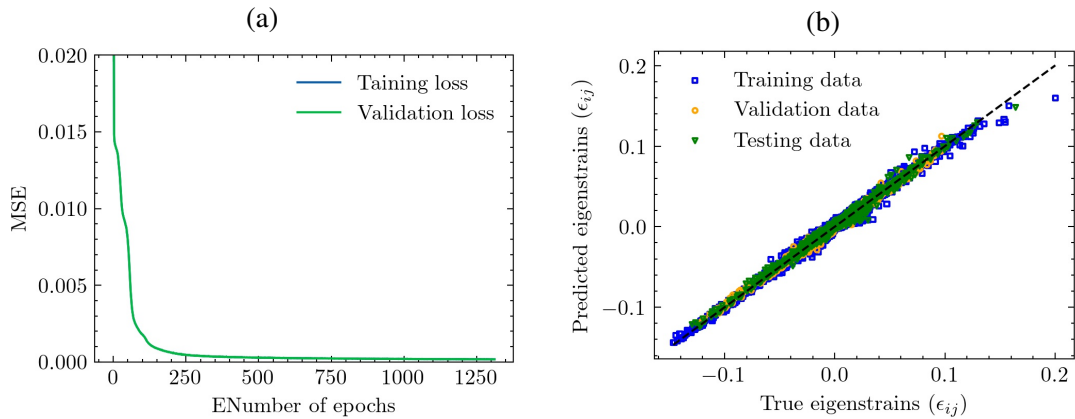


Fig. 4.35: The performance of ANN using the simulation dataset corresponding to explicit numerical simulation, as illustrated in the Appendix E, Fig. E.7. (a) The performance metric (MSE) is tracked during training on both the training and validation datasets. (b) The visualization depicts the predicted eigenstrains compared to the true eigenstrains from the trained ANN across the training, validation, and test datasets. A dashed line indicates perfect prediction (where the predicted value equals the true value).

In this study, another ANN is trained on simulation data to predict the eigenstrains resolved along the depth of the specimen in the source geometry based on equivalent pressure pulse parameters. This enables solving the inverse function ($P_{max}, n, T = g^{-1}(\epsilon_{i,j})$), elimi-

nating the need for explicit numerical simulations for each set of equivalent pressure pulse parameters, number of peening sequences, and the specimen's thickness. The performance curves as illustrated in Fig. 4.35, show that the ANN accurately predicts the eigenstrains at the end of the training process, which lasted over 1300 epochs before early stopping. The number of epochs needed is notably higher compared to the previous ANN training due to the substantial increase in training data.

The metrics of this ANN are tabulated in Table 4.3, indicating that the trained ANN can predict the test data accurately with an R^2 value exceeding 98.8%. This suggests that the model can generalize predictions within the scope of the training data.

Table 4.3: Performance metrics of the trained ANN on simulation data corresponding to the prediction of region-specific depth-resolved eigenstrains

| Performance metrics | | |
|---------------------|-----------|----------|
| Dataset | R^2 (%) | MSE |
| Train | 98.84 | 0.000738 |
| Validation | 98.70 | 0.000751 |
| Test | 98.71 | 0.000734 |

In the present work, a method for determining the equivalent maximum pressure of a generic pressure pulse (which was proposed in [74]) was established using a data-driven approach depending on the deformation observed in the LPF treated region for different combinations of process parameters. This method reduces the need for complex plasma modeling or experimental pressure determination and the number of required numerical simulations (both explicit and implicit) to map the experimental deformation data with numerical simulations making it cost-efficient.

By compiling an experimental database with various LPF process parameters and conducting a limited set of explicit and implicit numerical simulations with equivalent LPF parameters, ANNs trained on the generated simulation data can effectively map the parameter space of the experiments with simulations. This is accomplished by training two ANNs with the simulation data corresponding to the explicit and implicit numerical simulations. If expressed as mathematical functions, the two ANNs predict the inverses of the functions represented by Eqn. 3.12 and 3.13 (section 3.3.2). Two ANNs are necessary despite the inverse of Eqn. 3.13, being solved by the ANN trained on the deformation data and equivalent pressure pulse parameters because the implicit simulation requires depth-resolved eigenstrains corresponding to specific regions on the target geometry. Additionally, computing the eigenstrains by explicit simulation for each representative pressure pulse parameter and the number of peening sequences is significantly time-consuming. A trained ANN on the explicit simulation data can instantly predict the eigenstrains corresponding to each LPF simulation parameter set.

This approach demonstrates the capability of the ANN to recognize patterns and relationships within the data, enabling the generation of a reliable database of region-specific

eigenstrains and deformations with different equivalent pressure values from the trained ANN on simulation data. Aligning experimental LPF process parameters with equivalent simulation parameters, accurate predictions of deformation in the treated region for specific experimental process parameter sets can be obtained instantly, without the need for further simulations.

4.3.3 Validating the data-driven numerical approach with LPF experiments involving complex peening patterns.

A real application of LPF involves peening a specimen to obtain deformation in both directions, often involving a complex peening pattern and in some cases, peening in both directions and having to peen specimens with different sizes. The eigenstrain approach offers the flexibility to apply the obtained plastic strains from the source geometry to a target geometry with different sizes [120, 58, 65].

In this study, the eigenstrain approach is employed in a practical experimental scenario where LPF is used to bend flat sheets to a desired deformation, including complex peening patterns on both sides of the specimen and specimens of various dimensions. Two Ti6Al4V specimens, each with a thickness of 1 mm and dimensions of $80 \times 20 \text{ mm}^2$ and $100 \times 50 \text{ mm}^2$, underwent laser peening (no sacrificial overlay) with a laser energy of 3.0 J, using three peening sequences with different peening patterns as indicated below (see Fig. 4.36).

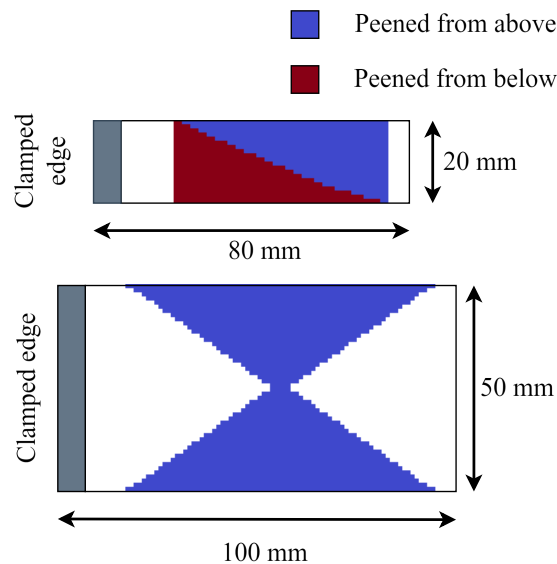


Fig. 4.36: Peening patterns on specimens of different sizes. The blue region indicates that the specimen is peened on the top surface while the red signifies peening on the bottom side of the specimen. The white region remained unpeened.

As illustrated in Fig. 4.37, the deformation maps from the LPF experiment and numerical simulation demonstrate that the eigenstrain approach can effectively map the deformation in real LPF experiments by approximating the maximum value of the equivalent

pressure pulse while maintaining the same number of peening sequences as in the experiments.

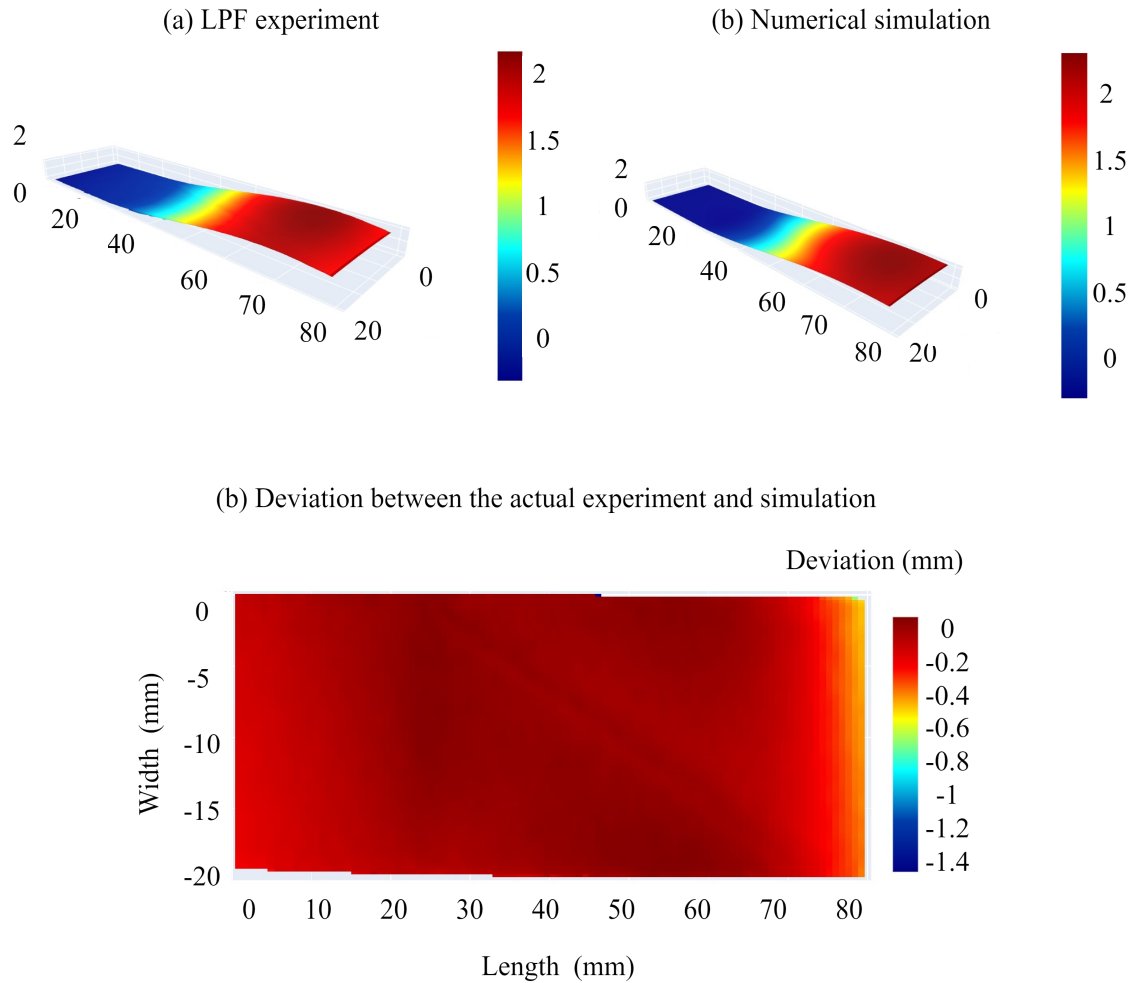


Fig. 4.37: Colormaps depicting the deformation in the 80 mm \times 20 mm specimens after LPF for (a) experiments, (b) numerical simulation, and (c) the deviation map between the experiments and simulations.

In this case, the specimen is peened on both sides, with a triangular peening patch and this resulted in torsional bending along the length of the specimen. A maximum deformation of 2 mm was observed at the free end of the specimen. The shape of the specimen after peening from both experiments and numerical simulation is compared by computing the deviation from the point clouds, respectively. The *'interpolate.griddata'* function from Scipy [157] is utilized to interpolate data points onto a regular grid. This function takes the X and Y coordinates of the data points along with their corresponding Z values. It is applied to interpolate the Z values of experimental and simulated point clouds onto a mesh grid. By specifying the X and Y coordinates of the desired interpolation points using a mesh grid, the function computes smooth Z values using the piecewise 'cubic' interpolation method. This process facilitates the creation of smooth surfaces for both experimental and simulated data, aiding in their visualization and comparison without losing the fea-

tures of the experimental point cloud. As a result, the deviation between the experiments and simulation point clouds is computed as indicated in Fig. 4.37(c), which reaches a maximum value of 0.4 mm at the free edge of the specimen.

Similarly, in the case of the larger specimen (as shown in Fig. 4.38), the peening pattern induced a deformation away from the laser beam. Even in this case, the deviation in deformation computed between the experimental and numerical simulation indicates a maximum of 0.4 mm. This demonstrates the potential of the eigenstrain approach combined with data-driven methods, which can effectively predict deformation after LPF for complex peening patterns within the defined experimental parameter space.

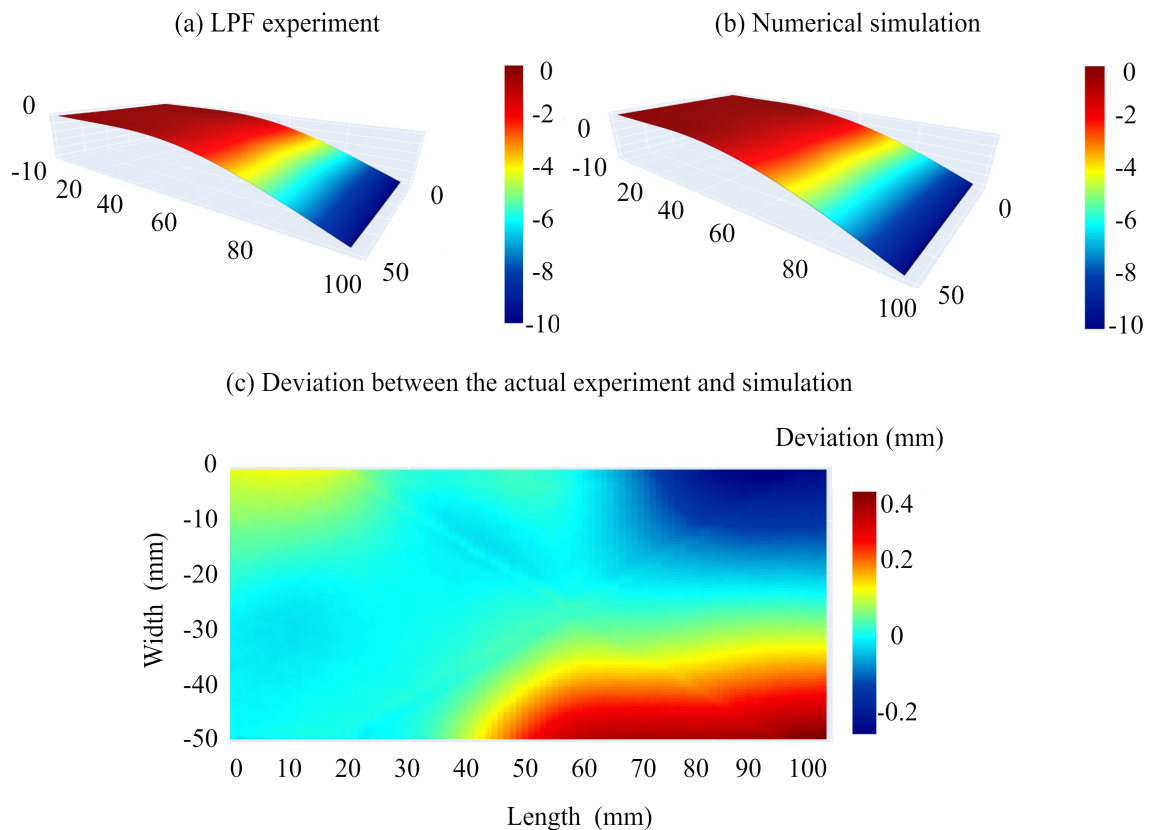


Fig. 4.38: The deformation in 100 mm \times 50 mm specimens after LPF represented in a colormap in case of (a) experiments, (b) numerical simulations, and (c) deviation map between experiments and simulations.

Additionally, using the same set of process parameters (i.e. laser energy and number of peening sequences without a sacrificial overlay), laser shock peening was conducted on three Ti6Al4V specimens with source geometry having a thickness of 1 mm, adhering to the constraints specified in the explicit simulation. The peened source geometry specimens were utilized to determine residual stresses through the incremental hole-drilling method [121] and compared with the volume-averaged residual stresses computed along the thickness of the specimen (as described in [120]) in the treated region after the implicit simulation (as shown in Fig. 4.39). It is observed that the determined compressive residual

stresses in the near-surface region of the actual specimen tend to be lower compared to the averaged stresses from the simulation. However, the magnitude of determined residual stresses through the thickness from a depth of 0.2 to 0.5 mm is coherent with the simulations. The measurement of residual stresses beyond a depth of 0.5 mm was not possible due to the limitations of the hole-drilling method [121].

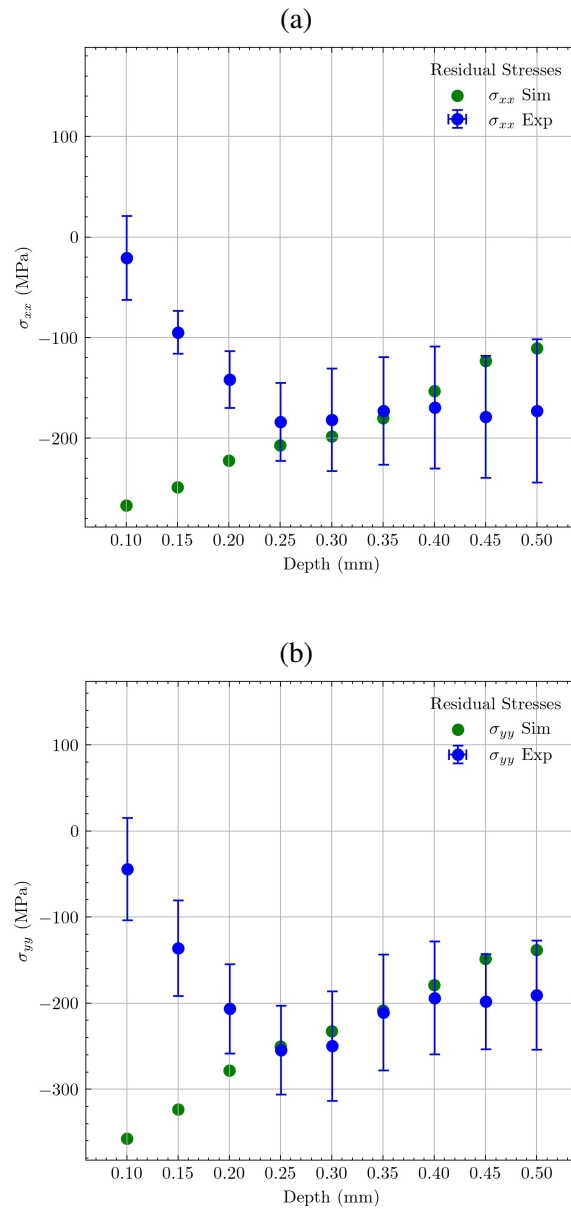


Fig. 4.39: Comparison of residual stresses determined in the treated region of a 1 mm thick Ti6Al4V specimen after being processed with laser energy of 3.0 J and three peening sequences with computed stresses from the simulation. The scatter in the experimentally determined stresses is obtained from three measurements on two different specimens.

The applications of LPF outlined above suggest that employing a data-driven methodology to map experimental parameters onto simulation parameters, characterized by equiv-

alent simulation parameters, offers an effective means to replicate unknown results within the parameter space without extensive experimentation. This approach presents several advantages, notably its adaptability to various real processing conditions and its capability to predict deformations with a high level of precision.

While the data-driven approach to mapping experimental parameters to simulation parameters offers several advantages, it also presents potential limitations. One limitation is the reliance on the quality and quantity of available data for accurate mapping. Insufficient or inaccurate data could lead to erroneous predictions or incomplete representations of the parameter space. Additionally, the effectiveness of the approach may be limited by the complexity of the underlying physical process of LPF (for instance, the effect of a sacrificial overlay), which may not be fully captured by the mapping method. Furthermore, the generalization of the model beyond the specific conditions for which it was trained may lead to decreased accuracy or reliability.

5

Summary and conclusions

This thesis delves into the development and optimization of the laser peening process for thin-walled Ti6Al4V structures, focusing on its application for shaping various components or correcting deformations in existing parts within the aerospace industry. Traditional manufacturing techniques for thin-walled structures [8, 135, 70, 152], such as cold forming, hot forming, and super-plastic forming, often face challenges like wrinkling, shearing, and springback, which adversely affect the quality and precision of the formed parts [56]. LPF is proven to be a capable forming technology offering precise control over the deformation process, enabling the creation of complex shapes with high accuracy and minimal surface damage. Additionally, LPF doesn't require component-specific tooling and can be implemented with minimal tooling which reduces waste and production costs and can be integrated into automated systems for high production efficiency, proving to be a potential alternative to traditional forming techniques. This research integrates experimental investigations, data-driven methodologies, and numerical simulations to enhance the understanding and improve the applicability of LPF process.

LPF process parameter identification

By adjusting LPF parameters such as laser energy, pulse overlap, and material thickness, precise control over material deformation is achievable. The use of a sacrificial overlay during LPF protects the treated region from surface damage and also enhances the deformation. Furthermore, trends in the achievable deformation in the treated region are observed by considering combinations of LPF process parameters. The main results achieved

from the defined set of experiments in the present work are the following:

- The current study has determined a range and combination of process parameters that allow for achieving the desired degree of bending in a flat specimen while ensuring a surface free from damage in the peened region following Laser Peen Forming (LPF) of 1 mm and 2 mm thick Ti6Al4V sheets.
- The defined parameter sets with different combinations and variations of LPF process parameters reveal insights into the various effects of deformation and surface quality of the treated region.
 - Impact of overlap and laser energy on sacrificial overlays during LPF: In experiments involving varying laser energy, overlap, and types of sacrificial overlays (aluminum and stainless steel foils), both types of overlays were destroyed even at a minimal overlap of 10/10. This failure led to surface damage in the peened region, attributed to factors like poor adhesion, air entrapment, or excessive overlap. When experiments were conducted without overlap, aluminum foil was found unsuitable even at the lowest laser power, leading to the use of stainless steel foil. Stainless steel foil sustained laser energies from 0.5 J to 3.1 J without damage, establishing a safe working range for LPF without causing surface damage.
 - The overlap during the LPF process significantly impacted the integrity of the sacrificial overlay. High overlap caused multiple intense shock waves in a short period, thinning the overlay and causing fractures.
 - Influence of laser energy, peening sequences, and overlap on deformation: Significant deformation was observed with varying laser energy (1.8 J to 3.1 J) and increasing the number of peening sequences (from 1 to 4). The peened region exhibited a convex curvature due to intensified near-surface local plastic strain in the treated region.
 - Experiments on 1 mm thick Ti6Al4V sheets at a laser energy of 3.1 J with varying overlap levels (0%, 25%, 50%) showed that increased overlap led to enhanced deformation. Higher overlap resulted in more laser shots per unit area, increasing local plastic strains and global deformation. Higher overlap with fewer peening sequences provided similar deformation results as lower overlap with more peening sequences, offering reduced process times and efficient utilization of laser shots.
 - Deformation in the peened region - with and without sacrificial overlay: Significant differences in deformation were observed between LPF processes with and without sacrificial overlays. Without the overlay, increased roughness and surface damage were noted due to ablation and oxidation.

- Surface roughness increased with higher laser energy and more peening sequences when no overlay was used. Using a sacrificial overlay helped maintain superior surface quality.
- LPF with higher laser energy and a sacrificial overlay resulted in distinct micro-indentations with an average height range of 2.5 to 4 μm . These indentations correspond to the cross-sectional area of the laser shots.
- LPF without a sacrificial overlay led to surface oxidation and ablation, as indicated by a blackened surface. SEM and EDX analyses showed marked differences in surface topography and chemical composition between peened and unpeened regions. The use of a sacrificial overlay is recommended for applications that require high surface quality, as it helps minimize roughness and maintain the integrity of the treated surface.

Application of data-driven approaches to predict deformation and peening patterns during LPF

Data-driven methods, particularly those involving ML and ANNs, offer significant advantages for LPF by providing precise predictions and optimizing process parameters to achieve desired deformations in sheet metals. Dimensional analysis played a crucial role in this thesis by providing a systematic method to reduce the complexity of the physical variables involved in the LPF process. By employing dimensional analysis using Buckingham's Pi theorem, key dimensionless groups that govern the LPF process were identified, thereby simplifying the relationships between different process and material parameters. This reduction in complexity enables the ANNs to more effectively learn and predict the relationships between process parameters and deformation in the treated region.

In this study, a data-driven approach is investigated for LPF to manipulate the deformation of Ti6Al4V sheets into desired geometries. The core of the study is the integration of ANN to predict and optimize LPF process parameters. This approach aims to address challenges in achieving precise deformations required in various industrial applications. The methodology involves several key steps. Initially, the deformation profiles of both the initial and target specimen shapes are obtained. The difference between these profiles is discretized, and corresponding arc radii are calculated. These input profiles are compared with predictions from an ANN that has been trained on experimental data to forecast deformation profiles. This process facilitated the mapping of the necessary LPF parameters. The mapping process is guided by physical constraints such as the thickness and number of peening sequences, enabling accurate prediction of the LPF process parameters. Three main use cases of LPF are demonstrated:

- Forming flat specimens into specific shapes, including an 'S'-shaped target geometry.

- Flattening of curved specimens.
- Correcting deformations by reducing the arc radii of pre-bent specimens to achieve a desired shape.

In all the scenarios, the results show that the LPF process can achieve the target profiles within a 10% tolerance level, validating the accuracy and reliability of the ANN predictions and the process planning methodology. The findings suggest that this data-driven approach can significantly enhance the precision and efficiency of LPF in practical applications, particularly in the aerospace and manufacturing industries, where high accuracy in component shaping is critical.

The present work also highlights the development of a CANN model to predict the peening pattern required during LPF to achieve complex deformations on a flat specimen. The model takes the curvature map of the specimen as input and outputs the optimal peening pattern to produce the desired geometry. This data-driven CANN allows for instantaneous prediction of the necessary peening patterns. Throughout the training process, the model's ability to predict accurate peening patterns improved, with training loss decreasing steadily. Stability during training was maintained using a pool of inputs, preventing catastrophic forgetting and ensuring consistent performance over many iterations. The trained CANN model demonstrated high accuracy in predicting peening patterns for various input curvatures, with mean squared error values indicating precise alignment with the target patterns. This advancement underscores the potential of data-driven models in optimizing LPF, significantly enhances the efficiency, and aids in increasing the applicability of LPF process to obtain complex deformations.

Numerical simulation of LPF process

The numerical simulations and experimental validations of LPF in the present study were performed on thin-walled Ti6Al4V strips using the well-established eigenstrain method and a simplified predictive numerical model. The simulations were able to accurately predict the resulting deformation and validate experimental findings, with potential scalability to larger specimens and complex peening patterns. The numerical simulations reveal that the LPF process induces localized plastic strains in the peened area, leading to significant deformation. The distribution of these plastic strains varies depending on the depth and position of the laser shot on the specimen, with distinct edge effects. The central region of each laser shot exhibits negative in-plane plastic strains, while the edges show positive strains due to wave reflection and interference.

Residual stresses post-peening show a "residual stress hole" at the center of each shot, with positive stresses at the center and negative towards the edges, which reflects the experimental observations of micro-indentations in the treated region after LPF. The edge effects

observed in the treated region during the numerical simulation required, tessellating the treated area into smaller sections designated as cardinal and ordinal directions thereby analyzing the average strains at different depths to understand the overall deformation. The numerical simulation findings indicate that the intensity of the induced plastic strain and residual stresses depends on factors such as the maximum applied pressure pulse, the number of peening sequences, and the material thickness. The plastic strains and residual stresses show predictable patterns, allowing for extrapolation and application to larger target geometries without simulating each shot individually. The simulations also demonstrate that increasing the maximum pressure and the number of peening sequences results in greater deformations, with a transition from convex to concave bending observed. This bending mode change aligns with experimental observations from existing literature, highlighting the influence of pressure pulse intensity on deformation patterns.

This thesis investigates a data-driven method for determining the equivalent maximum pressure of a generic pressure pulse for LPF process and the region-specific depth-resolved eigenstrains after LPF. The first ANN was trained on simulation data to predict the induced deformations in the treated region based on the maximum pressure of an equivalent pressure pulse, the number of peening sequences, and the thickness of the specimen. This ANN essentially acts as an inverse function, mapping the observed deformations to the corresponding pressure pulse parameters, eliminating the need for complex plasma modeling or experimental pressure determination. The second ANN was trained to predict region-specific depth-resolved eigenstrains based on the same LPF simulation parameters, which solely eliminates the need for time-consuming explicit simulations. The performance metrics of the first ANN revealed an R^2 value exceeding 99.5% for all training, validation, and testing datasets, while the second ANN achieved an R^2 value exceeding 98.8% for the test dataset, demonstrating their robustness and reliability in predicting deformation after LPF and region-specific eigenstrains accurately.

This data-driven approach relies on the data generated by a limited set of numerical simulations, which serve as equivalents to real experimental data obtained after LPF. The equivalency of the simulation database is validated by comparing the simulations and experiments using test cases with varied LPF process parameters. Further validation of this approach is achieved with LPF experiments involving complex peening patterns. In practical scenarios, such as bending flat sheets to desired deformations with intricate peening patterns on both sides, the eigenstrain approach successfully maps the deformation observed in real LPF experiments.

This thesis presents a comprehensive investigation into the development and optimization of the LPF process for thin-walled Ti6Al4V structures, offering insights into its application within the aerospace industry. Through a combination of experimental studies, data-driven methodologies, and numerical simulations, precise control over material deformation is achieved by adjusting key LPF parameters. The incorporation of ANNs facilitates

precise and rapid predictions, greatly improving the effectiveness in applicability of LPF in shaping intricate geometries with precision. Furthermore, the study highlights the potential of LPF as a viable alternative to traditional SMF in cases of correcting springback, reduced production costs, and minimal tooling requirements. The findings presented underscore the promising future of LPF in industrial applications, paving the way for advancements in sheet metal manufacturing and beyond.

6

Future scope of work

The study has successfully demonstrated the potential of LPF in enhancing the formability of thin-walled Ti6Al4V structures. This work achieved the desired deformation in the treated region while preserving the surface quality by optimizing the process parameters and employing sacrificial overlays. The findings provide a strong foundation for further advancements in this innovative manufacturing technology.

While the application of sacrificial overlay has been advantageous, its use presents challenges, especially for complex geometries. As observed in this study, sacrificial overlays can be damaged at high laser energies. Therefore, alternatives to the use of sacrificial overlays must be investigated. These alternatives could include protective coatings that can be applied specifically in regions to be treated, providing similar benefits without the drawbacks associated with sacrificial overlays.

The present work focuses on Ti6Al4V; nevertheless, LPF has been shown to be successful with other materials as demonstrated in the literature. Each material requires specific process parameter optimization to achieve the desired outcomes. The data-driven approaches developed as part of this work have introduced material properties into the model, aiming to create a generalized model applicable to various materials. Future research should test the effectiveness of such multilateral models for LPF through dimensional analysis. This will involve validating the model against experimental results for different materials to ensure its robustness and accuracy.

LPF can be effectively used in tandem with existing forming techniques, presenting a significant opportunity for future research. Investigating such scenarios will help realize the

full potential of LPF. While LPF may not be suitable for high-volume production of specific components due to its inherent process characteristics, it is highly viable for producing high-value parts that require precise geometry. Identifying and testing such applications in the aerospace industry, where precision and high performance are critical, could lead to significant advancements. Potential areas include integrating LPF with incremental sheet forming or superplastic forming to exploit the strengths of each method. By combining LPF for initial shaping with other techniques or for fine-tuning and finishing, the overall manufacturing process can be made more efficient and versatile.

The present work has demonstrated effective models to optimize process parameters and predict the peened regions with high accuracy. The reliability of these models has been proven within the scope of this research. Building on these findings, the proposed data-driven peen and measure approach can be further extended to real-time process monitoring using feedback sensors. Future work could aim at fully automating the LPF process by developing advanced AI algorithms that adaptively control LPF parameters in real time based on feedback from these sensors. Implementing machine learning models to predict and compensate for potential defects or deviations in the forming process would enhance precision and reliability. Additionally, creating a comprehensive digital twin of the LPF process to simulate and optimize operations before physical implementation could significantly advance the technology, ensuring higher efficiency and quality in manufacturing processes.

LPF has the potential to serve as a first aid process due to its effectiveness in correcting deformations, which could significantly reduce part rejections and save costs. Future research should consider the broader implications of adopting LPF in aerospace manufacturing by performing comprehensive life cycle assessments to quantify the environmental benefits and potential impacts of the LPF process. Analyzing the economic feasibility of LPF for different production volumes and component complexities, including cost-benefit analyses, will help determine its practicality. The observations and findings of this study lay a foundation for future research and development in LPF technology. By addressing these areas, future research can drive forward the development and industrial adoption of LPF as a transformative technology in SMF for aerospace applications.

Appendix

A Application of Buckingham's Pi theorem for LPF process parameters

Dimensional analysis can be performed by using Buckingham's Pi theorem which states that if a physically meaningful relationship k_1 involving n number of variables (such as P_1, P_2, \dots, P_n) exists in the form:

$$k_1(P_1, P_2, \dots, P_n) = 0, \quad (1)$$

with a minimum number of fundamental dimensions m to describe those variables, then they can be grouped into $(n - m)$ dimensionless groups referred as π groups in a relation k_2 such that,

$$k_2(\pi_1, \pi_2, \dots, \pi_{(n-m)}) = 0. \quad (2)$$

The independent dimensionless terms can be formulated as products of parameters (P_i) governing the physical model. A simple formulation of a π -term can be written in the form of:

$$\pi_{ij} = \prod_{i=1}^{(n-m)} P_i^{\alpha_j}, \quad (3)$$

with α_i in \mathbb{N}_0 , where \mathbb{N}_0 is a set of natural numbers. The application of this theorem to experimental and simulation variables that govern LPF is discussed below.

The experimental parameters governing LPF are illustrated in Fig. 3.12. Utilizing Buckingham's Pi theorem, it becomes apparent that there are nine experimental variables (n) and three fundamental dimensions (m) involved. Hence, the total number of dimensionless π -terms that can be derived is six ($n - k$). The π -terms (or dimensionless groups) formed by combining the selected variables are:

$$\pi_1 = \frac{ET^3}{E_L}, \pi_2 = n, \pi_3 = \frac{D}{T}, \pi_4 = \frac{T^5 \rho}{E_L \tau^2}, \pi_5 = \frac{A_f}{T^2}, \pi_6 = \frac{C\tau}{T}, \quad (4)$$

and it reflects fundamental physical relationships between experimental process parameters, material properties, and deformation after peening.

The deformation within the peened region following LPF experiments is quantified as a profile (refer to Fig. 3.5). Consequently, the deformation data exhibits a continuous function, denoted as $D(x)$, across the extent of the peened region. This function is discretized into 41 points, ranging from $D(30.0)$ to $D(50.0)$, with uniform intervals of 0.5 mm, as detailed below:

$$D = [d(x_j)] \quad \forall j \in [0, 40], \quad (5)$$

where $d(x_j)$ represents the deformation at the j^{th} position along the length of the peened region. To predict each deformation value within a deformation profile D , the ANN is furnished with information regarding the position j , which corresponds to the deformation value $d(x_j)$. Here, i denotes the total number of experiments in the parameter space. The structured dimensionless input space of the ANN model, which encompasses the experimental data, is described as follows:

$$X^{ij} := \left\{ \frac{ET_i^3}{E_L^i}, n_i, \frac{T_i^5 \rho}{E_L^i \tau^2}, \frac{A_f^i}{T_i^2}, \frac{C\tau}{T_i}, \frac{j}{41} \right\}, \quad (6)$$

whereas the output is defined as:

$$Y^{ij} := \left\{ \frac{d^i(x_j)}{T_i} \right\}. \quad (7)$$

Similar strategies involving the utilization of an index or positional parameter as input for ANNs have been employed in previous studies. For instance, Bock et al. [18] utilized this approach to predict induced residual stress profiles following laser shock peening, while Huber and Tsakmakis [68] utilized a similar method to solve an inverse problem aimed at identifying material parameters related to viscoplastic behavior, yielding satisfactory prediction performance.

In total, the dimensionless input space derived from experimental data encompassed 52 experiments, discretized into 41 segments. Consequently, the total number of unique input/output pairs for the ANN amounts to 2132 (i.e., 52×41), representing the comprehensive dataset. This dataset is partitioned into training, validation, and testing subsets in a ratio of 70/15/15. Specifically, the ANN was trained using 1476 data pairs derived from 36 experiments spanning the design space. The validation and testing subsets each comprise 328 data pairs, originating from 16 experiments within the experimental design space.

In the numerical simulations conducted in this study, the main goal is to determine the correct value for the maximum pressure (P_{max}) of the applied pressure pulse (ref. section

3.3.2). Hence, the variables taken into account for the simulation of LPF remain the same, except for the laser energy (E_L) parameter. Instead of using the actual laser energy value, it is substituted with the equivalent value of the maximum pressure applied by the pressure pulse in the simulation. As a result, the dimensionless terms for the simulation parameters formulated using Buckingham's Pi theorem are:

$$\pi_1 = \frac{E}{P_{max}}, \pi_2 = n, \pi_3 = \frac{D}{T}, \pi_4 = \frac{T^2 \rho}{P_{max} \tau^2}, \pi_5 = \frac{A_f}{T^2}, \pi_6 = \frac{C\tau}{T}. \quad (8)$$

The output of the numerical simulations consists of the deformation within the treated region. This data is derived by extracting nodal coordinate deformation from the peened region post-simulation, mirroring the methodology proposed for deformation measurement in the experiments (see section 3.1.5). The deformation is quantified according to eq. 5.

The dimensionless data derived from 88 numerical simulations, results in 3608 unique input/output pairs (88×41 , as deformation is discretized into 41 segments). Thus the dimensionless inputs and outputs ($X_{sim}^{ij}, Y_{sim}^{ij}$) corresponding to the simulation data are formulated as:

$$X_{sim}^{ij} := \left\{ \frac{E}{P_{max}^i}, n_i, \frac{T_i^2 \rho}{P_{max}^i \tau^2}, \frac{A_f^i}{T_i^2}, \frac{C\tau}{T_i}, \frac{j}{41} \right\}, \quad (9)$$

whereas the output is defined as:

$$Y_{sim}^{ij} := \left\{ \frac{d^i(x_j)}{T_i} \right\}. \quad (10)$$

B Data-driven LPF process planning

The LPF process parameters for each discretized unit in every use case, as provided by the optimizer developed for LPF process planning, are summarized in the table below.

Table B1: List of LPF process parameters suggested by the optimizer for each discretized unit in the use case specimens [133]

| Use case | Number of discretized units | Discretized unit | Length of each discretization (mm) | Predicted process parameters by the trained ANN |
|----------|-----------------------------|---|------------------------------------|---|
| 1 | 8 | $\Delta D_1(x), \Delta D_2(x), \Delta D_3(x)$ | 10 | Unpeened region |
| | | $\Delta D_4(x)$ | 10 | $E_L = 1.9 \text{ J}, n = 2$ |
| | | $\Delta D_5(x)$ | 10 | $E_L = 2.4 \text{ J}, n = 4$ |
| | | $\Delta D_6(x)$ | 10 | $E_L = 2.2 \text{ J}, n = 3$ |
| | | $\Delta D_7(x)$ | 10 | $E_L = 2.1 \text{ J}, n = 3$ |
| | | $\Delta D_8(x)$ | 10 | Unpeened region |
| 2 | 4 | $\Delta D_1(x)$ | 30 | Unpeened region |
| | | $\Delta D_2(x)$ | 20 | $E_L = 2.0 \text{ J}, n = 4$ |
| | | $\Delta D_3(x)$ | 20 | $E_L = 1.8 \text{ J}, n = 3$ |
| | | $\Delta D_4(x)$ | 10 | Unpeened region |
| 3 | 2 | $\Delta D_1(x)$ | 10 | Unpeened region |
| | | $\Delta D_2(x)$ | 66 | $E_L = 2.0 \text{ J}, n = 3$ |
| 4 | 3 | $\Delta D_1(x)$ | 10 | Unpeened region |
| | | $\Delta D_2(x)$ | 40 | $E_L = 2.2 \text{ J}, n = 1$ |
| | | $\Delta D_3(x)$ | 25 | $E_L = 2.0 \text{ J}, n = 4$ |

C Simplified numerical model - Bayesian optimizer

To determine the appropriate stress value, one can envision an error function that depends on the initial stress value. Various approaches exist for finding the optimal stress value within this error function, with grid search being the simplest. Grid search involves trying every parameter combination to identify the value with the lowest error. However, this method is computationally expensive and time-consuming when running simulations.

Bayesian optimization offers a more efficient alternative for iteratively converging to the minimum error value compared to grid search. Bayesian optimization is favored for its ability to make minimal assumptions about the underlying error function, making it a versatile technique often referred to as a Black-Box optimizer. The fundamental principle of Bayesian optimization involves sampling a function where the optimizer is most confident of improvement to identify the parameter with the maximum score. With each sample added, the confidence distribution is reassessed using a probability distribution that encapsulates beliefs about the function's behavior. This approach is implemented to optimize the initial stress value of the simulation model by computing the MSE between the target height map and the height map from the simulation. It is implemented using the available open-source Python library [105]. The bounds of initial stress are defined to be in the range of -1000 MPa to 1000 MPa, which is within the limits of measured residual stresses of the LPF process [132].

As an exemplary case, the approach is tested with a height map obtained after a specimen is processed with laser energy of 2.7 J, with 4 peening sequences on a 1 mm thick Ti6Al4V sheet (see Fig. C.1). The objective is to ensure that the deformed sample from the FE simulation closely matches the one observed in the experiment. Utilizing height maps, the disparity in displacement between the two samples serves as a measure of error. The height map of the experimental sample is subtracted from the FE simulation, and the MSE is computed. This MSE value needs to be minimized by the Bayesian optimizer. The process involves the following steps:

1. Initially, an experimental sample is obtained, and a height map is generated from it.

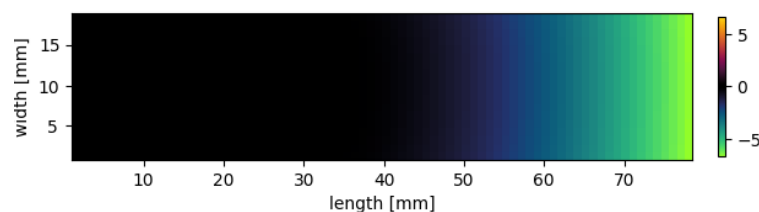


Fig. C.1: The average of height maps from four experimental samples is taken. Each sample had a thickness of 1 mm and underwent peening without a sacrificial layer, with four sequences at 2.7 J. The peen region measured 20 mm \times 40 mm.

2. A material model representing the experimental sample is created in ABAQUS (ref. section 2.4).
3. The Bayesian optimizer determines the initial stress value (320 MPa).
4. The model is simulated and converted into a mesh following the outlined procedure, and a height map is generated by sampling the mesh.
5. The MSE is calculated by comparing the height map obtained from the experiment with the one generated from the simulation. The optimizer then receives this result.

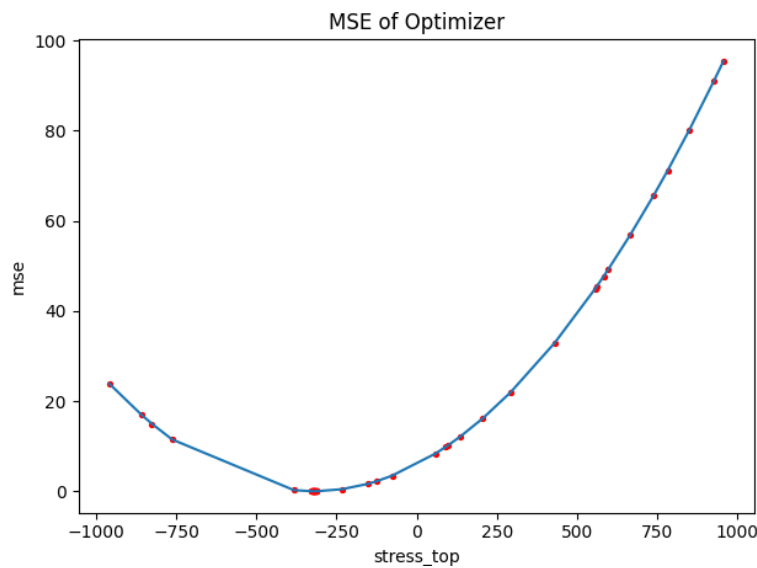


Fig. C.2: Bayesian optimization sampling to identify the minimum MSE across a range of initial top/surface stress values spanning from -1000 to 1000 MPa. The red dots are the FE simulations performed at different stress values.

6. The process is reiterated from step 3 until the minimum MSE is reached.

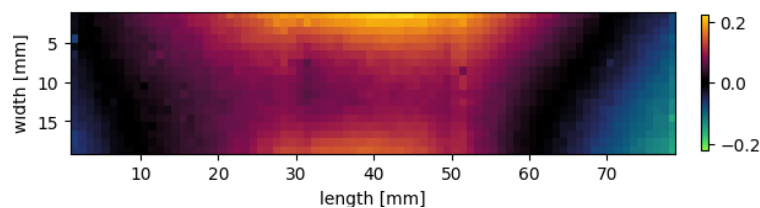


Fig. C.3: The computed difference between the height map from the experiment and the last iteration of the FE simulation. The MSE computed in this iteration of the Bayesian optimizer is 0.0076.

D Experimental 3D data acquisition after LPF

The analysis of deformation data from experiments is necessary to validate the numerical simulation models implemented in this study. The samples consist of Ti6Al4V alloy sheet metal, measuring 80 mm in length, 20 mm in width, and 1 mm in thickness (as shown below).

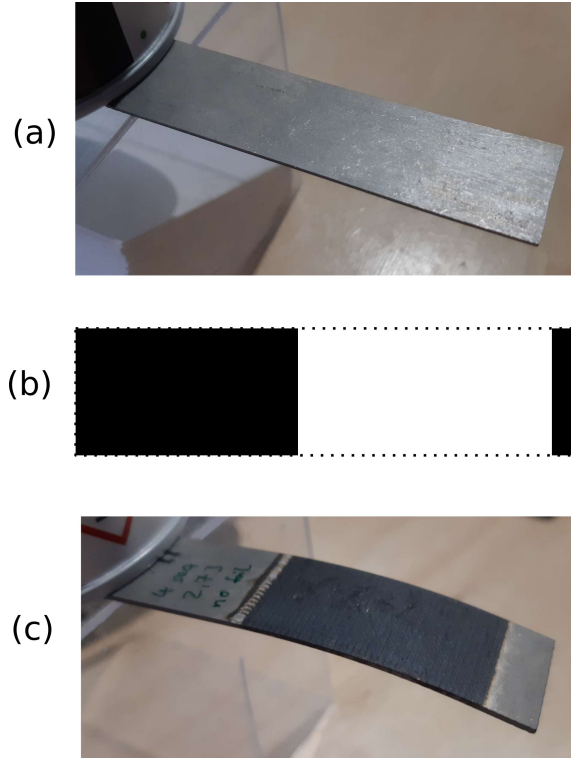


Fig. D.1: (a) A Ti6Al4V sample before peening; (b) Peening pattern indicated by white color representing the peened region; (c) Specimen post-LPF without protective overlay, exhibiting a black oxide layer formed on the treated region's surface. [83]

To enable digital post-processing techniques, the samples underwent digitization. The HandySCAN 3D, a 3D scanner, was employed for this purpose. The accompanying software facilitated the export of the scanned samples into a mesh .stl file with a resolution of 0.2 mm. Subsequently, in free open-source software called Meshlab [25], edges not part of the surface and scanning artifacts were meticulously cleaned. This cleanup process involved tasks such as deleting faces, closing holes, removing isolated pieces or self-intersecting faces, smoothing the surface, simplifying the mesh, and repairing non-manifold edges to ensure the integrity of subsequent processing steps. Both samples must be aligned within the same coordinate system for the digital FE model with the experimental results. The chosen coordinate system, as depicted in Fig. D.2, is based on the coordinate system utilized in the FE simulation and diverges from the coordinate system of the scanned mesh. In the scanned coordinate system, the origin is positioned at the center of the sample, with the bending direction oriented towards the y-axis.

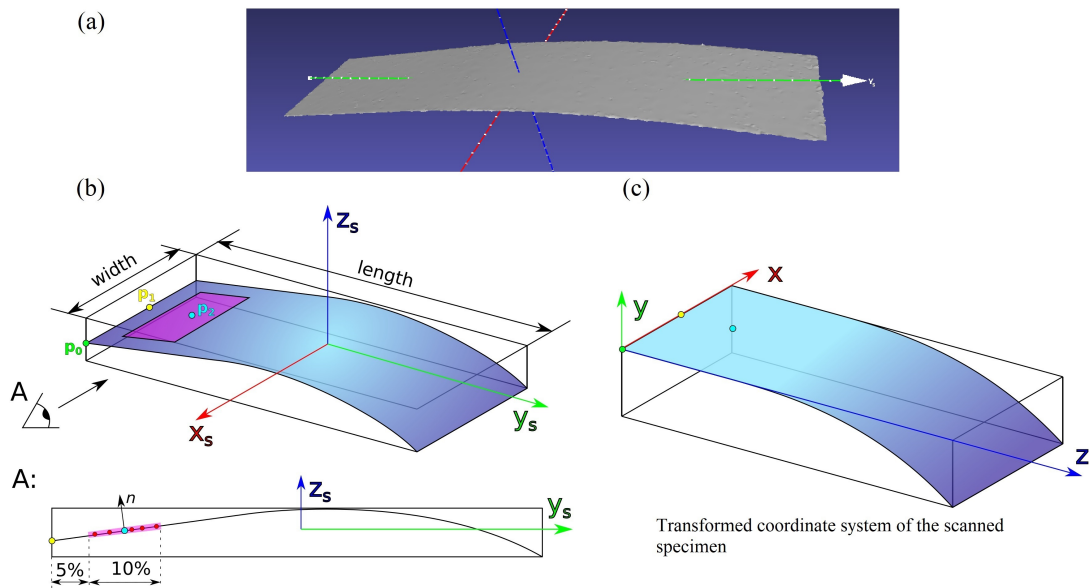


Fig. D.2: Transformation of the scanned coordinate system: (a) Coordinate system of the scanned sample after LPF (b) Coordinate transformation from scanned specimen to FE coordinate system [83]

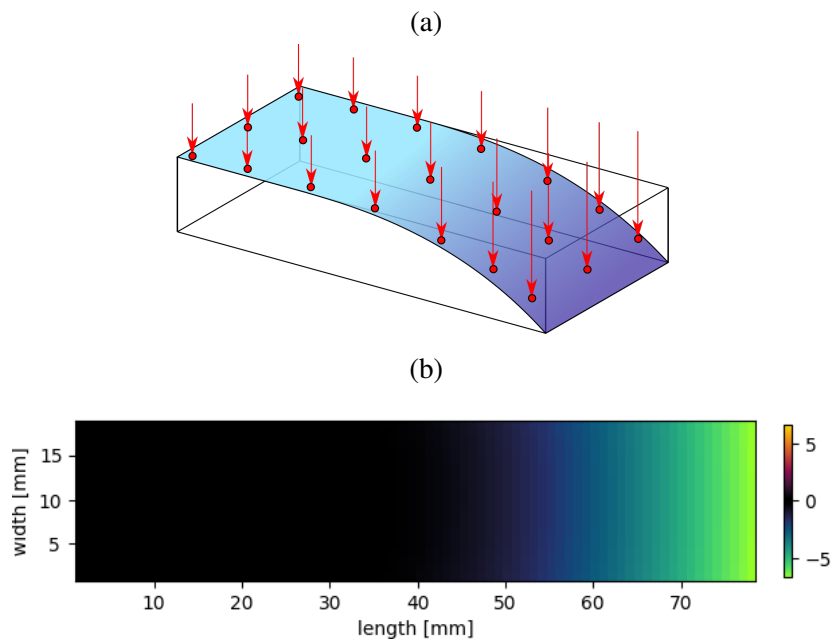


Fig. D.3: Computation of height map: (a) Illustration of map sampling visualization. Rays are projected from above the sample and intersect the surface. (b) Exemplary height map (after LPF with 2.7J, 4 peening sequences on 1 mm thick specimen), displaying the variations in surface height across the sample.[83]

The alignment process involves a coordinate transformation from the scanned (Fig. D.2(b)) to the FEA (Fig. D.2(c)) coordinate system. It is assumed that minimal deformation occurs near the clamping edge, referred to as the clamping plane. Vertices are sampled at the location where the sample was clamped, covering approximately 10% of the sample

length with a margin of about 5% (depicted by the purple area in Fig.D.2(b)). The median position (p_2) and median normal (n) of the clamping plane are calculated.

The position (p_1) is determined as the intersection of the clamping plane with the $X_s Z_s$ plane at the clamped edge of the sample. The origin (p_0) of the coordinate system of the sample is set to p_1 with X_s equal to the width divided by 2. The rotation from the measured to the FE simulation coordinate system is then accomplished using linear algebra techniques.

A heightmap can be generated by sampling the surface, as depicted below (see Fig. D.3(a)). Rays are projected from the top and intersected with the surface. The mesh must undergo proper cleaning, as outlined above, to ensure accurate ray intersections. Failure to clean the mesh may result in ray missing, leading to errors that this workflow is not designed to handle. Additionally, a margin of approximately 1 mm should be left around the edges to account for potential slight misalignment and imperfections in edge straightness. Extracting the z-coordinate of the intersection points provides the height map.

A curvature map is utilized to train a data-driven model, which is computed from the heightmap. The z-coordinates of the intersection points are sampled (see Fig. D.3(a)). By utilizing polynomials, it's possible to derive a piecewise function (spline) $y(x, z)$ from the heightmap. The curvature (κ) can be computed as:

$$\kappa = \frac{y''}{(1 + y'^2)^{3/2}} \quad (11)$$

In this study, y' can replace the partial derivatives y_x, y_z , and the total derivative $y_x + y_z$; while the second-order derivative y'' can stand for y_{xx}, y_{zz} , and $y_{xz} = y_{zx}$. Since mixed derivatives were not required for this study, 2D interpolation of the heightmap was not performed. Fig. D.4 shows an example of the curvature along the z-axis measured using the 3D scanner. The maps were typically supersampled, meaning there were more samples than pixels in the final map. This serves as a form of anti-aliasing.

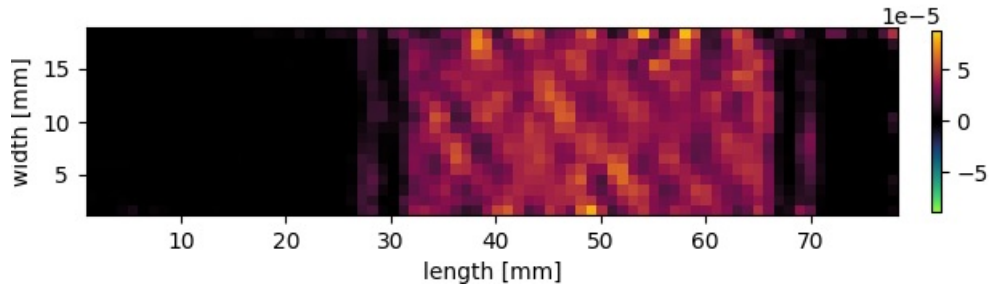


Fig. D.4: Computation of curvature map from the height map.[83]

E Numerical simulation of LPF - Effects of simulation parameters

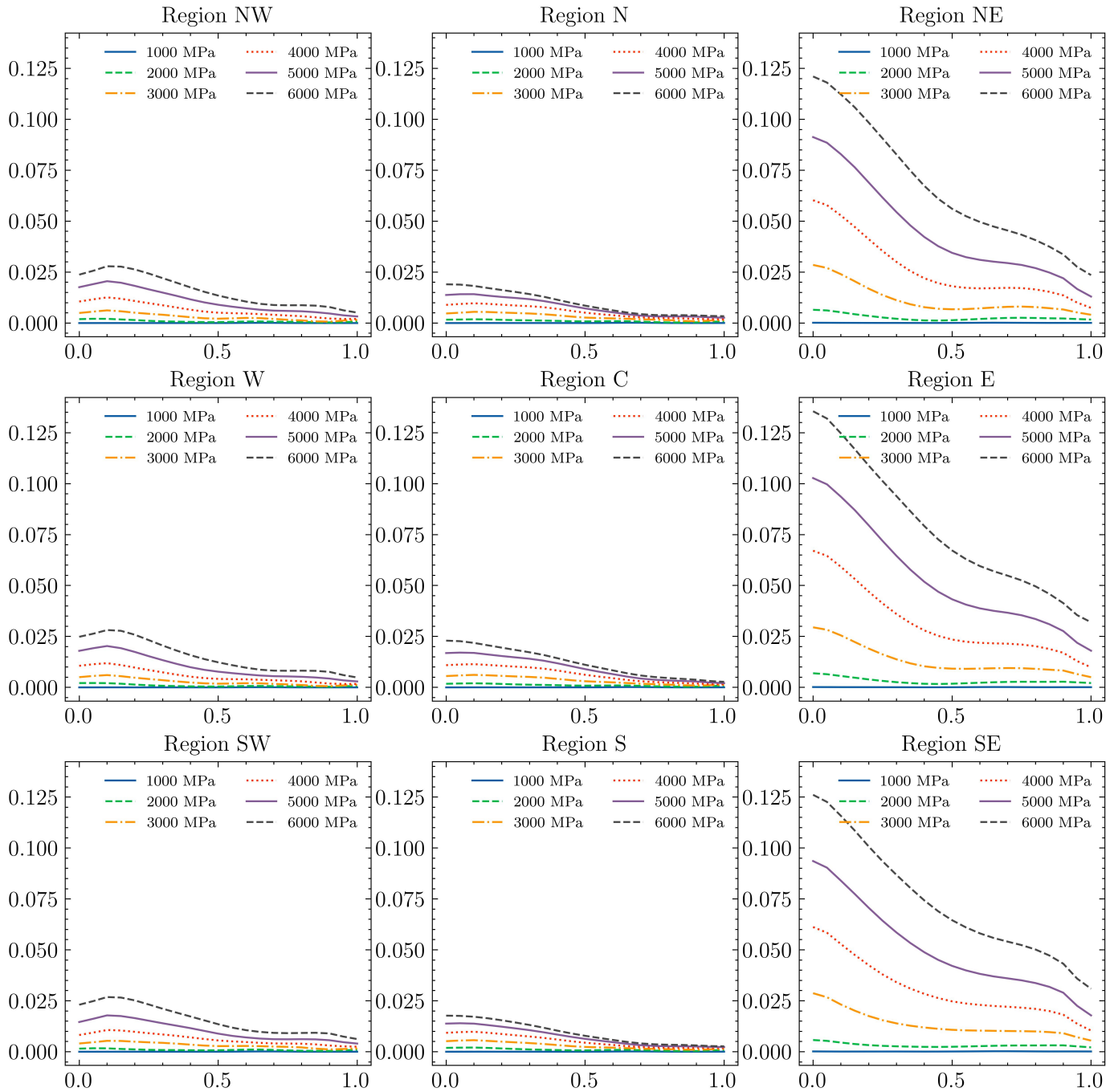


Fig. E.1: The plastic strain ϵ_{11} , resolved by depth and averaged across designated regions (N, E, W, S, NE, NW, SE, SW, and C), in the treated area of the source geometry at different values of maximum pressure (P_{max}) following four peening sequences.

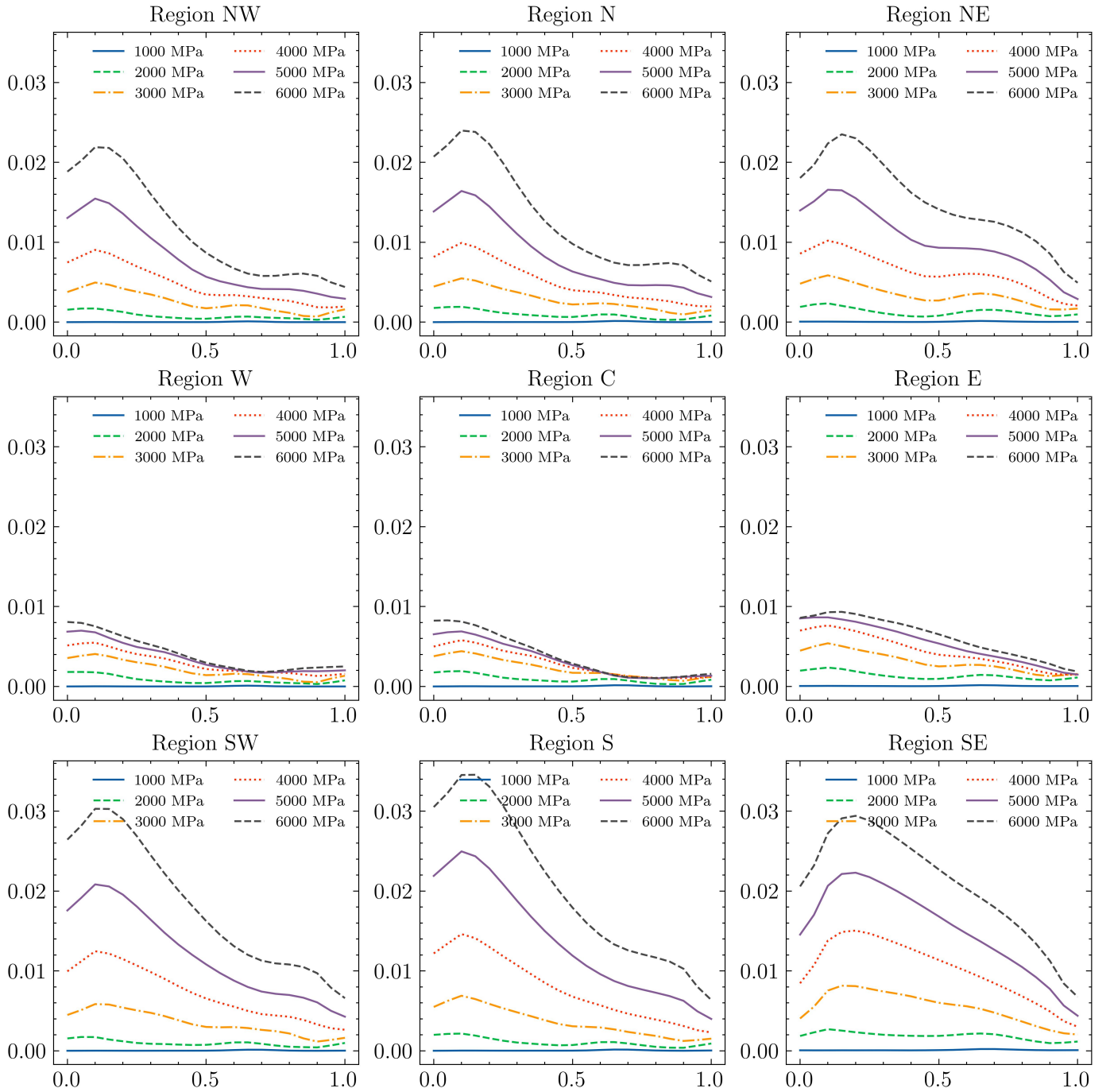


Fig. E.2: The plastic strain ε_{22} , resolved by depth and averaged across designated regions (N, E, W, S, NE, NW, SE, SW, and C), in the treated area of the source geometry at different values of maximum pressure (P_{max}) following four peening sequences.

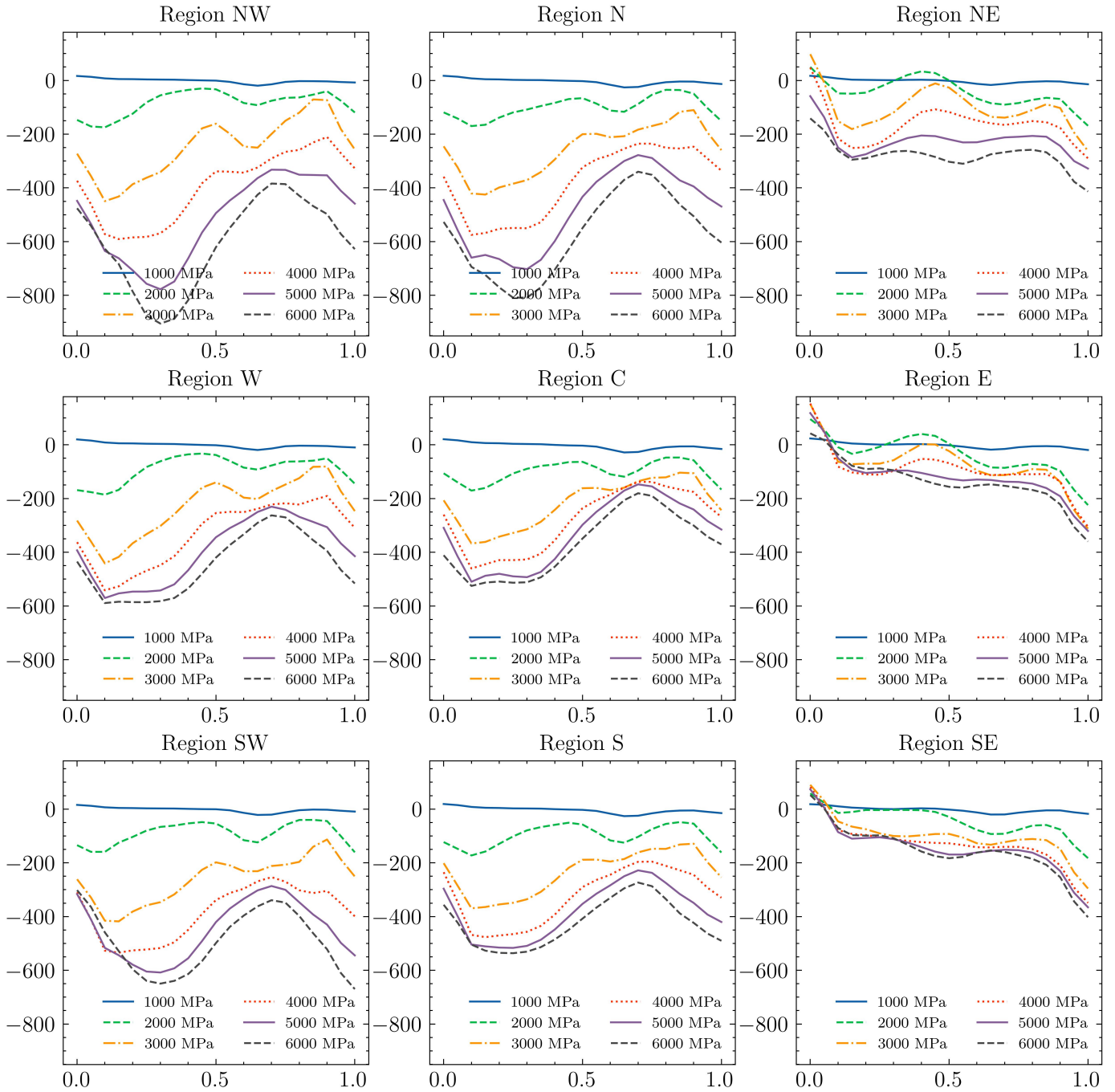


Fig. E.3: The residual stress σ_{11} , resolved by depth and averaged across designated regions (N, E, W, S, NE, NW, SE, SW, and C), in the treated area of the source geometry at different values of maximum pressure (P_{max}) following four peening sequences.

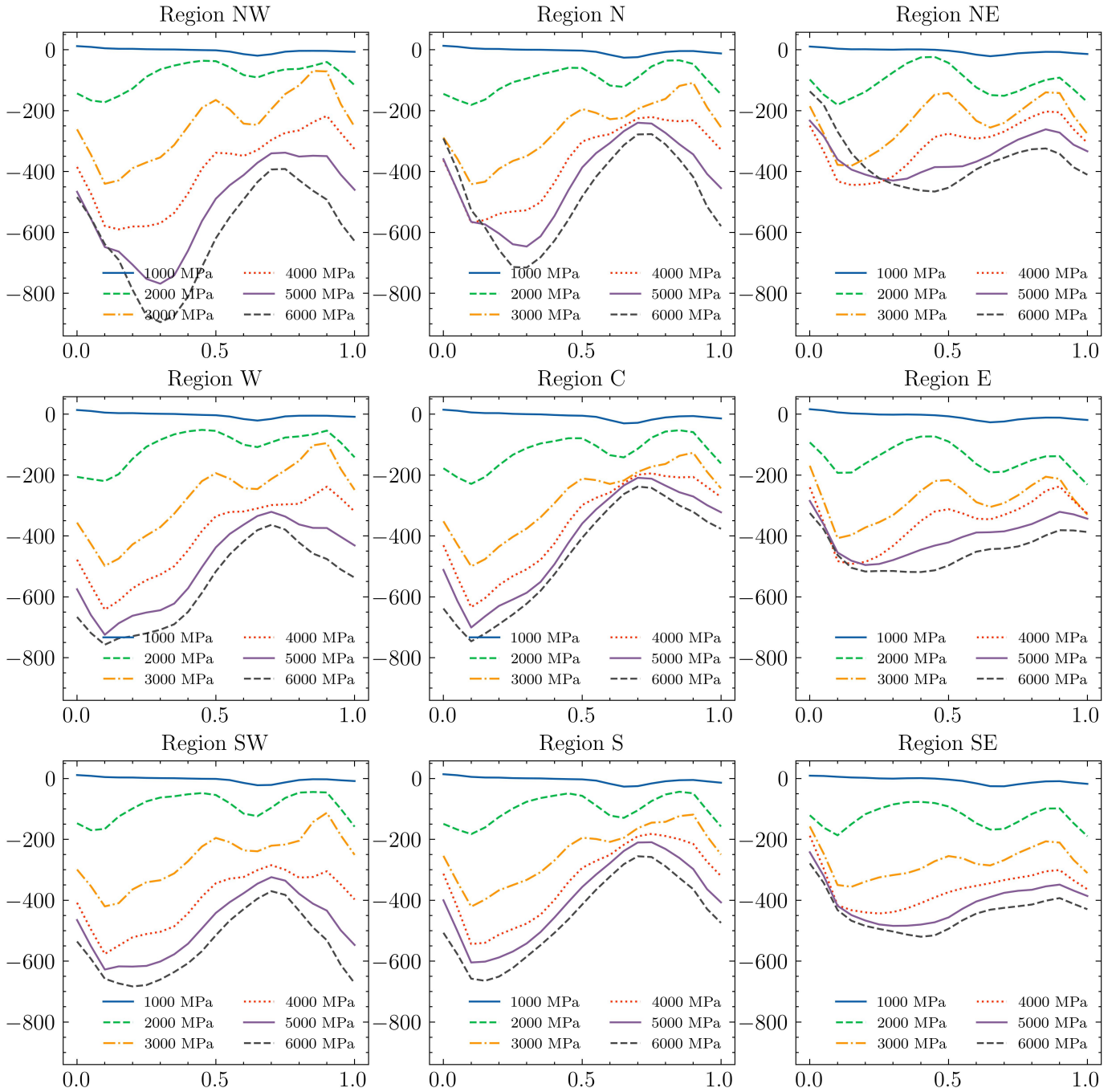


Fig. E.4: The residual stress σ_{22} , resolved by depth and averaged across designated regions (N, E, W, S, NE, NW, SE, SW, and C), in the treated area of the source geometry at different values of maximum pressure (P_{max}) following four peening sequences.

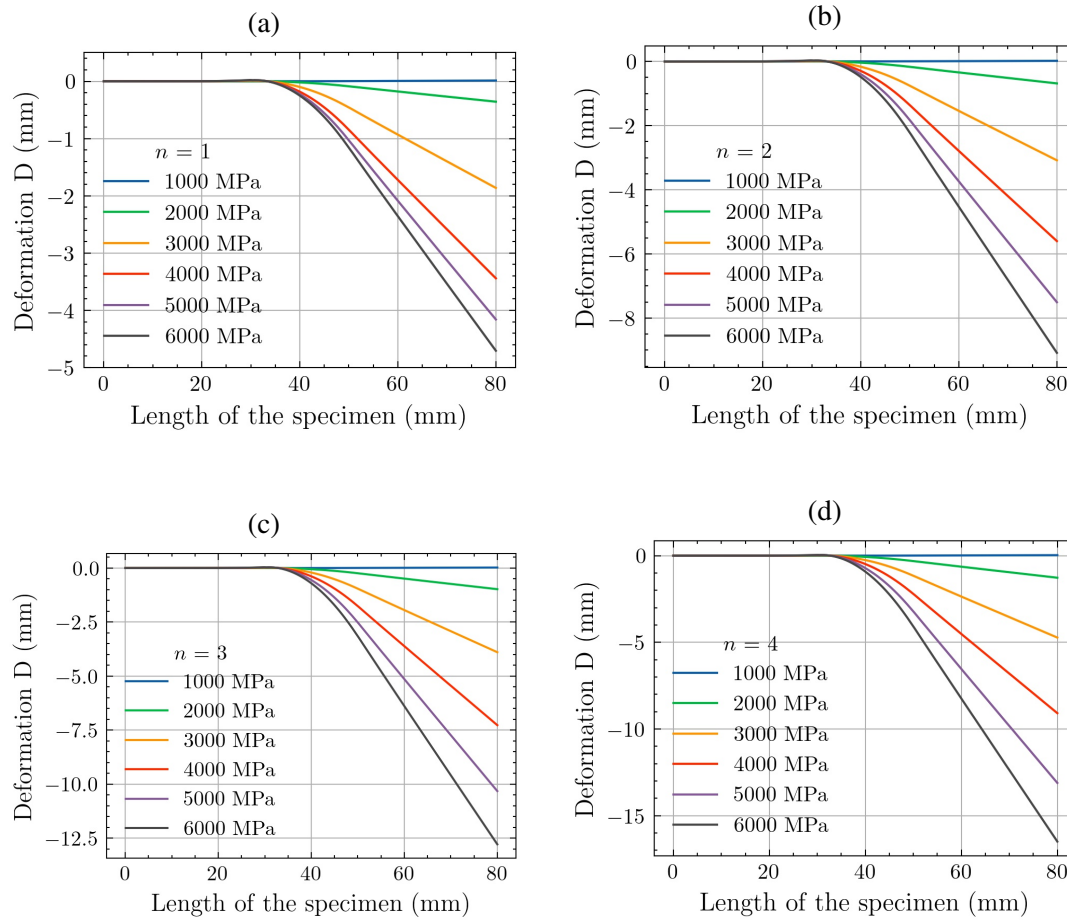


Fig. E.5: The deformation of 1 mm thick sheet of dimensions $80 \times 20 \text{ mm}^2$ subjected to different plasma pressure pulses with P_{max} from 1000 MPa and 6000 MPa with peening sequences (n) (a) 1, (b) 2, (c) 3, and (d) 4.

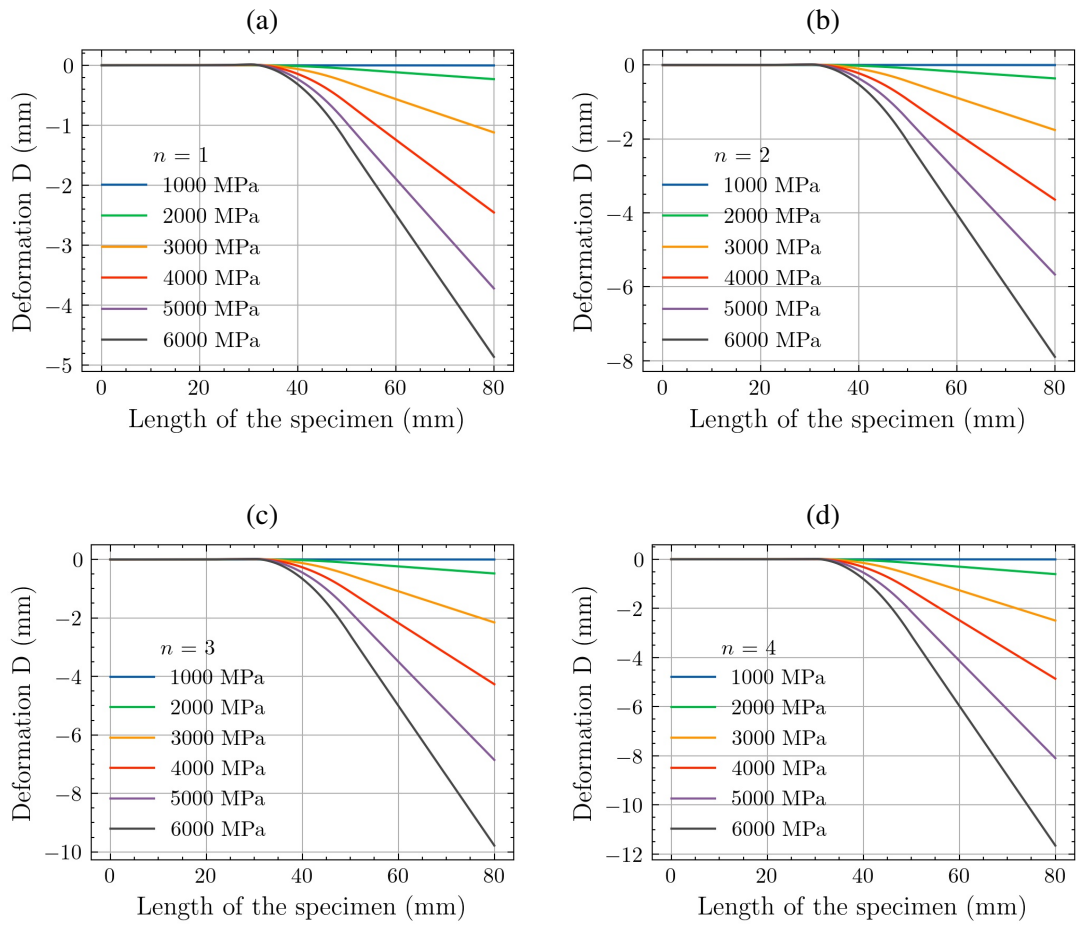


Fig. E.6: The deformation of 2 mm thick sheet of dimensions $80 \times 20 \text{ mm}^2$ subjected to different plasma pressure pulses with P_{max} from 1000 MPa and 6000 MPa with peening sequences (n) (a) 1, (b) 2, (c) 3, and (d) 4.

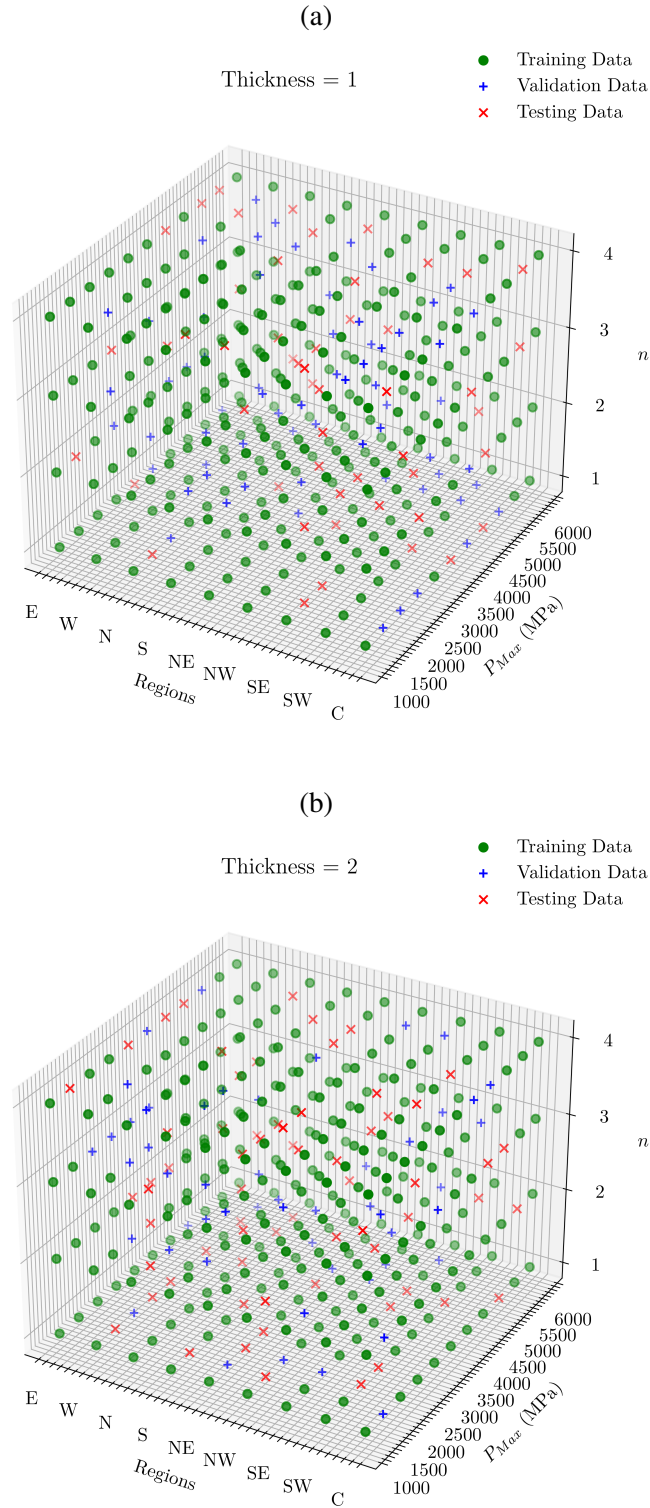
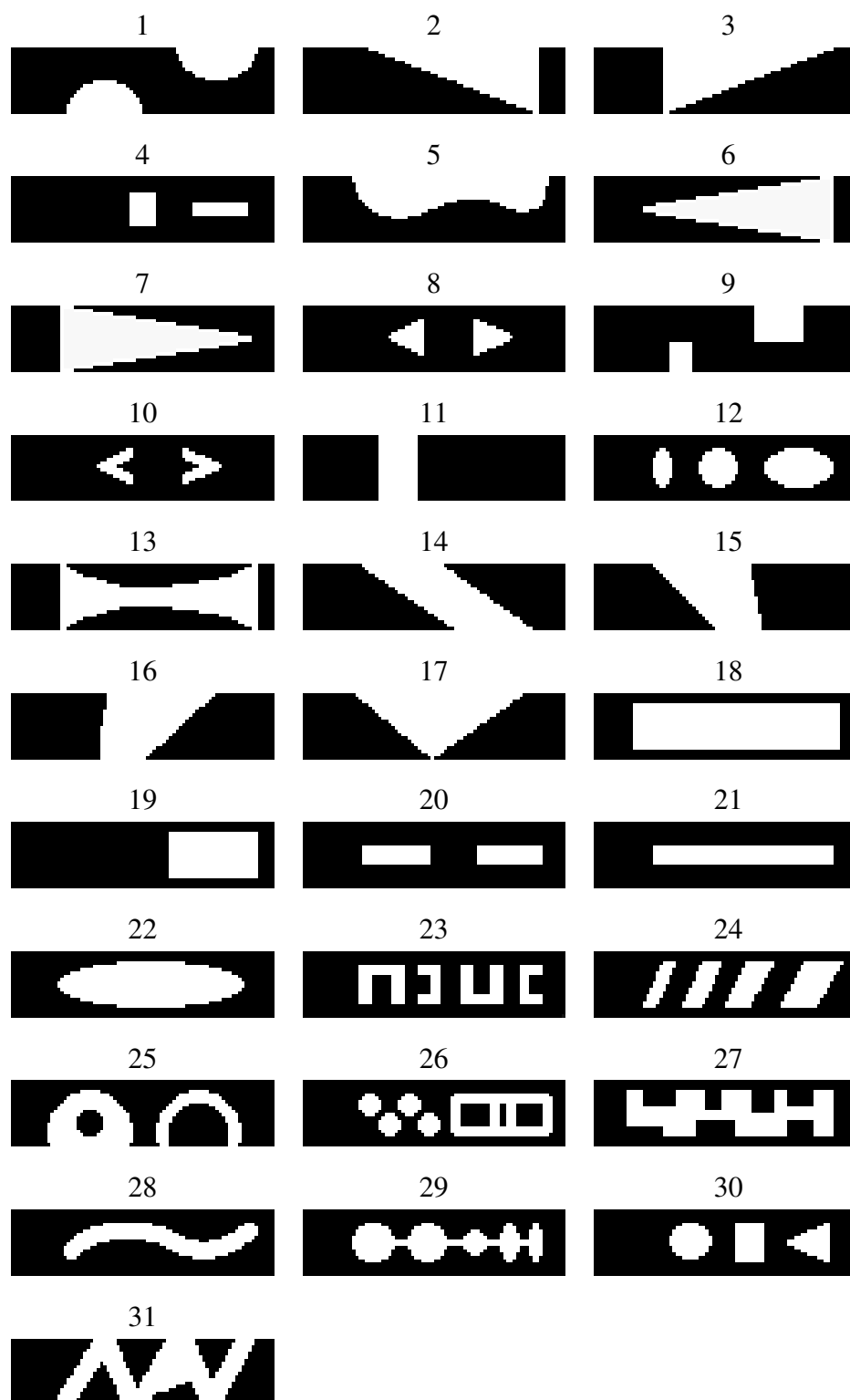


Fig. E.7: The datasets correspond to the explicit numerical simulations performed to determine the depth-resolved eigenstrains for different values of the equivalent LPF simulation pressure pulse parameters on the source geometry at different regions with a thickness of (a) 1 mm, and (b) 2 mm.

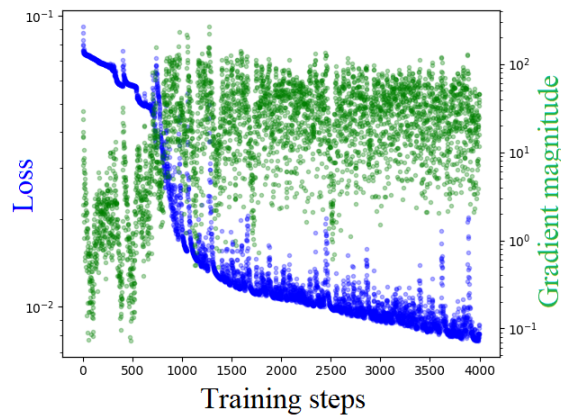
F Implementation of CANN

Table F1: Peening patterns resembling actual LPF specimens of dimensions $80 \times 20 \text{ mm}^2$ used to train the CANN



When using ANNs, the sigmoid activation function is commonly employed. However, since sigmoid functions tend to saturate at input values far from 0, data scaling and shifting are often necessary to facilitate convergence, aiming for a mean of 0 and a variance of about 1. In this work, the ReLU activation function is chosen due to its better performance in providing nonlinear behavior. The curvature data in this context has values on the order of 10^{-5} . Initially, it was believed that ReLU could eliminate the need for scaling through training the bias and weights. However, it was found that this approach significantly slows down convergence, likely because the initialized weights and biases range from -1 to 1, which is much larger than necessary if the data isn't scaled. By scaling the curvature values by a factor of 10^5 before training, the convergence rate improved significantly. Notably, it took approximately 2500 training steps without scaling, compared to only 100 with scaling, to achieve a loss of 10^{-2} .

(a)



(b)

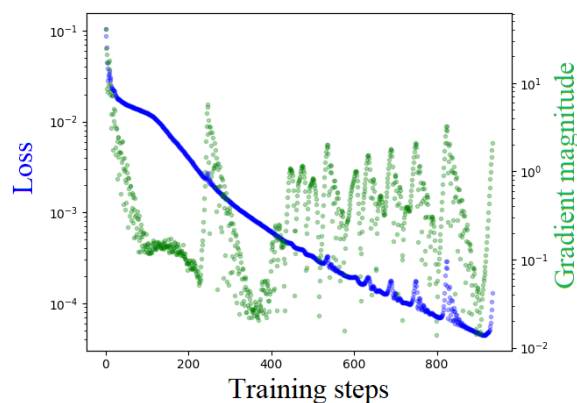


Fig. F.1: Training loss (a) without and (b) with scaled curvature data

The training of CNN in batches is common due to size and hardware constraints. A batch size of 1 can hinder finding the global minimum since it doesn't represent the entire dataset, causing the optimizer to lose direction. Conversely, very large batches can get

stuck in local minima [76]. Smaller batch sizes strike a balance by encouraging exploration and providing more general solutions without committing to a specific path. The batch size is varied during the training of CNN present work (as illustrated in Fig. F.2), it is observed that a higher batch size spreads the loss and the gradient during training, while a lower batch size leads to the spread of the gradient magnitude while the loss is lower, which could result in over-fitting.

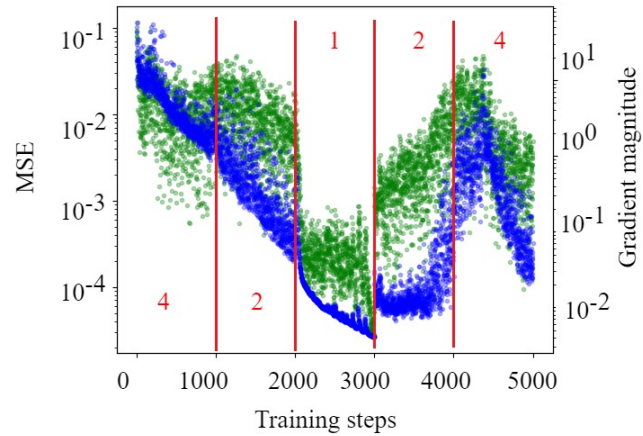


Fig. F.2: The influence of batch size during the training. The blue dots indicate the loss and the green dots indicate the change in magnitude of the gradient. The red numbers indicate the batch sizes.

References

- [1] Abbassi, F., Belhadj, T., Mistou, S., and Zghal, A. (2013). Parameter identification of a mechanical ductile damage using artificial neural networks in sheet metal forming. *Materials & Design*, 45:605–615.
- [2] Achintha, M. and Nowell, D. (2011). Eigenstrain modelling of residual stresses generated by laser shock peening. *Journal of Materials Processing Technology*, 211(6):1091–1101.
- [3] Achintha, M. and Nowell, D. (2014). Residual stress in geometric features subjected to laser shock peening. *Proceedings of the Institution of Mechanical Engineers, Part C: Journal of Mechanical Engineering Science*, 229(11):1923–1938.
- [4] Aguir, H., BelHadjSalah, H., and Hambli, R. (2011). Parameter identification of an elasto-plastic behaviour using artificial neural networks–genetic algorithm method. *Materials & Design*, 32(1):48–53.
- [5] Ahsan, M., Mahmud, M., Saha, P., Gupta, K., and Siddique, Z. (2021). Effect of data scaling methods on machine learning algorithms and model performance. *Technologies*, 9(3):52.
- [6] Amarchinta, H. K., Grandhi, R. V., Langer, K., and Stargel, D. S. (2008). Material model validation for laser shock peening process simulation. *Modelling and Simulation in Materials Science and Engineering*, 17(1):015010.
- [7] Antony, J. (2014). Full factorial designs. In *Design of Experiments for Engineers and Scientists*, pages 63–85. Elsevier.
- [8] Badr, O. M., Rolfe, B., Hodgson, P., and Weiss, M. (2015). Forming of high strength titanium sheet at room temperature. *Materials & Design*, 66:618–626.
- [9] Bakarji, J., Callaham, J., Brunton, S. L., and Kutz, J. N. (2022). Dimensionally consistent learning with buckingham pi.

- [10] Bałon, P., Rejman, E., Świątoniowski, A., Kielbasa, B., Smusz, R., Szostak, J., Cieślak, J., and Kowalski, Ł. (2020). Thin-walled integral constructions in aircraft industry. *Procedia Manufacturing*, 47:498–504.
- [11] Banabic, D. (2000). Forming limits of sheet metal. In *Formability of Metallic Materials*, pages 173–214. Springer Berlin Heidelberg.
- [12] Bao, Y., Wang, B., He, Z., Kang, R., and Guo, J. (2022). Recent progress in flexible supporting technology for aerospace thin-walled parts: A review. *Chinese Journal of Aeronautics*, 35(3):10–26.
- [13] Barralis, J. and Castex, L. (1990). Improvement of fatigue resistance of steel parts after various surface treatments. In *Surface Engineering*, pages 625–639. Springer Netherlands.
- [14] Baughman, D. (1984). An overview of peen forming technology. pages 28–33. Conf Proc: ICSP-2, Chicago, IL, USA.
- [15] Bellman, R. (1966). Dynamic programming. *Science*, 153(3731):34–37.
- [16] Berthe, L., Fabbro, R., Peyre, P., and Bartnicki, E. (1999). Wavelength dependent of laser shock-wave generation in the water-confinement regime. *Journal of Applied Physics*, 85(11):7552–7555.
- [17] Berthe, L., Fabbro, R., Peyre, P., Tollier, L., and Bartnicki, E. (1997). Shock waves from a water-confined laser-generated plasma. *Journal of Applied Physics*, 82(6):2826–2832.
- [18] Bock, F. E., Keller, S., Huber, N., and Klusemann, B. (2021). Hybrid modelling by machine learning corrections of analytical model predictions towards high-fidelity simulation solutions. *Materials*, 14(8):1883.
- [19] Box, G. E., Hunter, W. G., and Hunter, J. S. (1978). *Statistics for Experimenters*. John Wiley & Sons, Inc., New York.
- [20] Bras, C. L., Rondepierre, A., Seddik, R., Scius-Bertrand, M., Rouchousse, Y., Videau, L., Fayolle, B., Gervais, M., Morin, L., Valadon, S., Ecault, R., Furfari, D., and Berthe, L. (2019). Laser shock peening: Toward the use of pliable solid polymers for confinement. *Metals*, 9(7):793.
- [21] Brockman, R. A., Braisted, W. R., Olson, S. E., Tenaglia, R. D., Clauer, A. H., Langer, K., and Shepard, M. J. (2012). Prediction and characterization of residual stresses from laser shock peening. *International Journal of Fatigue*, 36(1):96–108.

- [22] Chamekh, A., Salah, H. B. H., and Hambli, R. (2008). Inverse technique identification of material parameters using finite element and neural network computation. *The International Journal of Advanced Manufacturing Technology*, 44(1-2):173–179.
- [23] Chernov, N. and Lesort, C. (2003). Least squares fitting of circles and lines.
- [24] Chollet, F. et al. (2015). Keras. <https://keras.io>.
- [25] Cignoni, P., Callieri, M., Corsini, M., Dellepiane, M., Ganovelli, F., and Ranzuglia, G. (2008). MeshLab: an Open-Source Mesh Processing Tool. In Scarano, V., Chiara, R. D., and Erra, U., editors, *Eurographics Italian Chapter Conference*. The Eurographics Association.
- [26] Clauer, A. H., Holbrook, J. H., and Fairand, B. P. (1981). Effects of laser induced shock waves on metals. In *Shock Waves and High-Strain-Rate Phenomena in Metals*. Springer US.
- [27] Cooper, D. R., Rossie, K. E., and Gutowski, T. G. (2016). An environmental and cost analysis of stamping sheet metal parts. *Journal of Manufacturing Science and Engineering*, 139(4).
- [28] Couturier, S., de Rességuier, T., Hallouin, M., Romain, J. P., and Bauer, F. (1996). Shock profile induced by short laser pulses. *Journal of Applied Physics*, 79(12):9338–9342.
- [29] Dai, F. Z., Zhang, Z. D., Zhou, J. Z., Lu, J. Z., and Zhang, Y. K. (2016). Analysis of surface roughness at overlapping laser shock peening. *Surf. Rev. Lett.*, 23(03):1650012.
- [30] Devaux, D., Fabbro, R., Tollier, L., and Bartnicki, E. (1993). Generation of shock waves by laser-induced plasma in confined geometry. *Journal of Applied Physics*, 74(4):2268–2273.
- [31] Devaux, D., Fabbro, R., and Virmont, J. (1991). Generation of shock waves by laser-matter interaction in confined geometries. *Le Journal de Physique IV*, 01(C7):C7–179–C7–182.
- [32] Dib, M., Ribeiro, B., and Prates, P. (2018). Model prediction of defects in sheet metal forming processes. In *Engineering Applications of Neural Networks*, pages 169–180. Springer International Publishing.
- [33] Dib, M. A., Oliveira, N. J., Marques, A. E., Oliveira, M. C., Fernandes, J. V., Ribeiro, B. M., and Prates, P. A. (2019). Single and ensemble classifiers for defect prediction in sheet metal forming under variability. *Neural Computing and Applications*, 32(16):12335–12349.

- [34] Ding, H., Shen, N., Li, K., Bo, W., Pence, C. N., and Ding, H. (2014). Experimental and numerical analysis of laser peen forming mechanisms of sheet metal. In *Volume 2: Processing*. American Society of Mechanical Engineers.
- [35] Domingos, P. (2012). A few useful things to know about machine learning. *Communications of the ACM*, 55(10):78–87.
- [36] Fabbro, R., Fournier, J., Ballard, P., Devaux, D., and Virmont, J. (1990). Physical study of laser-produced plasma in confined geometry. *Journal of Applied Physics*, 68(2):775–784.
- [37] Fabbro, R., Peyre, P., Berthe, L., and Scherpereel, X. (1998). Physics and applications of laser-shock processing. *Journal of Laser Applications*, 10(6):265–279.
- [38] Fairand, B. and Clauer, A. (1976). Effect of water and paint coatings on the magnitude of laser-generated shocks. *Optics Communications*, 18(4):588–591.
- [39] Fauchaux, P. A., Gosselin, F. P., and Lévesque, M. (2018). Simulating shot peen forming with eigenstrains. *Journal of Materials Processing Technology*, 254:135–144.
- [40] Fetene, B. N., Shufen, R., and Dixit, U. S. (2016). FEM-based neural network modeling of laser-assisted bending. *Neural Computing and Applications*, 29(6):69–82.
- [41] Friese, A., Lohmar, J., and Wustefeld, F. (2002). Current applications of advanced peen forming implementation. pages 16–20. Conf Proc: ICSP-8, Garmisch-Partenkirchen, Germany.
- [42] Friese, A., Lohmar, J., and Wüstefeld, F. (2006). Current applications of advanced peen forming implementation. In *Shot Peening*, pages 53–61. Wiley-VCH Verlag GmbH & Co. KGaA.
- [43] Fu, Z., Mo, J., Chen, L., and Chen, W. (2010). Using genetic algorithm-back propagation neural network prediction and finite-element model simulation to optimize the process of multiple-step incremental air-bending forming of sheet metal. *Materials & Design*, 31(1):267–277.
- [44] Gariépy, A., Miao, H., and Lévesque, M. (2014). Peen forming. In *Comprehensive Materials Processing*, pages 295–329. Elsevier.
- [45] Geiger, M. (1994). Synergy of laser material processing and metal forming. *CIRP Annals*, 43(2):563–570.
- [46] Geiger, M. and Vollertsen, F. (1993). The mechanisms of laser forming. *CIRP Annals*, 42(1):301–304.

- [47] Gill, A. S., Telang, A., and Vasudevan, V. K. (2015). Characteristics of surface layers formed on Inconel 718 by laser shock peening with and without a protective coating. *J. Mater. Process. Technol.*, 225:463–472.
- [48] Gisario, A., Barletta, M., Conti, C., and Guarino, S. (2011). Springback control in sheet metal bending by laser-assisted bending: Experimental analysis, empirical and neural network modelling. *Optics and Lasers in Engineering*, 49(12):1372–1383.
- [49] Google (2023). Neural CA from scratch - YouTube.
- [50] Gujba, A. and Medraj, M. (2014). Laser peening process and its impact on materials properties in comparison with shot peening and ultrasonic impact peening. *Materials*, 7(12):7925–7974.
- [51] Guo, Z. and Tang, W. (2017). Bending angle prediction model based on BPNN-spline in air bending springback process. *Mathematical Problems in Engineering*, 2017:1–11.
- [52] Hamouche, E. and Loukaides, E. G. (2018). Classification and selection of sheet forming processes with machine learning. *International Journal of Computer Integrated Manufacturing*, 31(9):921–932.
- [53] Hao, Z., Li, Z., Ren, F., Lv, S., and Ni, H. (2022). Strip steel surface defects classification based on generative adversarial network and attention mechanism. *Metals*, 12(2):311.
- [54] Hartmann, C., Opriteanu, D., and Volk, W. (2016). An artificial neural network approach for tool path generation in incremental sheet metal free-forming. *Journal of Intelligent Manufacturing*, 30(2):757–770.
- [55] Hong, X., Wang, S., Guo, D., Wu, H., Wang, J., Dai, Y., Xia, X., and Xie, Y. (1998). Confining medium and absorptive overlay. *Optics and Lasers in Engineering*, 29(6):447–455.
- [56] Hsu, C.-W., Ulsoy, A., and Demeri, M. (2002). Development of process control in sheet metal forming. *Journal of Materials Processing Technology*, 127(3):361–368.
- [57] Hu, Yongxiang, L., Mingsheng, H., Lan, J., and Zhenqiang (2020a). Efficient process planning of laser peen forming for complex shaping with distributed eigen-moment. *Journal of Materials Processing Technology*, 279:116588.
- [58] Hu, Y. and Grandhi, R. V. (2012). Efficient numerical prediction of residual stress and deformation for large-scale laser shock processing using the eigenstrain methodology. *Surface and Coatings Technology*, 206(15):3374–3385.

- [59] Hu, Y., Han, Y., Yao, Z., and Hu, J. (2010a). Three-dimensional numerical simulation and experimental study of sheet metal bending by laser peen forming. *Journal of Manufacturing Science and Engineering*, 132(6).
- [60] Hu, Y., Luo, M., Hu, L., and Yao, Z. (2020b). Efficient process planning of laser peen forming for complex shaping with distributed eigen-moment. *Journal of Materials Processing Technology*, 279:116588.
- [61] Hu, Y., Luo, M., and Yao, Z. (2016a). Increasing the capability of laser peen forming to bend titanium alloy sheets with laser-assisted local heating. *Materials and Design*, 90:364–372.
- [62] Hu, Y., Xie, Y., Wu, D., and Yao, Z. (2019). Quantitative evaluation of specimen geometry effect on bending deformation of laser peen forming. *International Journal of Mechanical Sciences*, 150:404–410.
- [63] Hu, Y., Xu, X., Yao, Z., and Hu, J. (2010b). Laser peen forming induced two way bending of thin sheet metals and its mechanisms. *Journal of Applied Physics*, 108(7):073117.
- [64] Hu, Y. and Yao, Z. (2008). FEM simulation of residual stresses induced by laser shock with overlapping laser spots. *Acta Metallurgica Sinica (English Letters)*, 21(2):125–132.
- [65] Hu, Y., Zhang, Z., and Yao, Z. (2016b). Shape prediction for laser peen forming of fiber metal laminates by experimentally determined eigenstrain. *Journal of Manufacturing Science and Engineering*, 139(4).
- [66] Hu, Y., Zheng, X., Wang, D., Zhang, Z., Xie, Y., and Yao, Z. (2015). Application of laser peen forming to bend fibre metal laminates by high dynamic loading. *Journal of Materials Processing Technology*, 226:32–39.
- [67] Huber, N., Nix, W. D., and Gao, H. (2002). Identification of elastic-plastic material parameters from pyramidal indentation of thin films. *Proceedings of the Royal Society of London. Series A: Mathematical, Physical and Engineering Sciences*, 458(2023):1593–1620.
- [68] Huber, N. and Tsakmakis, C. (2001). A neural network tool for identifying the material parameters of a finite deformation viscoplasticity model with static recovery. *Computer Methods in Applied Mechanics and Engineering*, 191(3-5):353–384.
- [69] Inamdar, M., Date, P., and Desai, U. (2000). Studies on the prediction of springback in air vee bending of metallic sheets using an artificial neural network. *Journal of Materials Processing Technology*, 108(1):45–54.

- [70] Jackson, M. (2011). Superplastic forming and diffusion bonding of titanium alloys. In *Superplastic Forming of Advanced Metallic Materials*, pages 227–246. Elsevier.
- [71] Jaremenko, C., Huang, X., Affronti, E., Merklein, M., and Maier, A. (2017). Sheet metal forming limits as classification problem. In *2017 Fifteenth IAPR International Conference on Machine Vision Applications (MVA)*. IEEE.
- [72] Karam, M. and Saad, T. (2021). BuckinghamPy: A python software for dimensional analysis. *SoftwareX*, 16:100851.
- [73] Kateb, Y., Khebli, A., and Meglouli, H. (2024). Classification of surface defects in steel sheets using developed nasnet-mobile cnn and few samples. *Revue d'Intelligence Artificielle*, 38(2):681–691.
- [74] Keller, S. (2021). *Fatigue crack growth retardation by laser shock peening – a combined experimental numerical investigation*. PhD thesis, Leuphana Universität Lüneburg.
- [75] Keller, S., Chupakhin, S., Staron, P., Maawad, E., Kashaev, N., and Klusemann, B. (2018). Experimental and numerical investigation of residual stresses in laser shock peened AA2198. *Journal of Materials Processing Technology*, 255:294–307.
- [76] Keskar, N. S., Mudigere, D., Nocedal, J., Smelyanskiy, M., and Tang, P. T. P. (2016). On large-batch training for deep learning: Generalization gap and sharp minima.
- [77] Kim, T. and Yang, D. (2000). Improvement of formability for the incremental sheet metal forming process. *International Journal of Mechanical Sciences*, 42(7):1271–1286.
- [78] Kingma, D. P. and Ba, J. (2014). Adam: A method for stochastic optimization.
- [79] Kirkpatrick, J., Pascanu, R., Rabinowitz, N., Veness, J., Desjardins, G., Rusu, A. A., Milan, K., Quan, J., Ramalho, T., Grabska-Barwinska, A., Hassabis, D., Clopath, C., Kumaran, D., and Hadsell, R. (2016). Overcoming catastrophic forgetting in neural networks.
- [80] Klocke, F. (2013). *Manufacturing Processes 4*. Springer Berlin Heidelberg.
- [81] Kohler, G. and Martin, R. (1979). Automatisiertes justieren in der feinwerktechnik.
- [82] Kopp, R. and Schulz, J. (2003). Optimising the double-sided simultaneous shot peen forming. In *8th International Conference on Shot Peening. Garmisch-Partenkirchen, Germany.*, pages 227–233. Wiley Online Library.

- [83] Körner, R. (2023). Prediction of a required pattern for laser peen forming of a pre-defined target geometry using numerical simulation, Master's thesis submitted at the Hamburg University of Technology, Hamburg, Germany.
- [84] Kubik, C., Knauer, S. M., and Groche, P. (2021). Smart sheet metal forming: importance of data acquisition, preprocessing and transformation on the performance of a multiclass support vector machine for predicting wear states during blanking. *Journal of Intelligent Manufacturing*, 33(1):259–282.
- [85] Kumar, N., Rajagopalan, P., Pankajakshan, P., Bhattacharyya, A., Sanyal, S., Balachandran, J., and Waghmare, U. V. (2018). Machine learning constrained with dimensional analysis and scaling laws: Simple, transferable, and interpretable models of materials from small datasets. *Chemistry of Materials*, 31(2):314–321.
- [86] Lee, D. S., Fahey, D. W., Forster, P. M., Newton, P. J., Wit, R. C., Lim, L. L., Owen, B., and Sausen, R. (2009). Aviation and global climate change in the 21st century. *Atmospheric Environment*, 43(22-23):3520–3537.
- [87] Lee, W.-S. and Lin, C.-F. (1998). High-temperature deformation behaviour of ti6al4v alloy evaluated by high strain-rate compression tests. *Journal of Materials Processing Technology*, 75(1-3):127–136.
- [88] Liewald, M., Bergs, T., Groche, P., Behrens, B.-A., Briesenick, D., Müller, M., Niemietz, P., Kubik, C., and Müller, F. (2022). Perspectives on data-driven models and its potentials in metal forming and blanking technologies. *Production Engineering*, 16(5):607–625.
- [89] Liewald, M., Karadogan, C., Lindemann, B., Jazdi, N., and Weyrich, M. (2018). On the tracking of individual workpieces in hot forging plants. *CIRP Journal of Manufacturing Science and Technology*, 22:116–120.
- [90] Liu, W., Liu, Q., Ruan, F., Liang, Z., and Qiu, H. (2007). Springback prediction for sheet metal forming based on GA-ANN technology. *Journal of Materials Processing Technology*, 187-188:227–231.
- [91] Low, D. W. W., Chaudhari, A., Kumar, D., and Kumar, A. S. (2022). Convolutional neural networks for prediction of geometrical errors in incremental sheet metal forming. *Journal of Intelligent Manufacturing*, 34(5):2373–2386.
- [92] Loyola-Gonzalez, O. (2019). Black-box vs. white-box: Understanding their advantages and weaknesses from a practical point of view. *IEEE Access*, 7:154096–154113.

- [93] Lu, J., Qi, H., Luo, K., Luo, M., and Cheng, X. (2014). Corrosion behaviour of AISI 304 stainless steel subjected to massive laser shock peening impacts with different pulse energies. *Corrosion Science*, 80:53–59.
- [94] Luo, K., Lin, T., Dai, F., Luo, X., and Lu, J. (2015). Effects of overlapping rate on the uniformities of surface profile of LY2 al alloy during massive laser shock peening impacts. *Surface and Coatings Technology*, 266:49–56.
- [95] Maleki, E., Bagherifard, S., Unal, O., Bandini, M., Farrahi, G. H., and Guagliano, M. (2021). Introducing gradient severe shot peening as a novel mechanical surface treatment. *Scientific Reports*, 11(1).
- [96] McCulloch, W. S. and Pitts, W. (1943). A logical calculus of the ideas immanent in nervous activity. *The Bulletin of Mathematical Biophysics*, 5(4):115–133.
- [97] Miao, H., Demers, D., Larose, S., Perron, C., and Lévesque, M. (2010). Experimental study of shot peening and stress peen forming. *Journal of Materials Processing Technology*, 210(15):2089–2102.
- [98] Miranda, S. S., Barbosa, M. R., Santos, A. D., Pacheco, J. B., and Amaral, R. L. (2018). Forming and springback prediction in press brake air bending combining finite element analysis and neural networks. *The Journal of Strain Analysis for Engineering Design*, 53(8):584–601.
- [99] Montgomery, D. C. (2001). *Design and Analysis of Experiments*. John Wiley & Sons, Inc., New York, 5th edition.
- [100] Moore, D. (1982). The application of shot peen forming technology to commercial aircraft wing skins. In *SAE Technical Paper Series*. SAE International.
- [101] Mordvintsev, A., Randazzo, E., Niklasson, E., and Levin, M. (2020). Growing neural cellular automata. *Distill*, 5(2).
- [102] Mura, T. (1987). *Micromechanics of defects in solids*. Springer Netherlands.
- [103] Mylavarapu, P., Bhat, C., Perla, M. K. R., Banerjee, K., Gopinath, K., and Jayakumar, T. (2021). Identification of critical material thickness for eliminating back reflected shockwaves in laser shock peening – a numerical study. *Optics & Laser Technology*, 142:107217.
- [104] Namba, Y. (1986). Laser forming in space. In *Proc. Int. Conf. Lasers' 85*, volume 403.
- [105] Nogueira, F. (2014–). Bayesian Optimization: Open source constrained global optimization tool for Python.

- [106] Ocaña, J., Correa, C., García-Beltrán, A., Porro, J., Díaz, M., de Lara, L. R., and Peral, D. (2015). Laser shock processing of thin al2024-t351 plates for induction of through-thickness compressive residual stresses fields. *Journal of Materials Processing Technology*, 223:8–15.
- [107] Ocaña, J., Morales, M., García-Ballesteros, J., Porro, J., García, O., and Molpeceres, C. (2009). Laser shock microforming of thin metal sheets. *Applied Surface Science*, 255(10):5633–5636.
- [108] Ocaña, J., Morales, M., Molpeceres, C., García, O., Porro, J., and García-Ballesteros, J. (2007). Short pulse laser microforming of thin metal sheets for MEMS manufacturing. *Applied Surface Science*, 254(4):997–1001.
- [109] O’Hara, P. (2002). Peen-forming - a developing technique. Conf Proc: ICSP-8, Garmisch-Partenkirchen, Germany.
- [110] O’Hara, P. (2006). Peen-forming - a developing technique. In *Shot Peening*, pages 215–226. Wiley-VCH Verlag GmbH & Co. KGaA.
- [111] O’Malley, T., Bursztein, E., Long, J., Chollet, F., Jin, H., Invernizzi, L., et al. (2019). Keras Tuner. <https://github.com/keras-team/keras-tuner>.
- [112] Pedregosa, F., Varoquaux, G., Gramfort, A., Michel, V., Thirion, B., Grisel, O., Blondel, M., Prettenhofer, P., Weiss, R., Dubourg, V., Vanderplas, J., Passos, A., Cournapeau, D., Brucher, M., Perrot, M., and Duchesnay, E. (2011). Scikit-learn: Machine learning in Python. *Journal of Machine Learning Research*, 12:2825–2830.
- [113] Pence, C., Ding, H., Shen, N., and Ding, H. (2013). Experimental analysis of sheet metal micro-bending using a nanosecond-pulsed laser. *The International Journal of Advanced Manufacturing Technology*, 69(1-4):319–327.
- [114] Peters, M., Hemptenmacher, J., Kumpfert, J., and Leyens, C. (2005). Structure and properties of titanium and titanium alloys. In *Titanium and Titanium Alloys*, pages 1–36. Wiley-VCH Verlag GmbH & Co. KGaA.
- [115] Petit-Renaud, F. (2006). Optimization of the shot peening parameters. In *Shot Peening*, pages 119–129. Wiley-VCH Verlag GmbH & Co. KGaA.
- [116] Peyre, P., Berthe, L., Scherpereel, X., Fabbro, R., and Bartnicki, E. (1998). Experimental study of laser-driven shock waves in stainless steels. *Journal of Applied Physics*, 84(11):5985–5992.
- [117] Peyre, P., Berthe, L., Vignal, V., Popa, I., and Baudin, T. (2012). Analysis of laser shock waves and resulting surface deformations in an al–cu–li aluminum alloy. *Journal of Physics D: Applied Physics*, 45(33):335304.

- [118] Peyre, P., Chaieb, I., and Braham, C. (2007). FEM calculation of residual stresses induced by laser shock processing in stainless steels. *Modelling and Simulation in Materials Science and Engineering*, 15(3):205–221.
- [119] Peyre, P. and Fabbro, R. (1995). Laser shock processing: a review of the physics and applications. *Optical and Quantum Electronics*, 27(12):1213–1229.
- [120] Pörtl, D., Keller, S., Chupakhin, S., Sala, S. T., Kashaev, N., and Klusemann, B. (2022). Numerical investigation of influence of spot geometry in laser peen forming of thin-walled Ti-6Al-4V specimens. *Key Engineering Materials*, 926:2293–2302.
- [121] Ponslet, E. and Steinzig, M. (2003). Residual stress measurement using the hole drilling method and laser speckle interferometry. part ii: analysis technique. *Experimental Techniques*, 27(4):17–21.
- [122] Qiao, H., Zhao, J., and Gao, Y. (2015). Experimental investigation of laser peening on TiAl alloy microstructure and properties. *Chinese J. Aeronaut.*, 28(2):609–616.
- [123] R, S., P, G., Gupta, R. K., G, R., Pant, B. K., Kain, V., K, R., Kaul, R., and Bindra, K. S. (2019). Laser shock peening and its applications: A review. *Lasers in Manufacturing and Materials Processing*, 6(4):424–463.
- [124] Ramati, S., Levasseur, G., and Kennerknecht, S. (1999). An overview of peen forming technology. pages 1–18. Conf Proc: ICSP-7, Warsaw, Poland.
- [125] Romero, P. E., Rodriguez-Alabanda, O., Molero, E., and Guerrero-Vaca, G. (2021). Use of the support vector machine (SVM) algorithm to predict geometrical accuracy in the manufacture of molds via single point incremental forming (SPIF) using aluminized steel sheets. *Journal of Materials Research and Technology*, 15:1562–1571.
- [126] Ruan, F., Feng, Y., and Liu, W. (2008). Springback prediction for complex sheet metal forming parts based on genetic neural network. In *2008 Second International Symposium on Intelligent Information Technology Application*. IEEE.
- [127] Ruder, S. (2016). An overview of gradient descent optimization algorithms.
- [128] Rumelhart, D. E., Hinton, G. E., and Williams, R. J. (1986). Learning representations by back-propagating errors. *Nature*, 323(6088):533–536.
- [129] Sagisaka, Y., Kamiya, M., Matsuda, M., and Ohta, Y. (2009). Thin-sheet-metal bending by laser peen forming with femtosecond laser. *Journal of the Japan Society for Technology of Plasticity*, 50(584):868–872.

- [130] Sagisaka, Y., Yamashita, K., Yanagihara, W., and Ueta, H. (2015). Microparts processing using laser cutting and ultra-short-pulse laser peen forming. *Journal of Materials Processing Technology*, 219:230–236.
- [131] Sala, S. T., Bock, F. E., Pörtl, D., Klusemann, B., Huber, N., and Kashaev, N. (2023a). Deformation by design: data-driven approach to predict and modify deformation in thin ti-6al-4v sheets using laser peen forming. *Journal of Intelligent Manufacturing*.
- [132] Sala, S. T., Keller, S., Chupakhin, S., Pörtl, D., Klusemann, B., and Kashaev, N. (2022). Effect of laser peen forming process parameters on bending and surface quality of Ti-6Al-4V sheets. *Journal of Materials Processing Technology*, 305:117578.
- [133] Sala, S. T., Körner, R., Huber, N., and Kashaev, N. (2023b). On the use of machine learning and genetic algorithm to predict the region processed by laser peen forming. *Manufacturing Letters*, 38:60–64.
- [134] Salimianrizi, A., Foroozmehr, E., Badrossamay, M., and Farrokhpour, H. (2016). Effect of laser shock peening on surface properties and residual stress of Al6061-T6. *Opt. Lasers Eng.*, 77:112–117.
- [135] Sana, G. (2020). Titanium sheet hot forming in the aerospace industry. *MATEC Web of Conferences*, 321:04020.
- [136] Sanchez, A. G., Leering, M., Glaser, D., Furfari, D., Fitzpatrick, M. E., Wharton, J. A., and Reed, P. A. S. (2021). Effects of ablative and non-ablative laser shock peening on AA7075-t651 corrosion and fatigue performance. *Materials Science and Technology*, 37(12):1015–1034.
- [137] Sano, Y., Mukai, N., Okazaki, K., and Obata, M. (1997). Residual stress improvement in metal surface by underwater laser irradiation. *Nuclear Instruments and Methods in Physics Research Section B: Beam Interactions with Materials and Atoms*, 121(1-4):432–436.
- [138] Scully, K. (1987). Laser line heating. *Journal of Ship Production*, 3(04):237–246.
- [139] Selamat, F., Cakar, S., and Kotan, M. (2022). Automatic detection and classification of defective areas on metal parts by using adaptive fusion of faster r-cnn and shape from shading. *IEEE Access*, 10:126030–126038.
- [140] Sharad, G. and Nandedkar, V. (2014). Springback in sheet metal u bending-fea and neural network approach. *Procedia Materials Science*, 6:835–839.

- [141] Siguerdidjane, W., Khameneifar, F., and Gosselin, F. P. (2020). Efficient planning of peen-forming patterns via artificial neural networks. *Manufacturing Letters*, 25:70–74.
- [142] Simard, R. and L'Ecuyer, P. (2011). Computing the two-sided kolmogorov-smirnov distribution. *Journal of Statistical Software*, 39(11).
- [143] Skinner, R. D. (1978). Stress-peen straightening of complex machined aircraft parts. In *Formability Topics-Metallic Materials - ASTM STP 647*, pages 100–121. American Society for Testing and Materials.
- [144] Smith, P., Shepard, M. J., Prev y III, P., and Clauer, A. (2000). Effect of power density and pulse repetition on laser shock peening of ti-6ai-4v. *Journal of Materials Engineering and Performance*, 9(1):33–37.
- [145] Soyama, H. (2019). Comparison between the improvements made to the fatigue strength of stainless steel by cavitation peening, water jet peening, shot peening and laser peening. *Journal of Materials Processing Technology*, 269:65–78.
- [146] Spradlin, T. J., Grandhi, R. V., and Langer, K. (2011). Experimental validation of simulated fatigue life estimates in laser-peened aluminum. *International Journal of Structural Integrity*, 2(1):74–86.
- [147] Sticchi, M., Schnubel, D., Kashaev, N., and Huber, N. (2014). Review of residual stress modification techniques for extending the fatigue life of metallic aircraft components. *Applied Mechanics Reviews*, 67(1).
- [148] Sticchi, M., Staron, P., Sano, Y., Meixer, M., Klaus, M., Rebelo-Kornmeier, J., Huber, N., and Kashaev, N. (2015). A parametric study of laser spot size and coverage on the laser shock peening induced residual stress in thin aluminium samples. *The Journal of Engineering*, 2015(13):97–105.
- [149] Stoerckle, D. D., Seim, P., Thyssen, L., and Kuhlenkoetter, B. (2016). Machine learning in incremental sheet forming. In *Proceedings of ISR 2016: 47st International Symposium on Robotics*, pages 1–7.
- [150] Su, B., Wang, H., Cao, Y., Pei, X., and Hua, G. (2020). Local deformation and macro distortion of TC4 titanium alloy during laser shock processing. *The International Journal of Advanced Manufacturing Technology*, 106(11-12):5421–5428.
- [151] Subramonian, S., Altan, T., Campbell, C., and Ciocirlan, B. (2013). Determination of forces in high speed blanking using FEM and experiments. *Journal of Materials Processing Technology*, 213(12):2184–2190.

- [152] Sweeney, K. and Grunewald, U. (2003). The application of roll forming for automotive structural parts. *Journal of Materials Processing Technology*, 132(1-3):9–15.
- [153] Takeshi, Y., Takayuki, T., Makoto, I., Shuzo, S., and Takahiro, O. (2002). Development of shot peening for wing integral skin for continental business jets. volume Vol.39 No.2, pages 57–61. Mitsubishi Heavy Industries Technical Review.
- [154] Trzepieciński, T. (2020). Recent developments and trends in sheet metal forming. *Metals*, 10(6):779.
- [155] Trzepieciński, T., Najm, S. M., Pepelnjak, T., Bensaid, K., and Szpunar, M. (2022). Incremental sheet forming of metal-based composites used in aviation and automotive applications. *Journal of Composites Science*, 6(10):295.
- [156] Virtanen, P., Gommers, R., Oliphant, T. E., and Haberland, e. a. (2020a). Scipy 1.0: fundamental algorithms for scientific computing in python. *Nature Methods*, 17(3):261–272.
- [157] Virtanen, P., Gommers, R., Oliphant, T. E., Haberland, M., Reddy, T., Cournapeau, D., Burovski, E., Peterson, P., Weckesser, W., Bright, J., van der Walt, S. J., Brett, M., Wilson, J., Millman, K. J., Mayorov, N., Nelson, A. R. J., Jones, E., Kern, R., Larson, E., Carey, C. J., Polat, İ., Feng, Y., Moore, E. W., VanderPlas, J., Laxalde, D., Perktold, J., Cimrman, R., Henriksen, I., Quintero, E. A., Harris, C. R., Archibald, A. M., Ribeiro, A. H., Pedregosa, F., van Mulbregt, P., and SciPy 1.0 Contributors (2020b). SciPy 1.0: Fundamental Algorithms for Scientific Computing in Python. *Nature Methods*, 17:261–272.
- [158] Volk, W., Groche, P., Brosius, A., Ghiotti, A., Kinsey, B. L., Liewald, M., Madej, L., Min, J., and Yanagimoto, J. (2019). Models and modelling for process limits in metal forming. *CIRP Annals*, 68(2):775–798.
- [159] Vollertsen, F. and Holzer, S. (1994). Laser beam forming - fundamentals and possible applications (in german). In *VDI-Z 136*, pages 35 – 38.
- [160] Wang, K.-S. (2013). Towards zero-defect manufacturing (ZDM)—a data mining approach. *Advances in Manufacturing*, 1(1):62–74.
- [161] Wang, M., Zeng, Y., Bai, X., and Lyu, F. (2020). Research on torsion deformation of integral stiffened panel by pre-stress shot peen forming. *Procedia Manufacturing*, 50:74–78. 18th International Conference on Metal Forming 2020.
- [162] Wang, T., Wang, J. B., Zhang, X. J., and Liu, C. (2021). A study on prediction of process parameters of shot peen forming using artificial neural network optimized by genetic algorithm. *Arabian Journal for Science and Engineering*, 46(8):7349–7361.

- [163] Wang, Z. and Rahman, M. (2014). *Comprehensive Materials Processing*, chapter 11.10 - High-speed machining. Elsevier, Oxford, pp. 221–253.
- [164] Wanhill, R. and Barter, S. (2011). Metallurgy and microstructure. In *Fatigue of Beta Processed and Beta Heat-treated Titanium Alloys*, pages 5–10. Springer Netherlands.
- [165] Watkins, K. G., Edwardson, S. P., Magee, J., Dearden, G., French, P., Cooke, R. L., Sidhu, J., and Calder, N. J. (2001). Laser forming of aerospace alloys. In *SAE Technical Paper Series*. SAE International.
- [166] Wu, B. and Shin, Y. C. (2005). A self-closed thermal model for laser shock peening under the water confinement regime configuration and comparisons to experiments. *Journal of Applied Physics*, 97(11):113517.
- [167] Xu, Y., Ren, X. D., Zhang, Y. K., Zhou, J. Z., and Zhang, X. Q. (2007). Coating influence on residual stress in laser shock processing. *Key Engineering Materials*, 353-358:1753–1756.
- [168] Yao, Y., Rosasco, L., and Caponnetto, A. (2007). On early stopping in gradient descent learning. *Constructive Approximation*, 26(2):289–315.
- [169] Yocom, C. J., Zhang, X., and Liao, Y. (2018). Research and development status of laser peen forming: A review. *Optics and Laser Technology*, 108:32–45.
- [170] Zhang, C., Dong, Y., and Ye, C. (2021). Recent developments and novel applications of laser shock peening: A review. *Advanced Engineering Materials*, 23(7):2001216.
- [171] Zhang, K. and Jiang, S. (2014). *Comprehensive Materials Processing*, chapter 5.18 - Superplastic forming. Elsevier, pp. 371–392.
- [172] Zhang, W. and Yao, Y. L. (2000). Improvement of laser induced residual stress distributions via shock waves. In *International Congress on Applications of Lasers and Electro-Optics*. Laser Institute of America.
- [173] Zhang, W., Yao, Y. L., and Noyan, I. C. (2004). Microscale laser shock peening of thin films, part 1: Experiment, modeling and simulation. *Journal of Manufacturing Science and Engineering*, 126(1):10–17.
- [174] Zhang, Y., Besshi, T., Tsuyama, M., Heya, M., and Nakano, H. (2023). Pliable solid medium as a plasma confinement layer for laser peening. *Journal of Laser Applications*, 35(1):012014.
- [175] Zhang, Y., Lu, J., and Luo, K. (2013). *Laser Shock Processing of FCC Metals*. Springer, Berlin, Heidelberg.

- [176] Zhong, R. Y., Newman, S. T., Huang, G. Q., and Lan, S. (2016). Big data for supply chain management in the service and manufacturing sectors: Challenges, opportunities, and future perspectives. *Computers & Industrial Engineering*, 101:572–591.
- [177] Zhou, J. Z., Fan, Y. J., Huang, S., Jiang, S. Q., and Du, J. J. (2008). Numerical simulation on laser peen forming of sheet metal. *Materials Science Forum*, 575–578:572–578.
- [178] Zhou, J. Z., Huang, S., Sheng, J., Fan, J., and Xu, Z. (2011). Theoretical calculation and numerical analysis of residual stress in laser peen forming of metal plate. *Key Engineering Materials*, 464:588–591.
- [179] Zhou, W. F., Ren, X. D., Wang, C. C., Yang, X. Q., and Larson, E. A. (2018). Residual stress induced convex bending in laser peen formed aluminum alloy. *Journal of Laser Applications*, 30(1):012001.

Curriculum vitae

| | |
|-----------------------|-----------------------|
| Family Name | Sala |
| Name | Siva Teja |
| Nationality | Indian |
| Date of Birth | 08 January, 1994 |
| Place of Birth | Visakhapatnam, India. |

| Time Period | Description |
|-------------------------------------|---|
| June 1999 - June 2009 | Primary and secondary education at Visakha Valley School, Visakhapatnam, India. |
| July 2009 - June 2011 | Senior secondary education at BHPV Senior Secondary School, Visakhapatnam, India. |
| July 2011 - August 2016 | Integrated dual degree programme at Andhra University - College of Engineering (A), Visakhapatnam, India. Bachelors (B.E) in Mechanical Engineering, Masters (M.E) in Machine Design. |
| October 2016 - November 2019 | M.Sc. Advanced Functional Materials at Technische Universität Chemnitz, Germany. |
| May 2018 - November 2019 | Graduate research assistant at Fraunhofer-Institut für Werkstoff- und Strahltechnik IWS, Dresden, Germany. |
| November 2019 - March 2020 | Preparation of applications for doctoral study. |
| April 2020 - December 2023 | Ph.D. student in the Department of Laser Material Processing and Structural Assessment at the Institute of Materials Research, Geesthacht, Germany. |
| Jan 2024 - Present | Materials Specialist at RIMOWA GmbH, Cologne, Germany. |
